High Resolution Imaging of Noise from Novel Integrated Propeller Systems

Malgoezar, Anwar

DOI
10.4233/uuid:93e4b064-c2fe-413f-b70b-9442a5a379ba

Publication date
2019

Document Version
Final published version

Citation (APA)
Malgoezar, A. (2019). *High Resolution Imaging of Noise from Novel Integrated Propeller Systems*. [Dissertation (TU Delft), Delft University of Technology]. https://doi.org/10.4233/uuid:93e4b064-c2fe-413f-b70b-9442a5a379ba

High Resolution Imaging of Noise from Novel Integrated Propeller Systems

High Resolution Imaging of Noise from Novel Integrated Propeller Systems

Proefschrift

ter verkrijging van de graad van doctor
aan de Technische Universiteit Delft,
op gezag van de Rector Magnificus prof. dr. ir. T. H. J. J van der Hagen,
voorzitter van het College voor Promoties,
in het openbaar te verdedigen op maandag 2 december 2019 om 12:30 uur

door

Anwar Masoed Naushahi MALGOEZAR

natuurkundig ingenieur, TU Delft, Nederland
geboren te 's-Gravenhage, Nederland.

Dit proefschrift is goedgekeurd door de promotor:

Prof. dr. D. G. Simons
Prof. dr. ir. L. L. M. Veldhuis

Copromotor: Dr. ir. M. Snellen

Samenstelling promotiecommissie:

Rector Magnificus,	voorzitter
Prof. dr. D. G. Simons,	Technische Universiteit Delft, promotor
Prof. dr. ir. L. L. M. Veldhuis,	Technische Universiteit Delft, promotor
Dr. ir. M. Snellen,	Technische Universiteit Delft, copromotor

Onafhankelijke leden:

Prof. dr. ir. G. J. T. Leus	Technische Universiteit Delft
Prof. dr. ir. M. Voskuijl	Nederlandse Defensie Academie
Prof. dr. ir. E. C. Slob	Technische Universiteit Delft
Prof. dr. ir. J. M. Hoekstra	Technische Universiteit Delft

Keywords: acoustic beamforming, numerical optimization, aeroacoustics, phased microphone array, array design

Printed by: IPSKAMP printing

Front & Back: Several microphones positioned in the field to record sound from an aircraft flyover.

ISBN 978-94-028-1843-7

An electronic version of this dissertation is available at
http://repository.tudelft.nl/.

Contents

Summary

Humans localize sound incessantly using the ears and it proves to be important of our awareness. It can also be a cause of annoyance to the community whenever sound is in the form of noise. Due to increase of wealth, industry, technology and corresponding globalization there is a large increase of noise. Especially with the increase of air traffic, noise is increased around the vicinities of airports. While environmental pollution is important and needs to be reduced, the accompanying noise is also of great importance. For example, while propeller-driven aircraft can be more efficient energy-wise, it also results in more noise compared to a traditional turbofan. For potential noise reduction it is necessary to first obtain both correct information about the origin and strength of these noise sources.

Similar to the human hearing, microphone arrays can be used to obtain both location and strength of sound sources. Identification of noise sources depends heavily on the hardware conditions and processing methods. In this thesis methods are presented to optimize the microphone array configuration and the post-processing part known as beamforming.

For microphone array optimization, several objective functions were formulated to capture the minimization goal. For source identification this was by reducing the false positives, known as sidelobes, and increasing the spatial resolution for the actual source. This resulted in several microphone configurations which reduced sidelobes in a predefined region-of-interest and simultaneously increased the spatial resolution.

High resolution methods were also developed, where the source localization process was optimized using a Global Optimization method. Here an objective function was formulated to minimize the error between measurement and a signal model. Super-resolution was achieved and identification is seen to be possible in all three spatial dimensions. Additionally, optimization was used to improve a current deconvolution method known as HR-CLEAN-SC achieving super-resolution with fast computation times.

The obtained microphone array from optimization and source localization methods were put to the test in the wind tunnel. An experiment was performed assessing the noise for pylon-propeller interaction. Clear noise increase was seen when a pylon was installed upstream the propeller. With blowing from the trailing-edge, noise was reduced comparable to the isolated propeller case. Beamforming showed noise primarily originated from the propeller and some originating from the support. Other experiments were performed regarding noise shielding. Cases

were studied of a propeller shielded by both a wing or duct as the shielding object. For theses cases shielding was observed if incoming flow is applied and the noise sources were seen to be positioned along the trailing and leading edges of both wing and duct.

The experiments proved that optimization methods are an important tool for both pre- and post-processing parts. Accuracy is improved for source localization and errors minimized when interpreting the beamform map.

Samenvatting

De mens is constant bezig geluid te lokaliseren met behulp van het gehoor. Dit kan vervolgens ook tot ergernis leiden voor de gemeenschap wanneer dit in de vorm van lawaai is. Door de toename van welvaart, industrie, technologie en de bijbehorende globalisering is er logischerwijs ook een behoorlijke toename in lawaai. Met name door de toename van vliegtuigverkeer, waar lawaai toeneemt in de nabijheid van de luchthaven. Alhoewel luchtvervuiling van de omgeving belangrijk is en verminderd moet worden, is het ook belangrijk om vliegtuiglawaai te verminderen. Als voorbeeld kan een op propeller aangedreven vliegtuig worden genomen. Hoewel dit meer efficiënt is in het gebruik van brandstof, produceert het ook meer lawaai vergeleken met een traditionele turbofan. Voor mogelijke geluidsvermindering is het belangrijk om eerst correcte informatie te verkrijgen van de oorsprong en de sterkte van de geluidsbronnen.

Net als het menselijk gehoor, kunnen gerangschikte microfoons gebruikt worden om zowel de locatie als wel het geluidsniveau te bepalen. Bepaling van de geluidsbronnen hangt sterk af van de gebruikte hardware als wel de verwerkingsmethodiek. In dit werk worden methoden gepresenteerd om de posities van zowel de microfoons als de geluidsbron te optimaliseren.

Voor het optimaliseren van gerangschikte microfoons, zijn verschillende objectieve functies geformuleerd welke de minimalisatie doel bevatten. Voor het identificeren van geluidsbronnen werd dit gerealiseerd door de vals positieven, ook bekend als zijlussen, te verminderen en het scheidend vermogen van de werkelijke bron te verbeteren. Ook zijn er hoge resolutie methoden ontwikkeld, waarbij lokalisatie voor de bron positie is toegepast met behulp van een globale optimalisatiealgoritmen. Hierbij was de objectieve functie zo geformuleerd om het verschil tussen metingen en signaal model te minimaliseren. Het resultaat is superresolutie en de mogelijkheid om de geluidsbron te bepalen in drie dimensies. Ook is optimalisatie gebruikt om een huidige deconvolutie methode te verbeteren bekend als HR-CLEAN-SC waar ook superresolutie is gerealiseerd met korte verwerkingstijden.

De verkregen microfoon posities uit het optimalisatie proces en de hoge resolutie methoden zijn toegepast voor wind tunnel metingen. Een experiment is uitgevoerd voor een pilaar-propeller interactie. Een duidelijke geluidstoename was te zien bij de installatie van de pilaar stroomopwaarts. Met behulp van een extra luchtstroom uit de achterrand van de pilaar was te zien dat het geluid nagenoeg

gereduceerd was tot de situatie met enkel de propeller. Ook andere experimenten zijn onderzocht voor afscherming van propeller geluid. Metingen zijn gedaan waarbij een propeller afgeschermd werd door een vleugel of een duct. Voor beide gevallen was te zien dat geluid gereduceerd wordt wanneer een inkomende luchtstroom wordt aangebracht. Met behulp van bundelvorming was te zien dat de geluidsbronnen op de voor- en achterrand worden gelokaliseerd voor zowel de vleugel als de duct.

De experimenten lieten zien dat het gebruik van optimalisatie technieken een belangrijk hulpmiddel is voor zowel voor- als nabewerking van het geluidslokalisatie proces. De precisie van het proces wordt verbeterd en daardoor interpretatiefouten van de geluidsbronnenmap verminderd.

1

Introduction

1.1. Motivation

The sector of air transport is one of the fastest growing transportation sectors around the world [1–3]. The increasing demand [4] of travel leads to the increase of airports or the desire to expand. Inevitably, this increases pollution, decreases safety and increases noise levels in densely populated areas. Most importantly, there will be an increase of fuel consumption. The public concern is to have less impact of flying on the environment through the emissions of greenhouse gases and noise. It is therefore desirable to decrease the fuel consumption with growing air traffic, while at the same time keep pollution and noise levels low. Aircraft design studies have shown a 10 to 20% fuel burn reduction by replacing turbofans with modern propellers of equivalent technology [5].

Propeller driven aircraft can provide this potential reduction of fuel burn compared to high bypass ratio turbofan engines. The trade-off for using propeller driven aircraft is the increase in noise. While advanced turbofan can provide noise reduction, the fuel consumption is still not as low as using a propeller or open rotor propulsion [6], see Fig 1.1. This can be a difficult issue to solve and both the scientific community and aircraft manufacturers are constantly at work to improve aircraft in this regard.

Similar to the turbofan, a propeller can also be made to be ducted. The duct can then act as a shielding object to reduce noise. Additionally, noise can also be shielded by simpler geometries like a wing. Research have shown recently that aircraft noise can be reduced significantly by shielding the noise by airframe structures [7–9]. It is considered an effective way of reducing the air traffic noise [10–12]. To assess quantitatively to which extent noise is reduced and where noise originates from the shielding object, source localization will be applied in two experiments described in this thesis.

For assessing these kind of aircraft noise, detailed noise investigations to both localizing noise sources and quantifying the levels are required.

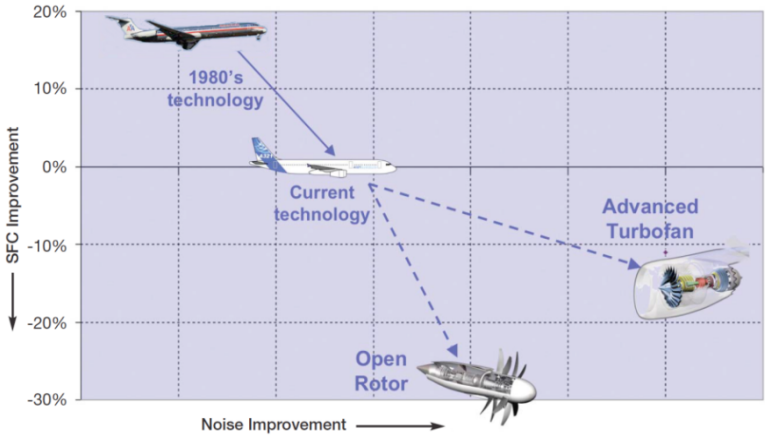

Figure 1.1: Current trend in the specific fuel consumption (SFC) versus the noise improvement.

1.2. Use of microphone arrays

Microphone arrays are a powerful tool to obtain spatial information of acoustic sources. With recorded sound data, beamforming can be applied to perform source localization and in turn identify noise sources for an aircraft flyover or parts of an aircraft in a wind tunnel setting. In aerospace and aeroacoustic studies, this has been used in various aspects, ranging from outdoor beamforming of fly-over aircraft [13], to beamforming for aeroacoustic studies in wind tunnels [14]. Further investigations of the source maps help researchers to understand characteristics of contributing noise sources. With these results a better understanding can be obtained for aircraft noise sources such as propellers or the airframe [15–20]. The obtained information allows manufacturers to more accurately include noise consideration in the development of an aircraft. The arrays are used in other fields as well, e.g. for high-speed trains or automotive vehicles [21–26].

The first system to use microphones as a way to localize sound sources was proposed in 1974 by Billingsley [27] with the use of a so-called acoustic telescope. A corresponding hardware system was presented as well [28] for real-time source localization on jet engines. Fourteen condenser microphones were used and digitized for the pressure values by 8 bits. For the time sampling 20 kHz was used. The data was also stored on magnetic tapes. Using two analog to digital converters a multiplexer (not all microphone values can be captured at the same instant) for the 14 channels with a sampling interval of 6 µs was used. This resulted in a spread of $7 \times 6\,\mu s = 36\,\mu s$ between microphones. The spread was not accounted for during the algorithm. The computer used consisted of 48 kilobytes of memory and the results were displayed on a colour coded TV screen.

The following decades saw a decrease in the cost of equipment and sampling frequency, digital resolution and memory increased dramatically. As a result a large number of microphones could be used. With the increasing possibilities of hardware, questions were raised for the microphone positioning. For example, po-

sitioning microphones on a plane allows to perform 2-D beamforming, but performance depends heavily on the relative microphone positions, or the beamforming method used.

Ideal source maps should visualize the sound sources at their correct locations. When there are multiple sources, the sources should be separable. Moreover, false positive source identifications due to side lobes should be minimized. These qualities in the source maps indicate the beamforming performance, and can be improved in two ways.

A first attempt at microphone optimization was done by Michel *et al.* [17] for flyover tests using 15 microphones. The used array resulted in the discovery that many aircraft emit tones from the wings. These are now known to be caused by cavities on the wing's surface. Other methods such as nested arrays [29], irregular or spiral-like configurations [30, 31] were investigated as well.

With the increased use of microphone arrays, investigations were also performed for the post-processing part which deals with the beamforming algorithm. Advanced methods have been developed and investigated to increase acoustic source localization. As the beamform result is degraded by the point spread function, deconvolution methods have been developed. However, the performance of it depends on the quality of the array design. The methods usually have some way for handling false positive source identification, dealing with coherent sources (or not), and the spatial resolution.

The two aspects of array optimization (pre-processing) and use of advanced beamforming methods (post-processing) are usually done separately. The interplay between optimized array designs and advanced beamforming algorithms has also not been investigated. The use of optimization techniques for both the pre- and post-processing parts can especially be interesting for the investigation of aircraft noise. The optimization procedures can be tailored to aeroacoustic studies by imposing the corresponding conditions.

1.3. Research objective

The aim of this research is to investigate how optimization methods can help to improve acoustic source identification. For the identification both location and strength of sound sources are important. The procedure will be focused for aircraft noise sources. Both optimization of the microphone positions (hardware part) as well as optimization of the source localization capability (software part) will be investigated. An optimized array will be searched with specific criteria imposed. The obtained parameter set from optimization are therefore the microphone positions. For optimizing the source localization process, it is investigated if global optimization techniques can correctly obtain the parameter set containing the coordinates for the source position(s). Additionally it will be tested if (unknown) environmental parameters can be introduced as well. For using optimization methods so-called objective functions are needed which need to be minimized. These functions captures the minimization goal. Therefore objective functions will be searched for deriving from signal models. It will also be investigated if optimization can improve existing deconvolution methods.

The developed methods are then tested using wind tunnel experiments. As noise sources speaker sources and propellers are used. For the first experiment the methods will be applied to study pylon-propeller interaction effects. A second experiment deals with shielding of noise sources where a wing and a duct are used as the shielding object.

The objectives can be summarized as follows:

- Optimize microphone array configurations;
- Optimize the source localization process;
- Apply methods to wind tunnel experiments.

1.4. Outline

As optimization and the beamforming procedure is important for deriving the objective functions, Chapter 2 will present the theory used throughout this thesis. The signal model at the microphones will be derived, beamforming methods presented and the used global optimization method introduced. Improving the current deconvolution beamforming method (CLEAN-SC) using optimization (HR-CLEAN-SC), will be presented as well.

Chapter 3 continues with presenting two kinds of array optimizations (Array Optimization I and II). Here, the objective functions are presented and tested for simulated and experimental data. Chapter 4 investigates the use of optimization for source localization. After obtaining appropriate objective functions, tests are performed for benchmark data and an experiment using a speaker.

Chapter 5 applies the HR-CLEAN-SC method developed in Chapter 2 to wind tunnel data for pylon-propeller interaction. It is also investigated how noise of the propeller is affected by negation of the wake of the pylon. Negation is realized by blowing of from the pylon's trailing edge. For the investigation conventional beamforming is presented as well.

A second wind tunnel test is investigated in Chapter 6. Here, several experiments were performed to assess shielding of noise. As sources an omni-directional sound sound and a propeller are used. For the shielding object a rectangular plate, NACA wing as well as a duct are used. The experiments are performed with the optimized array resulting from Chapter 3.

Chapter 7 presents the summary and conclusions of the work in this thesis.

References

[1] C. Lu and P. Morrell, *Determination and applications of environmental costs at different sized airports - aircraft noise and engine emissions*, Transportation **33**, 45 (2006).

[2] D. Chiron, *European research in the area of aeronautics and air transport*, in *Presented at Eur. Workshop New Aero Engine Concepts, Munich* (2010).

[3] I. A. T. Association, *Demand for air travel in 2015 surges to strongest result in five years,* (2016).

[4] M. Abramowitz and I. A. Stegun, *Handbook of mathematical functions: with formulas, graphs, and mathematical tables*, 55 (Courier Corporation, 1964).

[5] M. D. Guynn, J. J. Berton, W. J. Haller, E. S. Hendricks, and M. T. Tong, *Performance and environmental assessment of an advanced aircraft with open rotor propulsion*, Tech. Rep. (NASA-TM-2012-217772, 2012).

[6] N. Peake and A. B. Parry, *Modern challenges facing turbomachinery aeroacoustics,* Annual Review of Fluid Mechanics **44**, 227 (2012), https://doi.org/10.1146/annurev-fluid-120710-101231 .

[7] R. H. Thomas, C. L. Burley, and E. D. Olson, *Hybrid wing body aircraft system noise assessment with propulsion airframe aeroacoustic experiments,* International Journal of Aeroacoustics **11**, 369 (2012).

[8] M. J. Czech, R. H. Thomas, and R. Elkoby, *Propulsion airframe aeroacoustic integration effects for a hybrid wing body aircraft configuration*, **11**, 335 (2012).

[9] J. T. Bonet, H. G. Schellenger, B. K. Rawdon, K. R. Elmer, S. R. Wakayama, D. L. Brown, and Y. P. Guo, *Environmentally responsible aviation (era) project-n+ 2 advanced vehicle concepts study and conceptual design of subscale test vehicle (stv) final report*, (2011).

[10] A. Agarwal and A. P. Dowling, *The calculation of acoustic shielding of engine noise by the silent aircraft airframe,* The Journal of the Acoustical Society of America **116**, 25 (2005).

[11] Y. P. Guo, C. L. Nickol, C. L. Burley, and R. H. Thomas, *Noise and fuel burn reduction potential of an innovative subsonic transport configuration,* AIAA Paper 2014-0257 (2014).

[12] Y. P. Guo, C. L. Burley, and R. H. Thomas, *On noise assessment for blended wing body (bwb) aircraft*, (2014).

[13] D.G.. Simons, M. Snellen, B. van Midden, M. Arntze, and D.H.T.. Bergmans, *Assessment of noise level variations of aircraft flyovers using acoustic arrays,* Journal of Aircraft **52**, 1625 (2015).

[14] S. Oerlemans, L. Broersma, and P. Sijtsma, *Quantification of airframe noise using microphone arrays in open and closed wind tunnels,* International Journal of Aeroacoustics **6**, 309 (2007).

[15] G. P. Howell, M. A. Bradley, M. A. McCormick, and J. D. Brown, *De-Dopplerization and acoustic imaging of aircraft Flyover noise measurements,* Journal of Sound and Vibration **105**, 151 (1986).

[16] U. Michel, B. Barsikow, B. Haverich, and M. Schuttpelz, *Investigation of airframe and jet noise in high-speed flight with a microphone array,* in *3rd AIAA/CEAS Aeroacoustics Conference, Atlanta, Ga, May 12-14, 1997* (1997).

[17] U. Michel, B. Barsikow, J. Helbig, M. Hellmig, and M. Schuttpelz, *Flyover noise measurements on landing aircraft with a microphone array,* in *4th AIAA/CEAS Aeroacoustics Conference, Toulouse, France, June 2-4, 1998* (1998).

[18] U. Michel and W. Qiao, *Directivity of landing gear noise based on flyover measurements,* in *5th AIAA/CEAS Aeroacoustics Conference, Bellevue, Wa, May 10-12, 1999* (1999).

[19] R. P. Dougherty, *Beamforming for aircraft noise measurements,* Acoustical Society of America Journal **114**, 2339 (2003).

[20] P. Sijtsma and R. Stoker, *Determination of Absolute Contributions of Aircraft Noise Components Using Fly-over Array Measurements,* in *10th AIAA/CEAS Aeroacoustics Conference, Manchester, United Kingdom, 10-12 May 2004* (2004).

[21] W. F. King III and D. Bechert, *On the Sources of Wayside Noise Generated by High-Speed Trains,* J. Sound Vib. **66**, 311 (1979).

[22] B. Barsikow, W. F. King III, and E. Pfizenmaier, *Wheel/Rail Noise Generated by a High-Speed Train Investigated with a Line Array of Microphones,* J. Sound Vib. **118**, 99 (1987).

[23] B. Barsikow and W. F. King III, *On Removing the Doppler Frequency Shift from Array Measurements of Railway Noise,* J. Sound Vib. **120**, 190 (1988), letter to the editor.

[24] B. Barsikow, *Experiences with various configurations of microphone arrays used to locate sound sources on railway trains operated by the DB AG,* J. Sound Vib. **193**, 283 (1996).

[25] U. Michel and B. Barsikow, *Localisation of sound sources on moving vehicles with microphone arrays.* in *Proc. EuroNoise 2003, Neapel, 19.-21.05.2003*, paper ID 537 (2003).

[26] U. Michel, B. Barsikow, P. Bohning, and M. Hellmig, *Localisation of moving sound sources with phased microphone arrays,* in *Inter-Noise 2004, Prague, Czech Republic, 22-25 August 2004* (2004).

[27] J. Billingsley, *An acoustic telescope,* Aeronautical Research Council ARC 35/364, 1974 (1974).

[28] J. Billingsley and R. Kinns, *The Acoustic Telescope,* J. Sound Vib. **48**, 485 (1976).

[29] C. O. Paschereit and B. Barsikow, *The microphone array: a tool on the path towards reducing railway noise,* in *Proc. World Congress on Railway Research (WCRR '94)* (1994) pp. 371–376, proc. World Congress on Railway Research (WCRR '94), Paris, 1994.

[30] M. Mosher, *Phased Arrays for Aerocoustic Testing: Theoretical Development*, in *2nd AIAA/CEAS Aeroacoustics Conference, State College, Pa, May 6-8, 1996* (1996).

[31] C. Schulze, E. Sarradj, and A. Zeibig, *Characteristics of microphone arrays*, in *Inter-Noise* (2004).

2

Theory

In this chapter a description is given of the basic formulations in acoustics for a better understanding of subsequent sections and chapters. Starting with the acoustic wave equation, the expression for the pressure field is derived for a point source with and without a convective medium. This is used for establishing a model for the acoustic signals arriving at the microphones. The model is important for understanding the underlying physics of the signals at the microphones. The availability of a microphone array allows for the localization and quantification of individual sound sources, also known as acoustic beamforming. Several methods for beamforming will be discussed. The chapter is ended by explaining a high resolution deconvolution method allowing to surpass the conventional beamforming limits.

Parts of this chapter have been published in the International Journal of Aeroacoustics **16**, 274 (2017) [1].

2.1. The acoustic wave equations

This chapter describes the formulations in acoustics and presents solutions to the wave equation. The solution is of importance when the signal at the microphones needs to be modelled in Section 2.3 or beamforming needs to be applied as explained in Section 2.4.

2.1.1. Linear wave equation: no source

For the simple case where the region under consideration does not contain any source, is a lossless medium and has no wind flow (i.e. no convection) the following wave equation holds [2]

$$\nabla^2 p(\vec{x},t) - \frac{1}{c^2}\frac{\partial^2}{\partial t^2} p(\vec{x},t) = 0, \tag{2.1}$$

where $p(\vec{x},t)$ is the sound pressure field at position $\vec{x} = (x,y,z)$ at time t and c the speed of sound. Equation (2.1) is also known as the homogeneous wave equation due to the lack of a source or source distribution.

Transforming Eq. (2.1) to the frequency domain results in the Helmholtz equation

$$\nabla^2 p(\vec{x},\omega) + \left(\frac{\omega}{c}\right)^2 p(\vec{x},\omega) = 0, \tag{2.2}$$

with $\omega = 2\pi f$ the angular frequency. The solution of both Eqs. (2.1) and (2.2) can be constructed of plane waves.

If spherical acoustic waves are considered, it is convenient to write Eq. (2.1) in spherical coordinates using $\nabla^2 \rightarrow \frac{1}{r^2}\frac{\partial}{\partial r}\left(r^2\frac{\partial}{\partial r}\right)$ as

$$\frac{1}{r^2}\frac{\partial}{\partial r}\left(r^2\frac{\partial p}{\partial r}\right) - \frac{1}{c^2}\frac{\partial^2 p}{\partial t^2} = 0, \tag{2.3}$$

with $r = \sqrt{x^2+y^2+z^2}$. The general solution of Eq. (2.3) is

$$p(r,t) = \frac{1}{r}\left[f(t-r/c) + g(t+r/c)\right], \qquad r \neq 0, \tag{2.4}$$

where f is a *diverging* and g a *converging* spherical wave. From the argument of causality, only outgoing, i.e. diverging, spherical waves will be considered, i.e. $g = 0$. The solution of such a wave then is

$$p(r,t) = \frac{1}{r} f(t-r/c), \tag{2.5}$$

in the time domain and

$$p(r,\omega) = F(\omega)\frac{\mathrm{e}^{-j\omega r/c}}{r}, \qquad r \neq 0, \tag{2.6}$$

in the frequency domain. $F(\omega)$ is the Fourier Transform of $f(t)$ defined as

$$F(\omega) = \frac{1}{2\pi}\int_{-\infty}^{\infty} f(t)\mathrm{e}^{-j\omega t}\,dt. \tag{2.7}$$

In the case the signal only consists of a harmonic of frequency ω with amplitude A, Eq. (2.6) can be written as

$$p(r,\omega) = A\frac{e^{-j\omega r/c}}{r}, \qquad r \neq 0. \tag{2.8}$$

2.1.2. Linear wave equation: point source

In the case a field is considered with a point source, Eq. (2.1) changes to an inhomogeneous equation as

$$\nabla^2 p(\vec{x},t) - \frac{1}{c^2}\frac{\partial^2}{\partial t^2} p(\vec{x},t) = -\sigma(t)\delta(\vec{x}-\vec{x}_s), \tag{2.9}$$

where $\sigma(t)$ is the source emitted signal, $\delta(\vec{x}-\vec{x}_s)$ the Dirac delta function and $\vec{x}_s$ the source position. From the Fourier transformation Eq. (2.9) becomes

$$\nabla^2 p(\vec{x},\omega) + \frac{\omega^2}{c^2} p(\vec{x},\omega) = -\sigma(\omega)\delta(\vec{x}-\vec{x}_s), \tag{2.10}$$

where $\sigma(\omega)$ can be seen as the amplitude and phase of the signal for the frequency ω. Here it can be recognized that $p(\vec{x},\omega) \rightarrow g(\vec{x},\omega)$ is the Green's function for the equation of

$$\nabla^2 g(\vec{x},\omega) + \left(\frac{\omega}{c}\right)^2 g(\vec{x},\omega) = -\delta(\vec{x}-\vec{x}_s), \tag{2.11}$$

where $g(\vec{x})$ can be seen as the impulse response of the differential equation. This is solved using the Sommerfeld radiation condition [3] to obtain the Green's function[1] for Eq. (2.11) by

$$g(\vec{x}) = \frac{e^{-j\omega r/c}}{4\pi r}, \tag{2.12}$$

where $r = \|\vec{x}-\vec{x}_s\|$. The distance r is the separation distance between the source and the point of interest (e.g. a microphone position) as seen in Fig. 2.1. Using the

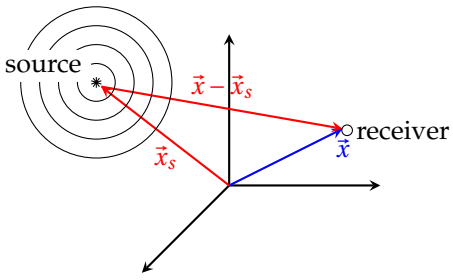

Figure 2.1: Relation between the source vector $\vec{x}_s$ and receiver vector $\vec{x}$.

[1] Note that by using the Green's function from this equation any source distribution can be considered and the solution can be constructed by convolving the Green's function with the source distribution function as $p(\vec{x},\omega) = g(\vec{x},\omega) * \rho(\vec{x})$ if $\rho(\vec{x})$ is the source distribution in space.

Green's function Eq. (2.12), the solution to Eq. (2.10) is easily obtained as

$$p(\vec{x},\omega) = \sigma(\omega)\frac{\mathrm{e}^{-j\omega r/c}}{4\pi r}. \tag{2.13}$$

The solution in the time domain of Eq. (2.9) has therefore the form

$$p(\vec{x},t) = \frac{\sigma(t-r/c)}{4\pi r}. \tag{2.14}$$

2.1.3. Convective wave equation of a point source

When considering wind tunnel experiments or fly-over applications the convective term which is neglected in Eqs. (2.1) and (2.9) has to be taken into account. With the inclusion of convection the following partial differential equation holds for a point source [4–6]

$$\nabla^2 p(\vec{x},t) - \frac{1}{c^2}\left(\frac{\partial}{\partial t} + \vec{U}\cdot\nabla\right)^2 p(\vec{x},t) = -\sigma(t)\delta(\vec{x}-\vec{x}_s), \tag{2.15}$$

where $\vec{U}$ is the uniform flow and the right hand side represents again the acoustic source.

The solution to Eq. (2.15) is given by [7]

$$p(\vec{x},t) = \frac{\sigma(t-\Delta t_\mathrm{e})}{4\pi\sqrt{\left[\vec{M}\cdot(\vec{x}-\vec{x}_s)\right]^2 + \beta^2\left\|\vec{x}-\vec{x}_s\right\|^2}}, \tag{2.16}$$

where

$$\beta^2 = 1 - \vec{M}\cdot\vec{M} = 1-(U/c)^2, \tag{2.17}$$

and $\vec{M}$ is a vector of Mach numbers given by

$$\vec{M} = \frac{\vec{U}}{c}. \tag{2.18}$$

The time emission delay is given by Δt_e as

$$\Delta t_\mathrm{e} = \frac{1}{c\beta^2}\left\{-\vec{M}\cdot(\vec{x}-\vec{x}_s) + \sqrt{\left[\vec{M}\cdot(\vec{x}-\vec{x}_s)\right]^2 + \beta^2\left\|\vec{x}-\vec{x}_s\right\|^2}\right\}, \tag{2.19}$$

from which it is noted that the distance r/c of Eq. (2.14) gets 'adapted' by Eq. (2.19) in the numerator. In the denominator there is an additional term in the square-root determined by the factor β. Note that Eq. (2.19) reduces to Eq. (2.14) for $\beta = 0$.

In the frequency domain, and using a notation more resembling Eq. (2.13), the solution can be written by a changing r as

$$p(\vec{r},\omega) = \frac{\sigma(\omega)\mathrm{e}^{-j\omega r''/c}}{4\pi r'}, \tag{2.20}$$

with

$$r' = \sqrt{\delta r^2 + \beta^2 r^2}, \tag{2.21}$$

$$r'' = \frac{1}{\beta^2}\left(-\delta r + r'\right), \tag{2.22}$$

from which is seen that the distances get adapted by β and

$$\delta r = \vec{M} \cdot (\vec{x} - \vec{x}_s). \tag{2.23}$$

If $\vec{M} = 0$ then $r' \to r$, $r'' \to r$ and Eq. (2.20) reduces to Eq. (2.13).

Equation (2.20) can be seen as an expression where the time delay due to wind changes. The distances of r'' for the delay and r' for the geometrical spreading differ. This can be understood by thinking that while the wavefront[2] can either be delayed or ahead r''/c due to the flow, the *actual* distance travelled r' is still different affecting the actual propagation distance. That is, the time it takes for a point on the wavefront to reach the observer can be longer (or shorter) than the actual distance travelled related by the speed of sound c. The delay can be related to a 'distance', in this case r'', as $\Delta t_e = r''/c$ which determines the time delay.

Equations (2.13) and (2.20) are of importance for source localization process, using either beamforming or optimization methods explained in the next sections.

2.2. Sound pressure level

When sound propagates it consists of small disturbances as deviations from the ambient pressure value which are compressions and rarefactions in the medium such as air. The human hearing is able to detect a wide range of sound pressures and, like other senses, behaves logarithmically [8]. The sound pressure level (SPL) is therefore defined in dB as

$$L_\mathrm{p} = 10\log_{10}\left(\frac{p_\mathrm{rms}^2}{p_0^2}\right), \tag{2.24}$$

where $p_0 = 20\,\mu\mathrm{Pa}$ is the reference pressure and p_rms is determined over the time signal using

$$p_\mathrm{rms} = \sqrt{\frac{1}{T}\int_0^T p^2(t)\mathrm{d}t} \tag{2.25}$$

with T the duration of the signal.

In this work the sound is recorded using a microphone array. This gives the flexibility for both single and multiple microphone analysis. Equation (2.24) would then be determined for a single microphone

For assessing the noise reduction by a shielding object for a single microphone, the noise reduction factor ΔL_p in dB can be used, given by a ratio of the root-mean-square (RMS) signals

$$\Delta L_\mathrm{p} = 20\log_{10}\left(\frac{p_\mathrm{rms}^\mathrm{object}}{p_\mathrm{rms}^\mathrm{source}}\right). \tag{2.26}$$

In the experiment this factor is obtained from the case where the source is obstructed by an object, $p_\mathrm{rms}^\mathrm{object}$, and when only the source is positioned, $p_\mathrm{rms}^\mathrm{source}$. For

[2] The wavefront is characterized by a locus of points which have identical phase.

the case of propeller noise Eq (2.26) is typically evaluated over frequencies corresponding to the blade-passage-frequency or its harmonics. Then a bandpass filter is used with an appropriate bandwidth. In this thesis an 80 Hz bandwidth is used.

In order to obtain the narrowband frequency spectrum of the source the *Spectrum Level* is used. First the power spectral density (PSD) is first obtained the individual microphones. To obtain the Spectrum Level, the PSD is integrated over consecutive (narrow) frequency bands to obtain the root mean square of the pressure signal over the given band. In this work a band of 5 Hz is chosen. The Spectrum Level relative to $p_0 = 20\,\mu\text{Pa}$ is then obtained as

$$L_\text{p}(\omega_\text{band}) = 10\log_{10}\left(\frac{\int_\text{band} S(\omega)\text{d}\omega}{p_0^2}\right), \tag{2.27}$$

for the PSD given by $S(\omega)$ for frequency ω. Note that Eq. (2.27) reduces to Eq. (2.24) if the band encompasses the whole frequency range of the signal. This follows from Parseval's theorem. Equation (2.27) is also evaluated in later chapters over the array. To obtain this the average PSD is taken for all the microphones. The averaged PSD is then used in Eq. (2.27) to obtain the Spectrum Level over the array. This will be used in both Chapters 5 and 6. When interpreting spectrum levels one always has to take into account over which frequency band the value is evaluated. Using a larger band will result in a higher levels than a smaller band.

2.3. The signal model

In order to understand beamforming, a general description of the signals at the microphones needs to be formulated. Consider an acoustic source given by $s(t)$, the sound pressure at a distance r can then be given as

$$p(t) = as(t - t'), \tag{2.28}$$

where the factor a is a factor indicating the *transfer* of the signal to the distance r and t' the time delay. That is, the pressure signal is a time delayed and scaled version of the source signal. The time delay is due to the distance the wave needs to travel as seen in the previous section and is given by

$$t' = r/c, \tag{2.29}$$

where c is the speed of sound and r the distance between the source and a given observation point. The value a can depend on the type of source and environmental conditions. The expression for a for the case of a point source was derived in the previous section to be $a = 1/4\pi r$ for the simple case of no wind, corresponding to the free-field Green's function of the Helmholtz equation. A more advanced expression was given as well with wind. To keep it general the function a will be used throughout this section. This can represent any sound source mechanism such as absorption, non-uniform directivity or propagation through non-uniform media [9].

If the frequency domain of the signal in Eq. (2.28) is considered, the time shift will correspond to a phase shift and Eq. (2.28) together with Eq. 2.29 can be written as[3]

$$p(\omega) = ae^{-j\omega r/c}s(\omega), \tag{2.30}$$

with ω the frequency considered and $s(\omega)$ the Fourier transform of the source $s(t)$.

In Figure 2.2 the case of several observation points, which can correspond to microphone positions, and a single source can be seen.

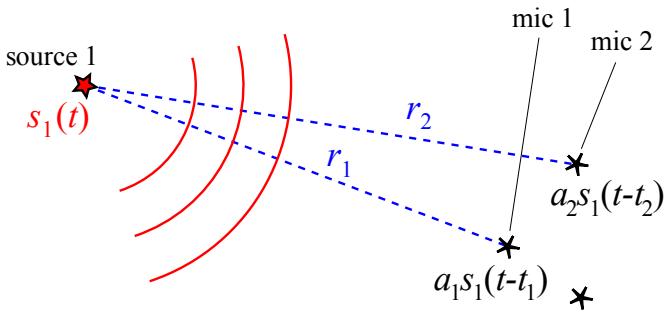

Figure 2.2: Depiction of a single source indicated by the red star and microphones given by the black stars.

Here the case of a hypothetical three-microphone array is depicted by the black stars with a source $s_1(t)$. The corresponding scaled and time delayed pressure time signals are noted in the figure. As the positions differ, the time delays can differ as well. The factor a, which depends on the distance, will also differ between positions. Generally for N positions, or an N-microphone array, the expression for the pressure time signals at the microphones is

$$\mathbf{p}_1(t) = \begin{bmatrix} a_1 s_1(t-t_1) \\ \vdots \\ a_N s_1(t-t_N) \end{bmatrix}. \tag{2.31}$$

Using Eq.(2.30) the expression for frequency domain signal becomes

$$\mathbf{p}_1(\omega) = \begin{bmatrix} a_1 e^{-j\omega r_1/c} s_1(\omega) \\ \vdots \\ a_N e^{-j\omega r_N/c} s_1(\omega) \end{bmatrix} = \mathbf{a}(\omega) s_1(\omega), \tag{2.32}$$

[3]The transfer function a is considered not to be dependent on time.

Note that the subscript for the source stays the same, as the influence of only one source s_1 is considered. The vector $\mathbf{a}$ is known as the *transfer vector* containing both the factors a and phase shifts $e^{-j\omega r/c}$. The convenience of working in the frequency domain can be noted from this, as it allows for easy factorization of the transfer vector $\mathbf{a}$ and source s_1 for the given frequency ω.

The expression for the pressure signals at the microphones can be extended to include more than one source. As an example, in Figure 2.3 two sources can be seen together with the expression for the received signal at the microphones. For the variables containing two subscripts, the first indicates which source is considered and the second which microphone. The subscript can be read as

$$\boxed{\text{subscript } (k,n)\text{: source } k \text{ to microphone } n.} \tag{2.33}$$

It can be seen that the distance, and thus the corresponding time delay and factor a, will differ for the given pair of source and microphone position.

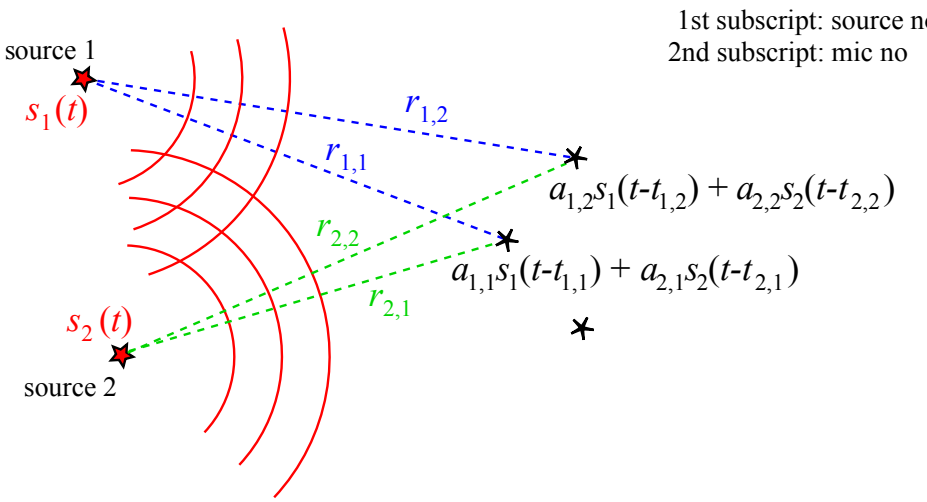

Figure 2.3: Depiction of two sources, s_1 and s_2, and the corresponding expressions for the received signals at the microphones. For a single microphone the contribution of both sources needs to be taken into account.

The gist is that for an arbitrary amount of sources the contribution of *every* source must be taken into account for a given microphone position. In the frequency domain the expression will be a summation of the form of Eq. (2.30) for the different sources. For K sources and a single microphone (indicated by number 1) this can be given as

$$\begin{aligned} p_{\text{multi}}(\omega) &= a_{1,1}e^{-j\omega r_{1,1}/c}s_1(\omega) + \cdots + a_{K,1}e^{-j\omega r_{K,1}/c}s_K(\omega) \\ &= \sum_{k=1}^{K} a_{k,1}e^{-j\omega r_{k,1}/c}s_k(\omega). \end{aligned} \tag{2.34}$$

For a set of microphones Eq. (2.34) has to be repeated for all the positions, the signal at the microphones will then have the form

$$\mathbf{p}(\omega) = \begin{bmatrix} \sum_{k=1}^{K} a_{k,1} e^{-j\omega r_{k,1}/c} s_k \\ \vdots \\ \sum_{k=1}^{K} a_{k,N} e^{-j\omega r_{k,N}/c} s_k \end{bmatrix}, \tag{2.35}$$

where Eq. (2.34) is calculated for every microphone position and represented as an element of the vector. This can be rewritten as a summation of Eq. (2.32) for the different sources as

$$\mathbf{p}(\omega) = \sum_{k=1}^{K} \mathbf{a}_k(\omega) s_k(\omega) = \mathbf{A}(\omega)\mathbf{s}(\omega), \tag{2.36}$$

where $\mathbf{A} = [\mathbf{a}_1 \dots \mathbf{a}_K]$ is the $N \times K$ transfer matrix and $\mathbf{s}$ the $K \times 1$ source vector given by

$$\mathbf{s}(\omega) = \begin{bmatrix} s_1 \\ s_2 \\ \vdots \\ s_K \end{bmatrix}, \tag{2.37}$$

with each element presenting the source power for a frequency ω. For a known amount of sources, Eq. (2.36) completely describes the pressure at the microphones. The problem of source localization and quantification comes down to determining Equation (2.37) from the measured $\mathbf{p}$ vector. In later sections different methods will be presented to achieve this.

2.3.1. The cross-spectral matrix

Throughout this work, and in general for acoustic beamforming, the measurement matrix used often is the so-called cross-spectral matrix (CSM) $\mathbf{C} \in \mathbb{C}^{N \times N}$. This can be defined as

$$\mathbf{C} = \mathbb{E}\left[\mathbf{p}\mathbf{p}^H\right], \tag{2.38}$$

where superscript H denotes the hermitian transpose and $\mathbf{p}$ is given by Equation (2.36). Equation (2.38) contains the powers of the recorded microphone signals on the diagonal. The cross-powers and the relative phase-shifts between microphones are seen off-diagonal.

The CSM can be obtained from measurements. It is then important to take into account that the measurement can be contaminated by additive noise [10, 11]. The signal at the microphones with noise then has the form

$$\mathbf{p}(\omega) = \mathbf{A}(\omega)\mathbf{s}(\omega) + \mathbf{e}(\omega), \tag{2.39}$$

with $\mathbf{e}$ the vector containing noise and assumed to be independent from the source vector $\mathbf{s}$. If the signal *is stationary* an estimate of the CSM can be obtained which reduces the noise as

$$\mathbf{C}_{\text{meas}} = \mathbb{E}\left[\mathbf{p}(\omega)\mathbf{p}(\omega)^H\right], \tag{2.40}$$

with $\mathbb{E}(\cdot)$ the expectation operator and the subscript indicates the CSM to be obtained from the measurement. This way, statistical variations due to $\mathbf{e}$ can be averaged out. Additionally, this helps to distinguish coherent from incoherent sources which will be explained in the next subsection.

In practice, the calculation of $\mathbf{C}_{\text{meas}}$ means that the *time* signal is divided into many blocks and the CSM is calculated as an average. In this work Welch's method is used [12] with 50% overlap. Using 50% overlap increases the amount of total blocks and thus the reliability of the estimate.

The CSM can also be modelled assuming the signal model derived in this section. Inserting Equation (2.36) and assuming no additional noise results in

$$\mathbf{C}_{\text{model}} = \mathbf{APA}^H, \tag{2.41}$$

with

$$\mathbf{P} = \mathbb{E}\left[\mathbf{s}(\omega)\mathbf{s}(\omega)^H\right]. \tag{2.42}$$

For uncorrelated sources, the ensemble-averaged $\mathbf{P} \in \mathbb{C}^{N\times N}$ is a diagonal matrix, as the cross terms of the sources average to zero. Each element of the diagonal matrix presents the power of a source. This is explained in more detail in Section 2.3.2.

2.3.2. Coherent and incoherent sources

With the expression for the CSM and the signal model for multiple sources, *coherency* in the field of beamforming can be better understood. For clarity, a distinction has to be made first regarding coherency as

- Coherency of signals between microphones
- Coherency between different sources (also noted as (un)correlated sources in literature)

This is also illustrated in Fig. 2.4.

The first is of importance in beamforming as phase differences are essential to perform correct shifting of signals explained in the next section. Therefore, it is very desired to have coherency between signals on the microphone array. For the second, generally, beamforming is easier if sources are incoherent.

To understand coherent and incoherent sources we look at the cross-spectral matrix more closely. To avoid complicated expressions we assume only two sources and three microphones. Eq. (2.35) will then be

$$\mathbf{p}(\omega) = \begin{bmatrix} a_{1,1}e^{-j\omega r_{1,1}/c}s_1 + a_{2,1}e^{-j\omega r_{2,1}/c}s_2 \\ a_{1,2}e^{-j\omega r_{1,2}/c}s_1 + a_{2,2}e^{-j\omega r_{2,2}/c}s_2 \\ a_{1,3}e^{-j\omega r_{1,3}/c}s_1 + a_{2,3}e^{-j\omega r_{2,3}/c}s_2 \end{bmatrix} = \begin{bmatrix} p_{1,1} + p_{2,1} \\ p_{1,2} + p_{2,2} \\ p_{1,3} + p_{2,3} \end{bmatrix}, \tag{2.43}$$

where $p_{k,n}$ is the pressure signal on microphone n due to source k. In Eq. (2.43) it can be seen that each microphone has a contribution from both sources.

Now, the cross-spectral matrix will become

$$\mathbf{C} = \mathbf{pp}^H = \begin{bmatrix} p_{1,1} + p_{2,1} \\ p_{1,2} + p_{2,2} \\ p_{1,3} + p_{2,3} \end{bmatrix} \begin{bmatrix} (p_{1,1} + p_{2,1}) & (p_{1,2} + p_{2,2}) & (p_{1,3} + p_{2,3}) \end{bmatrix}^*. \tag{2.44}$$

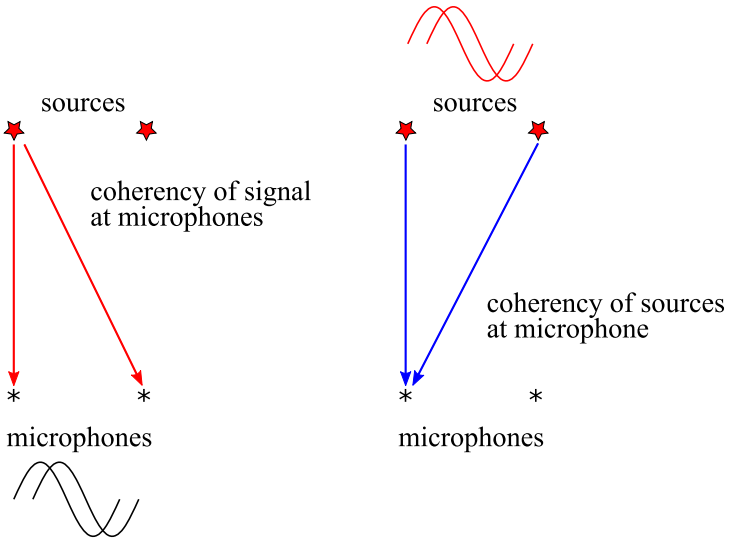

Figure 2.4: Difference between coherence of sources and coherence at the microphones.

From this a diagonal element, which only contains the power at a microphone, can be taken as an example. For the first diagonal element this is

$$(p_{1,1} + p_{2,1})(p_{1,1} + p_{2,1})^* = p_{1,1}p_{1,1}^* + p_{2,1}p_{2,1}^* + p_{2,1}p_{1,1}^* + p_{1,1}p_{2,1}^*. \tag{2.45}$$

Four power terms can be observed: power from the two sources (first two) and cross-powers between the two sources (last two). These terms get higher in number for more sources.

For the case of incoherent sources, the last two terms should be close to zero, i.e. the cross-powers should be

$$\langle p_{2,1}p_{1,1}^* \rangle = 0, \tag{2.46}$$

$$\langle p_{1,1}p_{2,1}^* \rangle = 0 \tag{2.47}$$

To ensure this, the time signal can be divided in blocks and the CSM calculated as an ensemble average. The bigger the ensemble (time blocks) the closer the cross-terms of Eq. (2.46) (hence the term correlated) will reach zero for incoherent sources. If the cross-terms are not zero after the ensemble average, the sources are coherent.

The same analysis can be performed for an off-diagonal element, e.g. an element from the first row and third column of Eq. (2.44)

$$(p_{1,1} + p_{2,1})(p_{1,3} + p_{2,3})^* = p_{1,1}p_{1,3}^* + p_{2,1}p_{2,3}^* + p_{2,1}p_{1,3}^* + p_{1,1}p_{2,3}^*. \tag{2.48}$$

The first two terms contains the relative phase shifts of source one (first term) and source two (second term) between microphone one and three. These terms are essential for performing beamforming. The last two terms are cross-terms and of

relevance when dealing with coherent sources. For incoherent sources it is also desired that these averages to zero as

$$\langle p_{2,1} p_{1,3}^* \rangle = 0, \tag{2.49}$$

$$\langle p_{1,1} p_{2,3}^* \rangle = 0. \tag{2.50}$$

In the case that the aforementioned cross-terms for both diagonal and off-diagonal elements of the CSM in Equation (2.38) can not be neglected, the problem deals with *coherent* sources. If, after obtaining the ensemble average, the cross-terms are close to zero, the sources are said to be *incoherent*.

If there are incoherent sources taking only one time block (i.e. no average) wll not result in a cross-term approximating zero. Otherwise the CSM for *incoherent sources* can be simplified and written as [1]

$$\mathbf{C} = \sum_{k=1}^{K} \mathbb{E}\left[\mathbf{p}_k \mathbf{p}_k^H\right], \tag{2.51}$$

where $\mathbf{p}_k$ is given by Eq. (2.32) for every different source k. For coherent sources the full description of Eq. (2.38) together with pressure signals $\mathbf{p}$ containing the contribution of all the sources needs to be used (resulting in a similar expression as Eq. (2.41)).

In the next section beamforming is discussed primarily for incoherent sources. Methods exist which do especially tackle the problem of coherent sources as explained by Brooks and Humphreys [13].

2.4. Beamforming

Determining the acoustic source distribution given in a problem or experiment is the main problem throughout this thesis. Section 2.1 discussed the wave equation governing the pressure disturbances induced by acoustic sources. Given a set of observations it should be possible to start to infer properties of the sources such as its location, similar to an organism's hearing mechanism. The human hearing is an example of such source localization using only two observations, i.e. from the ears. Unlike the human hearing having only two eardrums, it is possible to have more observation points by using microphones. It can be argued that having 'more' observation points, with the use of microphones, can increase accuracy of getting information of sources. For this the model explained in Section 2.3 can be used as a start.

In this section a clear distinction between transfer vectors and steering vectors is made. This is done to clarify that, as in practice, both are not necessarily equal to each other[4]. Differences between the two can occur making source identification troublesome. Having more physics incorporated in the steering vector can result in more accurate results. While it is desired to have a perfect match between transfer and steering, having an exact idea of what the transfer vector looks like can be difficult in practice. Especially for complicated sources which can have non-uniform

[4]This is the basis on which CLEAN-SC is derived on, see in Section 2.4.4

directivity such as a propeller. It can also depend on the environmental conditions and as such it can be hard to predict in advance. Better physics can be incorporated, e.g. effects of convection (explained in the previous section), refraction of sound or a moving source to obtain more accurate localization. In the end what is done is to be sure the steering vector has the form of the expected transfer vector as much as possible.

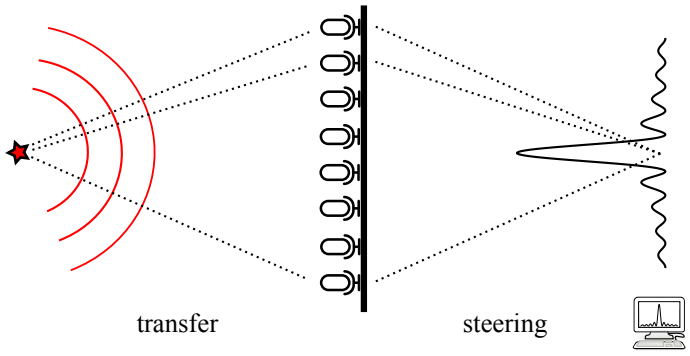

Figure 2.5: A conceptual microphone array with a single source on the left side where the *transfer* of the signal takes place to the microphones. On the right side the post-processing part is done with a computer using the *steering* of the acquired microphone signals. Ideally, the transfer- and steering-functions are inverse functions of each other.

This section is started with the most commonly used beamforming methods known as Delay-and-Sum Beamforming and Conventional Beamforming (CB). In this work most results from source localization will be compared to this base method. Afterwards, a deconvolution method based on CLEAN will be discussed. The section is ended with a high-resolution deconvolution method.

2.4.1. Delay-and-sum beamforming

A single microphone provides the acoustic level resulting from all sources as seen in Section 2.3. Using multiple microphones, i.e., the acoustic array, allows for imaging also the individual noise sources. The most classical technique for finding the acoustic sources is delay-and-sum beamforming [14].

When a source emits an acoustic signal in space, it is expected that the signal, without obstruction, arrives at the array with a certain time delay due to the distance it must travel as seen in Equation (2.28). Time domain beamforming uses the delayed signals measured at various positions in space. These positions are the microphones on the array.

By eliminating the delays and summing the signals resulting from all microphones for all potential source locations, a so-called source map is obtained. This process is known as beamforming. To get the beamformer output for N microphones the source strength for a given position can be estimated using Equation (2.28) N times.

For a single microphone n, Equation (2.28) can be shifted in time by t'_n as

$$p_n^{\text{meas}}(t + t'_n) \sim a_n s(t) = \frac{s(t)}{r_n}, \tag{2.52}$$

or

$$s(t) \sim r_n p_n^{\text{meas}}(t + t'_n), \tag{2.53}$$

where for convenience $a_n = 1/r_n$ is used as the transfer factor as derived in Section 2.1 for the case of the spherical wave equation. Equation (2.53) will provide an estimate for the source $s(t)$ at a distance r_n (hence the ∼-sign) from the microphone, but since sound is recorded from every direction the estimate can be influenced by any other disturbances. To get a better estimate, Equation (2.53) can be obtained as an average over the other microphones as well. By using r_n corresponding to a specific point in space, i.e. it will differ between microphones, the *steered* averaged output is obtained as

$$s_{\text{avg}}(t) = \frac{1}{N} \sum_{n=1}^{N} r_n p_n^{\text{meas}}\left(t + t'_n\right), \tag{2.54}$$

for a given *scan point* given by $\vec{x}_t$ matching the source position $\vec{x}_s$, see Figure 2.6. To obtain the source at a reference point $\vec{x}_0$ given by a distance r_0 from the source (usually the source to the center of the microphone array) the averaged signal $s_{\text{avg}}(t)$ is propagated to a distance r_0 using $a_0 = 1/r_0$, i.e. Equation (2.54) is divided by r_0 to obtain the delay-and-sum beamformer output [15]

$$p_F(\vec{x}_t, t) = \frac{1}{N} \sum_{n=1}^{N} \frac{r_n}{r_0} p_n^{\text{meas}}\left(t + t'_n\right). \tag{2.55}$$

In the case the scan point does not match the source position, i.e. $\vec{x}_t \neq \vec{x}_s$ as seen in Figure 2.6, the output of the beamformer will be low. The beamformer output in Equation (2.55) can be used to scan the space of possible sound sources by evaluating Equation (2.55) for different $\vec{x}_t$. Usually a scan plane is selected parallel to the microphone array.

2.4.2. Conventional beamforming

By going from the time domain to the frequency domain, beamforming can be performed per frequency. This is usually denoted as Conventional Beamforming (CB) and most commonly used in acoustic beamforming. In this section a more general start is made with the so-called beamform filter output from an array of N microphones. After transforming the signal $\mathbf{p}(t) \in \mathbb{R}^{N\times 1}$ to the frequency domain $\mathbf{p}(\omega)$, the steering vector $\mathbf{h}(\vec{x}_t) \in \mathbb{C}^{N\times 1}$ is used as

$$p_{\text{F}}(\vec{x}_t) = \mathbf{h}(\vec{x}_t)^H \mathbf{p}(\omega). \tag{2.56}$$

The output is a weighted sum of the microphone sound pressures in $\mathbf{p}$ using $\mathbf{h}(\vec{x}_t)$ as the weights. Instead of Equation (2.56) the autopower spectrum is used to construct the beamforming source map as

$$B(\vec{x}_t) = \mathbb{E}\left[p_{\text{F}}(\vec{x}_t) p_{\text{F}}(\vec{x}_t)^H\right] = \mathbf{h}(\vec{x}_t)^H \mathbb{E}\left[\mathbf{p}\mathbf{p}^H\right] \mathbf{h}(\vec{x}_t), \tag{2.57}$$

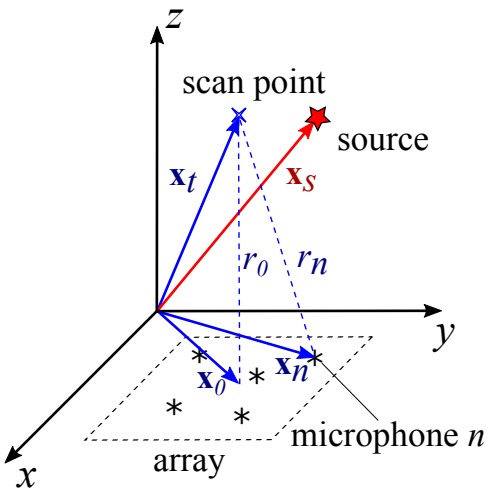

Figure 2.6: Schematic for the vectors and distances used in this section for an array of 5 microphones on the xy-plane. As an example this case has the scan point $\vec{x}_t$ not matching the source position at $\vec{x}_s$.

where it can be recognised from Section 2.3.1 that factor of the last part of Equation (2.57) for the expectation operator to be the CSM. The final expression for the CB output for a given position $\vec{x}_t$ and frequency ω can the be given as

$$\boxed{B(\vec{x}_t,\omega) = \mathbf{h}^H(\vec{x}_t)\mathbf{C}_{\text{meas}}\mathbf{h}(\vec{x}_t)}. \tag{2.58}$$

Using Equation (2.58), the general approach is to define a number of scan points and estimate the source powers for each given point. The points are defined on a plane parallel to the array at a certain distance z_{bf} from the array. The beamformer provides the estimated source level for each scan point. When there is a mismatch with the actual source position, the beamformer output is expected to be small.

The ability to discern between closely spaced sources is for conventional beamforming, approximately, limited by the Rayleigh criterion and related to the angular resolution of an imaging device. For a *planar* microphone array this is given by

$$\Delta\ell = 1.22\frac{cz_{\text{bf}}}{Df}, \tag{2.59}$$

with D the effective aperture of the array, $f = \omega/2\pi$ and z_{bf} the perpendicular distance of the planar array to the scan points. In Chapter 3 the derivation for this equation can be found.

The SPL value can be found as

$$L_p(\vec{x}_t,\omega) = 20\log_{10}\left(\frac{\sqrt{B(\vec{x}_t,\omega)}}{p_0}\right), \tag{2.60}$$

with $p_0 = 20\,\mu\text{Pa}$, the reference pressure. Where the SPL of Eq. (2.60) is evaluated, is of importance and depends on where the power of Eq. (2.58) is determined.

For beamforming Eq. (2.58) two properties are of importance:

- Provide a maximum output power when the assumed and actual source are the same, i.e. provide the correct position

$$B(\vec{x}_t = \vec{x}_s) > B(\vec{x}_t \neq \vec{x}_s). \tag{2.61}$$

- When these coincide it should provide the measure of the source strength, i.e. provide the correct power

$$B(\vec{x}_t = \vec{x}_s) = \mathbb{E}\left[ss^*\right]. \tag{2.62}$$

Which property is fulfilled depends on the steering vector chosen. First four different steering vectors will be given according to the approach of Sarradj [16]. For the formulations the exponential part with of $e^{r_{t,0}}$ and the factor $1/r_{t,0}$ are added to propagate the source to the center of the array. Therefore the 4π factors seen for the monopole expression in Eq. (2.13) are cancelled out. The obtained powers are therefore evaluated at the array center $\vec{x}_0$. The distances used can be seen in Fig. 2.6. For the formulation $r_{t,n} = |\vec{x}_t - \vec{x}_n|$ is the distance between the scan point and microphone n and $r_{t,0} = |\vec{x}_t - \vec{x}_0|$ the distance between the scan point and the center of the array.

This work does not consider the steering vector for the minimum variance distortionless response (MVDR) beamforming, also known as Capon or robust adaptive beamforming (RAB). For aeroacoustic noise sources this beamforming method showed that it is sensitive to small perturbations [17]. It quickly affects the performance for the application of beamforming with airflow.

Formulation I

The first and most basic steering factor only compensates for the phase delay [18] between source and microphone. An element for such a steering vector is given by

$$h_n = \frac{1}{N} e^{-jk(r_{t,n} - r_{t,0})}. \tag{2.63}$$

The division by N is needed as the phase delay will be compensated N times, the amount of microphones, to obtain the averaged strength over all microphones. The power is evaluated at the array center using Eq. (2.58). This steering vector provides a good description for plane wave beamforming.

For the formulation given in Eq. (2.63) condition Eq. (2.61) is met while condition Eq. (2.62) is met only approximately. That is, it provides the correct position at the expense of an error in the source power.

Formulation II
The second formulation used often in literature also compensates for the changes in amplitude between source and receiver [19, 20]

$$h_n = \frac{1}{N}\frac{r_{t,n}}{r_{t,0}} \mathrm{e}^{-jk(r_{t,n}-r_{t,0})}, \tag{2.64}$$

seen by the $r_{t,n}$ in the numerator. Condition Eq. (2.62) is met while condition Eq. (2.61) is not. This means there is no maximum when $\vec{x}_t = \vec{x}_s$. Therefore, it provides the correct power with a slight error in position.

Formulation III
A third and very frequently used steering vector formulation for aeroacoustics is

$$h_n = \frac{1}{r_{t,n} r_{t,0} \sum_{n=1}^{N} \left(1/r_{t,n}^2\right)} \mathrm{e}^{-jk(r_{t,n}-r_{t,0})}, \tag{2.65}$$

which is found by the minimization of the filter response to white noise [21, 22] in a least-squares sense. Solving the optimization problem results in Eq. (2.65) when propagating the solution to the array center. Similar to Formulation II, the condition of Eq. (2.62) is met but Eq. (2.61) is not. Therefore, a slight error in position can be seen as well.

Formulation IV
A similar minimization can be performed whereby a different normalization procedure is used [23, 24]. This results in

$$h_n = \frac{1}{r_{t,n}\sqrt{N \sum_{n=1}^{N} \left(1/r_{t,n}^2\right)}} \mathrm{e}^{-jk(r_{t,n}-r_{t,0})}, \tag{2.66}$$

where Eq. (2.61) is met while condition Eq. (2.62) is not. This results in an approximate source strength. This formulation can be seen as a combination of Fomulation I and III.

Formulation IV can be very useful in case of 3-D beamforming, where the position of the source is more important than the strength. For planer microphone arrays, resolution is especially low whenever considering the dimension perpendicular to the array. Formulation IV however is performing best in this aspect. It is also applicable whenever several scan planes are compared for different beamforming distances, e.g. when the distance to the object of interest is not precisely known. For these cases Eq. (2.66) can provide better information about the position of the source.

Comparison of the formulations
This subsection shows the comparison between the formulations when using conventional beamforming. A sound source is simulated at the position of $\vec{x}_s = (0, 0, 1)$ m with a frequency of 1000 Hz and with an SPL of 100 dB. The microphone array

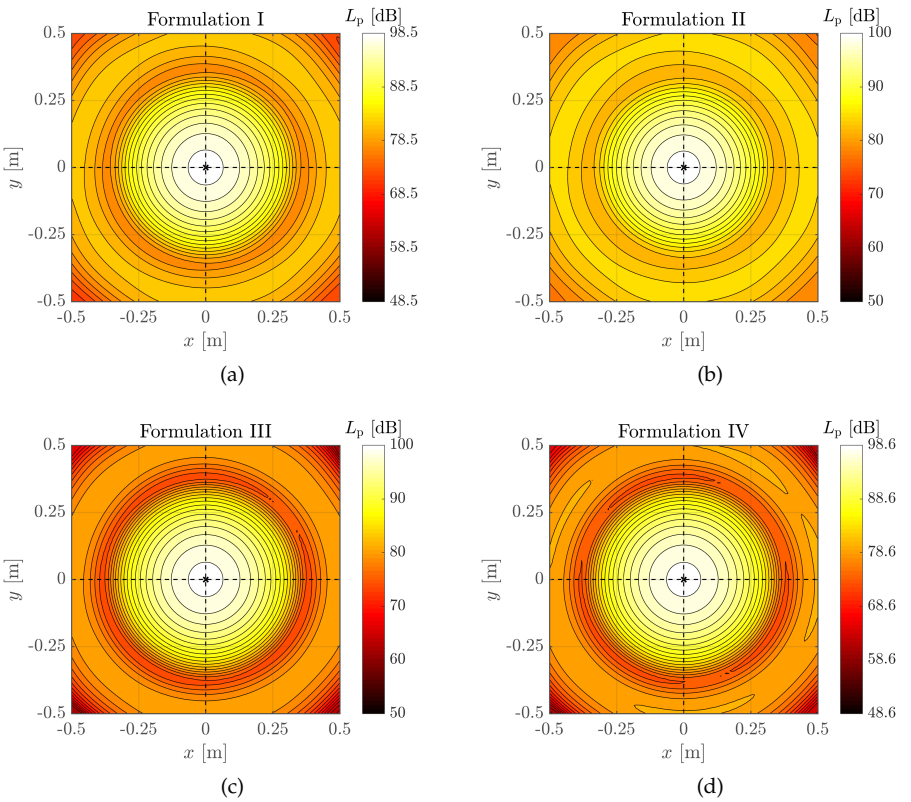

Figure 2.7: Comparison of beamforming results for the different steering formulations of the xy plane which is parallel to the planar microphone array.

used is parallel to the xy plane with an aperture of 1 m. In Fig. 2.7 a comparison is made for the xy plane where beamforming is performed at $z = 1$ m and Fig. 2.8 the xz plane at $y = 0$ m.

The maximum value resulting from beamforming can be seen from the colour bar. The position where the simulated source is positioned is indicated by the cross. The position where beamforming observes its maximum is given by the intersection of the dashed vertical and horizontal lines.

In Fig. 2.7 it can be seen that when a single source is positioned at the origin, all the formulations provide good result for the position. For Formulation I and IV the source strength is seen to be off as expected from the properties of the formulations.

With beamforming for the planes in xz the result in Fig. 2.8 is obtained. Here the strength of Formulation I and IV can be observed where the maximum value of beamforming corresponds to the actual source position. Again the differing source strengths can be seen as well for Formulation I and IV in the colour bar. The poor resolution in the depth-wise direction can be seen for all the formulations owing to

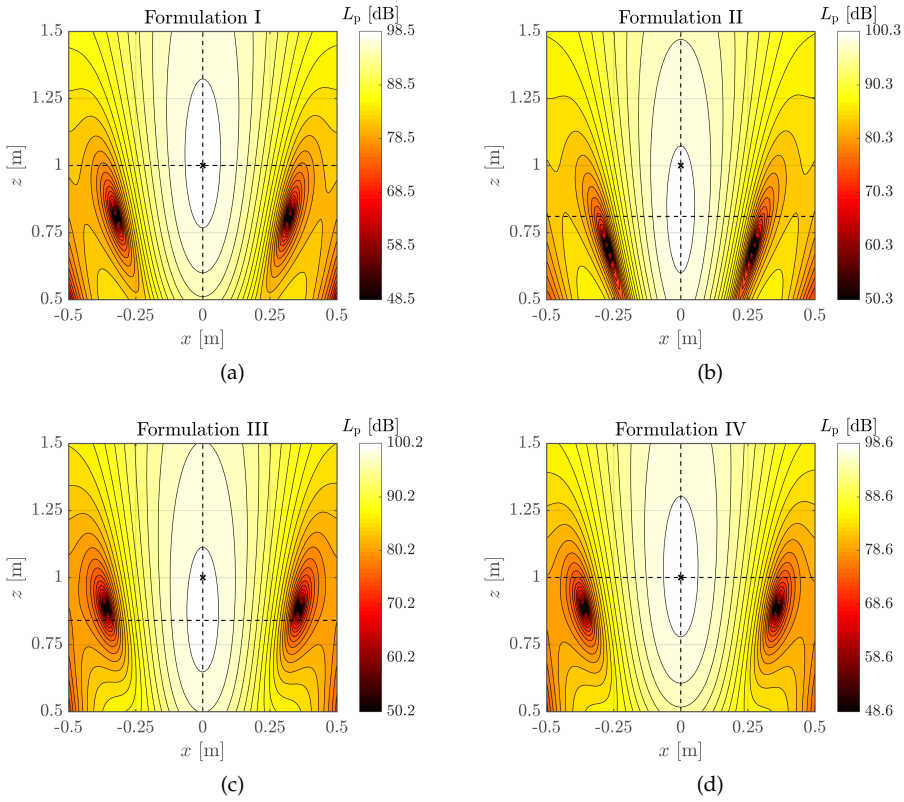

Figure 2.8: Comparison of beamforming of the different steering formulations of the xz plane which is perpendicular to the planar microphone array.

the microphone array being planar.

The effect on the sidelobes can be found in Appendix B and Fig. B.4. It is therefore recommended to use either Formulation III or IV depending on the importance of source strength or position.

Alternative notation for Formulation II and III

As Formulation II and III are most often used, another notation will be presented. Conform Sijtsma [6] the symbol $\mathbf{g}$ is used for the steering vector and the elements from Eq. (2.12). The power is not evaluated at a specific distance on the array for different microphones, and therefore not included in the steering vector. An element of $\mathbf{g}$ has the form

$$g_n = \frac{1}{4\pi r_{t,n}} \mathrm{e}^{-jkr_{t,n}}, \tag{2.67}$$

note that $\mathbf{g} \rightarrow \mathbf{a}$ for $a = 1/(4\pi r_{t,n})$.

For Formulation II the beamforming equation will result in

$$B(\vec{x}_t,\omega) = \sum_{n1=1}^{N}\sum_{n2=1}^{N}\frac{1}{N^2}\frac{\mathbf{C}_{\text{meas}}[n1,n2]}{g^*_{n1}g_{n2}}, \tag{2.68}$$

where $n1$ and $n2$ present the corresponding indices of the matrix $\mathbf{C}_{\text{meas}}$ and the element of the steering vector $\mathbf{g}$. Note that Eq. (2.68) cannot be presented as succinct matrix multiplication due to the element-wise division of $\mathbf{g}$.

Formulation III will get the form

$$B(\vec{x}_t,\omega) = \frac{\mathbf{g}^H\mathbf{C}_{\text{meas}}\mathbf{g}}{(\mathbf{g}\cdot\mathbf{g})(\mathbf{g}\cdot\mathbf{g})} = \frac{\mathbf{g}^H\mathbf{C}_{\text{meas}}\mathbf{g}}{|\mathbf{g}|^4}. \tag{2.69}$$

Using this beamforming equation will *not* result in an output at the array center as the signal for each scan point $\vec{x}_t$ is not propagated towards the array center from every (distinct) microphone position[5]. The output of Eq. (2.69) is therefore an estimate of the source strength at $1/4\pi$ m from the source.

For obtaining the SPL a reference distance R_0 can be used instead as

$$L_p(\vec{x}_t,\omega) = 20\log_{10}\left(\frac{\sqrt{B(\vec{x}_t,\omega)}}{4\pi R_0 p_0}\right), \tag{2.70}$$

where the source power is propagated to R_0 by the factor $4\pi R_0$. Usually a reference of 1 m is taken when using Eq. (2.70).

Important to note is that setting R_0 to the distance to the array center *will not* result in the exact same map when using Eq. (2.60) for the same steering vector formulation. Using Eq. (2.70) the distance is fixed for every scan point. Using a different R_0 for every different scan point will result in the same map. Although it can be argued that using a single reference distance as in Eq. (2.70) results in a more representative beamforming image[6]. An example for three sources with the same SPL of 100 dB can be seen in Fig. 2.9. It can therefore be useful to assess beforehand if only the source strength is of interest or the noise at a specific observer position (e.g. the array center).

The steering vector $\mathbf{g}$ given by the elements Eq. (2.67) will be used for the derivation of the CLEAN deconvolution method.

Adaptation of steering for convection and shear layer refraction of sound

The steering vector given in the previous subsection only takes into account the static condition, i.e. no wind. In the case of non-zero wind velocity, a correction has to be applied due to convection of the sound. The expression for the signal was presented in Eq. (2.20). To take into account the wind velocity a similar procedure as in Section 2.1.3 can be followed for every steering vector formulation. In the end

[5] That is, from the microphone back to the scan point position and then forward to the array center. Otherwise, Eqs. (2.68) and (2.69) would be exactly equal to Eqs. (2.64) and (2.65) using Eq. (2.58).

[6] For example, two sources of the same strength, propagating back to the array center can result in a beamform map of differing strengths, due to the different distances it may have to the array center.

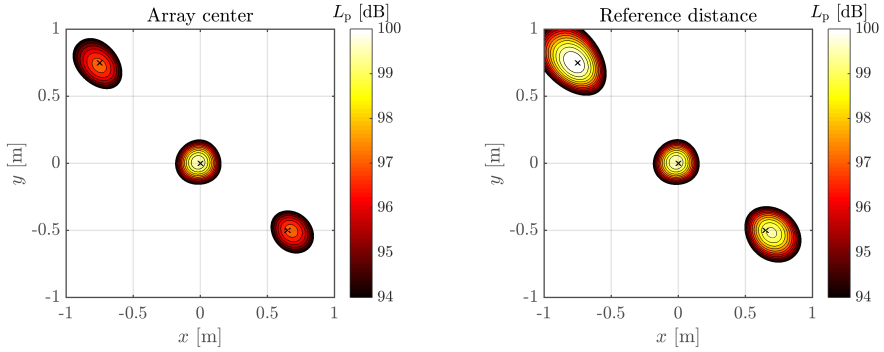

Figure 2.9: Comparison of beamforming when evaluating the source map to the array center (a) or to a constant reference distance R_0 in (b). The source positions are given by the crosses and are simulated having the same SPL of 100 dB at R_0. In (a) the SPL differs as the distances of the array center to the outer sources are larger than to the source at the origin.

only $r_{t,n}$ changes accordingly, i.e. in the exponential it will become $r''_{t,n}$ and $r'_{t,n}$ otherwise. Taking Formulation III as an example this becomes

$$h_n^{\text{conv}} = \frac{1}{r'_{t,n} r_{t,0} \sum_{n=1}^{N} \left(1/r'^2_{t,n}\right)} e^{-jk(r''_{t,n} - r_{t,0})}, \tag{2.71}$$

with

$$r'_{t,n} = \sqrt{\delta r^2 + \beta^2 r^2_{t,n}}, \tag{2.72}$$

$$r''_{t,n} = \frac{1}{\beta^2}\left(-\delta r + r'_{t,n}\right), \tag{2.73}$$

$$\delta r = \vec{M} \cdot (\vec{x}_n - \vec{x}_t), \tag{2.74}$$

and

$$\beta^2 = (1 - \vec{M} \cdot \vec{M}), \tag{2.75}$$

with $\vec{M} = \vec{U}/c$ and $\vec{U}$ being the flow speed.

Simple shear layer correction

For non-static measurements the microphone array is situated outside the flow. Beamforming with the steering vector including convection can result in a too large shift for the sources. This is caused by additional refraction effects when the sound leaves the flow. Whenever shear layer correction is applied throughout this thesis, a simple correction is used given as [21, 25]

$$\vec{M}_c = \vec{M}\left(\frac{z_{\text{bf}} - z_{\text{sl}}}{z_{\text{bf}}}\right). \tag{2.76}$$

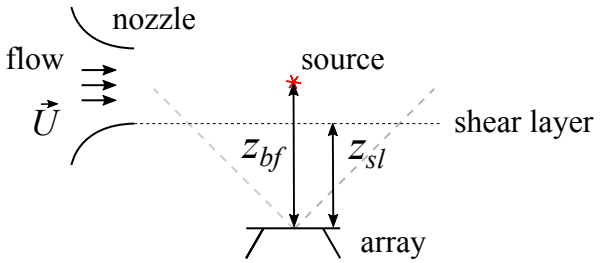

Figure 2.10: Schematic of the distances used for the simple shear layer correction. The correction provide good results for scan points within the dashed gray lines and $M < 0.25$.

Where it is assumed that the flow is perpendicular to the planar microphone array orientation, with z_{sl} the distance from the array to the shear layer and z_{bf} the scan point z-coordinate. With the obtained $\vec{M}_c$ the same procedure can be followed when accounting for convective effects with the corrected Mach number (or flow speed).

Usually the shear layer is not well defined. An approximate distance can be used which provides good results. Additionally, the *effective* shear layer distance could be determined with the use of a calibration source, see Appendix C.4. The simple correction provides good result [25] for moderate Mach numbers, $M < 0.25$ and for large angles between the shear layer and the propagation direction (larger than 45°). This is indicated by the gray lines in Fig. 2.10.

2.4.3. CLEAN-PSF

Up to this point only conventional beamforming methods were discussed. By inspection of Fig. 2.7 it was seen that even though a point source is used positioned at the origin, a main lobe is seen centered at the aforementioned position instead along sidelobes in the region around it. This 'response' to a point source is also known as the point spread function (PSF). The PSF can depend on various parameters, such as the microphone configuration or frequency of the source. If it is possible to know this PSF behaviour beforehand, it would be possible to assign a point source to it accordingly. This would remove all the side lobes and narrow the main lobe to a point. Performing this process for every scan point of interest is known as *deconvolution*. This procedure becomes necessary if weaker secondary sound sources are masked by sidelobes of dominant sources.

A deconvolution method is CLEAN [26] which is commonly used in astronomy [27]. Deconvolution is performed by assuming the measurement to be exactly proportional to the steering (or transfer[7]) vector $\mathbf{g}$ with the elements given by Eq. (2.67).

Under the assumption of incoherent sources, the CSM can have the form of Eq. (2.51). It is then possible to use an iterative deconvolution procedure by determining the position and corresponding source strength for which CB provides the

[7]For the CLEAN algorithms the transfer vector is needed, here $\mathbf{a} = \mathbf{g}$ and is noted by steering vector from this point on.

maximum at each step. At every step this is saved to construct the clean beams.

For the first step the position and power will give a clean CSM according to

$$\mathbf{C}_1 = \phi B_1 \mathbf{g}_1 \mathbf{g}_1^H, \tag{2.77}$$

where ϕ is the loop gain or damping factor and the subscript indicates the steering vector and CSM constructed for source 1 only. The degraded CSM is then constructed as

$$\mathbf{C}_{\text{degraded}} = \mathbf{C}_{\text{meas}} - \mathbf{C}_1, \tag{2.78}$$

which is the CSM with the first source removed. Conventional beamforming is then performed on Eq. (2.78) to obtain the subsequent source strength and position and the procedure is repeated. For second or higher iteration $\mathbf{C}_{\text{meas}}$ in Eq. (2.78) is replaced by $\mathbf{C}_{\text{degraded}}$ from the previous step.

2.4.4. CLEAN-SC

CLEAN-SC goes a step further by finding the so-called source components $\mathbf{a}_{\text{sc}}$ which more closely resemble the measured data contained in $\mathbf{p}$ and using the fact that sidelobes are *spatially coherent* with the main lobe[8]. Again, source contributions are removed at each step from the CSM and replaced with clean beams in the source map.

In CLEAN-SC, the measured CSM is decomposed as follows:

$$\mathbf{C}_{\text{meas}} = \sum_{k=1}^{K} \mathbf{p}_k \mathbf{p}_k^H + \mathbf{C}_{\text{degraded}}, \tag{2.79}$$

meaning that the measured CSM consists of two parts. The first part represents the contribution of the K identified incoherent sound sources. The second part, $\mathbf{C}_{\text{degraded}}$, represents the remaining part in $\mathbf{C}_{\text{meas}}$, where the source information is not (yet) extracted. As discussed in Section 2.3.2, the assumption of Eq. (2.79) is valid under the following conditions:

- All sound sources present are incoherent.
- The CSM is calculated from a large number of time blocks, so that the ensemble averages of the cross-products $\mathbf{p}_k \mathbf{p}_l^H, k \neq l$, can be neglected.
- There is no decorrelation of signals from the same source between different microphones (e.g. due to sound propagation through turbulence).
- There is no additional incoherent noise.

Let the highest power $\tilde{B}(\vec{x}_s)$ be noted by its grid point $\vec{x}_s$ with the corresponding weight vector $\mathbf{w}(\vec{x}_s) = \mathbf{g}(\vec{x}_s) / \left[\mathbf{g}(\vec{x}_s) \cdot \mathbf{g}(\vec{x}_s)\right]$, the source power at any grid point $\vec{x}_t$ is

[8] Note the emphasis on the symbol **a** used presenting the *transfer* vector. Like previously noted, the exact model for the transfer can be hard to model.

Part of Section 2.4.4 has been submitted to the International Journal of Aeroacoustics.

spatially coherent with this source power peak [26], or

$$\mathbf{w}^H(\vec{x}_t)\mathbf{C}_{\text{meas}}\mathbf{w}(\vec{x}_s) = \mathbf{w}^H(\vec{x}_t)\left[\sum_{k=1}^{K}\mathbf{p}_k\mathbf{p}_k^H + \mathbf{C}_{\text{degraded}}\right]\mathbf{w}(\vec{x}_s). \tag{2.80}$$

At the first iteration step of CLEAN-SC, the exact number of sources K is not yet known, and all information is still contained in $\mathbf{C}_{\text{meas}}$, i.e. $\mathbf{C}_{\text{meas}} = \mathbf{C}_{\text{degraded}}$. The CLEAN-SC algorithm extracts the constituting source information from $\mathbf{C}_{\text{meas}}$ and transfers it to the first term on the RHS of Eq. (2.79). To achieve this, CLEAN-SC starts with the result of CB from Eq. (2.69), focusing at the grid point $\vec{x}_s$ where the strongest source is identified as

$$\tilde{B}(\vec{x}_s) = \mathbf{w}^H(\vec{x}_s)\mathbf{C}_{\text{meas}}\mathbf{w}(\vec{x}_s) = \mathbf{w}^H(\vec{x}_s)\left[\sum_{k=1}^{K}\mathbf{p}_k\mathbf{p}_k^H + \mathbf{C}_{\text{degraded}}\right]\mathbf{w}(\vec{x}_s). \tag{2.81}$$

By cancelling out $\mathbf{w}^H(\vec{x}_s)$ and expanding the summation term, we have

$$\mathbf{C}_{\text{meas}}\mathbf{w}(\vec{x}_s) = (\mathbf{p}_1^H\mathbf{w}(\vec{x}_s))\mathbf{p}_1 + \sum_{k=2}^{K}(\mathbf{p}_k^H\mathbf{w}(\vec{x}_s))\mathbf{p}_k + (\mathbf{p}_{\text{degraded}}^H\mathbf{w}(\vec{x}_s))\mathbf{p}_{\text{degraded}} \tag{2.82}$$

At $\vec{x}_t = \vec{x}_s$, it can be assumed that the last two terms on the RHS of Eq. (2.82), i.e. the contribution from the other sources, are small compared to the first term, and the following approximation can be made:

$$\mathbf{C}_{\text{meas}}\mathbf{w}(\vec{x}_s) \approx (\mathbf{p}_1^H\mathbf{w}(\vec{x}_s))\mathbf{p}_1. \tag{2.83}$$

In the same manner:

$$\tilde{B}(\vec{x}_s) = |\mathbf{p}_1^H\mathbf{w}(\vec{x}_s)|^2 + \sum_{k=2}^{K}|\mathbf{p}_k^H\mathbf{w}(\vec{x}_s)|^2 + |\mathbf{p}_{\text{degraded}}^H\mathbf{w}(\vec{x}_s)|^2 \approx |\mathbf{p}_1^H\mathbf{w}(\vec{x}_s)|^2. \tag{2.84}$$

Dividing Eq. (2.83) by $|\mathbf{p}_1^H\mathbf{w}(\vec{x}_s)|^2$ yields

$$\frac{\mathbf{C}_{\text{meas}}\mathbf{w}(\vec{x}_s)}{|\mathbf{p}_1^H\mathbf{w}(\vec{x}_s)|^2} \approx \frac{\mathbf{p}_1}{|\mathbf{p}_1^H\mathbf{w}(\vec{x}_s)|} \equiv \mathbf{a}_{\text{sc}}(\vec{x}_s), \tag{2.85}$$

assuming that the phase of $\mathbf{p}_1^H\mathbf{w}(\vec{x}_s)$ is irrelevant, and can be written as $|\mathbf{p}_1^H\mathbf{w}(\vec{x}_s)|$. The so-called *source component*, $\mathbf{a}_{\text{sc}}(\vec{x}_s)$, representing the identified source's contribution in the measured CSM is defined. This contribution is to be removed from the measured CSM before proceeding to the next iteration. Equation (2.84) assumes that the source power at $\vec{x}_t = \vec{x}_s$ is approximately only the result of one source $k = 1$. However, there is also a small contribution from the other unidentified sources at $\vec{x}_t = \vec{x}_s$ [1]. Therefore, a safety factor is used to account for their contributions. This is the so-called *loop gain* [26], ϕ. As an extension to Eq. (2.84), we define

$$|\mathbf{p}_1^H\mathbf{w}(\vec{x}_s)|^2 = \phi\tilde{B}(\vec{x}_s). \tag{2.86}$$

The loop gain $0 < \phi \leq 1$ indicates to which extent we assume the source power at grid point s to contain the influence of the identified source $k = 1$. For example, ϕ is set to 0.99 in this manuscript, meaning that 99% of source power results from the identified source.

Finally, the influence of the source is taken away from the measured CSM by

$$\mathbf{C}_{\text{degraded}} = \mathbf{C}_{\text{meas}} - \mathbf{p}_1\mathbf{p}_1^H = \mathbf{C}_{\text{meas}} - |\mathbf{p}_1^H\mathbf{w}(\vec{x}_s)|^2\mathbf{a}_{\text{sc}}(\vec{x}_s)\mathbf{a}_{\text{sc}}(\vec{x}_s)^H \tag{2.87}$$

$$= \mathbf{C}_{\text{meas}} - \phi\tilde{B}(\vec{x}_s)\mathbf{a}_{\text{sc}}(\vec{x}_s)\mathbf{a}_{sc}^H(\vec{x}_s), \tag{2.88}$$

yielding $\mathbf{C}_{\text{degraded}}$ which replaces $\mathbf{C}_{\text{meas}}$ in the next iteration. First, $\mathbf{C}_{\text{degraded}}$ replaces $\mathbf{C}_{\text{meas}}$ in Eq. (2.69) to identify the next source. Then the CLEAN-SC process is repeated. The stopping criterion for CLEAN-SC is when $\mathbf{C}_{\text{degraded}}$ is *empty* after the source components for all sources have been taken away. In other words, its norm should be sufficiently small compared to the original CSM: $\|\mathbf{C}_{\text{degraded}}\| < \varepsilon\|\mathbf{C}_{\text{meas}}\|$, where ε is a constant here taken as 0.01.

At this point, the exact number of sources K is known. Let the set S contain the indices of grid points where the sources are identified by CLEAN-SC such that $s \in S$ and $|S| = K$, the new source map is obtained by the summation of all the clean beams from the K identified sources and the remaining degraded CSM as

$$\tilde{B}(\vec{x}_t) = \sum_{k' \in S} \phi\tilde{B}_{k'} 10^{-\beta d_{t,k'}^2} + \mathbf{w}^H(\vec{x}_t)\mathbf{C}_{\text{degraded}}\mathbf{w}(\vec{x}_t). \tag{2.89}$$

where β is the clean beam shape parameter and $d_{t,k'}$ the distance from grid point $\vec{x}_t$ to the identified source location $\vec{x}_s$ for source k'.

The CLEAN-SC method results in the improvement of both the main lobe width (MLW) and the maximum sidelobe level (MSL) in the source map. The MSL is lowered by the elimination of sidelobes which are spatially coherent to the main lobe improving the dynamic range. The MLW is controlled by β and selected by the user, $\beta = 480$, in this case. While this can provide smaller beam widths, it does not provide spatial resolution beyond the Rayleigh criterion given in Eq. (2.59). For sources which are spaced closer than this limit, CLEAN-SC locates the source marker in between.

2.4.5. HR CLEAN-SC

CLEAN-SC marks the source locations where the peak of the sources are. For HR-CLEAN-SC, the source markers given from the previous section are relocated such that the relative contribution of the other $(K-1)$ sources is minimal [1, 28]. The new source marker location which matches this requirement for a given source originally marked at $\vec{x}_s$ is determined by searching for $\vec{x}_m$ which minimizes the cost function as [1, 28]

$$\vec{x}_m = \text{argmin}_t \left\{ F(\mathbf{u}_t) = \frac{\|\sum_{k' \in S, k' \neq s} (\mathbf{g}_{k'}^H \mathbf{u}_t)\mathbf{g}_{k'}\|^2}{|\mathbf{g}_t^H\mathbf{u}_t|^2\|\mathbf{g}_t\|^2} \right\}, \tag{2.90}$$

where t corresponds to the scan points with position $\vec{x}_t$.

With this, the original weight vector $\mathbf{w}(\vec{x}_s)$ is replaced by $\mathbf{u}_m$, where m associates with a grid point $\vec{x}_m$ where the new source marker is to be placed. At this grid point, the total relative contribution of the other sources located at $k' \in S$ is minimized.

The choices for the marker location are restricted to a predefined set of T grid points representing the scan plane. Therefore, employing the brute force approach, i.e. evaluating Eq. (2.90) for all T grid points is sufficient to determine $\mathbf{u}_m$ in a short time.

The corresponding source component for the new marker $\mathbf{u}_m$ then becomes

$$\mathbf{a}_{\mathrm{sc}}(\vec{x}_m) = \frac{\mathbf{C}_{\mathrm{meas}}\mathbf{u}_m}{\mathbf{u}_m^H\mathbf{C}_{\mathrm{meas}}\mathbf{u}_m}. \tag{2.91}$$

The source power estimates for the grid points due to a source marked at $\vec{x}_t = \vec{x}_m$ are calculated by varying $\mathbf{w}^H(\vec{x}_t)$ to cover all remaining grid points as

$$\tilde{B}(\vec{x}_t) = (\mathbf{u}_m^H\mathbf{C}_{\mathrm{meas}}\mathbf{u}_m)|\mathbf{w}^H(\vec{x}_t)\mathbf{a}_{\mathrm{sc}}(\vec{x}_m)|^2. \tag{2.92}$$

For this map, the maximum $\tilde{B}(\vec{x}_s)$ is determined in the same manner as shown previously, $\vec{x}_s = \mathrm{argmax}_t(\tilde{B}(\vec{x}_t))$, where $\vec{x}_t = \vec{x}_s$ represents the *actual* location of the source. It is important to highlight that, for HR-CLEAN-SC, it is possible that $\vec{x}_m \neq \vec{x}_s$, meaning that the source markers are not necessarily at the source's peak.

For the next source, $\mathbf{C}_{\mathrm{meas}}$ is replaced by $\mathbf{C}_{\mathrm{degraded}}$ calculated as in Eq. (2.88). Then the process from Eq. (2.90) to (2.92) is repeated for all the remaining sources found in CLEAN-SC until all marker locations and actual source locations do not change anymore, or the maximum number of iterations is reached [1]. Finally, the source map is computed using Eq. (2.89).

To avoid division by zero in Eq. (2.90), a constraint has to be set for any arbitrary source marker $\mathbf{u}_t$ as

$$|\mathbf{g}_t^H\mathbf{u}_t|^2 \geq \mu > 0. \tag{2.93}$$

The parameter μ will be the source marker constraint of the minimization problem in Eq. (2.90) and limits how far the source marker is allowed to move from the main lobe's peak. It is desirable to stay on the main lobe as actual sources might have different PSFs [26]. Therefore, μ should be larger than the MSL. In the work of Sijtsma et al. [1, 28], no improvement in resolution was found for μ below 0.25 for the acoustic array configuration used. Therefore, a constant $\mu = 0.25$ was taken, which is equivalent to $10\log_{10}(0.25)$ = -6 dB relative to the main lobe's peak [1, 28].

Figure 2.11 schematically illustrates the aforementioned concepts of the HR-CLEAN-SC algorithm. Supposing that there are two closely-spaced sound sources placed at a distance d apart, which is lower than the Rayleigh resolution limit ($d < \Delta\ell$), these two sources are represented by PSF 1 and 2. Figure 2.11 shows the resolved two sources with the alternated source marker locations at the final iteration of HR-CLEAN-SC. For PSF 1, the source marker is shifted to the grid point where the influence of PSF 2 is minimized, according to Eq. (2.90). The same applies for the source marker of PSF 2. In HR-CLEAN-SC, the source marker is

allowed to shift within the source marker constraint μ defined in Eq. (2.93). Therefore, for the case shown in Fig. 2.11, the sources can still be resolved even though they are closer together, as long as the grid point where the influence of the other PSF is minimized is within the furthest allowable source marker shift distance.

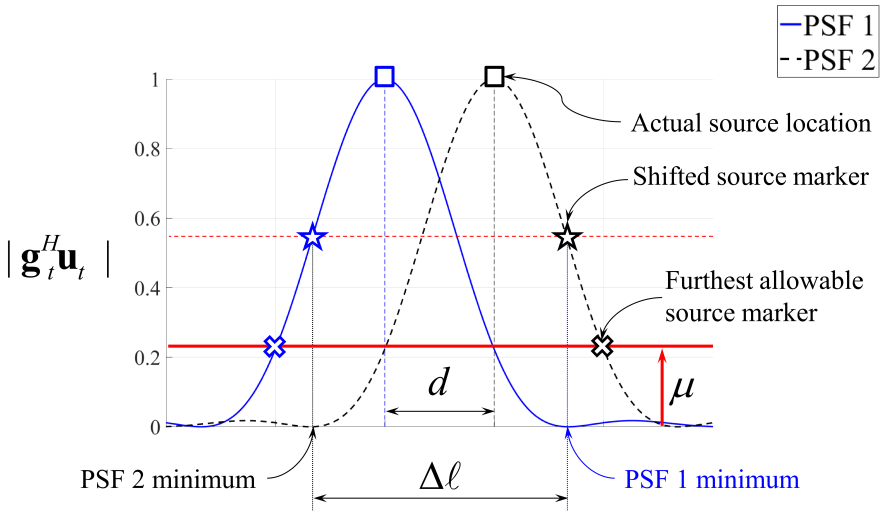

Figure 2.11: Schematic of two closely-spaced sound sources resolved by HR-CLEAN-SC after the source markers have been shifted. The source marker constraint μ is also shown.

Adaptive HR-CLEAN-SC

As mentioned in the previous section, the parameter μ should be larger than the MSL, which strongly depends on the sound frequency considered f and the acoustic array design. Hence, an adaptive version of HR-CLEAN-SC was recently proposed [29] in order to benefit from the usage of acoustic arrays with low MSL at low frequencies, where μ varies per frequency as

$$\mu(f) = 10^{\mathrm{MSL}(f)/10}. \tag{2.94}$$

Thus, for a finite predefined scan grid, $\mathrm{MSL}(f) < 0$ is calculated for each frequency of interest as the relative level in dB between the main lobe's peak and the maximum sidelobe's peak. In practice, evaluating the PSF per frequency is performed as part of the HR-CLEAN-SC algorithm where the term $|\mathbf{g}_t^H \mathbf{u}_t|^2$ is evaluated for all T grid points. Therefore, evaluating the exact value of MSL hardly incurs additional computation time. However, in case very wide frequency ranges or very fine grids are required, the MSL per frequency can be approximated by empirical formulae [30] to ease the computational effort.

References

[1] P. Sijtsma, R. Merino-Martinez, A. M. N. Malgoezar, and M. Snellen, *High-resolution clean-sc: Theory and experimental validation,* International Journal of Aeroacoustics **16**, 274 (2017).

[2] W. C. Elmore and M. A. Heald, *Physics of waves* (Dover Publications Inc., 1985).

[3] A. Sommerfeld, *Partial differential equations in physics* (Academic Press, 1949).

[4] M. E. Goldstein, *Aeroacoustics* (McGraw-Hil, Inc., 1976).

[5] S. W. Rienstra and A. Hirschberg, *An introduction to acoustics,* Eindhoven University of Technology (2004).

[6] P. Sijtsma, *Experimental techniques for identification and characterisation of noise sources*, Tech. Rep. (National Aerospace Laboratory NLR, 2004).

[7] Y. Liu, A. R. Quayle, A. P. Dowling, and P. Sijtsma, *Beamforming correction for dipole measurement using two-dimensional microphone arrays,* The Journal of the Acoustical Society of America **124**, 182 (2008).

[8] E. H. Weber, H. E. Ross, and D. J. Murray, *E.H. Weber on the tactile senses*, 2nd ed. (Hove : Erlbaum (UK) Taylor & Francis, 1996).

[9] D. Bergman, *Modeling beamformers in refractive media,* in *Berlin Beamforming Conference 2016* (2016).

[10] P. Stoica and R. L. Moses, *Spectral Analysis of Signals* (Prentice Hall, Upper Saddle River, NJ, 2005).

[11] H. Van Trees, *Optimum Array Processing: Part IV of Detection, Estimation, and Modulation Theory*, Detection, Estimation, and Modulation Theory (Wiley, 2004).

[12] P. Welch, *The use of fast Fourier transform for the estimation of power spectra: A method based on time averaging over short, modified periodograms,* **15**, 70 (1967).

[13] T. F. Brooks and W. M. Humphreys, *Extension of DAMAS phased array processing for spatial coherence determination (DAMAS-C),* AIAA paper **2654** (2006).

[14] B. D. Van Veen and K. M. Buckley, *Beamforming: A versatile approach to spatial filtering,* IEEE assp magazine **5**, 4 (1988).

[15] G. Zechel, A. Zeibig, and M. Beitelschmidt, *Time-domain beamforming on moving objects with known trajectories,* in *Berlin Beamforming Conference 2010-12* (2010).

[16] E. Sarradj, *Three-dimensional acoustic source mapping with different beamforming steering vector formulations,* Advances in Acoustics and Vibration **2012** (2012).

[17] X. Huang, L. Bai, I. Vinogradov, and E. Peers, *Adaptive beamforming for array signal processing in aeroacoustic measurements*, The Journal of the Acoustical Society of America **131**, 2152 (2012).

[18] D. H. Johnson and D. E. Dudgeon, *Array Signal Processing, Concepts and Techniques* (P T R Prentice Hall, Englewood Cliffs, 1993).

[19] M. Mosher, *Phased Arrays for Aerocoustic Testing: Theoretical Development*, in *2nd AIAA/CEAS Aeroacoustics Conference, State College, Pa, May 6-8, 1996* (1996).

[20] T. F. Brooks and W. M. Humphreys, Jr, *Effect of Directional Array Size on the Measurement of Airframe Noise Components*, in *Fifth AIAA/CEAS Aeroacoustics Conference, May 10-12, 1999, Bellevue, Washington* (1999).

[21] P. Sijtsma, *Acoustic beamforming for the ranking of aircraft noise*, Tech. Rep. (National Aerospace Laboratory NLR, 2012).

[22] E. Sarradj, *A fast signal subspace approach for the determination of absolute levels from phased microphone array measurements*, J. Sound Vib. **329**, 1553 (2010).

[23] R. P. Dougherty, *Beamforming in acoustic testing*, in *Aeroacoustic Measurements* (Springer, 2002) pp. 62–97.

[24] T. Suzuki, *A review of diagnostic studies on jet-noise sources and generation mechanisms of subsonically convecting jets*, Fluid Dyn. Res. **42**, 014001 (2010).

[25] S. Oerlemans, *Detection of aeroacoustic sound sources on aircraft and wind turbines*, Phd thesis, University of Twente, Enschede (2009).

[26] P. Sijtsma, *CLEAN based on spatial source coherence*, International journal of aeroacoustics **6**, 357 (2007).

[27] J. A. Hogbom, *Aperture synthesis with a non–regular distribution of interferometer baselines*, Astronomy and Astrophysics Supplement Series **15**, 417 (1974).

[28] P. Sijtsma, R. Merino-Martinez, A. M. N. Malgoezar, and M. Snellen, *High–Resolution CLEAN–SC: Theory and Experimental Validation*, in 23^{rd} *AIAA/CEAS Aeroacoustics Conference. June 5 – 9 2017. Denver, Colorado, USA* (2017) AIAA paper 2017–3841.

[29] S. Luesutthiviboon, A. M. N. Malgoezar, M. Snellen, and D. G. Simons, *Maximizing source discrimination performance by using an optimized array and adaptive high-resolution clean-sc beamforming*, in *Berlin Beamforming Conference 2018* (2018).

[30] J. J. Christensen and J. Hald, *Beamforming*, Technical Review No. 1 - 2004 (2004), brel & Kjær Sound & Vibration Measurements A/S.

3

Microphone array optimization

Assigning proper positions to microphones within arrays is essential in order to reduce or eliminate side- and grating lobes in 2D beamform images. In this chapter objective functions are derived providing a measure for the presence of these side- and grating lobes. Using the global optimization method Differential Evolution, an optimized microphone configuration is obtained by minimization of this objective function. Results show that optimizing the microphone locations can significantly enhance the array performance. In a large part of he scan region surrounding the true source location, no side- or grating lobes are present, meaning that the source can be unambiguously located. Two different optimization procedures are presented. The first method allows for placement of all microphones without restrictions. This procedure found that the optimized array configuration shows the microphones distributed at almost constant distance. This distance decreases with increasing frequency as $d = 1.38\lambda$, but no firm design rules could be derived as optimal performance required additional small perturbations. Therefore, for the second procedure a method was developed with more restrictions and also taking into account the main lobe width. This optimization procedure resulted in a spiral-like configuration which showed significant decrease of sidelobes and the main lobe width for a broad frequency range.

Parts of this chapter have been presented in the Berlin Beamforming Conference 2016 [1] and 2018 [2].

3.1. Introduction

Using a single point source, apart from the reconstructed main lobe, the presence of side lobes is seen due to a finite number of pressure time signals in space. The side lobes originating from a primary source can lead to obfuscation of the main lobe of a secondary source. This phenomenon can be suppressed using a different beamforming method as seen in the previous section. Another way would be to efficiently place a beforehand known amount of microphones on certain locations.

There are several ways to reduce the presence of grating lobes and side lobes, one more practical and easier to perform than the other. The impractical choices are to use an infinitesimal small distance between microphones to eliminate grating lobes for all frequencies. The other is the use of an infinite amount of microphones to reduce (but not eliminate) the levels of the side lobes, which in turn requires a microphone array of infinite dimension. Alternatively, weighting can be applied. However, this effectively decreases the array aperture and thus the array resolution. Because for practical applications one works with a finite amount of microphones, other solutions need to be looked for.

One way to eliminate side lobes is to apply dedicated beamforming techniques described in the previous chapter such as adaptive beamforming [3] and functional beamforming [4–6], or deconvolution methods such as CLEAN-PSF, CLEAN-SC [7] and DAMAS [8–10]. These methods start their deconvolution algorithm with source maps obtained by the well-known sum-and-delay beamforming, or, conventional beamforming. Although deconvolution methods work well in certain situations, the quality of the results depends strongly on the quality of the initial source map.

The other approach is to minimize side lobes through array design. Previous work [11–13] shows that careful selection of the microphone locations and array aperture can reduce side lobe levels.

In this work optimizing the array configuration is the focus. As a first step, an objective function is selected which is a measure for the presence of artificial sources. By minimizing this function an optimal microphone distribution is obtained, providing minimal appearance of side lobes. The unknowns are the microphone positions. In order to allow optimization for the large number of unknowns, use is made of Differential Evolution (DE) as the global optimization method. DE is a variant of the well-known genetic algorithm (GA) [14]. Previous work in the field of geo-acoustics [15] showed promising results using the DE method for global optimization problems. As with GA, also DE has a number of setting parameters that need to be chosen well in order to obtain optimal DE performance, i.e., a high probability of locating the optimum at a minimum number of forward calculations. For the geo-acoustic inversion problem [15] an optimal DE setting was derived. However, for the problem considered in this contribution the number of parameters is much larger, requiring an additional effort to find those values for the DE setting parameters that provide good DE performance also for the application at hand. Given this optimal setting, the optimization is readily extended to other objective functions.

3.2. The optimization method

Differential evolution (DE) is a method that optimizes a problem by iteratively trying to improve candidate solutions with regard to a given measure of quality and was introduced by Storn and Price [16, 17]. It can be classified as a metaheuristic method making few or no assumptions about the problem being optimized and can search very large spaces of candidate solutions. However, this metaheuristic method does not guarantee an optimal solution is ever found.

DE is used for multidimensional real-valued functions and does not require the user to calculate the gradient of the problem being optimized, which in turn implies that DE does not require the optimization problem to be differentiable.

DE starts with an initial population of randomly chosen parameter value combinations each containing trial values for the unknown parameters. The parameter value combinations are improved each generation over a maximum amount of successive generations N_G. At each generation l, members of the partner population are created from the original population members $\mathbf{m}_{l,i}$ as

$$\mathbf{p}_{l,i} = \mathbf{m}_{l,r_1} + F\left(\mathbf{m}_{l,r_2} - \mathbf{m}_{l,r_3}\right), \tag{3.1}$$

with $i = 1 \cdots q$. Indices $r_1, r_2, r_3 \in \{1, 2, \cdots, q\}$ are integer, differ from each other and are chosen at random. F is a scalar multiplication factor between 0 and 1. A higher value of F indicates an increased difference between original parameter vector $\mathbf{m}_{l,i}$ and those contained in the partner population $\mathbf{p}_{l,i}$.

The next step is to calculate its descendant $\mathbf{d}_{l,i}$ by applying crossover to $\mathbf{m}_{l,i}$ and $\mathbf{p}_{l,i}$ with a probability p_c. For each parameter j of $\mathbf{d}_{l,i}$ we get

$$d_{l,ij} = \begin{cases} p_{l,ij} & \text{if } [\mathscr{U}(0,1)]_j \leq p_c \\ m_{l,ij} & \text{if } [\mathscr{U}(0,1)]_j > p_c \end{cases}, \tag{3.2}$$

with $[\mathscr{U}(0,1)]_j$ the j-th evaluation of a uniform distribution with values between 0 and 1. Setting the value of p_c high means that more values are replaced by those of the partner population, while a low value of p_c results in generations that differ only slightly regardless of the value of F.

To create the new generation $l+1$ from the previous generation l, the member $\mathbf{m}_{l,i}$ is replaced by $\mathbf{d}_{l,i}$ only if it yields a smaller value for the objective function E

$$\mathbf{m}_{l+1,i} = \begin{cases} \mathbf{d}_{l,i} & \text{if } E(\mathbf{d}_{l,i}) < J(\mathbf{m}_{l,i}) \\ \mathbf{m}_{l,i} & \text{if } E(\mathbf{d}_{l,i}) \geq J(\mathbf{m}_{l,i}) \end{cases}. \tag{3.3}$$

Doing this for all members i in the population we obtain the next generation $l+1$. This process is repeated for N_G generations. For decreasing energy values a member would converge to the correct parameter values (in this problem the). For this work this can either be the microphone positions for array optimization or the positions and strengths of all the sources for source localization.

The performance of global optimization methods, i.e., their success in localizing the global optimum in an efficient way, is dependent on a number of so-called setting parameters. For DE these are

- Population size q,
- Multiplication factor F,
- Crossover probability p_c,
- Number of generations N_G.

These settings must be set beforehand to suitable values, and can be problem specific, to maximize the probability of localizing the global optimum.

All the steps for the DE optimization method can be seen in a flowchart in Fig. 3.1.

3.3. Array optimization I

3.3.1. The objective function for sidelobe minization

To obtain the objective function, the so-called aperture function is derived using the beamforming filter expression in Eq. (2.56) with steering vector Formulation I from Eq. (2.63). Therefore the assumption is made (by using Formulation I) that the array is in the far field, such that the distance between the array and the source is large enough to assume the incoming signals to be plane waves. In this case we are in the far field and only interested in the direction of the sound. The pressure signal can be described as

$$p(\vec{r}_n) = \mathrm{e}^{i\vec{k}\cdot\vec{r}_n}, \tag{3.4}$$

where $\vec{r}_n = \vec{x}_n - \vec{x}_t$ is the vector connecting the scan point and the n-th microphone and $\vec{k}$ the wave vector which should satisfy

$$\frac{\omega^2}{c^2} - \vec{k}\cdot\vec{k} = 0, \tag{3.5}$$

with c the speed o sound and ω the frequency of the signal.

Considering a source with unit amplitude and wave vector $\vec{k}_0$, the pressure received at the microphones of the array are

$$\mathbf{P}^{\text{meas}} = \begin{bmatrix} \mathrm{e}^{\vec{k}_0\cdot\vec{r}_1} \\ \vdots \\ \mathrm{e}^{\vec{k}_0\cdot\vec{r}_N} \end{bmatrix}. \tag{3.6}$$

The steering vector towards a scan point in direction $\vec{k}$ is

$$\mathbf{h} = \begin{bmatrix} \mathrm{e}^{\vec{k}\cdot\vec{r}_1} \\ \vdots \\ \mathrm{e}^{\vec{k}\cdot\vec{r}_N} \end{bmatrix}, \tag{3.7}$$

where $\vec{k}_0$ and $\vec{k}$ both satisfy Eq. (3.5) i.e. correspond to the same frequency. We obtain

$$\mathbf{h}^*\mathbf{h} = \left(\mathrm{e}^{-i\vec{k}\cdot\vec{r}_1}\mathrm{e}^{i\vec{k}\cdot\vec{r}_1} + \cdots + \mathrm{e}^{-i\vec{k}\cdot\vec{r}_N}\mathrm{e}^{i\vec{k}\cdot\vec{r}_N}\right) = N, \tag{3.8}$$

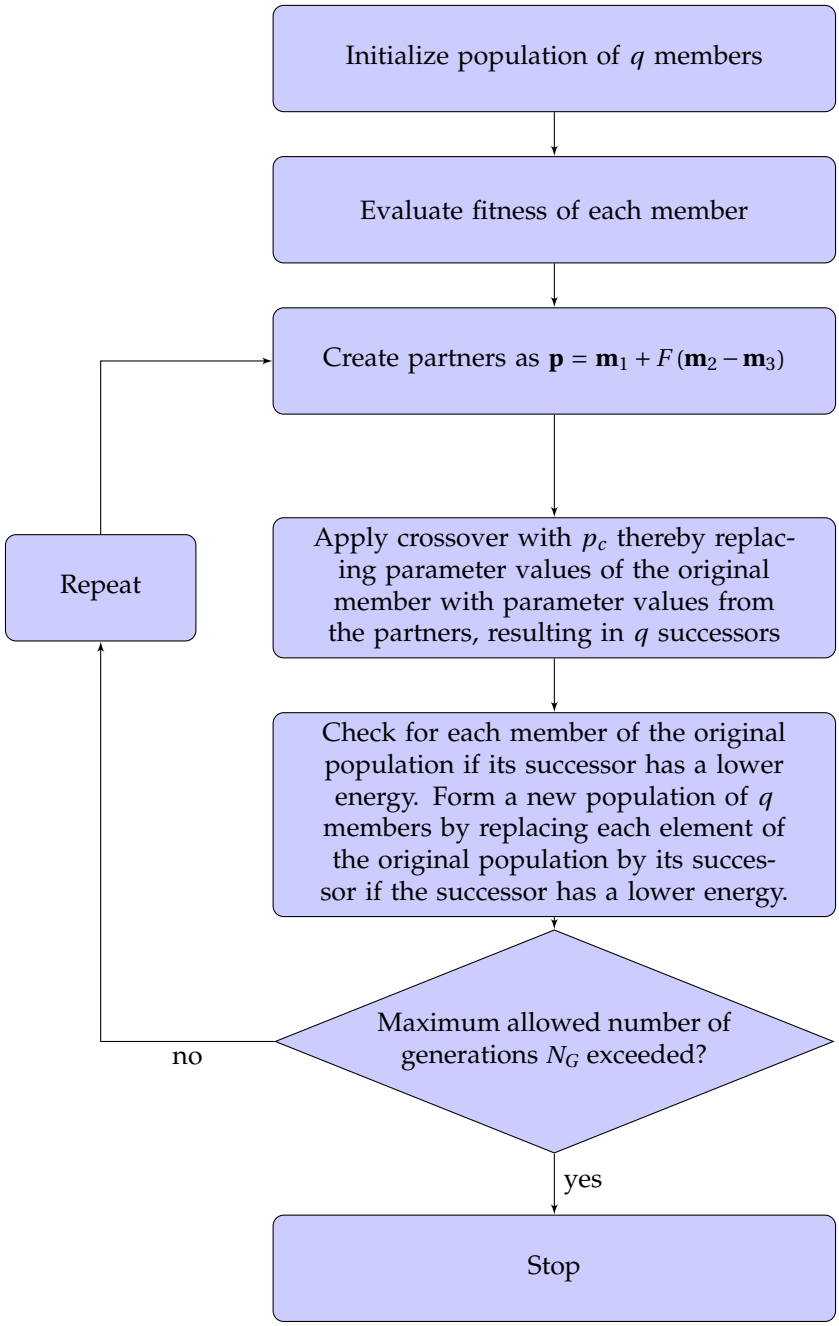

Figure 3.1: Steps taken to use Differential Evolution.

and

$$\mathbf{h}^* \mathbf{P}^{\text{meas}} = \left(\mathrm{e}^{-i\vec{k}\cdot\vec{r}_1} \mathrm{e}^{+i\vec{k}_0\cdot\vec{r}_1} + \cdots + \mathrm{e}^{-i\vec{k}\cdot\vec{r}_N} \mathrm{e}^{i\vec{k}_0\cdot\vec{r}_N} \right). \tag{3.9}$$

Similar to using Eq. (2.56) with Eq. (2.63), the beamformer output for this special case with the wave vector notation is

$$\hat{P}_0(\omega) = \frac{1}{N} \sum_{n=1}^{N} \mathrm{e}^{i(\vec{k}_0 - \vec{k})\cdot\vec{r}_n}. \tag{3.10}$$

3

Eq. (3.10) can be seen as an aperture smoothing function W,

$$W\left(\vec{k}_0 - \vec{k}\right). \tag{3.11}$$

To eliminate side lobes the aperture function should satisfy

$$W\left(\vec{k}_0 - \vec{k}\right) = \begin{cases} 1 & \text{if } \vec{k} = \vec{k}_0 \\ 0 & \text{if } \vec{k} \neq \vec{k}_0 \end{cases}. \tag{3.12}$$

Using only a finite number of microphones N makes this impossible.

If plane wave beamforming is considered with a planar microphone array in $z = 0$, this results in

$$(\vec{k}_0 - \vec{k}) \cdot \vec{r}_n = (k_{0,x} - k_x) x_n + (k_{0,y} - k_y) y_n, \tag{3.13}$$

and for the aperture function

$$W(k_x, k_y) = \frac{1}{N} \sum_{n=1}^{N} \mathrm{e}^{i\left[(k_{0,x} - k_x) x_n + (k_{0,y} - k_y) y_n\right]}, \tag{3.14}$$

from where it is seen that beamforming results are shift-invariant with respect to the wave numbers k_x and k_y. In other words, an incoming wave with wave numbers $k_x = k_{0,x}$ and $k_y = k_{0,y}$ gives the same results as with $k_x = 0$ and $k_y = 0$, but shifted by $(k_x, k_y) = (k_{0,x}, k_{0,y})$. It can therefore be written as

$$W(k_x, k_y) = \frac{1}{N} \sum_{n=1}^{N} \mathrm{e}^{-i(k_x x_n + k_y y_n)}. \tag{3.15}$$

Now, to minimize side lobes the following objective, or energy, function is defined

$$J(\vec{r}_1, \cdots, \vec{r}_N) = \int_{\Omega} |W(k_x, k_y)|^2 \mathrm{d}k_x \mathrm{d}k_y = \frac{1}{N^2} \iint_{\Omega} \left| \sum_{n=1}^{N} \mathrm{e}^{-i(k_x x_n + k_y y_n)} \right|^2 \mathrm{d}k_x \mathrm{d}k_y, \tag{3.16}$$

where J is the function to be minimized, i.e. the aperture function squared, conform Sijtsma [18]. The power of 2 is used for ease of implementation and computational considerations. The domain Ω contains all scan directions of interest. In order to minimize the side lobes, the domain will be chosen such that it includes all scan directions of interest, but excludes the main lobe.

Eq. (3.16) can be rewritten as

$$J(\vec{r}_1,\cdots,\vec{r}_N) = \frac{\pi k}{N^2}\Big(Nk\left[\sin^2(\phi_{max}) - \sin^2(\phi_{min})\right] + 4\sum_{m=1}^{N-1}\sum_{n=m+1}^{N}\frac{\sin(\phi_{max})J_1[k\sin(\phi_{max})d_{mn}] - \sin(\phi_{min})J_1[k\sin(\phi_{min})d_{mn}]}{d_{mn}}\Big), \tag{3.17}$$

where d_{mn} is the distance between microphone m and n, $k = |\vec{k}|$ and J_1 is the first order Bessel function of the first kind. The derivation of Eq. (3.17) can be found in Appendix A The angles ϕ are elevation angles as can be seen in Fig. 3.2; ϕ_{min} and

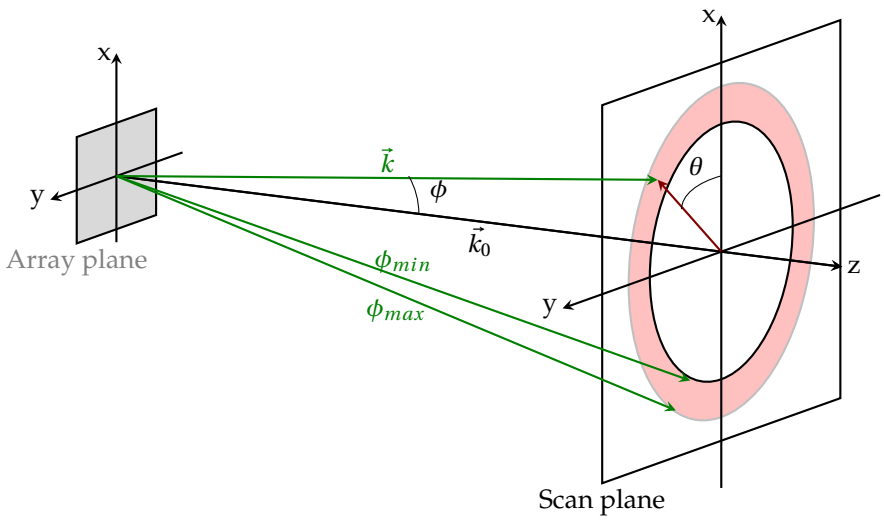

Figure 3.2: Relation between the wavevector $\vec{k}$, polar angle ϕ and azimuthal angle θ. The area of integration is shown in red. In practice the inner radius will be much closer to the origin.

ϕ_{max} determine the domain Ω.

3.3.2. Deriving the Rayleigh criterion and obtaining the integration bounds

In order to minimize the side lobes while excluding the main lobe, the integration boundaries ϕ_{min} and ϕ_{max} need to be selected carefully. The problem of beamforming with an array of microphones is very similar to the descriptions of the best focused spot of light that a perfect lens with a circular aperture can make, limited by the diffraction of light. Whereas in optics the lens 'applies' the (fixed) phase shift [19], in acoustic beamforming this would be the microphones. While the lens is a continuous medium limited by the aperture, the microphone array has only limited 'points'. That is, the microphone array can be seen as a 'sampled' optical lens where the phase shift can be adjusted as desired. This analogy is also going to be used to obtain practical choices for ϕ_{min} and ϕ_{max}. Like with diffraction optics it is expected that the signal resulting from beamforming has the behaviour of

a Bessel function. To clarify this, assume an infinite amount of microphones on a circular array with radius R. The aperture function Eq. (3.15) then has the form of

$$W(k_x, k_y) \sim \frac{1}{\pi R^2} \iint_{\Omega} \mathrm{e}^{-i(k_x x + k_y y)} \mathrm{d}x\mathrm{d}y \tag{3.18}$$

$$= \frac{1}{\pi R^2} \int_0^R \int_0^{2\pi} r\mathrm{e}^{-irk\sin(\phi)} \mathrm{d}\theta\mathrm{d}r \tag{3.19}$$

$$= \frac{2J_1\left(kR\sin(\phi)\right)}{kR\sin(\phi)}, \tag{3.20}$$

with $r = \sqrt{x^2 + y^2}$ and using similar coordinate transformations and steps as deriving the objective function in Appendix A. Eq. (3.20) squared is known as the Airy pattern and can be seen in Fig. 3.3. Using this expression the lower boundary ϕ_{min}

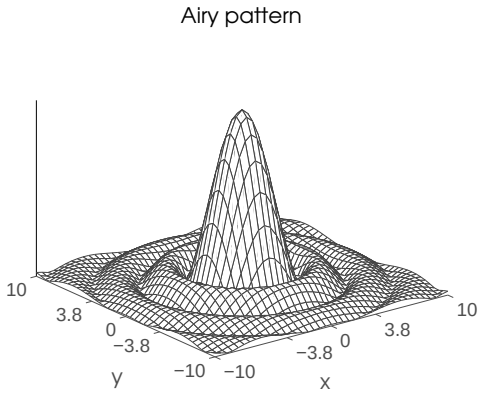

Figure 3.3: Surface plot of the Airy pattern.

can be defined to exclude the main lobe which occurs at the first zero crossing of Eq. (3.20). For a Bessel function of the first order this corresponds to $J_1(u) = 0$, or $u \approx 3.83$. Thus

$$kR\sin(\phi_{min}) = 3.83. \tag{3.21}$$

For small angles ϕ this results in

$$\phi_{min} = 2\frac{3.83}{Dk} = 1.22\frac{c}{Df}, \tag{3.22}$$

with $D = 2R$ the diameter of the circular array. Eq. (3.22) is known as the *Rayleigh criterion* and is known as the angular resolution of an imaging device for the given frequency f. This angle can be related to a spatial resolution with

$$\frac{\Delta\ell}{2z} = \tan\left(\frac{\phi_{min}}{2}\right), \tag{3.23}$$

for small angles this leads to

$$\Delta\ell = 2z\frac{\phi_{min}}{2} = 1.22\frac{zc}{Df}. \tag{3.24}$$

with z and the relation between distances given in Fig. 3.4.

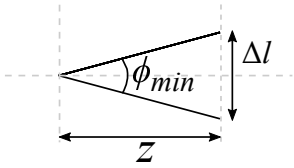

Figure 3.4: Relation of the angular to spatial resolution by the Rayleigh criterion.

For the maximum angle ϕ_{max} a value based on the desired angular field-of-view (FOV) of 60° or $\phi_{max} = 30°$ is selected.

Additionally, the lowest possible maximum sidelobe level[1] for a planar array can be obtained using Eq. (3.20). The angle of the first ring (highest sidelobe) of the Airy pattern can be obtained using $\partial W^2/\partial\phi = 0$. For which the first ring is at $kR\sin(\phi) = 5.13562\ldots$, therefore the lowest attainable *maximum sidelobe level* relative to the main lobe is

$$MSL_{\text{lowest}} = 20\log_{10}\left[W\left(kR\sin(\phi) = 5.13562\ldots\right)\right] = -17.57\ldots\,[\text{dB}]. \tag{3.25}$$

Some examples for circular-aperture microphone arrays which show the limits can be found in Appendix B.

3.3.3. Interpretation of the objective function

In the ideal case, the value of the objective function should yield zero by excluding the origin in the integration. However, due to the nature of an acoustic array, side lobes are inevitable and therefore values of zero for optimized configurations are not feasible. Therefore two exemplary configurations accompanied with a beamformed image of a point source located at the origin are considered. The frequency of the point source is $f = 2000$ Hz with an SPL of 100 dB. The source is positioned in the far field at a distance of 35 m. One configuration exhibits relatively high side lobe levels in the Ω-minimization region while the other has lower levels. The microphone configuration, the corresponding beamformed image and an intersection of the beamform output at $y = 0$ can be seen in Figs. 3.5 to 3.7 respectively. The boundaries corresponding to ϕ_{min} and ϕ_{max} are indicated by two concentric circles in the beamform images in Fig. 3.6. Dashed lines indicate these boundaries in the plots showing the intersection in Fig. 3.7. The radii of the circles are, using Eq (3.22) and a FOV of 60°, 3.68 and 20.21 m. Within this range it is seen that for the configuration corresponding to $J = 43.5$ relatively high side lobe levels are

[1] That is, for the point spread function of the array a highest sidelobe can always be identified. This sidelobe can then be minimized by an appropriate selection of microphone positions.

present compared to the configuration of $J = 8.48$. Outside the optimization region, i.e. $r > 20.21$ m, it is seen that the occurrence and levels of the side lobes are of the same order.

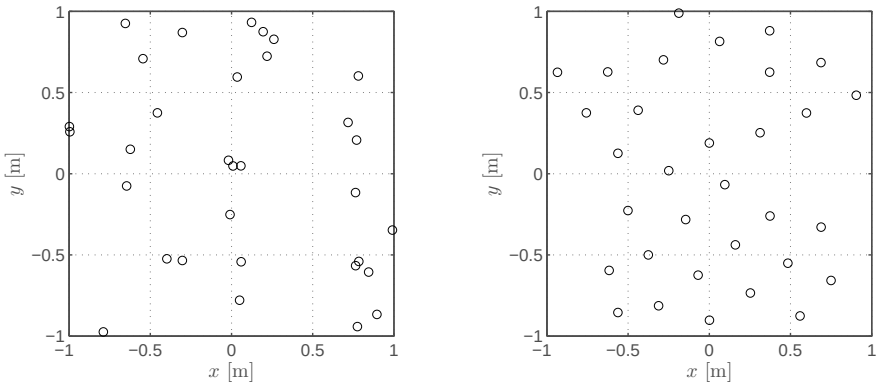

(a) (b)

Figure 3.5: Comparison of two microphone configurations with corresponding value of $J = 47.52$ for (a) and $J = 8.48$ for (b).

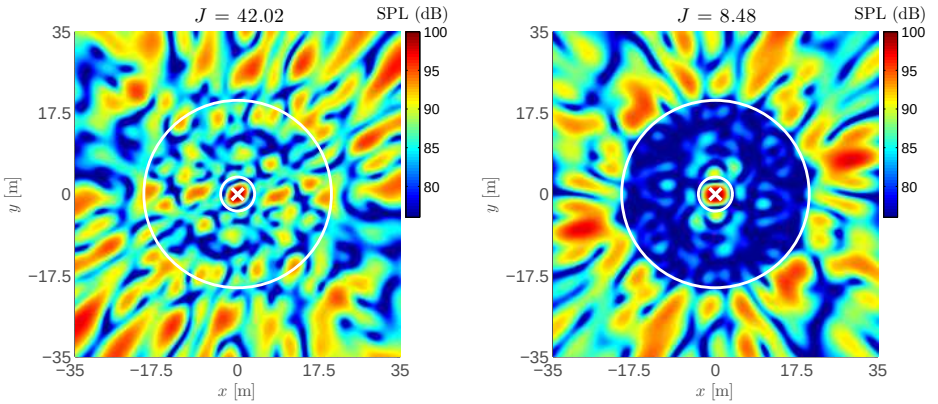

(a) (b)

Figure 3.6: Comparison of the two beamforming images for the microphone configurations given in Fig. 3.5 with corresponding value of $J = 47.52$ for (a) and $J = 8.48$ for (b).

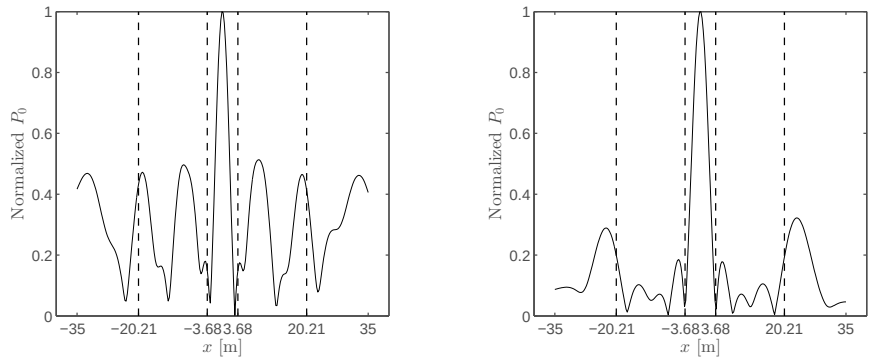

Figure 3.7: Comparison of two 2-D intersections of the beamforming images of Fig. 3.6 at $y = 0$ m with corresponding value of $J = 47.52$ for (a) and $J = 8.48$ for (b). The normalized pressure amplitude is given on the vertical axis.

3.3.4. Using the optimization method

Problems related to optimizing an objective function, possibly being nonlinear and non-differentiable over continuous space, can be solved using global optimization methods. In this section the global optimization method used is differential evolution (DE) explained in Section 3.2.

For the array optimization the population consists of q members which in this problem equals 64 values corresponding to the (x, y)-coordinates of the 32 microphones. For the other parameters the optimal settings has to be found.

Finding the optimal settings: number of forward generations and population size

As it is not known beforehand for which combination of setting parameters DE performs best, several tests are carried out to determine the number of generations, population size, multiplication factor and crossover probability.

First the optimal setting for the amount of generations and population size are determined. Hereafter the multiplication factor and crossover probability are selected.

To determine the optimal value for the amount of generations and population sizes, the multiplication factor and crossover probability were set to $F = 0.7$ and $p_c = 0.6$ in accordance with Snellen [15] for a geo-acoustic inversion problem and the same DE implementation.

A Monte Carlo simulation is performed for population sizes q of 64, 96 and 128, where for each setting 10 independent DE runs are carried out. The result of the energy as a function of generation for the various runs for each population size can be seen in Fig. 3.8. A large variation at 4000 generations can be seen for all population sizes. At 4000 generations the larger population size, $q = 128$, does not outperform $q = 64$. Eight out of the ten runs for $q = 128$ have an energy value

between 16 and 18, while for $q = 64$ at least half of the ten runs have a value below 16. To further compare between the different population sizes the amount of forward calculations qN_G is looked at. For the three figures in Fig. 3.8 the vertical dashed line indicates the generation for which the number of forward calculations amounts to 256000.

From this it can be seen that a value for $q = 128$ does not on average produce lower values for the energy. This motivates us to use a population size of $q = 64$. While the variation is slightly larger for $q = 64$, the chance to arrive at a lower value for the energy is significantly larger. The same holds when comparing to $q = 96$. Although no full convergence has yet been achieved for $q = 64$ at 4000 generations,

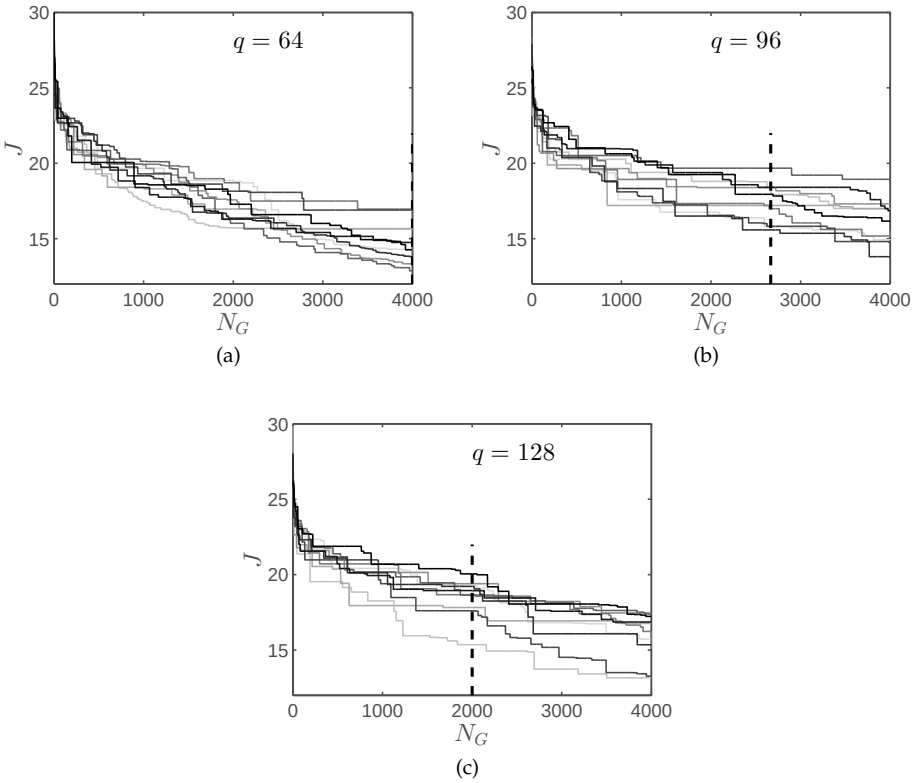

Figure 3.8: The value of the objective function J as a function of the amount of generations N_G for 10 independent runs with $F = 0.7$, $p_c = 0.6$ for (a) $q = 64$, (b) $q = 96$ and (c) $q = 128$.

the amount of generations is not increased due to computational constraints. To this end the amount of generations is set to $N_G = 4000$ with a population size of $q = 64$.

Finding the optimal settings: multiplication factor and crossover probability
Having decided on the value for the population size and the amount of generations, two settings remain to be determined. In order to find suitable values for the multiplication factor F and cross over probability p_c, the DE performance is assessed for values for p_c between 0.2 and 1 and F between 0 and 1 with steps of 0.1. For each combination 10 independent runs are done and the average value for the energy value J is determined. The results are shown in Fig. 3.9. From Fig. 3.9

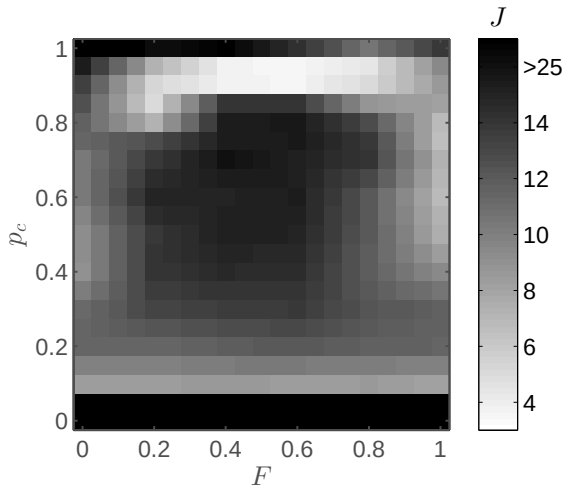

Figure 3.9: Map of the energy J as a function of p_c and F for $q = 64$ and $N_G = 4000$.

low values of the energy can be seen in the region for $p_c = 0.9$ and $F = 0.2$ to $F = 0.8$. Based on this figure, the best combination to use for DE is found as $p_c = 0.9$ and $F = 0.5$.

3.3.5. Results of array optimization I

Optimizing the objective function J of Eq. (3.17) resulted in various microphone array configurations having low energy values. In Fig. 3.10 several configurations are shown at various stages of an optimization run.

First it can be seen that the configuration for generation 333 becomes more compact compared to the initial configuration by having some microphones closer together. This results in an energy decrease of $J = 23.57$ to $J = 15.86$. From generation 333 and on it can be seen that, while roughly retaining the dimensions of the compact microphone geometry, the microphone positions get more evenly distributed within this geometry, which roughly resembles a circular disc. This can seen to happen from generation 333 to 666 with a decrease of $J = 15.86$ to $J = 9.6$. While the configuration at generation 666 and 1500 are very similar, an additional significant decrease of energy can be achieved by going from $J = 9.6$ to $J = 3.96$ by DE through slightly adjusting the microphones and achieving an even more regular pattern. This indicates that the minimum energy corresponds to a specific distance

between a microphone and its neighbours. Figure 3.11 shows the histogram of all

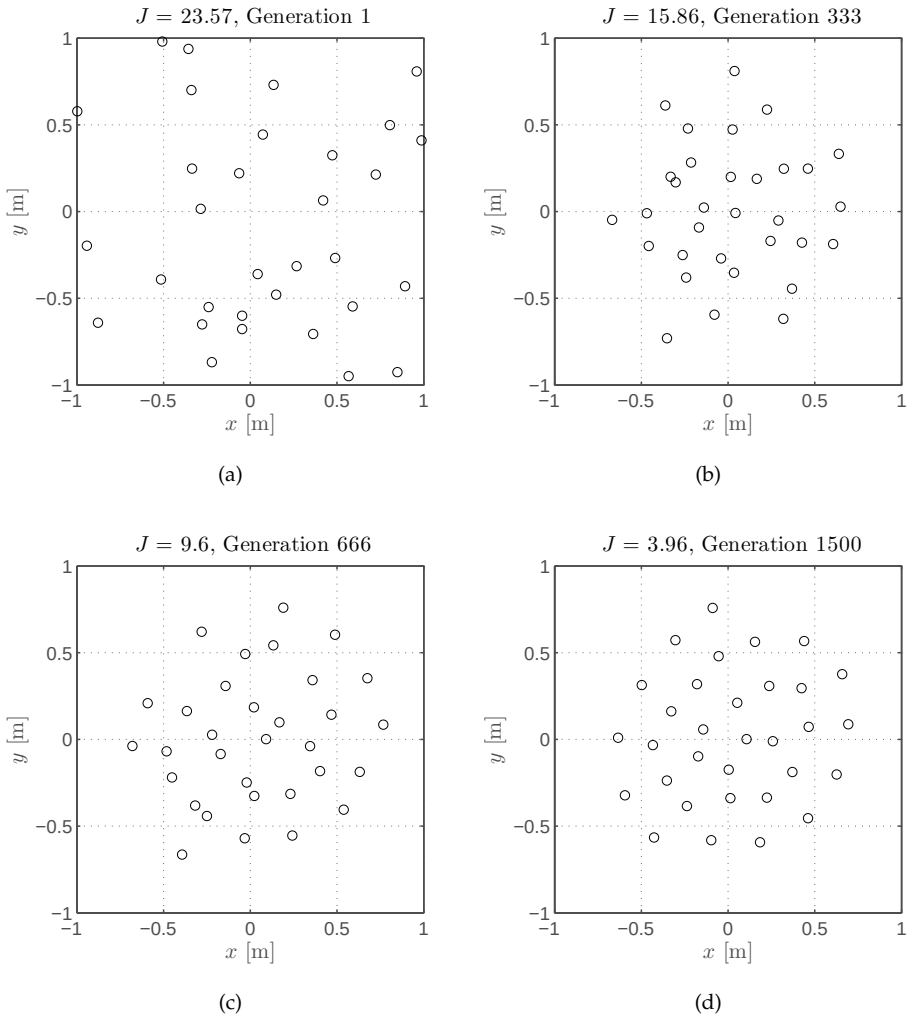

Figure 3.10: Microphone configurations obtained using $F = 0.2$ and $p_c = 0.8$ for several values of J (a) $J = 23.57$, (b) $J = 15.86$, (c) $J = 9.6$ and (d) $J = 3.96$.

distances between the microphones and their closest neighbour for the array configurations of Fig. 3.10. From these histograms it can be seen that towards the final generation these distances tend to fall within the range of 0.16 to 0.28 m. The histograms confirm the formation of a more compact configuration as the variance of the distance decreases, as well as the mean.

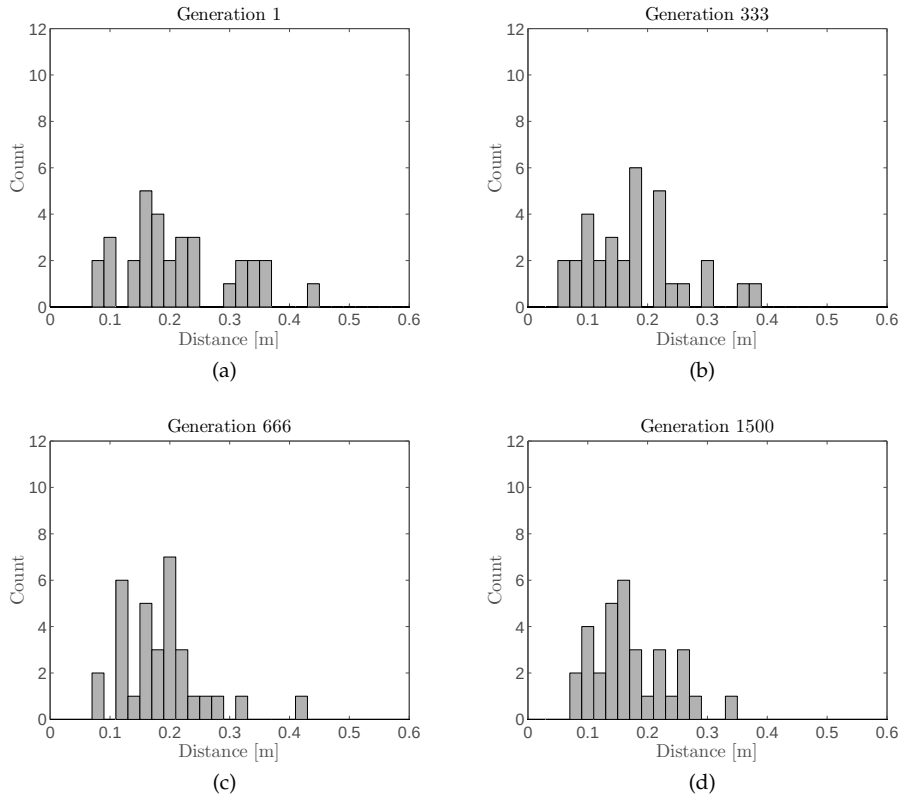

Figure 3.11: Histograms of the closest-neighbour-distances of the corresponding configurations in Fig. 3.10, (a) $J = 23.57$, (b) $J = 15.86$, (c) $J = 9.6$ and (d) $J = 3.96$.

3.3.6. Beamforming with the ideal configuration

For the results presented in the previous section, the frequency selected for optimization was 2000 Hz. Beamforming using the optimized microphone configuration should result in side lobes that are significantly reduced in the optimization region defined in Section 3.3.2. To demonstrate this, and to investigate how the beamforming behaviour is for other frequencies, beamforming is used for three different frequencies, i.e. lower than 2000 Hz, equal to 2000 Hz and larger than 2000 Hz using the optimal configuration obtained in the previous section. To do this a 100 dB monopole sound source is simulated at the origin at a distance of 35 m. The result of beamforming is shown in Fig. 3.12 for the frequencies 1500, 2000 and 3000 Hz, where the white circles indicate the optimization boundaries corresponding to ϕ_{min} and ϕ_{max}. From Fig. 3.12b it can be seen beamforming at the frequency for which the array was optimized (2000 Hz) results in a source map with no side lobes visible in the region of interest and side lobes which are above 80 dB, residing just outside the outer boundary. The main lobe resides just inside

the inner boundary indicating that the optimum microphone configuration provides an aperture close to the array diameter. This is confirmed by Fig. 3.10d. It can therefore be concluded that beamforming at the frequency for which the microphone configuration was optimized results in side lobes being reduced for the directions of interest.

For the lower frequency (1500 Hz) see Fig. 3.12a, it is seen that the inner boundary lies inside the main lobe. This is expected according to Eq. (3.22) indicating that lower frequencies result in a wider main lobe while a higher frequencies result in a smaller main lobe. The latter is seen in Fig. 3.12c. Considering the performance of the optimized array at ϕ_{max} Fig. 3.12a indicates for lower frequencies good performance for the FOV of interest but also for larger values of ϕ. In contrast, for higher frequencies the FOV is reduced as side lobes start to appear for values of ϕ smaller than ϕ_{max}.

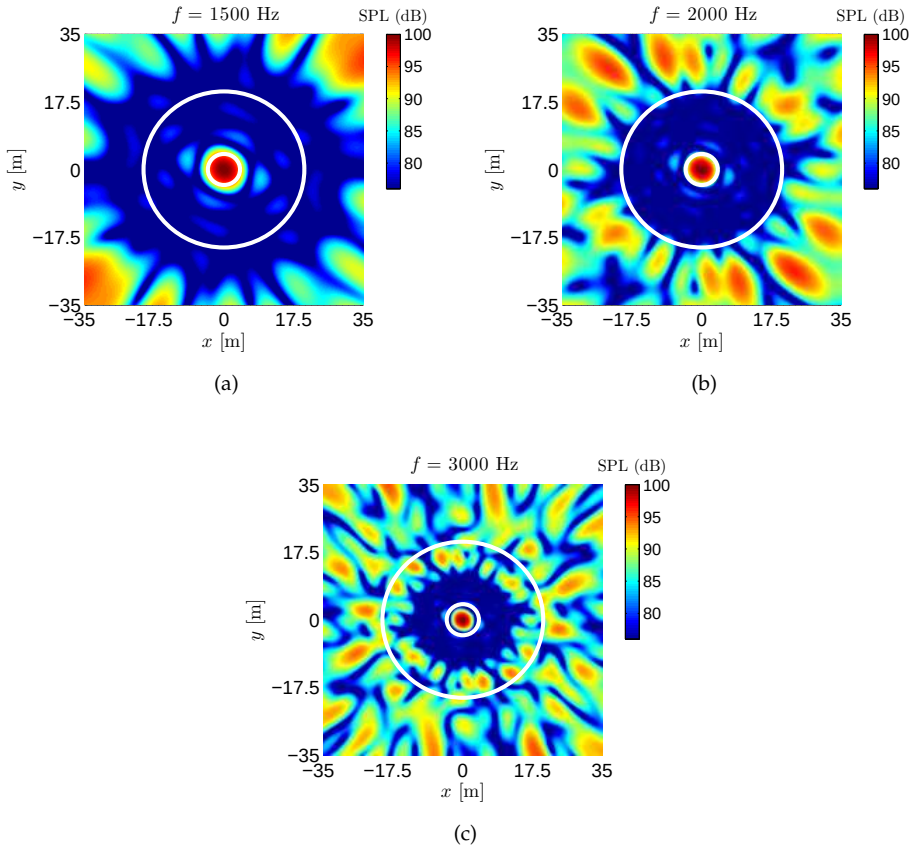

Figure 3.12: Beamforming with the microphone configuration given in Fig. 3.10d for a simulated source signal at the origin at frequency (a) $f = 1500$ Hz, (b) $f = 2000$ Hz and (c) $f = 3000$ Hz.

3.3.7. Minimum side lobe array design

As a next step the optimization was carried out for frequencies from 1000 Hz to 10000 Hz in 1000 Hz steps. Fig. 3.13 shows the optimized arrays for 2000, 4000 and 6000 Hz, respectively. It can be seen that the separation distance between microphones gets smaller for higher frequencies.

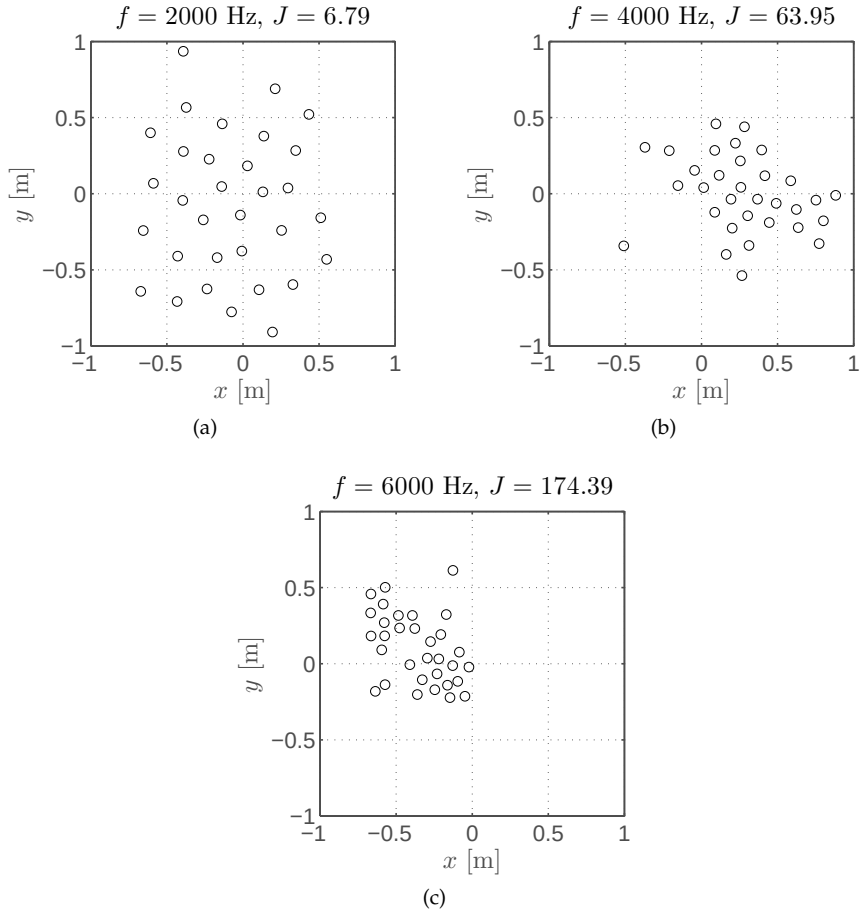

Figure 3.13: Microphone configurations after optimization for frequencies (a) f = 2000 Hz, (b) f = 4000 Hz and (c) f = 6000 Hz.

We can also see the energy J getting larger for higher frequencies. This is due to including part of the main lobe. The main lobe size is selected by the lower bound according to Eq. (3.22). The angle ϕ_{min} will correspond to the main lobe only if the full size of the array, D, is used. Microphone distributions that span only a part of the array, such as seen in Fig. 3.13, will result in larger main lobes. Inclusion of the main lobe will result in a microphone configuration optimized as a compromise between minimum side lobes and small main beamwidth. This is exemplified in

Fig. 3.14 and explains why for $f = 4000$ Hz and $f = 8000$ Hz the configuration is not as compact as it could be. An outlier or two for the microphones or a not-as-compact configuration can somewhat restrict the further increase of the main lobe width.

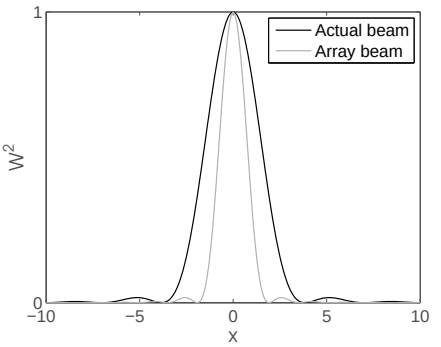

Figure 3.14: Cross-section of Fig. 3.3 through (0,0) of Airy pattern for the maximum array aperture (array beam) and aperture typically encountered during the optimization (actual beam). Actual beams are always larger or equal to the array beam.

Figure 3.15 shows the histograms for the configurations seen in Fig. 3.13 for the closest-neighbour-distances. Also from the histograms it is clear that the mean of distances decreases with increasing frequency.

To illustrate this more explicitly Fig. 3.16 presents the relation between the *mean* of the closest neighbour distance versus the frequency and wavelength. An approximate linear relation between the distance and the wavelength can be seen. A least squares linear fit for the mean values results in

$$d = 1.38\lambda, \tag{3.26}$$

for the relation between the closest-neighbour distance d and the wavelength λ, a practical formula which can help in array design.

In order to assess whether the relation found in Eq. (3.26) can be used to design a microphone configuration, a configuration is by having as many neighbours as possible to have this particular distance.

The configuration was made as a hexagonal pattern by setting three microphones at the vertices of an equilateral triangle and extending this pattern from the origin, ending at the amount of 32. The edges of the equilateral triangle correspond to the closest-neighbour distance. The result can be seen in Fig. 3.17a. The distance was set according to Eq. (3.26) to $d = 0.2346$ m at the optimization frequency of 2000 Hz. This configuration is such that maximally 6 and at minimum 2 neighbours are at this situated distance.

This configuration results in an energy value of $J = 7.56$, which is a low value relative to a random configuration and comparable to the value obtained in the full inversion, see Fig. 3.13a. As a further illustration of the performance of the configuration seen in Fig. 3.17a the corresponding beamform image is shown in

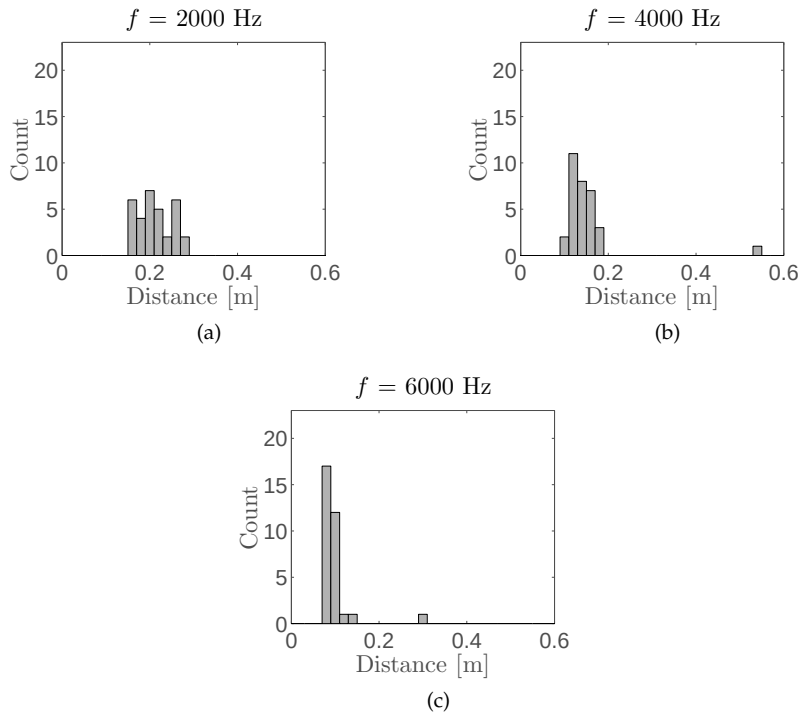

Figure 3.15: Histograms of closest-neighbour-distance of (a) f = 2000 Hz, (b) f = 4000 Hz and (c) f = 6000 Hz.

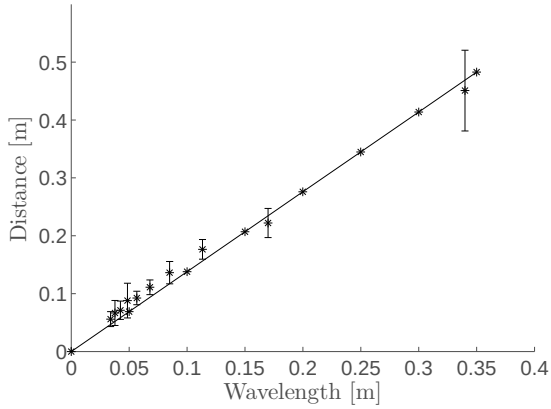

Figure 3.16: Relation between the closest-neighbour-distance versus the wavelength.

Fig. 3.17b. Good performance with low side lobe levels is seen. However, due to the regular pattern of the hexagonal configuration, side lobes are now visible inside

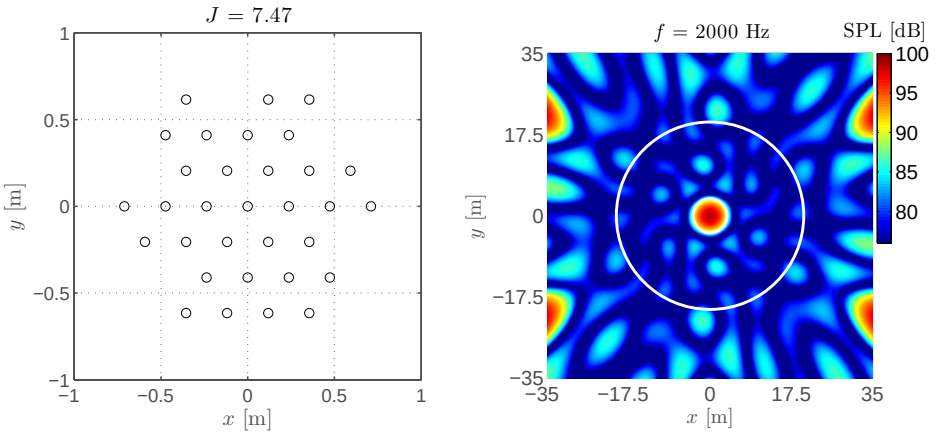

(a) (b)

Figure 3.17: (a) A hexagonal configuration created using the relation in Eq. (3.26) and (b) a corresponding beamform image using the configuration.

the optimization region.

3.4. Array optimization II

3.4.1. Quantifying beamforming performance by MSL and MLW

The parameters used to describe the beamforming performance of an array can be derived from the source map it produces. In Sections 3.3.1 and 3.3.2 an analytical source map produced by a finite-aperture circular array with the diameter D having an infinite number of microphones was derived. This pattern is called the *Point Spread Function* (PSF) or the *Airy Pattern*. It was seen that the source maps consist of a series of lobes. The lobe with the highest peak represents the sound source. This lobe is the main lobe. Since the source is actually a point source, it is desirable to have as narrow as possible main lobe in order to better localize the source and distinguish this source from another source when they are placed closely together, i.e. having a high resolution. The parameter Main Lobe Width (MLW) is defined to measure this quality of the array. The MLW is usually defined as the width of the main lobe at SPL = -3 dB relative to the main lobe's peak [20, 21]. In a three-dimensional plot, the MLW is the maximum distance between a pair of points representing the main lobe's -3 dB contour.

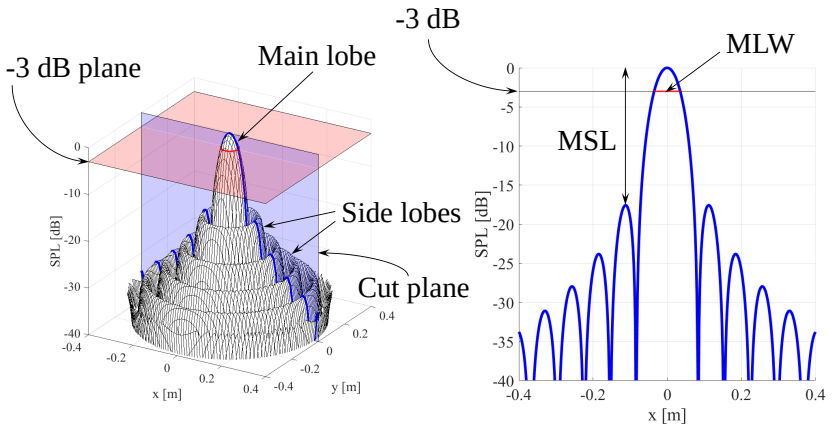

Figure 3.18: Source map resolved by a finite-aperture array with infinite number of microphones and definitions of MSL and MLW

Apart from the main lobe, there is a series of lobes around it which do not represent any sound sources. These are the sidelobes. When the level of the side lobes is high, they are more likely to be misinterpreted as true sound sources. Therefore, it is ideal that their levels are as low as possible. To measure this quality, the Maximum Sidelobe Level (MSL) is defined as the relative SPL of the main lobe's peak and the highest side lobe's peak [20]. The analytical case was seen in Section 3.3.2, where the number of microphones can be assumed as infinite, shows that the minimum attainable MSL to be approximately -17.57 dB from Eq. (3.25).

3.4.2. Reducing design variables for array optimization

As mentioned for the Array Optimization I, the number of microphones on the acoustic array is finite. Because of that, the beamforming performance will deviate from the ideal-case shown in Fig. 3.18, i.e. having higher MLW and MSL. Microphone placement optimization is usually done to obtain low MLW and MSL.

Many studies have shown that lower MSL can be obtained by having the microphones densely distributed close to the array's center. In contrast, when the microphones are more densely placed close to the array's edge, the MLW decreases at the cost of increasing MSL [20, 22]. Therefore, the aim is to search for an array design which gives the best trade-off between these two qualities [21, 23, 24].

It has been found that acoustic arrays with microphones arranged in a multi-arm spiral manner can potentially give the best trade-off between MSL and MLW [22]. More specifically, for an array with 64 microphones, multi-arm spiral arrays with nine arms and seven microphones per arm (plus one microphone in the center) are likely to give the lowest MSL and MLW [23]. Additionally it was seen in the previous section that the distance from each particular microphone to its nearest-neighbor microphone can be linked to the side lobe suppression ability when beamforming is performed at a specific frequency [1].

For Array Optimization II again the random search evolutionary algorithms Differential Evolution (DE) is used. The feature for this algorithm is the evaluation of a set of multiple designs in each iteration. This process can be time-consuming and sometimes does not lead to satisfactory results. One way to facilitate the optimization process is to utilize the known relationship between the array's geometric features and the beamforming performance. For example, instead of parametrizing the location of every single microphone in the optimization, the microphone locations can be collectively defined by some parameters which correlates to MLW and MSL [21, 25]. With a reduced number of acoustic array design variables, the optimization process can provide acoustic array designs with satisfactory performance with a reduced computational effort.

3.4.3. Designing the array optimization method

The concept of the optimization method to be described in this subsection is to use a minimum number of design variables to shorten the optimization time. To achieve that, the formulated optimization problem links geometric parameters of the acoustic array directly to the beamforming performance; such as the microphone distribution density along the array's radial distance. Apart from that, weighing is applied to the side lobes, aiming to minimize the side lobe levels close to the main lobe so that the array is suitable for the HR CLEAN-SC algorithm.

A schematic diagram of the optimization routine is illustrated in Fig. 3.19. There are two optimization loops; the main and the nested loop. The main optimization loop has four design variables which are used to describe the microphone distribution as a function of the array's radial distance, and the distances between every pair of nearest neighbouring microphones in relation to the microphone's radial distance on the array. The nested optimization loop has eleven design variables which are used to generate a set of multi-arm spiral arrays, which

have the geometry as close as possible to that defined by the main loop. The beamforming performance of the generated arrays is then determined by beamforming simulation. It is hypothesized that the arrays generated by the same set of design variables from the main optimization loop will have similar performance, i.e. will cluster in the same area when plotted as shown on the right side of Fig. 3.19. The main optimization loop attempts to find the optimal design variables which gives as low as possible MLW and weighted MSL. The optimized array can be selected from the set of arrays generated by these optimal variables. Further details of both optimization loops are given in the following paragraphs.

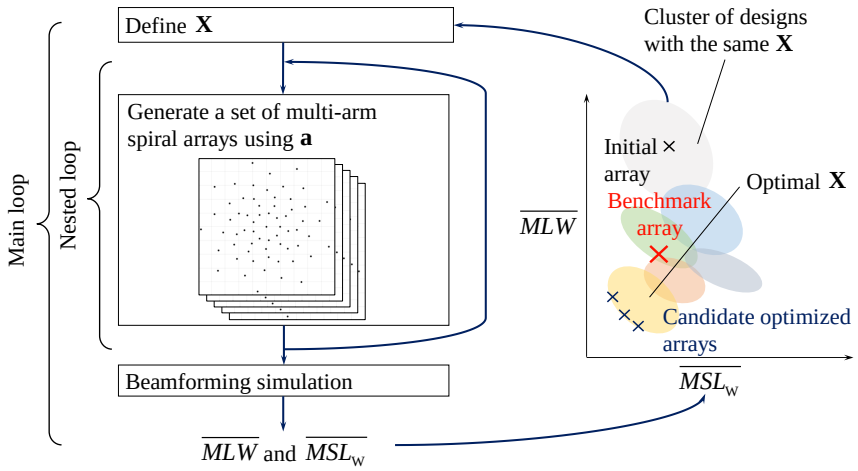

Figure 3.19: Schematic diagram of the optimization method used

The design vector of the main optimization loop (**X**) consists of four design variables which affect the descriptions of the array's geometry as follows:

- X_1 and X_2 describe the microphone distribution density along the array's radial distance
  - X_1 indicates the radial location of the microphone density distribution peak
  - X_2 indicates the standard deviation of the microphone density distribution
- X_3 and X_4 describe the geometry of a curve that represents the relationship between the microphone's radial distance on the array and the distance from that microphone to its nearest neighboring microphone. It is assumed that the further the microphone is from the array's center, the further it is from its nearest neighboring microphone.
  - X_3 indicates the location of the curve's inflection point

– X_4 indicates the smoothness of the curve

This design vector is used in the optimization loop to control the generation of the arrays. Having obtained a set of arrays that satisfy these design variables, the arrays' beamforming performance is evaluated by beamforming simulation.

The beamforming simulation considers a point source emitting white noise at $h = 1.5$ m aligned with the array's center. Although the intended scan plane size in real applications is 1×1 m, the scan plane used in the optimization is a circular area with the diameter of 2 m to account for the uncertainty of the source's location. The design frequencies of the array range from 1 to 10 kHz. The MLW is evaluated only at 1 kHz. The MSL is evaluated at 4 to 10 kHz with a step of 1 kHz. The MSL is also linearly weighted according to its distance from the main lobe; the closer it is to the main lobe, the more weight it gets.

Let $\overline{MLW}$ and $\overline{MSL_{\mathrm{w}}}$ represent the averaged MLW and weighted MSL from all arrays at all relevant frequencies generated by a certain $\mathbf{X}$, the main optimization loop attempts to minimize the objective function:

$$J_{\mathrm{main}} = \frac{\overline{MLW} - MLW_{\mathrm{ref}}}{MLW_{\mathrm{ref}}} + \frac{\overline{MSL_{\mathrm{w}}} - MSL_{\mathrm{w,\,ref}}}{-MSL_{\mathrm{w,\,ref}}}, \tag{3.27}$$

where the subscript 'ref' represents the reference values of MLW and MSL. In each term of the objective function, the value is subtracted from the averaged reference value. With this, the further it is from the reference value, the higher J_{main} becomes. The division by the reference values scales the evaluated differences of MLW and MSL, and allows the summation of these qualities, which have different units.

Although the optimization in the main loop contains only four design variables, the objective function evaluation is computationally expensive since it requires beamforming simulations. Therefore, an optimization algorithm, which has a potential to handle this requirement, should be selected. In this case, the *Generalized Pattern Search* (GPS) [26] or the *Hooke-Jeeves* (HJ) [27] algorithm was used. The detailed explanation of these algorithms can be found in [26–28].

The task of the nested optimization loop is to generate coordinates of acoustic arrays which have the geometry closest to that defined by the design vector of the main optimization loop ($\mathbf{X}$). To confine the number of the design variables used and to limit the optimization to only potential designs, the acoustic arrays are set to be multi-arm spiral arrays with nine arms and seven microphones per arm (plus one microphone in the center). For acoustic arrays with 64 microphones, this been found to achieve the best performance [23].

The design vector ($\mathbf{a}$) for the nested optimization loop has eleven design variables. They are linked to the microphone locations on one spiral arm. Once the location of all microphones on this arm is defined, the remaining microphone coordinates on this array can be obtained by equiangular rotation. The design variables in $\mathbf{a}$ specify the microphone locations on the first spiral arm as follows:

- a_1 specifies the radial distance of the innermost microphone measured from the array's center

- a_2 specifies the angular distance of the outermost microphone measured from the array's center (The radial distance of this microphone is fixed at 0.95 m, corresponding to the array's size.)
- a_3 and a_5 specify the radial distances of two control points for generating a Bezier curve which is the spiral arm's curve
- a_4 and a_6 specify the angular distances of the points specified by a_3 and a_5
- a_7 to a_{11} specify the locations of five remaining microphones on the spiral arm's curve

The geometry of the generated arrays is then evaluated for how much it satisfies the desired geometry given by the main loop. Referring to the design vector $\mathbf{X}$, the array's geometry is specified in two aspects; the distribution density of microphones as a function of the array's radial distance, and the relationship between the microphone's radial distance with the distance to the nearest neighbor microphone.

The first aspect is evaluated as follows: Let the radial distance of the array be divided equally into n_{bin} bins (intervals). Each bin centers at the radial distance r_b and the microphone density distribution specified by X_1 and X_2 will determine the expected number of microphones in each bin. If N_{r_b} is the expected number of microphones in a bin centered at r_b and N'_{r_b} is the actual number of microphones in this bin of the generated array, the mismatch between the desired and actual number is $|N'_{r_b} - N_{r_b}|$.

The second aspect is evaluated for every microphone. Let the n^{th} microphone be located at the radial distance r_n measured from the array's center, the distance from this microphone to its nearest neighboring microphone specified by X_3 and X_4 is supposed to be d_{nn,r_n}. In the generated array, the distance from this microphone to its nearest neighbor is actually d'_{nn,r_n}. With this, the mismatch of the desired and the actual distance is $|d'_{nn,r_n} - d_{nn,r_n}|$.

The objective of the nested optimization loop is to minimize the summation of all aforementioned mismatches. The objective function for the nested optimization loop is defined as

$$J_{\text{nested}} = \frac{1}{n_{\text{bin}}} \sum_{b=1}^{n_{\text{bin}}} \frac{|N'_{r_b} - N_{r_b}|}{N_{r_b}} + \frac{1}{N} \sum_{n=1}^{N} \frac{|d'_{nn,r_n} - d_{nn,r_n}|}{d_{nn,r_n}}. \tag{3.28}$$

The summation in the first and second terms of Eq. (3.28) sums up the mismatches over all radial distance bins and microphones, respectively. The normalization in the summation normalizes the mismatch and allows both terms to be added. The division by n_{bin} and N ensure that the summation in both terms are having equal relative importance.

For the nested optimization loop, there is no known relationship between the design variables and the objective function. Moreover, multiple designs are desirable for a certain X to ensure the design flexibility. Due to these conditions, the

Differential Evolution (DE) algorithm [15, 17] which is a variant of the Genetic Algorithm (GA) is implemented. The detailed explanation of the DE algorithm can be found in Section 3.2.

The structure of the optimization method is summed up in Table 3.1. This was implemented in a MATLAB program. Then optimization runs were executed.

Table 3.1: Summary of the implemented optimization method

	Main optimization loop	Nested optimization loop
Design vector	**X** containing four design variables describing the array's geometric features	**a** containing eleven design variables used for defining microphone locations on a spiral arm in a multi-arm spiral array
Objective function	Equation (3.27) minimizing the MLW and weighted MSL	Equation (3.28) minimizing the mismatches between the array's actual and desired geometric features
Optimization algorithm	HJ/GPS	DE

3.4.4. Results of array optimization II

Figure 3.20 shows the scatter plots of $\overline{MLW}$ and $\overline{MSL_{\mathrm{W}}}$ of all arrays evaluated in the optimization. The markers of the arrays generated by the initial and optimal design vectors (**X**) are highlighted in red and blue, respectively. A marker showing the performance of the Underbrink array [29] is also shown. It can be seen that the performances of the arrays generated by the initial and optimal **X** are separated. A clear reduction of $\overline{MLW}$ can be seen. Almost all arrays generated by the optimal **X** have somewhat lower $\overline{MLW}$ and $\overline{MSL_{\mathrm{W}}}$ than the Underbrink array[2].

A candidate array is selected from the initial and optimal set of array designs for further investigations. These arrays are pointed by the arrows in Fig. 3.20. Let them be called the *initial* and *optimal* arrays. The Underbrink, initial, and the optimal arrays are shown in Fig. 3.21.

The unweighted MSL and MLW of the selected arrays at different beamforming frequencies when a white noise point source is simulated at 1.5 m away from the array are shown in Fig. 3.22. It can be seen that the MSL shows an increasing trend with the beamforming frequency while the MLW reduces with the beamforming frequency. At most beamforming frequencies, the MSL of the optimized array is somewhat lower than the Underbrink array. The low MSL values at the low beamforming frequencies result from the fact that the MLW is large at those frequencies, so most of the side lobes are not yet captured in the beamforming region.

[2]Some averaged weighted MSLs ($\overline{MSL_{\mathrm{W}}}$) are lower than -17.6 dB due to the weights applied.

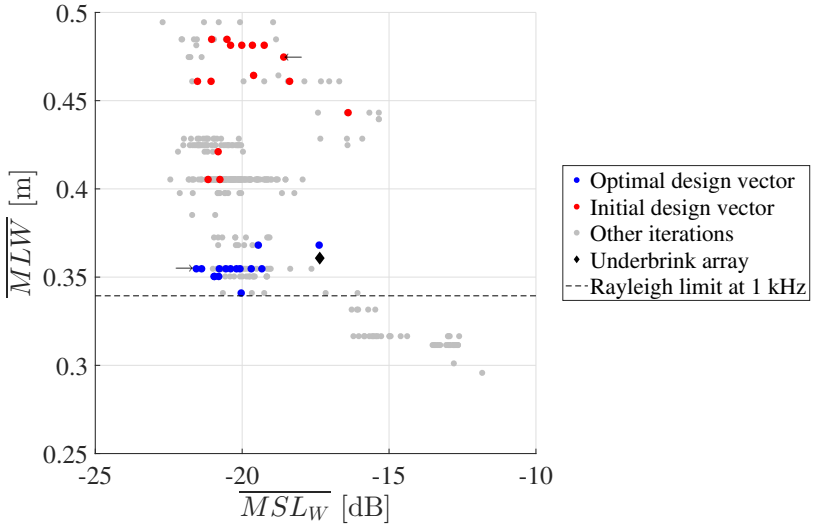

Figure 3.20: $\overline{MLW}$ and $\overline{MSL_W}$ of all array configurations considered in the optimization including the benchmarking Underbrink array, the arrows show the selected initial and optimal arrays

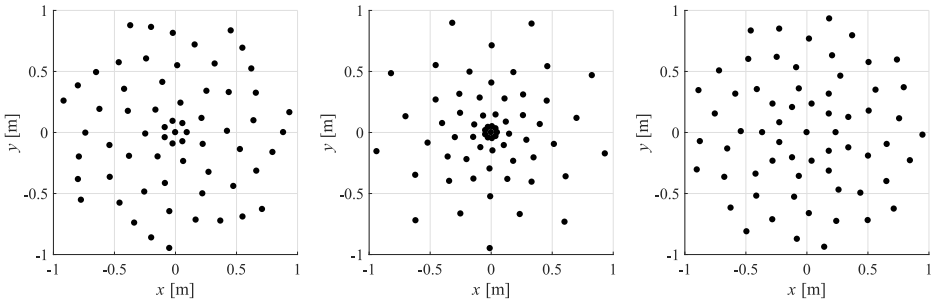

(a) Underbrink array (b) Initial array (c) Optimized array

Figure 3.21: Microphone arrays considered

Interestingly, the MSL of the optimized array is higher than the Underbrink array at the beamforming frequency of 4 kHz. The source maps produced by beamforming of a single white noise source using the three arrays in Fig. 3.21 are shown in Fig. 3.23. It can be seen that, although the MSL of the optimized array is higher than the Underbrink array, the side lobes of the optimized array appear far away from the main lobe. The side lobe levels up to 0.5 m around the main lobe of the optimized array at 4 kHz are lower than -15 dB. These are the results of applying side lobe weighing. It is also notable that the MLW of the optimized array is comparable to the Underbrink array and lower than the initial array.

From this point on, only the optimized array is compared with the Underbrink

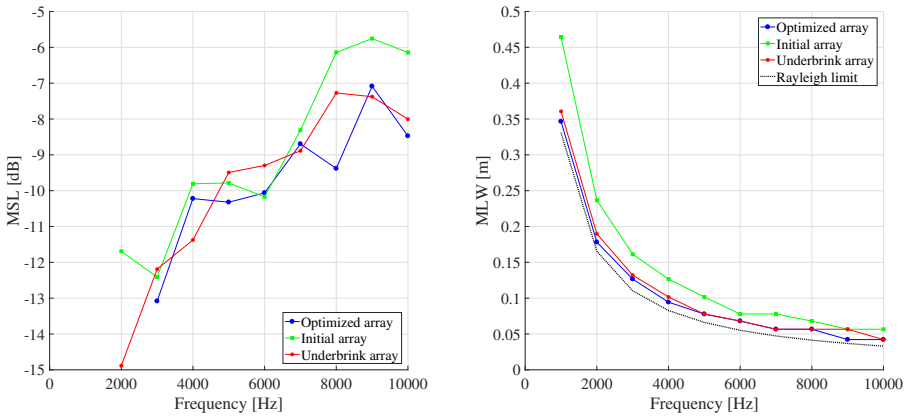

(a) MSL (b) MLW

Figure 3.22: MSL and MLW of the optimized array obtained from simulations compared with those from the initial and the Underbrink arrays

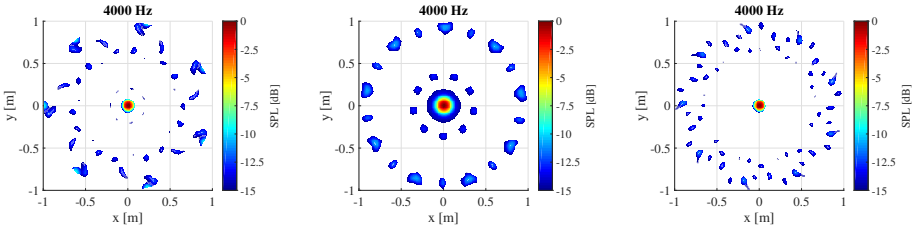

(a) Underbrink array (b) Initial array (c) Optimized array

Figure 3.23: Source maps from beamforming simulation of a single source at 4 kHz

array. The ability of the optimized array to aid the HR CLEAN-SC algorithm in resolving two closely-spaced sources is investigated. Two incoherent point white noise sources are simulated with 10 cm separation at 1.5 m away from the array. With this setting, the Rayleigh criterion in Eq. (3.24) suggests a limit for which the sources should be resolvable above the beamforming frequency of 3.3 kHz.

The resolvability of two closely spaced sound sources as a function of beamforming frequency can be anticipated by investigating a plot of the resolved SPL of the sources compared with the *exact* SPLs as done in [30]. At frequencies lower than the Rayleigh limit, the CLEAN-SC algorithm tends to overestimate the SPL of one source, and underestimate that of the other source with a wrong localization for both sources. Above the Rayleigh limit, the source localization and the their resolved SPLs converge to the correct values. The HR CLEAN-SC algorithm usually resolves two sound sources as one source with a slightly higher SPL up

to a certain beamforming frequency, but below the frequency associated with the Rayleigh limit. After that point, the localization and SPL estimation of both sources get closer to the exact values. The frequency range from that certain frequency up to the Rayleigh limit is the improvement caused by the HR CLEAN-SC algorithm. Therefore, the lower the frequency where the resolved SPLs converge to the exact values, the larger the improvement is.

Plots showing the resolved SPLs of two closely spaced sources using the CLEAN-SC and HR CLEAN-SC algorithms with a constant μ = 0.25 are shown in Fig. 3.24. The results from the Underbrink array and the optimized array are shown separately. The resolved values are compared with the exact values obtained by beamforming each source individually using the CLEAN-SC algorithm.

From both plots, it can be seen that the CLEAN-SC algorithm can resolve the sources only above the Rayleigh limit. The HR CLEAN-SC algorithm resolves the sources from a frequency slightly higher than 2000 Hz for the Underbrink array and slightly lower than 2000 Hz for the optimized array. Therefore, there is a slight improvement caused by the optimized array.

As explained earlier, the source marker constraint (μ) in the HR CLEAN-SC algorithm can be adjusted to improve the resolution. However, this needs to be done carefully to prevent the source marker from staying on the side lobes. It is observed from Fig. 3.24 that the source resolvability is critical at low frequencies. Fortunately, it is also observed that the MSL values are low at low frequencies as shown in Fig. 3.22a. We can make use of this fact by adapting μ with beamforming frequency. It is assumed that the MSL is -17.5 dB at 100 Hz and increases linearly to -5 dB at 10000 Hz. With this assumption, the adaptive μ ($\mu(f)$) can be calculated for each frequency from Equation (2.94).

The curve of μ versus frequency is shown in Fig. 3.25. This is applied to the the same simulated data as in Fig. 3.24. The results are shown in Fig. 3.26. It can be seen that for HR CLEAN-SC, the resolved SPLs converge to a value close to the exact value at a lower frequency than the HR CLEAN-SC beamforming with a constant μ. Again, for the optimized array, this frequency is slightly lower than for the Underbrink array. Thus, the adaptive μ and an array with low MSL can help widen the frequency range where the beamforming resolution is improved by the HR CLEAN-SC algorithm.

Finally, the source maps produced by conventional beamforming, CLEAN-SC, HR CLEAN-SC with μ = 0.25, and HR CLEAN-SC with adaptive μ, using the Underbrink and the optimized arrays at 1 kHz are shown in Figs. 3.27 and 3.28. The intersections of the dashed lines show the exact locations of the simulated sources. It can be seen that for conventional beamforming, CLEAN-SC, and HR CLEAN-SC with constant μ, the results from both arrays are similar, i.e. the sources are not resolved. On the other hand, two sources can most clearly be distinguished when the HR CLEAN-SC with adaptive μ is used with the optimized array.

3.4.5. Experimental validation

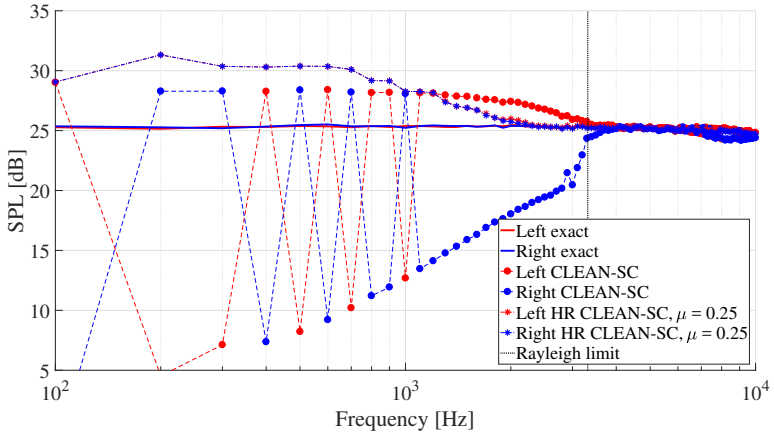

(a) Underbrink array

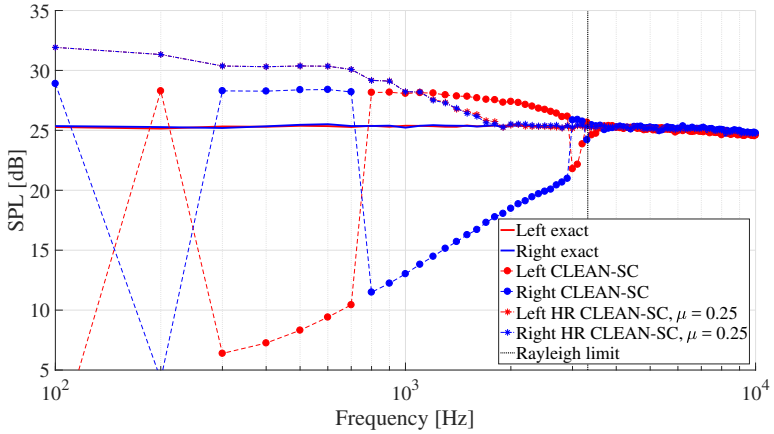

(b) Optimized array

Figure 3.24: Resolved SPL of two closely-spaced sound sources versus beamforming frequency, obtained from CLEAN-SC and HR CLEAN-SC beamforming simulations, compared with the exact SPL values

Experimental set-up

Figure 3.29 shows the experimental set-up in the AV-tunnel. The Underbrink and the optimized array were installed on a 2 × 2 m grid in the V-tunnel. Both arrays contain 64 G.R.A.S. 40PH Free-Field microphones. Since the actual grid contains a finite number of small microphone housing holes arranged in a square-lattice manner, the microphone configurations to be tested were adjusted to the closest housing holes.

Up to five Visaton K50 SQ speakers were used in the experiment. Each speaker emitted 30-second long white noise signals generated by MATLAB. The speakers

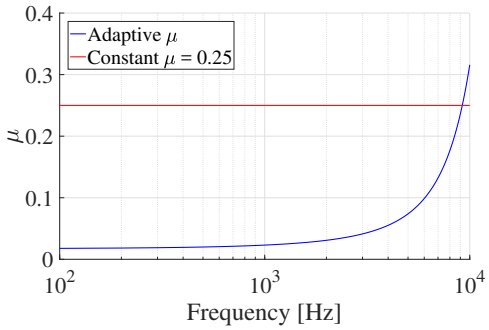

Figure 3.25: Values of adaptive μ used versus beamforming frequency

were independently controlled. The signals played by each speaker were incoherent. To ensure the comparability of the results, the same speaker always played exactly the same signal file. The speakers were placed on a plane at 1.9 m away from the array in two arrangements as shown in Fig. 3.30. The following arrangements were considered:

- Five-speaker arrangement: The speakers were placed adjacent to each other. The distance between the center of the speakers was 6.5 cm. By independently controlling the speakers, different source arrangements can be replicated. In this chapter, the two following schemes are presented:
  - Single-source scheme: This was done by playing the signal using only the middle speaker.
  - Line source scheme: This was done by playing the signals using all the speakers. This scheme can replicate the line source, which is the frequently-encountered source configuration in aeroacoustics research, i.e. trailing-edge noise.
- Two-speaker arrangement: Two speakers were placed with varying separation from each other. The separation was varied from 6.5 cm (the minimum separation), to 10 cm, 20 cm, 30 cm, and 50 cm. With this, the ability of the array in separating two closely-spaced sources can be investigated. Additional recordings, where each speaker played the signal individually, were carried out to determine the exact SPL emitted by each speaker. To keep this section concise, only the results with 10 cm separation are shown.

The sampling frequency of the array's data acquisition system was 50 kHz. The length of the recorded signal per session is 30 seconds. The signal was then divided into 0.01 second chunks with a 50 % overlap. Then the Fourier transform was applied and the CSMs were constructed and averaged from all signal chunks. With this, the frequency resolution is 100 Hz.

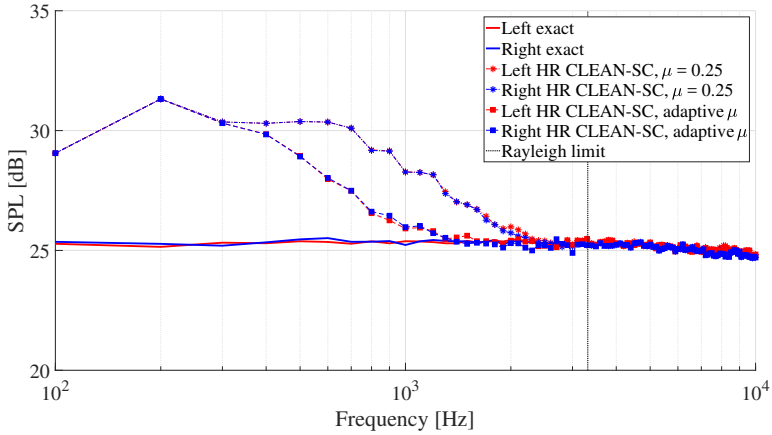

(a) Underbrink array

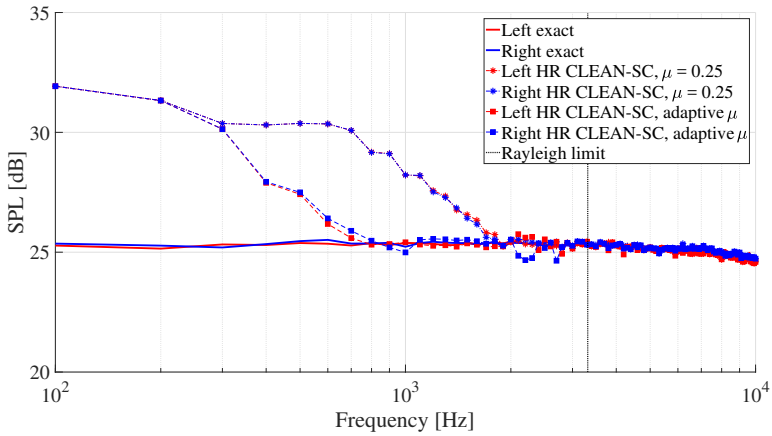

(b) Optimized array

Figure 3.26: Resolved SPL of two closely-spaced sound sources versus beamforming frequency, obtained from HR CLEAN-SC beamforming simulations with a constant and adaptive μ, compared with the exact SPL values

Experimental results: five-speaker arrangement

The source maps obtained from the single-source scheme (i.e. other four are not activated) at 4 kHz using the Underbrink array and the optimized array are shown in Fig. 3.31. The corresponding source maps obtained from simulated data are also shown. The noise source and the microphone locations are simulated at exactly the same locations as in the experiment. By comparing the source maps from the experiment and the simulation, it can be seen that the MLW and the side lobe locations are well predicted by the simulation. However, the side lobe levels from the experiment appear to be slightly higher than those in the simulation. This could be

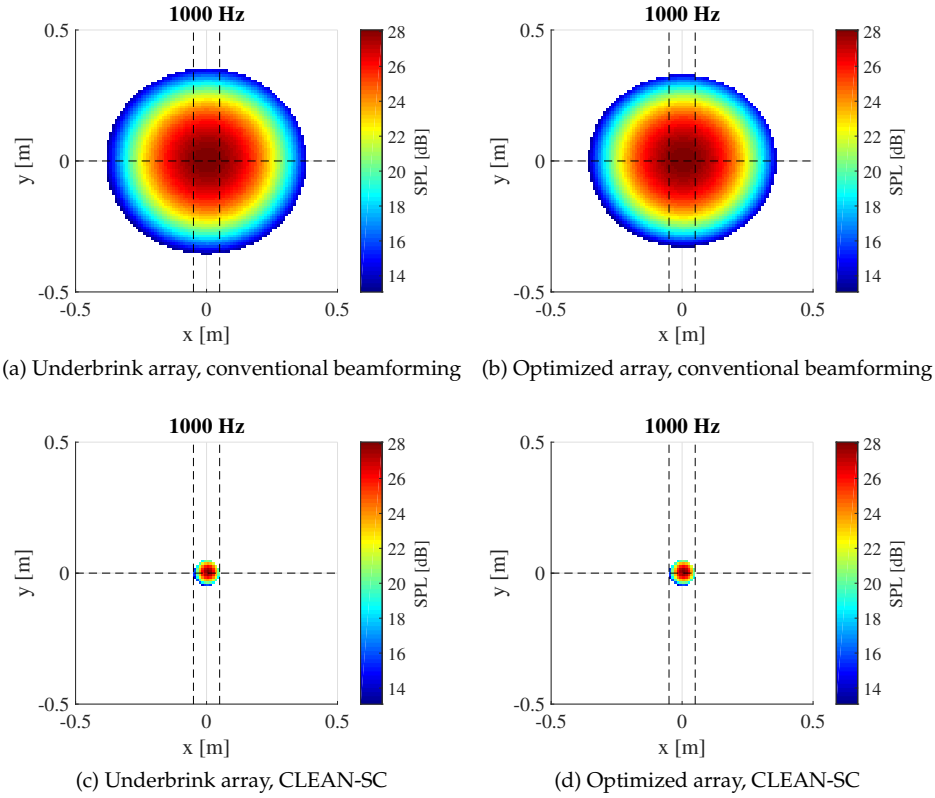

(a) Underbrink array, conventional beamforming (b) Optimized array, conventional beamforming

(c) Underbrink array, CLEAN-SC (d) Optimized array, CLEAN-SC

Figure 3.27: Source maps of two closely-spaced sources for various beamforming algorithms (CB and CLEAN-SC) at 1 kHz, using synthetic data

due to the speaker's characteristics, i.e. not fully omnidirectional, and the fact that there is an offset between the anechoic chamber's ability to replicate the free-field condition and the ideal free-field condition.

The same finding is also reflected in Fig. 3.32 where the MSL and MLW from these source maps for frequencies ranging from 1 to 10 kHz are shown. Although the MSL of the optimized array is predicted to be lower than the Underbrink array by the simulation, the MSL of both arrays are comparable for almost all frequencies in the measurements.

The line source scheme is obtained when all five speakers play the signals. Source maps obtained from beamforming at 4 kHz using the Underbrink and the optimized arrays are shown in Fig. 3.33. It can be seen that, as a result of weighing the side lobes, the optimized array can provide an area with lower side lobe levels around the line source compared to the Underbrink array. The size of the region representing the sound sources, equivalent to the MLW, of both arrays are comparable. From this observation, it can be deduced that the features of the source

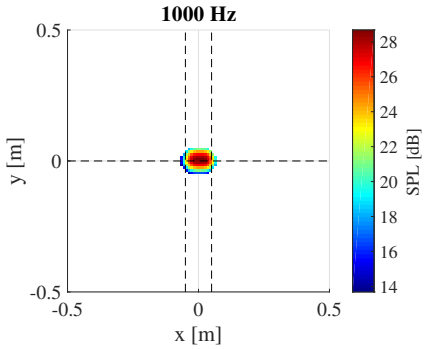

(a) Underbrink array, HR CLEAN-SC, $\mu = 0.25$

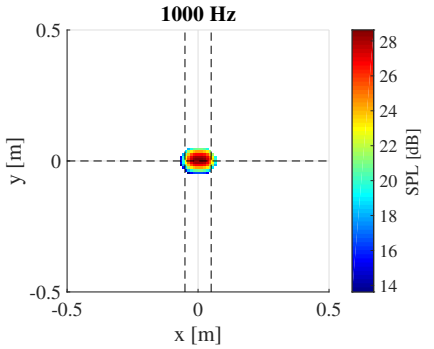

(b) Optimized array, HR CLEAN-SC, $\mu = 0.25$

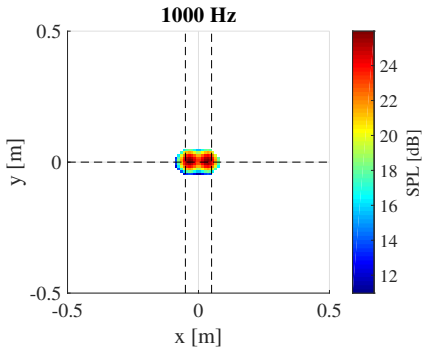

(c) Underbrink array, HR CLEAN-SC, adaptive μ

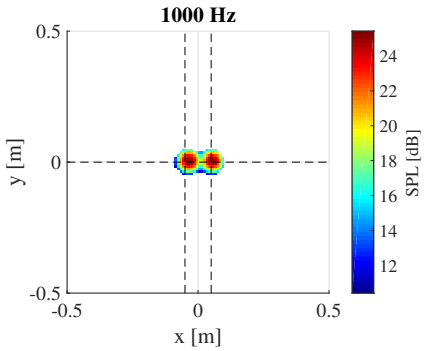

(d) Optimized array, HR CLEAN-SC, adaptive μ

Figure 3.28: Source maps of two closely-spaced sources for HR CLEAN-SC algorithm at 1 kHz, using synthetic data

maps in the case of multiple sources produced by a certain array configuration will still follow the same trend as is observed in the single-source case of that particular array.

Experimental results: two-speaker arrangement

Two speakers emitting incoherent white noise were placed with a separation of 10 cm at 1.9 m away from the optimized and the Underbrink array. With this setting, the Rayleigh limit in Eq. (3.24) suggests that the sources are resolvable at the frequencies above 4.2 kHz. The resolved sources' SPLs versus beamforming frequency using these two arrays and two beamforming algorithms (the CLEAN-SC and HR CLEAN-SC with $\mu = 0.25$) are shown in Fig. 3.34. The exact values are obtained from CLEAN-SC beamforming when only one source is playing the signal. The dashed line indicates the Rayleigh limit.

The behavior as observed in Fig. 3.24 can still be seen. Obviously, the CLEAN-SC algorithm can resolve both sources correctly at frequencies above the Rayleigh limit. However, the HR CLEAN-SC algorithm makes it possible for both sources to

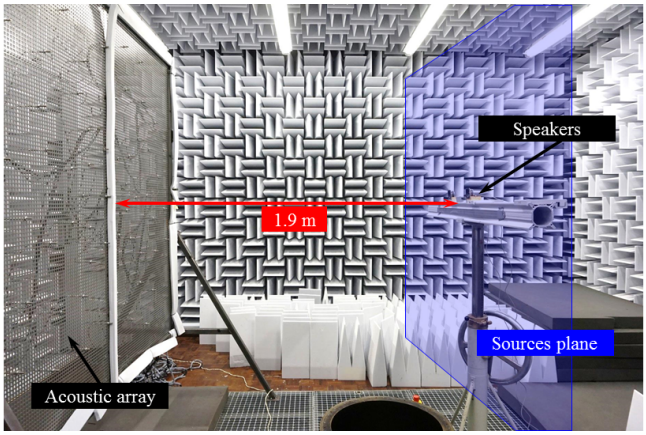

Figure 3.29: Experimental set-up in TU Delft V-tunnel

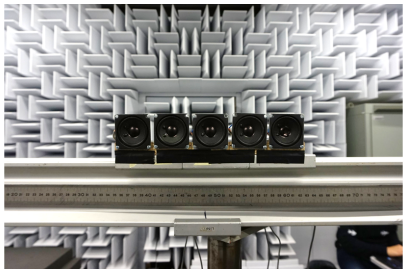

(a) Five-speaker arrangement

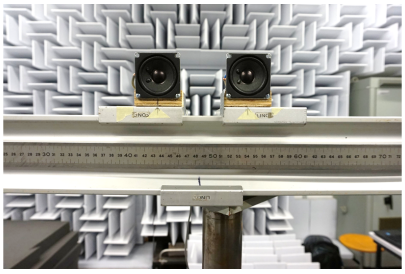

(b) Two-speaker arrangement

Figure 3.30: Speaker arrangements used in the experiment

be resolved also at frequencies below the Rayleigh limit. The sources are resolved by both arrays from around 2000 Hz.

Further investigation is done by applying the adaptive μ (same as in Fig. 3.25) to this experimental data. The resolved source's SPLs by the HR CLEAN-SC algorithm with $\mu = 0.25$, adaptive μ, and the exact SPL values are shown in Fig. 3.35 for the Underbrink and the optimized array. Again, for both arrays, the adaptive μ makes the HR CLEAN-SC algorithm resolve the sources at a lower frequency than the constant μ case. The optimized array resolves the sources from around 600 Hz while the Underbrink array resolves the sources from around 1000 Hz.

Finally, the source maps produced by both arrays using the conventional beamforming, the CLEAN-SC algorithm, the HR CLEAN-SC algorithm with $\mu = 0.25$, and the HR CLEAN-SC algorithm with adaptive μ at 800 Hz are shown in Figs. 3.36 and 3.37. The intersections of the dashed lines indicate the centers of the speakers. As expected, this frequency is lower than the Rayleigh limit, the conventional beamforming fails to resolve the sources while the CLEAN-SC and HR CLEAN-SC algorithms resolve both sources with overestimated SPLs. Only the HR-CLEAN-

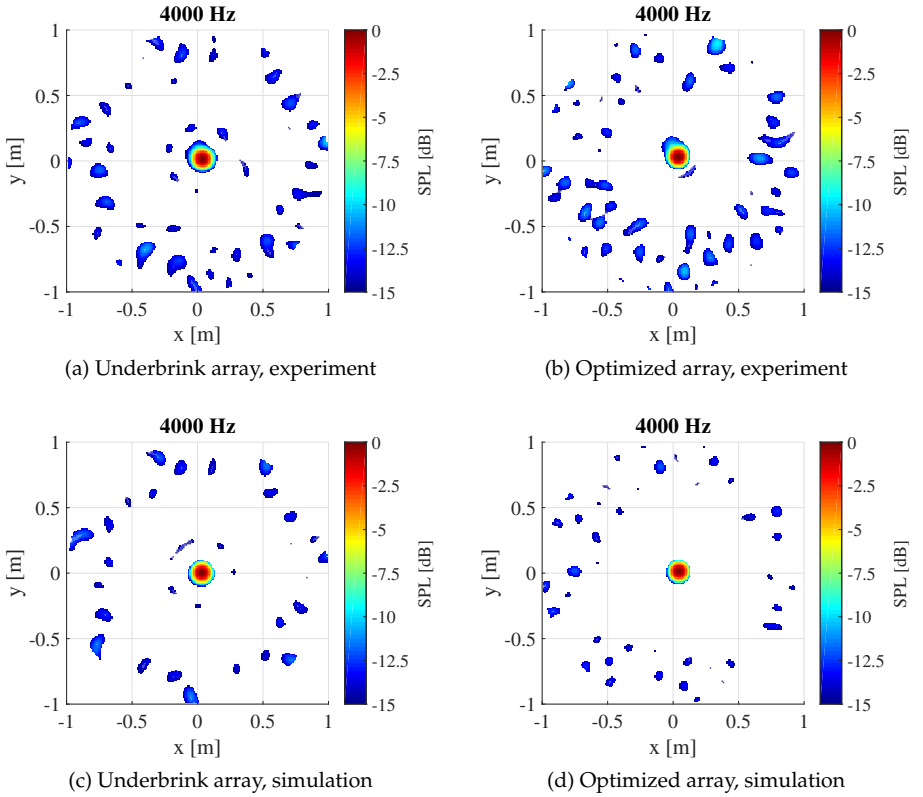

(a) Underbrink array, experiment

(b) Optimized array, experiment

(c) Underbrink array, simulation

(d) Optimized array, simulation

Figure 3.31: Source maps from beamforming of the five-speaker arrangement (single-source scheme) at 4 kHz compared with those from corresponding beamforming simulations

SC algorithm using the optimized array with adaptive μ can clearly resolve the two sound sources. Source localization offsets can be seen. This could be due to the fact that the source is not a perfect point source and the maximum SPL at 800 Hz might be dominantly emitted by a certain part of the speakers.

3.5. Conclusions

This chapter presented two methods for optimizing the microphone configurations. The objective function is selected such that it provides a measure for the presence of side- and grating lobes. Minimization of this objective function provides microphone locations, such that no side- and grating lobes are present in a scan region of interest.

3.5.1. Array optimization I

For Array Optimization I a region used which corresponds to the full azimuth and elevation angles ϕ_{min} and ϕ_{max}. The angle ϕ_{min} corresponds to the width of the

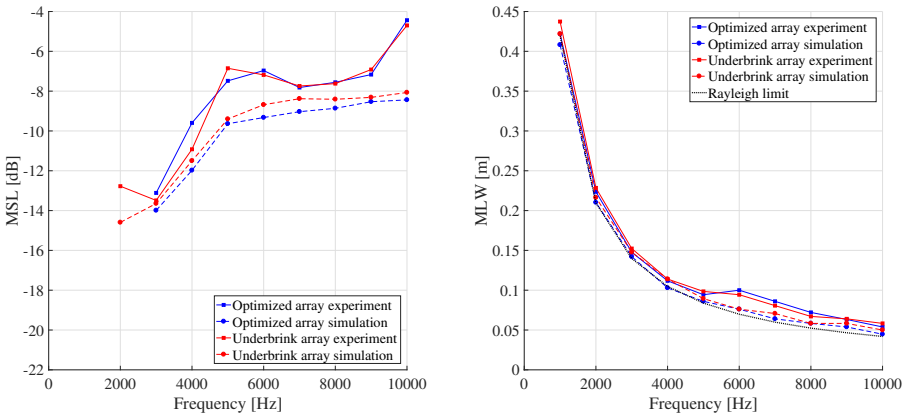

(a) MSL (b) MLW

Figure 3.32: MSL and MLW of the Underbrink and the optimized arrays from the experimental results compared with those obtained from simulations

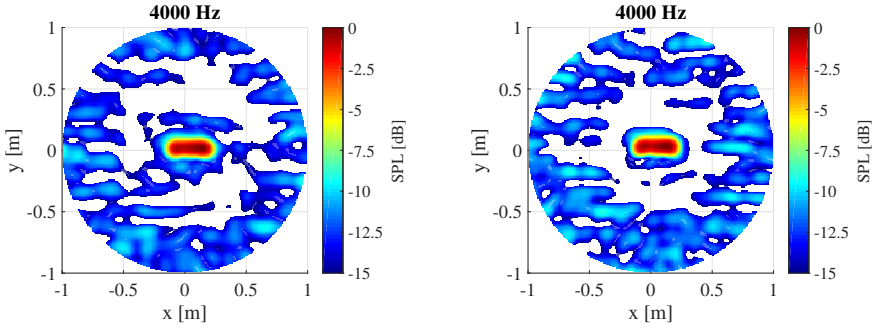

(a) Underbrink array (b) Optimized array

Figure 3.33: Source maps from beamforming of the five-speaker arrangement (line source scheme) at 4 kHz

main lobe, whereas ϕ_{max} corresponds to the maximum elevation angle of interest. For this research, a value of 30 degrees was selected. Low values of the objective function indicate hardly any grating and side lobes present in the region of interest.

For finding the minimum of the objective function use is made of the differential evolution (DE) optimization method. An optimal setting for DE was selected to maximize the probabilities of locating the optimal solution at a minimum number of forward calculations. Optimized array configurations were found using DE which confirmed the desired performance, i.e. low side lobes inside the region of interest.

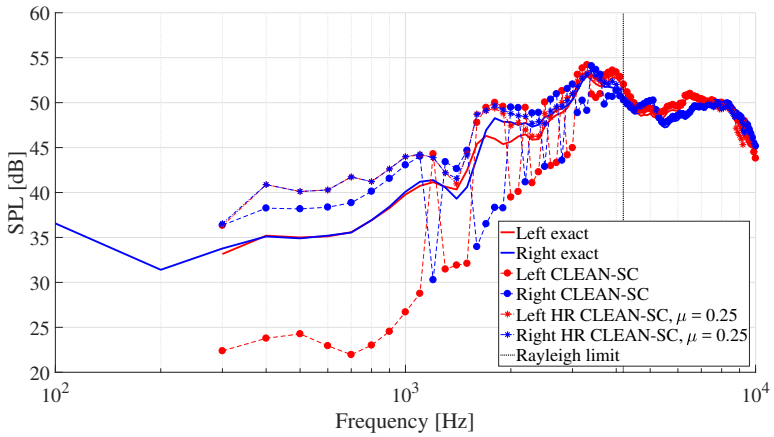

(a) Underbrink array

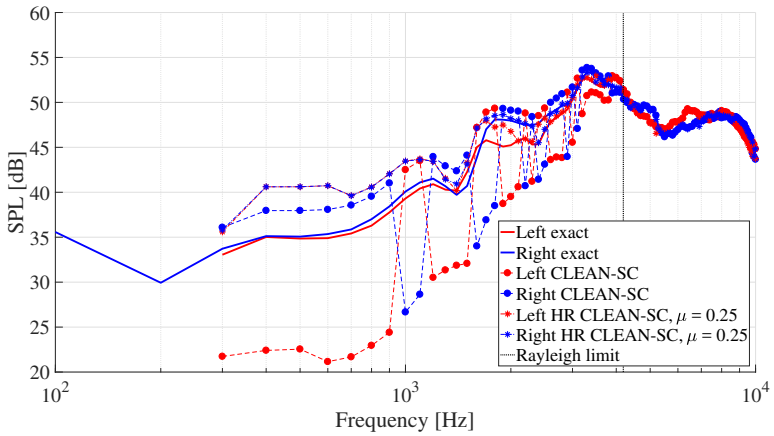

(b) Optimized array

Figure 3.34: Resolved SPLs of two sound sources with 10 cm separation versus beamforming frequencies, obtained from CLEAN-SC and HR CLEAN-SC beamforming of experimental data, compared with the exact SPL values

It is found that the optimized array configuration shows a regular behaviour with the microphones distributed at almost constant distances. From inversions for different frequencies it is found that these distances decrease with frequency and show almost linear behaviour with wavelength. Arrays with microphones positioned based on this linear behaviour show improved performance compared to a random array. Still, the regular pattern gives rise to side lobes that are not present for the microphone configuration obtained through the DE optimization. This indicates the need for small variations of the microphone distances around the distance prescribed by the linear fit.

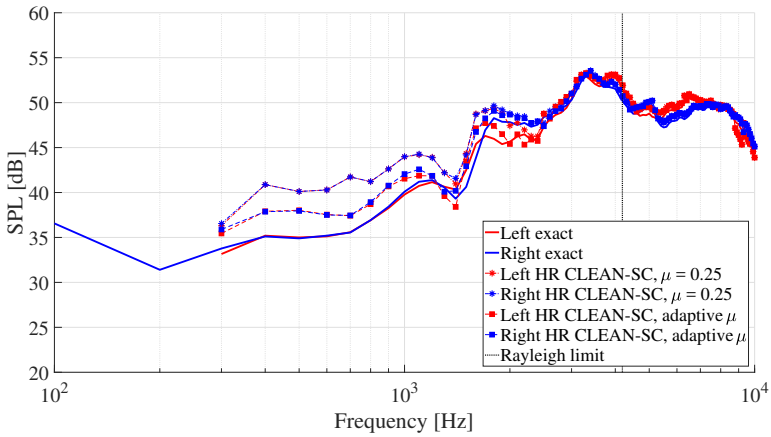

(a) Underbrink array

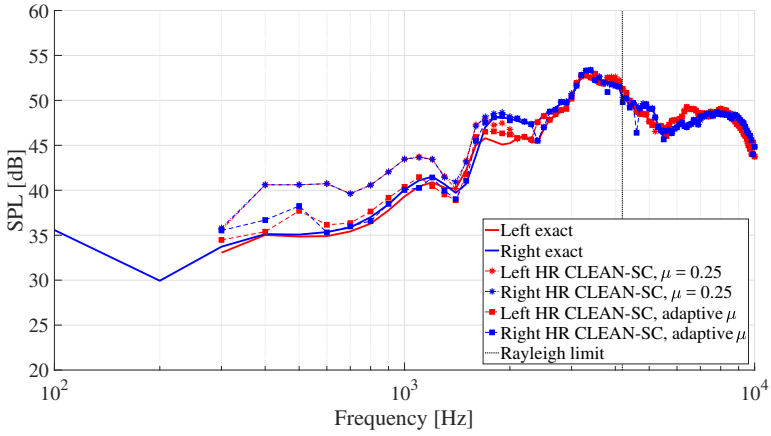

(b) Optimized array

Figure 3.35: Resolved SPL of two sound sources with 10 cm separation versus beamforming frequency, obtained from HR CLEAN-SC beamforming of experimental data with a constant and adaptive μ, compared with the exact SPL values

3.5.2. Array optimization II

With Array Optimization II a different procedure was followed. The microphone configuration has been optimized for an acoustic array in an open-jet anechoic wind tunnel. The effects of the optimized design on the performance of the High-Resolution (HR) CLEAN-SC beamforming algorithm have also been investigated.

The proposed optimization method focuses on using a minimal number of design variables. The optimization aims to reduce both the Main Lobe Width (MLW) and Maximum Side lobe Level (MSL). The weights are applied to the side lobes according to their distances from the main lobe. This resulted in a region with

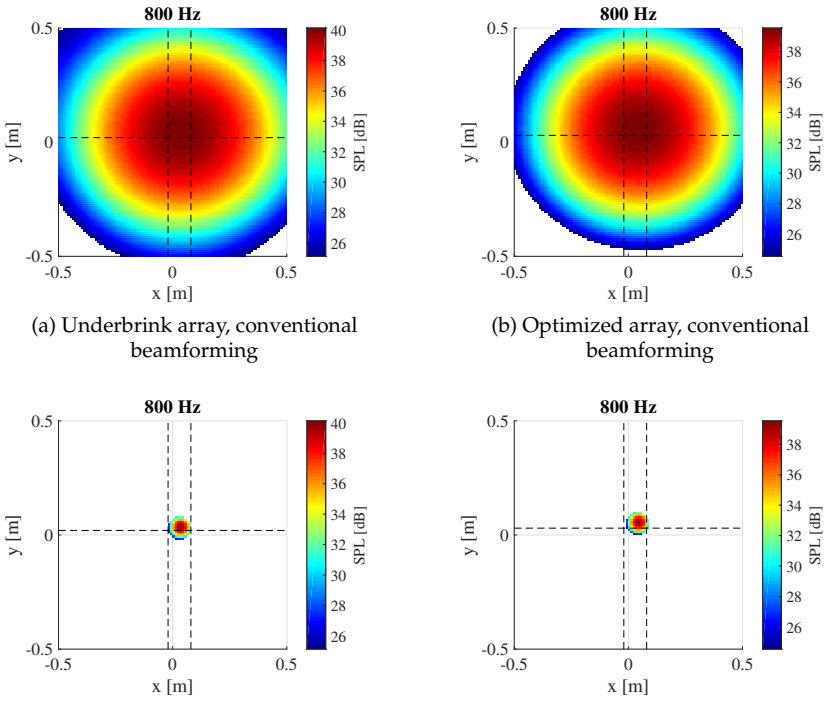

(a) Underbrink array, conventional beamforming

(b) Optimized array, conventional beamforming

(c) Underbrink array, CLEAN-SC

(d) Optimized array, CLEAN-SC

Figure 3.36: Source maps of two closely-spaced sources for various beamforming (CB and CLEAN-SC) algorithms at 800 Hz, using experimental data

side lobe levels lower than -15 dB around the main lobe. Low MLW has also been maintained.

The fact that the array design gives low side lobe levels can be further exploited by the HR CLEAN-SC algorithm. It was found that, when the optimized array is used to resolve two closely-spaced sound sources using the HR CLEAN-SC algorithm with an adaptive source marker constraint (μ), the two sources can be resolved in the broadest range of frequency below the Rayleigh criterion.

Two recommendations can be given based this study. First, only attempting to minimize the MSL may not be sufficient for designing an acoustic array since the location of the side lobes also matters. In this study, the side lobes are associated with their distances from the main lobe through weighing. The produced source maps both from conventional beamforming and the advanced beamforming algorithms show satisfactory results. Second, to best exploit the ability of the HR CLEAN-SC algorithm, the source marker constraint (μ) should be adjusted according to the MSL at the frequency of interest. This should be done especially at the frequencies below the Rayleigh limit where the source resolvability is low, but the side lobe levels are generally low as well.

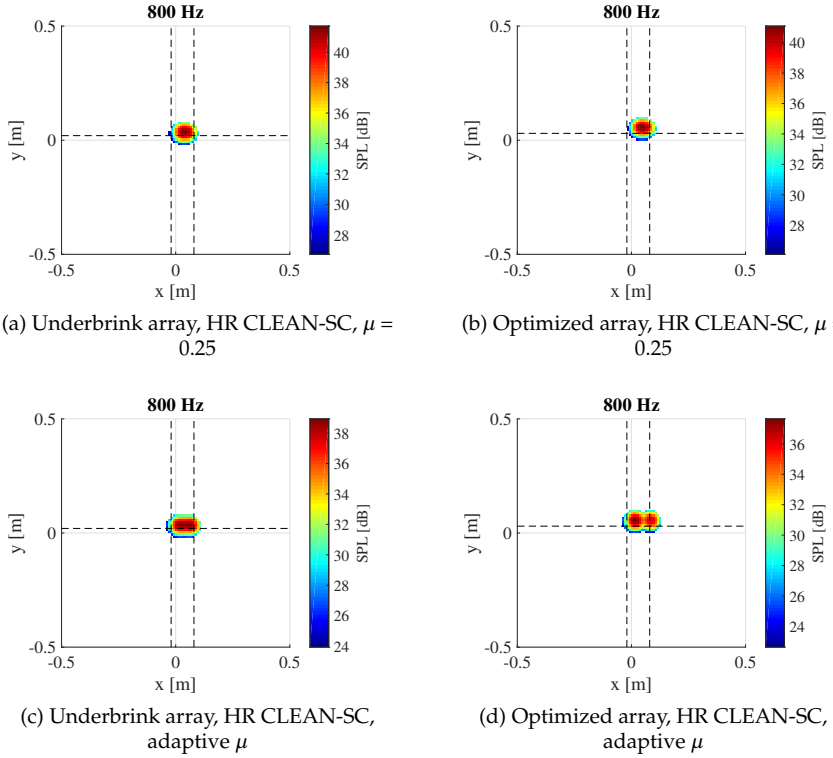

(a) Underbrink array, HR CLEAN-SC, μ = 0.25

(b) Optimized array, HR CLEAN-SC, μ = 0.25

(c) Underbrink array, HR CLEAN-SC, adaptive μ

(d) Optimized array, HR CLEAN-SC, adaptive μ

Figure 3.37: Source maps of two closely-spaced sources for HR CLEAN-SC algorithm at 800 Hz, using experimental data

References

[1] A. M. N. Malgoezar, M. Snellen, P. Sijtsma, and D. G. Simons, *Improving beamforming by optimization of acoustic array microphone positions*, in *6th Berlin beamforming conference, BeBeC-2016-S5* (2016).

[2] S. Luesutthiviboon, A. M. N. Malgoezar, M. Snellen, and D. G. Simons, *Maximizing source discrimination performance by using an optimized array and adaptive high-resolution clean-sc beamforming*, in *Berlin Beamforming Conference 2018* (2018).

[3] X. Huang, L. Bai, I. Vinogradov, and E. Peers, *Adaptive beamforming for array signal processing in aeroacoustic measurements*, The Journal of the Acoustical Society of America **131**, 2152 (2012).

[4] R. P. Dougherty, *Functional Beamforming*, in *Berlin Beamforming Conference 2014-1* (2014).

[5] R. P. Dougherty, *Functional Beamforming for Aeroacoustic Source Distributions*, AIAA paper **3066** (2014).

[6] R. Merino-Martinez, M. Snellen, and D. G. Simons, *Functional Beamforming Applied to Imaging of Fly-Over Noise on Landing Aircraft*, Journal of Aircraft (2016).

[7] P. Sijtsma, *CLEAN based on spatial source coherence*, International journal of aeroacoustics **6**, 357 (2007).

[8] R. P. Dougherty, *Extensions of DAMAS and Benefits and Limitations of Deconvolution in Beamforming*, AIAA paper **2961** (2005).

[9] T. F. Brooks and W. M. Humphreys, *A deconvolution approach for the mapping of acoustic sources (DAMAS) determined from phased microphone arrays*, Journal of Sound and Vibration **294**, 856 (2006).

[10] T. F. Brooks and W. M. Humphreys, *Extension of DAMAS phased array processing for spatial coherence determination (DAMAS-C)*, AIAA paper **2654** (2006).

[11] R. P. Dougherty, *Spiral-shaped array for broadband imaging*, (1998), US Patent 5,838,284.

[12] J. R. Underbrink, *Aeroacoustic phased array testing in low speed wind tunnels*, in *Aeroacoustic measurements* (Springer, 2002) pp. 98–217.

[13] E. J. G. Arcondoulis, C. J. Doolan, A. C. Zander, and L. A. Brooks, *Design and calibration of a small aeroacoustic beamformer*, in *International Congress on Acoustics (ICA)(20th: 2010: Sydney, New South Wales)* (2010).

[14] D. G. Simons and M. Snellen, *Multi-frequency matched-field inversion of benchmark data using a genetic algorithm*, Journal of Computational Acoustics **6**, 135 (1998).

[15] M. Snellen and D. G. Simons, *An Assessment of the Performance of Global Optimization Methods for GEO-Acoustic Inversion*, Journal of Computational Acoustics **16**, 199 (2008).

[16] R. Storn, *On the usage of differential evolution for function optimization*, in *Fuzzy Information Processing Society, 1996. NAFIPS., Biennial Conference of the North American* (IEEE, 1996) pp. 519–523.

[17] R. Storn and K. Price, *Differential evolution–a simple and efficient heuristic for global optimization over continuous spaces*, Journal of global optimization **11**, 341 (1997).

[18] P. Sijtsma, *Experimental techniques for identification and characterisation of noise sources*, Tech. Rep. (National Aerospace Laboratory NLR, 2004).

[19] E. Hecht, *Optics*, Pearson education (Addison-Wesley, 2002).

[20] F. Le Courtois, J.-H. Thomas, F. Poisson, and J.-C. Pascal, *Genetic optimisation of a plane array geometry for beamforming. application to source localisation in a high speed train*, Journal of Sound and Vibration **371**, 78 (2016).

[21] E. Sarradj, *A generic approach to synthesize optimal array microphone arrangements*, in 6^{th} *Berlin Beamforming Conference, February 29 – March 1 2016, Berlin, Germany* (GFaI, e.V., Berlin, 2016) BeBeC–2016–S4.

[22] Z. Prime and C. Doolan, *A comparison of popular beamforming arrays*, Australian Acoustical Society AAS2013 Victor Harbor **1**, 5 (2013).

[23] Z. Prime, C. Doolan, and B. Zajamsek, *Beamforming array optimisation and phase averaged sound source mapping on a model wind turbine*, in *Inter-Noise and Noise-Con Congress and Conference Proceedings*, Vol. 249 (Institute of Noise Control Engineering, 2014) pp. 1078–1086.

[24] N. Jin and Y. Rahmat-Samii, *Advances in particle swarm optimization for antenna designs: Real-number, binary, single-objective and multiobjective implementations*, IEEE Transactions on Antennas and Propagation **55**, 556 (2007).

[25] J. Yu and K. D. Donohue, *Geometry descriptors of irregular microphone arrays related to beamforming performance*, EURASIP Journal on Advances in Signal Processing **2012**, 249 (2012).

[26] V. Torczon, *On the convergence of pattern search algorithms*, SIAM Journal on optimization **7**, 1 (1997).

[27] R. Hooke and T. A. Jeeves, *"direct search"solution of numerical and statistical problems*, Journal of the ACM (JACM) **8**, 212 (1961).

[28] R. M. Lewis and V. Torczon, *Pattern search algorithms for bound constrained minimization*, SIAM Journal on Optimization **9**, 1082 (1999).

[29] J. R. Underbrink, *Circularly symmetric, zero redundancy, planar array having broad frequency range applications*, (2001), uS Patent 6,205,224.

[30] P. Sijtsma, R. Merino-Martinez, A. M. N. Malgoezar, and M. Snellen, *High–Resolution CLEAN–SC: Theory and Experimental Validation*, in 23^{rd} *AIAA/CEAS Aeroacoustics Conference. June 5 – 9 2017. Denver, Colorado, USA* (2017) AIAA paper 2017–3841.

4

Acoustic source localization using global optimization methods

As seen in the previous chapters, conventional beamforming with a microphone array is a well-established method for localizing and quantifying sound sources. Estimates are provided for the source strengths on a predefined grid by determining the agreement between the pressures measured and those modeled for a source located at the grid point under consideration. As such, conventional beamforming can be seen as an exhaustive search for those locations that provide a maximum match between measured and modeled pressures. In this chapter instead of this exhaustive search, a different approach is taken with the use of an efficient global optimization method to search for both the source locations as well as strengths. In order to obtain such a result the agreement between model and measurement is maximized using a so-called cost function. The advantages of considering it as a global optimization problem are two-fold. First, the efficient optimization allows for the inclusion of more unknowns, such as environmental parameters like the speed of sound. Secondly, the model for the received pressure field can be readily adapted to reflect, for example, the presence of more sound sources or environmental parameters that affect the received signals. For the work considered, the global optimization method Differential Evolution is used. Results with simulated and experimental data show that sources can be accurately identified, including the distance from the source to the array.

Parts of this chapter have been published in the The Journal of the Acoustical Society of America **141**, 1 (2017) [1].

4.1. Introduction

When it is assumed that sound sources behave like acoustic monopoles, often a least-squares approach is used for obtaining an estimate for the source strength at a potential source location [2]. Since both source strength and source location are unknown, the general approach is to define a grid of potential source locations and estimate the sound pressure level for each grid point. By depicting these estimates in a so-called source map, an image is established where high levels indicate the presence of a sound source. This approach can be considered as an exhaustive search, estimating the source strength for all grid points and identifying those with high values as source locations.

The above described approach is subject to a number of drawbacks. First, it restricts the optimization problem to a limited number of unknowns due to computational constraints induced by the approach of an exhaustive search. Typically, beamforming is applied in searches for the source in two dimensions, often assuming a scan plane parallel to the array at a known distance. Secondly, the assumption of a single monopole limits the suitability of beamforming for situations with multiple sound sources. In chapter, we propose to consider the search for source locations and source pressure amplitudes as a global optimization problem. In this way, the procedure of estimating the source strength for each grid point is abandoned and focus is only put on identifying the actual source locations and source strengths.

The presence of sidelobes, indicating relatively high beamforming output levels without a source being present, will, however, hamper the optimization as they act as local optima against which the global optimum needs to be found. In literature, a number of mathematical methods are presented that allow for optimization problems with many unknowns and with the ability to escape local optima. These methods are generally denoted as global optimization methods. Well-known examples of these type of methods are genetic algorithms [3–5], simulated annealing [6, 7] and ant colony optimization [8, 9]. In contrast to local search methods, e.g. gradient methods, these global optimization methods have the capability to escape local optima. This ability is essential for the application considered here with sidelobes present. In this chapter, we use the method explained in Chapter 2 of Differential Evolution (DE) [10, 11] for obtaining the source positions and source strengths. This method is a variant of the genetic algorithm. This type of global optimization methods mimics the natural evolution of species. They use populations of solutions, where promising solutions are given a higher probability to reproduce than bad solutions.

The approach taken in this work is in line with that of, for example, the "Deconvolution Approach for the Mapping of Acoustic Sources" (DAMAS) [12, 13] technique and the approach of Cross-Spectral Matrix (CSM) inversion [14, 15], where the aim is to obtain maximum information about the acoustic sources by maximizing the agreement between the measured and modeled microphone pressure field. In DAMAS, the delay-and-sum beamformer result is used as a starting point. The idea is that the delay-and-sum beamforming output can be considered as the summation of point-spread functions (PSF) of all sources present, weighted by the

source strengths, where the PSF is defined as the beamformer response to a point source with unit strength at a given position of a grid. The deconvolution is based on solving the resulting inverse problem for retrieving the source distribution that resulted in the observed delay-and-sum beamformer output. In general, unless the scan grid is very small, the problem is ill-conditioned, preventing a direct inversion of the matrix, and an iterative scheme is used to solve the inverse model. In general, a significant number of iterations can be required. Depending on the chosen grid size, this can become time consuming. In Refs. [14] and [15] alternative approaches were developed to solve the inverse problem. Two of these are known as sparsity constrained DAMAS (SC-DAMAS) and a sparsity preserving Covariance Matrix Fitting (CMF) approach. In both techniques, sparsity is maximized by searching for the minimum amount of sources for which the deconvolution holds. The assumption is that the amount of sources is considerably smaller than the amount of scan points. The SC-DAMAS method employs the output of the delay-and-sum beamformer with which agreement has to be maximized, whereas the CMF approach directly optimizes the agreement with the measured covariance matrix. The latter has the advantage to skip the delay-and-sum beamforming and directly estimate the source locations and strengths from the covariance matrix.

The work presented in this chapter is also based on a direct comparison between modeled and measured pressure fields, similarly to the CMF approach. However, instead of considering a predefined grid of potential source locations, here the locations of the sources are sought for by using a global optimization method. In this way, estimates for source positions and source strengths are obtained as a solution of the optimization and do not need to be obtained from the delay-and-sum beamformer result. The efficiency of the global optimization compared to an exhaustive search, allows for an increased number of unknowns, without having a significant increase in computational time. In this chapter, for example, localization of the source in 3D is investigated, but also its potential in estimating the sound speed, i.e., a property of the propagation medium. Including environmental parameters can be of interest also for complex wind tunnel measurements in aeroacoustic research. The proposed approach is comparable to the approach of matched field processing and matched field inversion that is well-known in the field of underwater acoustics [4, 5, 7, 16–18].

4.2. The energy functions considered

To obtain the energy function for solving both source positions and strengths Eqs. (2.40) and (2.41) will be used. As seen in Chapter 3, for conventional beamforming with a scan plane parallel to the array the resolution of the source plot is limited by the width of the main lobe given by Eq. (2.59).

In the present study a different approach is followed to locate and quantify acoustic sources. A predefined scan-grid is not used and the amount of sources K is considered to be known beforehand. An objective function, sometimes denoted as energy function, is defined such that it provides a measure for the difference between the measured CSM and the predicted CSM from Eqs. (2.40) and (2.41), given a set of values for the unknown parameters. For this research, both synthetic

and measured covariance matrices are data considered for $\mathbf{C}_{\text{meas}}$. The synthetic data were obtained from benchmark cases that were generated in the framework of the Benchmarking Array Analysis Methods workshop in Dallas 2015 [19].

The first energy function considered is the well-known Bartlett processor given by [16–18, 20]

$$E_{\text{Bartlett}}(\mathbf{y}) = \frac{\mathbf{p}(\mathbf{y},\omega)^H \mathbf{C}_{\text{meas}}(\omega)\mathbf{p}(\mathbf{y},\omega)}{\mathbf{p}(\mathbf{y},\omega)\,\text{tr}\,[\mathbf{C}_{\text{meas}}]} \tag{4.1}$$

with $\mathbf{C}_{\text{meas}}$ the measured cross-spectral matrix at frequency ω, $\mathbf{p}(\mathbf{y},\omega)$ the prediction for the pressures at the microphones and tr$[\cdot]$ denotes the trace of a matrix. This is just the beamformers output equation which can be modeled using the result of Eq. (2.36). Here steering vector formulation III is used from Section 2.4.2 resulting in the expression

$$\mathbf{p}(\mathbf{x}_{s,k},\omega) = \sum_{k=1}^{K} \mathbf{a}_k(\mathbf{x}_{s,k},\omega)\, s_k(\omega), \tag{4.2}$$

where $\mathbf{a}_k = \left[a_{k,1}(\mathbf{x}_{s,k},\omega),\cdots,a_{k,N}(\mathbf{x}_{s,k},\omega)\right]^T$ is the steering vector, $s_k(\mathbf{x}_{s,k},\omega)$ the acoustic waveform for source k and $[\cdot]^T$ denotes the transpose of the vector. In Eq. (4.2) the dependency on the position of the source $\mathbf{x}_{s,k} = \left(x_{s,k}, y_{s,k}, z_{s,k}\right)$, in this case source k, is explicitly noted. The steering vector $\mathbf{a}_k$ depends on the relative position between the microphones and the sources. This will be part of the input $\mathbf{y}$ for the optimization method.

The element of $\mathbf{a}_k$ for microphone n is given by the adapted formulation III as

$$a_{k,n} = \frac{1}{r_{k,n}} \mathrm{e}^{-j\omega r_{k,n}/c}, \tag{4.3}$$

by omitting the consideration at the array center and instead assuming the reference distance of 1 m. The speed of sound is given by c and $r_{k,n} = |\mathbf{x}_{s,k} - \mathbf{x}_n|$ the distance between source k and microphone n.

Vector $\mathbf{y}$ contains the trial values for the unknown parameters. For example, in the case of one source it would have the form of $\mathbf{y} = \mathbf{y}\left(\mathbf{x}_{s,1}, s_1\right)$ which would be 4 parameters considering only the spatial position (3 coordinates) and amplitude of the source. In the example of four sources it would have the form of $\mathbf{y} = \mathbf{y}\left(\mathbf{x}_{s,1},\mathbf{x}_{s,2},\mathbf{x}_{s,3},\mathbf{x}_{s,4}, s_1, s_2, s_3, s_4\right)$. A drawback of the energy function given in Eq. (4.1) is that the source amplitude, s_k, information does not affect its value. Therefore, it will not be possible to estimate the source amplitude when using this function.

An alternative energy function, which includes the estimation of the source amplitude, is defined as follows [21]

$$E_{\text{CSM}}(\mathbf{y}) = \sum_{\text{elements of CSM}} \left\{ \left[\text{Re}(\mathbf{C}_{\text{meas}}) - \text{Re}(\mathbf{C}_{\text{model},\mathbf{y}})\right]^2 + \left[\text{Im}(\mathbf{C}_{\text{meas}}) - \text{Im}(\mathbf{C}_{\text{model},\mathbf{y}})\right]^2 \right\} \tag{4.4}$$

where $\mathbf{C}_{\text{model},\mathbf{y}}$ is the modeled covariance matrix corresponding to parameter vector $\mathbf{y}$, calculated using Eq. (2.41). The summation is done over all $N \times N$ elements of the matrices containing the differences between $\mathbf{C}_{\text{meas}}$ and $\mathbf{C}_{\text{model},\mathbf{y}}$. The covariance matrices are defined for a specific frequency ω.

Both energy fuctions in Eqs. (4.1) and (4.4) will be used with the Differential Evolution (DE) as the optimization method discussed in Section 3.2. The settings for DE must be selected beforehand to suitable values, which can be problem specific, to maximize the probability of localizing the global optimum. In this work, the best values for the setting parameters are determined in Section 4.4.

4.3. The test cases considered

Three test cases will be considered in this chapter. Two simulated cases consisting of a single sound source and four sound sources; and an experimental case for which one speaker is used in an anechoic chamber.

4.3.1. Test case I: a single monopole sound source

In this test case, a single monopole sound source is considered, located at $\mathbf{x}_s = (0.3, 0.4, 1.0)$ m with source amplitude of 1.0 Pa. The array consists of 48 microphones. Fig. 4.1a shows the array geometry. The data provided is simulated and consists of the cross-spectral matrix of the microphone measurements at the frequencies 500 Hz to 6000 Hz in 500 Hz steps. In Section 4.5, conventional beamforming and inversion will be applied for each frequency.

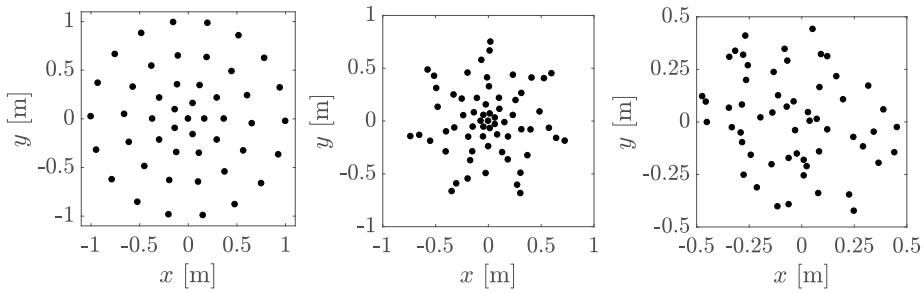

Figure 4.1: The microphone array configurations used for the test cases.

4.3.2. Test case II: four monopole sound sources

In this case, four uncorrelated monopole sources are considered at corners of an 0.2 m by 0.2 m square emitting white noise. The distance between the center of the source plane and the center of the 64 microphone array is 0.75 m. The source locations are denoted as

$$\begin{aligned} \mathbf{x}_{s,1} &= (0.1, 0.1, 0.75), \\ \mathbf{x}_{s,2} &= (0.1, -0.1, 0.75), \\ \mathbf{x}_{s,3} &= (-0.1, 0.1, 0.75), \\ \mathbf{x}_{s,4} &= (-0.1, -0.1, 0.75), \end{aligned} \tag{4.5}$$

all with equal and known power [19].

In this case, the array consists of a seven arm logarithmic spiral arrangement with an aperture of 1.5 m seen in Fig. 4.1b. All the sources have the same power and are simulated as white noise in the time domain. The cross-spectral matrix contains values of 513 frequencies in 50 Hz steps. In Section 4.5, nine frequencies will be selected for beamforming and inversion.

4.3.3. Test case III: one speaker in an anechoic chamber

In addition to the test cases with simulated data, an experiment was performed in the anechoic chamber of the Faculty of Applied Sciences at the Delft University of Technology. The walls, ceiling and floor of this room are covered in wedges made from glass wool in order to prevent sound reflections, leaving a space of 8 m × 8 m × 8 m inside. A 56 microphone array with a random distribution and an aperture of approximately 1 m was employed. The acoustic source for this experiment was a small speaker located at a distance of 1.87 m from the array plane and aligned with the array center, as shown in Fig. 4.2. The array plane formed an angle of 4 degrees with the vertical, which was accounted for in the microphone positions. Hence, the expected sound source position with respect to the array reference system is $\mathbf{x}_s$ = (0 m, 0 m, 1.87 m). The Overall A-weighted Sound Pressure Level inside the anechoic chamber with the assembled experimental setup, measured using a calibrated Bruel & Kjær 2231 modular precision sound level meter, was found to be lower than 20 dBA. For this example, the speaker was emitting sound at a single frequency of 5000 Hz. The sampling frequency used for the microphone array was 50 kHz and the recording time was 60 s. In order to obtain the time-averaged CSM, the acoustic data was separated in 49 time blocks with a 50% data overlap. The sound pressure level at the array center microphone was 80.25 dB.

4.4. The optimal settings for Differential Evolution

To find good solutions with DE, its setting parameters need to be selected appropriately. A similar procedure will be followed as Snellen and Simons [5]. For this test the number of generations was set to N_G = 600. Data from test case 1 was used at the maximum frequency of 6000 Hz which will exhibit more sidelobes and of higher value than the lower frequencies, and ensures the DE settings to be appropriate also for the lower frequencies in escaping local optima. For each combination of DE setting parameters, 50 independent runs were performed. The fraction of successful runs out of these 50 is denoted as p_s, and serves as an estimate for the probability of success.

4.4.1. Bartlett energy function

For the Bartlett energy function, a run is considered successful if any of the elements of the final population has a value for the objective function lower than 0.1. Various population sizes were considered. Figure 4.3 shows the percentage of converged runs as a function of both p_c and F for q = 12, 32, 64 and 128. In order to find suitable values, the DE performance is assessed for values between 0 and 1 with steps of 0.1 for p_c and F. From Fig. 4.3 it can be seen that p_s has the largest value at

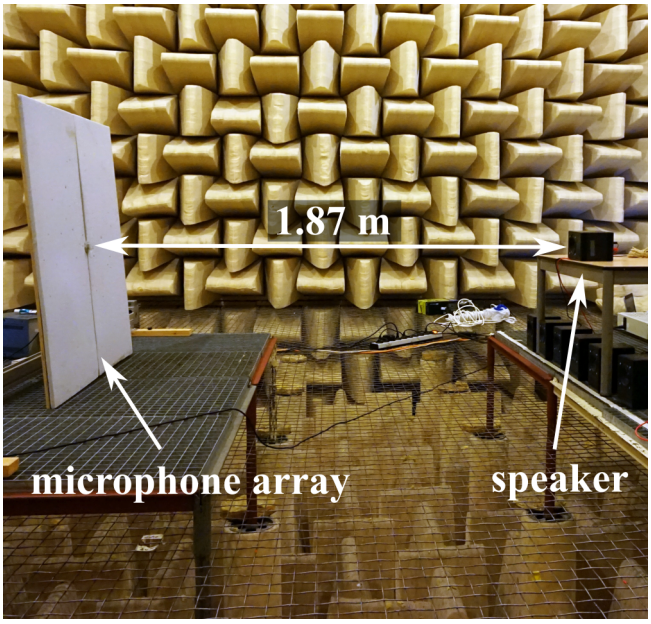

Figure 4.2: Experimental setup in the anechoic chamber with the microphone array in the left and the speaker in the right.

the population size of $q = 128$ for $F = 0.45$ and $p_c = 0.75$ with a value of around 70%. In Fig. 4.4, the energy landscape can be seen as a function of the spatial coordinates of the source for all the runs. Regions of local optima can be seen especially for the z-coordinate. This explains the success-rate of 70%. Because the microphone array is two-dimensional, the sensitivity in the direction pointing away from the array, i.e., the z-direction, is worse than that in the lateral directions [2]. Additional runs or generations could prevent solutions from being stuck in local optima. For the inversion tests, $p_s = 70\%$ will be considered adequate since multiple independent inversion runs are carried out for each test case. Figure 4.5 shows the convergence of the spatial position of the source for three runs. It can be seen that the correct source position $(0.3, 0.4, 1.0)$ m is found well within the 600 generations.

4.4.2. Cross-spectral matrix energy function

When using the CSM energy function given in Eq. (4.4), to also determine the source strength, s_k, a similar procedure is followed as in the previous section. For the CSM energy function, a run is considered successful if any of the elements of the final population has a value for the objective function lower than 10×10^{-3} , due to the small values, in general, for this energy function. The result for test Case I for a frequency of 6000 Hz is given in Fig. 4.6. A slight shift of optimal values can be seen to $F = 0.35$ and $p_c = 0.75$, and a significant drop to 40% in p_s. The energy landscape for this parameter setting is given in Fig. 4.7. Figure 4.8 illustrates the convergence behaviour, showing one run to have converged to a local optimum,

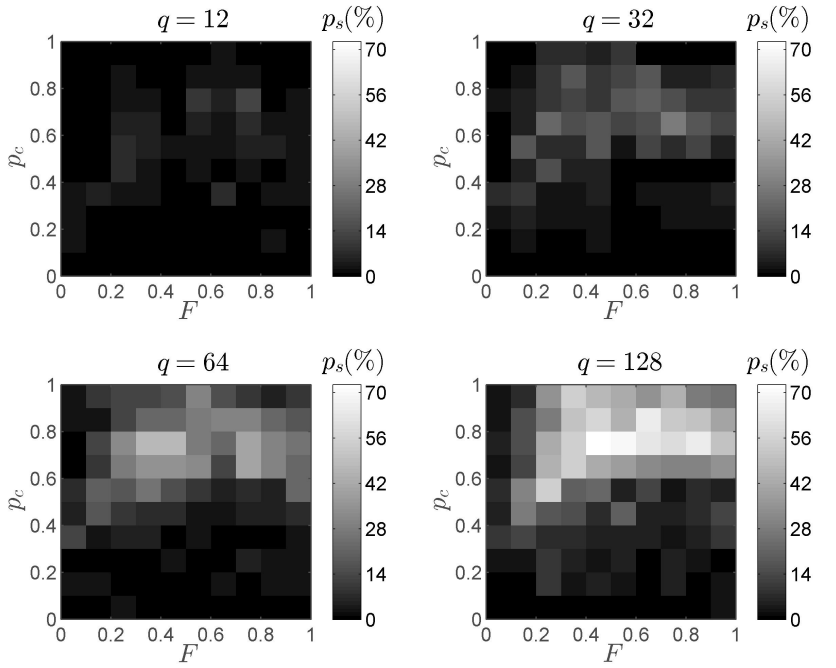

Figure 4.3: p_s as a function of p_c and F for four different population sizes q = 12, 32, 64 and 128 with N_G = 600 using the highest frequency, f = 6000 Hz, for the Bartlett energy function.

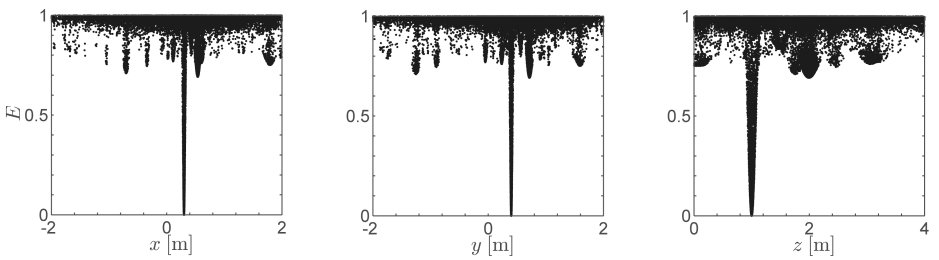

Figure 4.4: Energy landscape of the Bartlett energy function as function of the spatial coordinates (x, y, z) for the optimal setting of F = 0.45, p_c = 0.75 at the population size of q = 128.

with values for the x, y and z position deviating from the true positions.

4.5. Global optimization results

4.5.1. Test case I: single monopole

As a reference, we start with applying conventional beamforming, for which we define a scan grid at the source location parallel to the array. Beamforming is per-

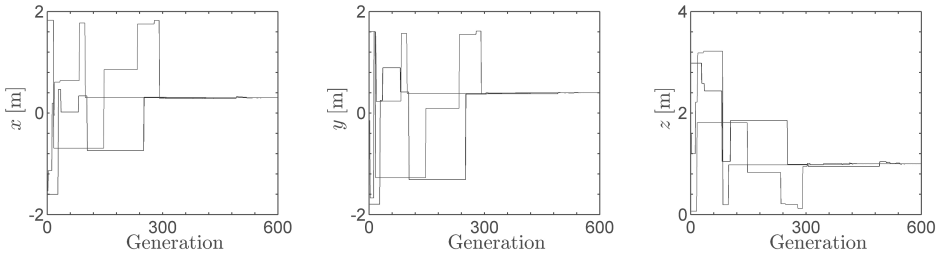

Figure 4.5: Convergence of the spatial coordinates (x, y, z) belonging to three runs for the optimal setting of $F = 0.45$, $p_c = 0.75$ at the population size of $q = 128$.

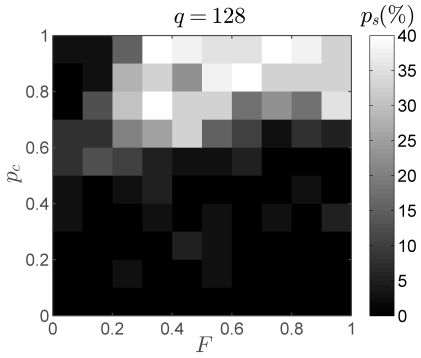

Figure 4.6: p_s as a function of p_c and F for $q = 128$ and $N_G = 600$ using the highest frequency, $f = 6000$ Hz, for the CSM energy function. Note the different colorbar scale.

formed for twelve different frequencies from 500 to 6000 Hz in steps of 500 Hz. Figure 4.9 shows the results for 500, 3000 and 6000 Hz. As expected, it is seen that the source is well localized with the resolution improving for higher frequencies. The appearance of sidelobes also increases with higher frequencies. Figure 4.10 shows the results for the three frequencies by using the proposed inversion method, employing the Bartlett energy function. To obtain this result, the settings of DE were set to $q = 128$, $N_G = 600$, $p_c = 0.75$ and $F = 0.45$. The number of independent runs was selected to be 50. For all frequencies, it can be seen that the source position is retrieved correctly, since the values for x, y and z that correspond to the lowest energy values are in agreement with the true source position. To show the rate of convergence, Fig. 4.11 is presented, where the energy is given as a function of the number of generations for the frequencies 500, 3000 and 6000 Hz. For 500 and 3000 Hz, convergence to the correct position is achieved well within the 600 generations. For 6000 Hz, three out of ten runs are seen not to have reached zero energy value at 600 generations.

The same procedure is repeated using the CSM energy function given in Eq. (4.4) with $q = 128$, $N_G = 600$, $p_c = 0.75$ and $F = 0.35$. In Fig. 4.12 the source can be seen to be well localized, with minimum energy corresponding to the correct position. For

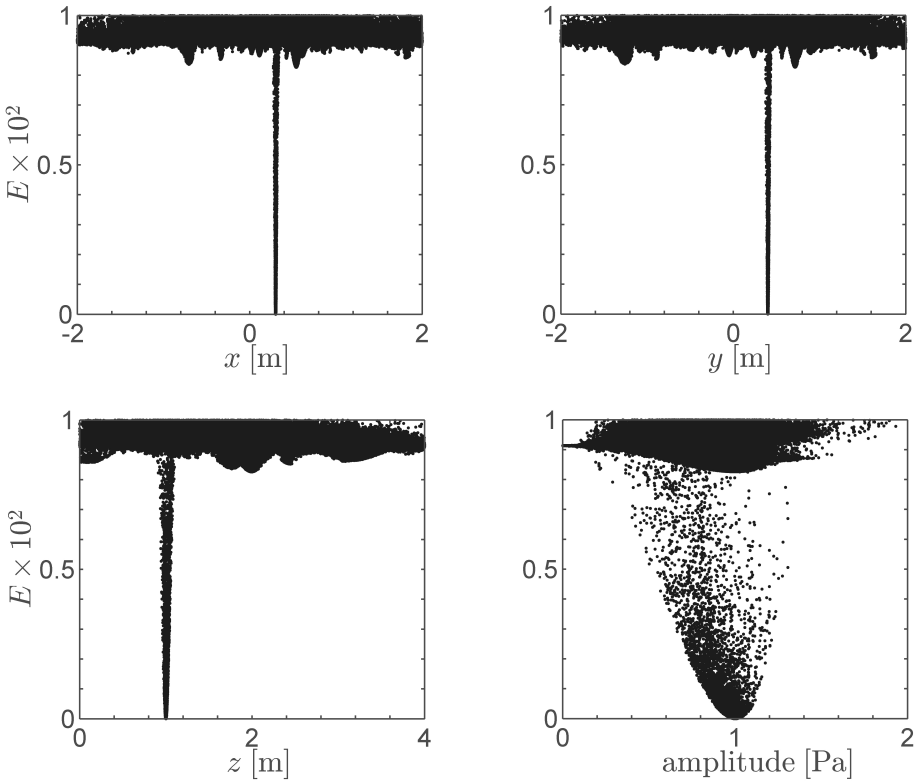

Figure 4.7: Energy landscape of the CSM energy function as function of the spatial coordinates (x, y, z) and the source amplitude for the optimal setting of $F = 0.35$, $p_c = 0.75$ at the population size of $q = 128$.

3000 and 6000 Hz, more runs are seen to be stuck in a local minimum. This can also be seen in Fig. 4.13, where at the last generation, some runs have not converged to the minimum energy possible yet. The value for the amplitude is obtained correctly at 1.0 Pa. From Fig. 4.6 it is expected that the rate of success is lower than that of the Bartlett energy function. This is confirmed by Fig. 4.13, where fewer runs reach zero energy for higher frequencies. The runs that do reach close to zero energy, do it relatively quickly within the 600 generations. The runs which seem to be stuck in local optima are unable to get to a much lower energy throughout the generations, indicating the need for carrying out sufficient independent runs. Using the given parameter settings for DE the runtime this case is around an hour per frequency for non-optimized code.

4.5.2. Test case II: four monopoles

Test case 2 concerns the situation with 4 monopoles present. For the frequencies of 500, 1000, 1500, 2000, 2850, 3500, 6650, 8400 and 10000 Hz conventional beamforming is applied. The result can be seen in Fig. 4.14. For the first four frequencies,

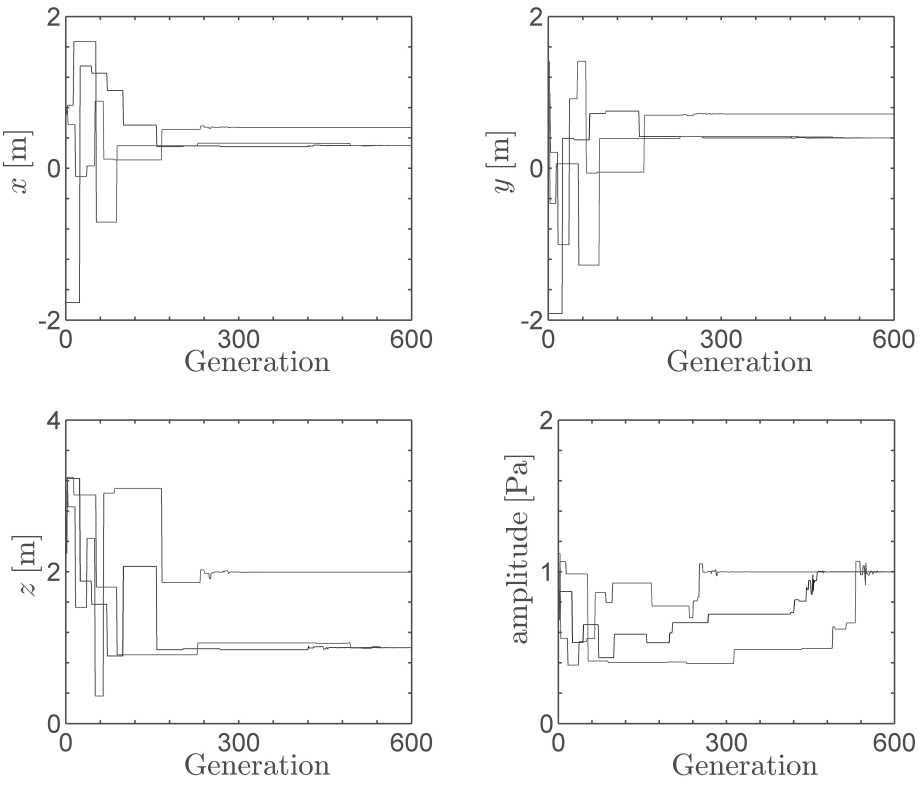

Figure 4.8: Convergence of the spatial coordinates (x, y, z) and source amplitude belonging to three runs for the optimal setting of $F = 0.35$, $p_c = 0.75$ at the population size of $q = 128$.

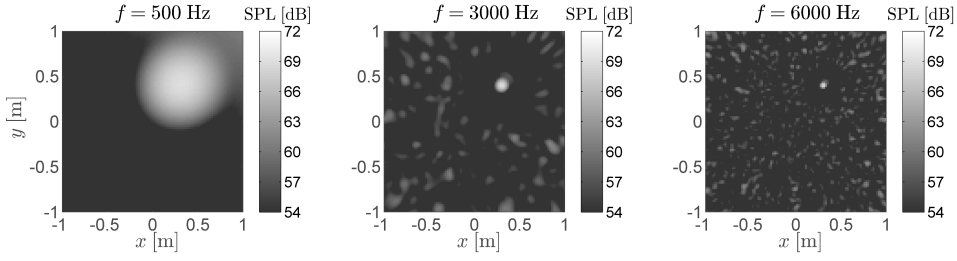

Figure 4.9: Beamforming of the monopole source for 500, 3000 and 6000 Hz.

the sources cannot be separated. This can be understood from Eq. (2.59) with the distance to the source being 0.75 m, the resolution will be too low. For the frequencies of 2850 Hz and higher, the source can be properly identified. The sidelobes become more prominent for higher frequencies and the sources become harder to localize. It should be noted that, although indeed at sufficiently high frequencies,

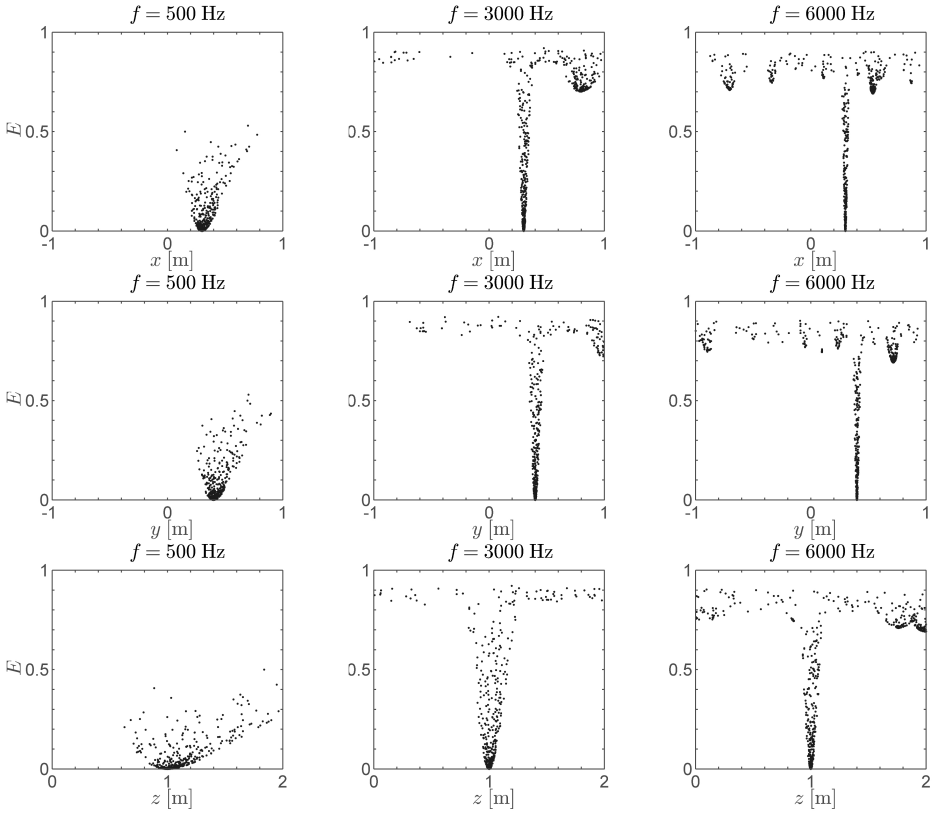

Figure 4.10: Inversion using Bartlett as the energy function for 500, 3000 and 6000 Hz.

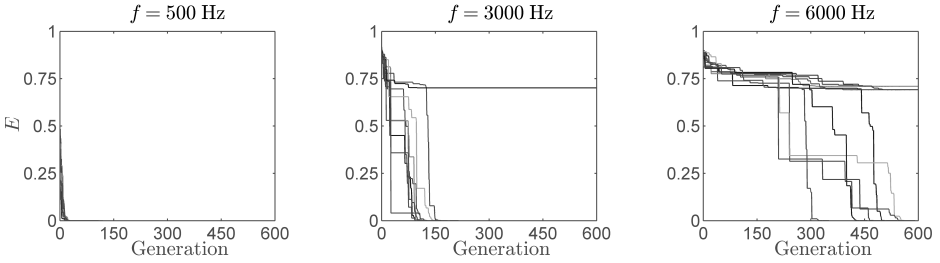

Figure 4.11: Energy (E) as function of generation for three different frequencies and 10 independent runs.

4 sources can be identified in the source plots, the localization is affected by the mismatch between the modeled situation with a single noise source only and the actual situation with four sources present simultaneously. This is not the case when using Eq. (4.4) and modeling the CSM according to Eq. (2.41) for 4 sources. This model is then employed in the inversion method with the parameters for DE found

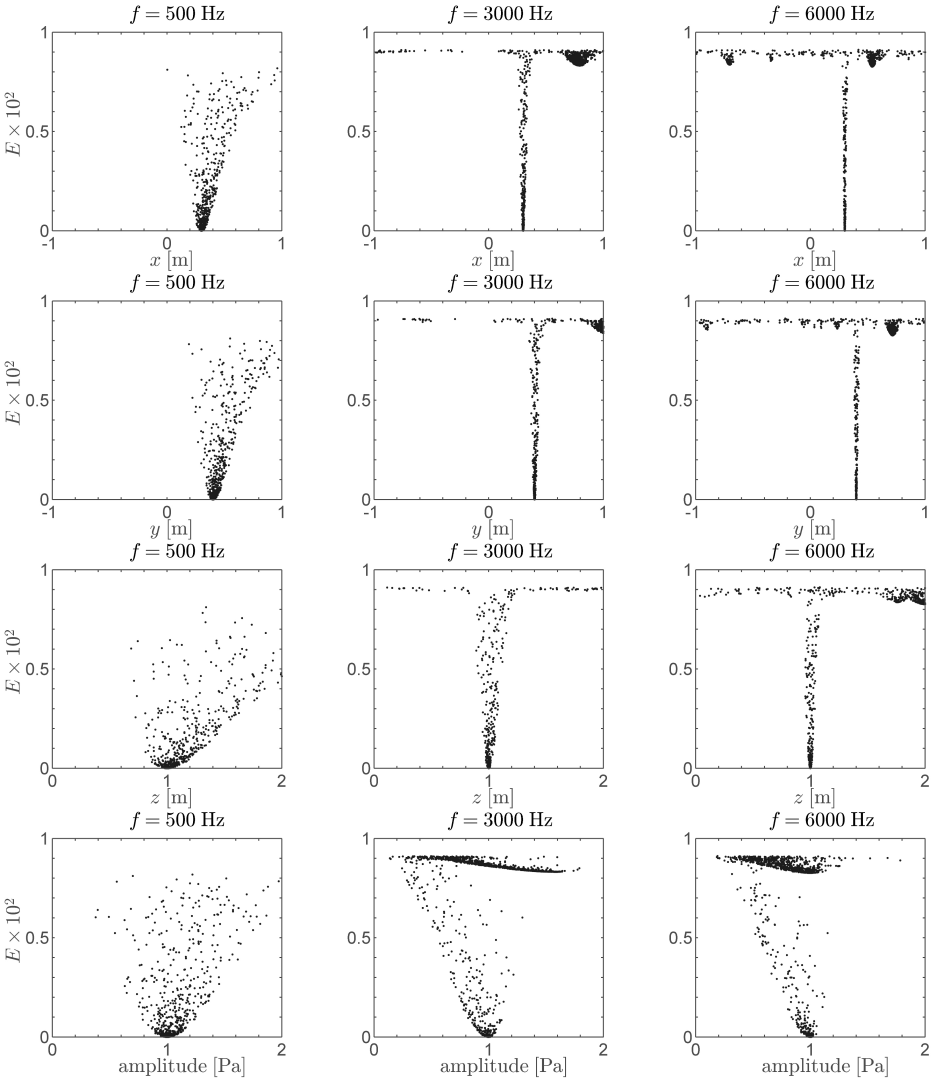

Figure 4.12: Inversion using CSM as the energy function for 500, 3000 and 6000 Hz including the amplitude.

in Section 4.4.2. In this case, only the CSM energy function is used because of its additional advantage of estimating the source amplitude. The result can be seen in Fig. 4.15, indicating that from 1000 Hz on the sources can be identified accurately with good resolution. Upon inspection of Fig. 4.16, it can also be seen that many runs converge to zero energy, even at frequencies as high as 10000 Hz. It can be noted that the CSM energy function works better compared with the single monopole case. Whereas at 10000 Hz nine out of ten runs reach close to zero

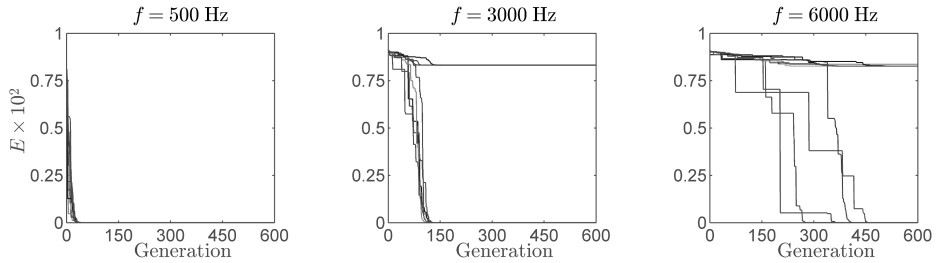

Figure 4.13: Energy (E) as function of generation for three different frequencies and 10 independent runs using CSM.

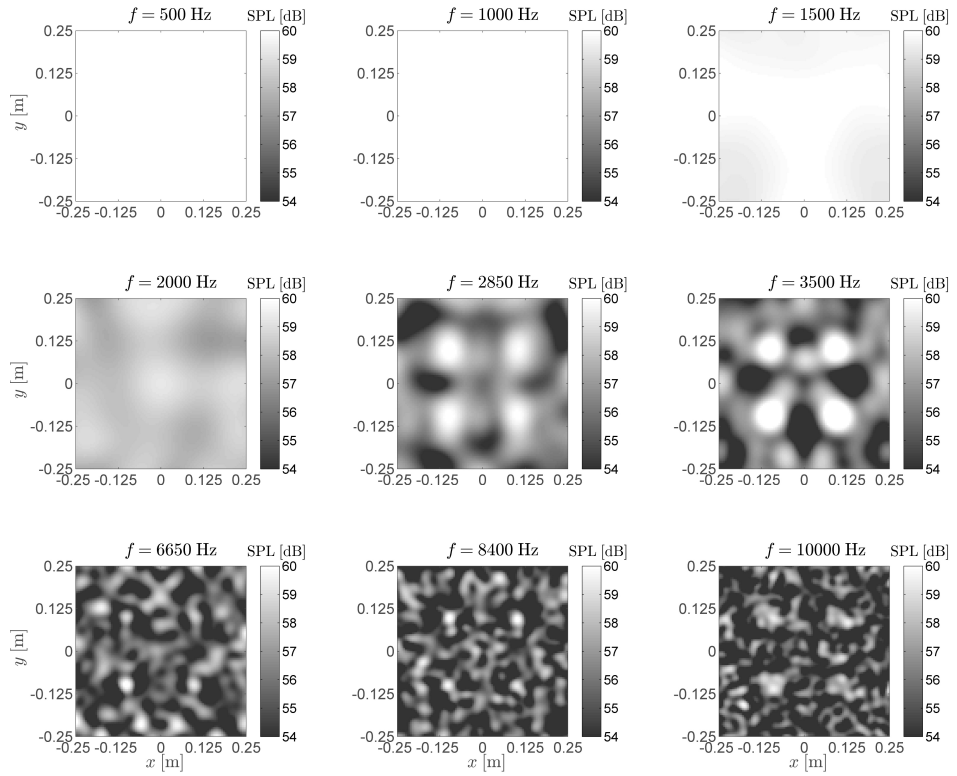

Figure 4.14: Conventional beamforming source plots of four monopole sources for various frequencies. The corresponding resolutions according to Eq. (2.59) are 0.47, 0.21, 0.14, 0.11, 0.074, 0.060, 0.032, 0.025 and 0.021 m for the increasing frequencies.

energy, this is only 7 out of ten for the single monopole case at 6000 Hz. A disadvantage of this method is the need to know the amount of sources beforehand. In Fig. 4.16 the convergence behaviour is seen for 10 different runs at frequencies of

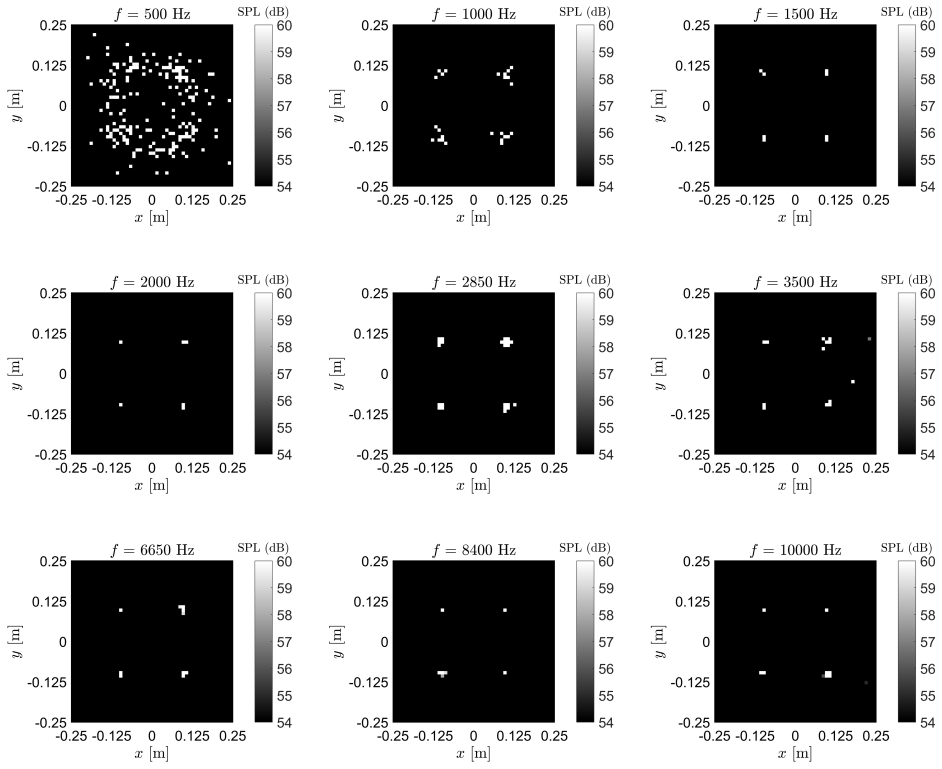

Figure 4.15: Inversion using the CSM energy function for four monopoles for various frequencies. Results are shown for all 50 runs and are the solutions with the lowest value for the energy per run

1500, 3500 and 10000 Hz. It can be seen that for the first two frequencies, 600 generations are sufficient. For 10000 Hz it can be observed that the energy is getting closer to zero around 600 generations for most runs. From this, it can be concluded that the chosen DE setting parameters in general work well for this problem. However, for frequencies from 10000 Hz on, a higher amount of generations is recommended. The runtime for the four sources was within 3 hours per frequency for non-optimized code. As a further illustration of using optimization methods, the problem is extended to include estimation for parameters other than those directly related to the acoustic source. To this end, the 4 monopole case is taken for 6650 Hz and the speed of sound is considered as the additional unknown parameter. This was set to 343 m/s for the simulation. The result from the optimization is presented in Fig. 4.17. For low energies, it provides the values for the speed of sound to be in the range of 342 to 346 m/s. For the best three runs, it presents the value for the speed of sound converging to 343 m/s. This shows that, despite of a relatively broad range of sound speeds corresponding to low energies, the best runs result in a sound speed of 343 m/s. Including these type of environmental parameters can

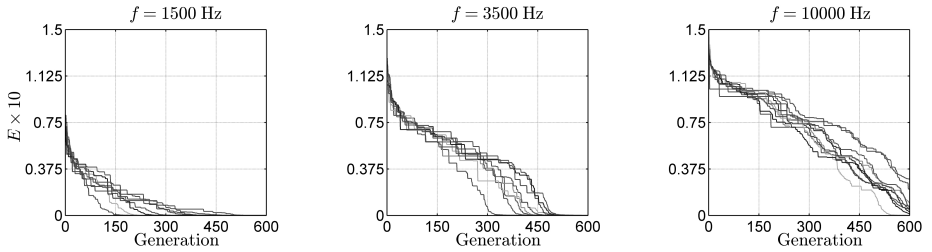

Figure 4.16: Energy as function of generation for a frequency of 1500, 3500 and 10000 Hz (10 independent runs).

be of interest also for complex wind tunnel experiments in aeroacoustic research.

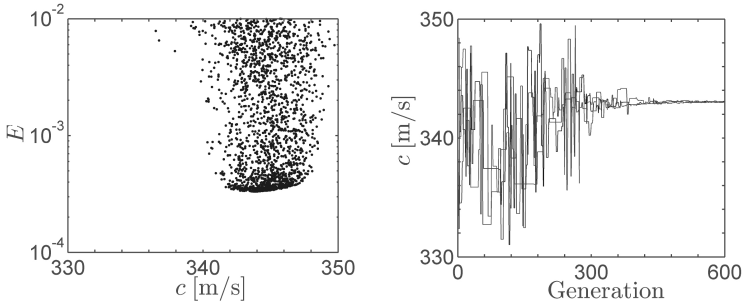

Figure 4.17: Estimation of the speed of sound for the 4 monopole case at f = 6650 Hz.

4.5.3. Test case III: speaker in anechoic camber

Conventional beamforming was applied again to the acoustic data from the microphone array to obtain a reference baseline result. Figure 4.18 presents the source map obtained for 5000 Hz. The position of the source is found with the expected spatial resolution but several sidelobes are displayed as well. Figure 4.19 presents the results for 5000 Hz by using the proposed inversion method with the Bartlett energy function. Use was made of Bartlett since this energy function showed a high probability of success for cases with a single source present. For this situation with a single source, the source strength follows directly from from the beamformer output Eq. (2.58) for the source position derived through inversion. To achieve this result, DE was set to q = 128, N_G = 600, p_c = 0.75 and F = 0.4. The number of independent runs was selected to be 50. It can be observed that the source position is obtained correctly, since the values for x, y and z that correspond to the lowest energy values are in agreement with the actual source position. To study the convergence rate for each coordinate in this case, Fig. 4.20 is presented, where the parameter value for three independent runs is given as a function of the number of generations. It can be observed that after approximately 50 generations, the result

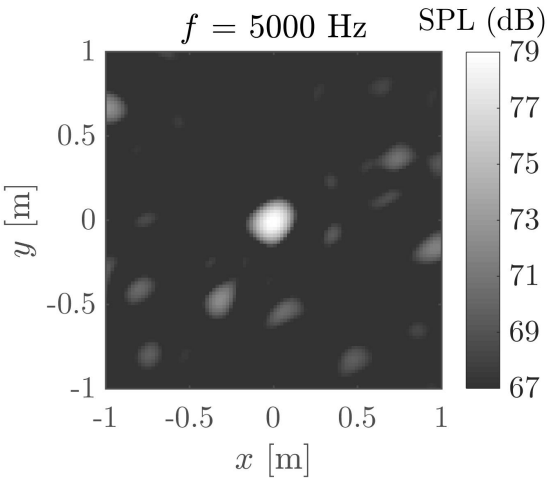

Figure 4.18: Beamforming result for the speaker sound source at 5000 Hz using the randomly distributed array.

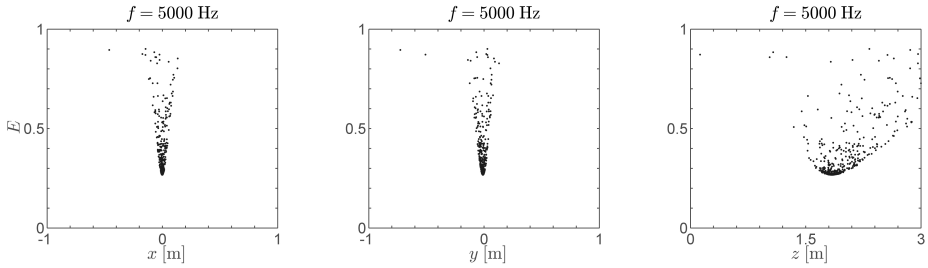

Figure 4.19: Inversion results for the speaker source case at 5000 Hz using the Bartlett energy function.

has rapidly converged to the correct solution for the three coordinates. In Fig. 4.20 the convergence behaviour of the energy is presented for 10 different runs (out of the 50 used) at 5000 Hz. It can be clearly stated that 600 generations are more than sufficient to obtain convergence. However, in this case, an asymptotic energy value of approximately 0.25 is reached instead of zero, reflecting the always present imperfections of the measurement such as small errors in the microphone positions.

4.6. Conclusions

In this work, an inversion method is presented using the global optimization method Differential Evolution (DE) to localize sound sources with a microphone array and determine the corresponding source strengths. For this purpose, two energy functions were formulated. The first energy function used was the Bartlett processor. The second energy function is based upon modeling the cross-spectral matrix (CSM). The Bartlett energy function has the disadvantage of not determining the

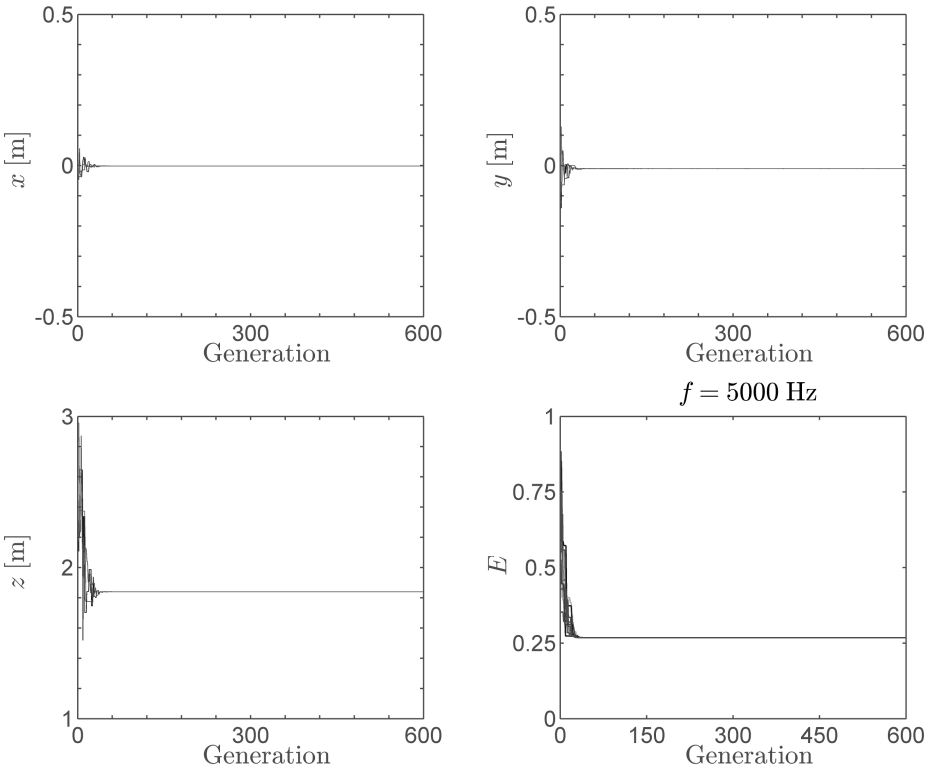

Figure 4.20: Convergence of the spatial coordinates (x, y, z) belonging to three runs for the optimal setting of $F = 0.4$, $p_c = 0.75$ at the population size of $q = 128$ and the case with the speaker emitting at 5000 Hz. In the last figure the energy (E) is given as a function of generation for 10 independent runs.

source strength, while the CSM energy function has no such disadvantage.

For both energy functions, the best parameters for DE were determined and subsequently used for source identification for three test cases: one simulated monopole source, four incoherent simulated monopole sources and one speaker emitting at a single frequency in an anechoic room. For the single simulated monopole case, the performance of the localization of the source was better by using the Bartlett energy function. Still, both energy functions performed better compared with conventional beamforming by having few to no sidelobes. The improvement when using inversion as source identification was also clearly seen for the case with four sources. While conventional beamforming had trouble identifying the source at low and high frequencies, the inversion method was able to localize the sources accurately and with high resolution. Extending the optimization for four sources to include the estimation of the speed showed that in addition to the source locations, also the sound speed could be estimated. Moreover, for the experimental case with a speaker, the x, y and z positions of the source were correctly obtained using the

Bartlett energy function.

The main advantage of the proposed inversion approach is that by employing global optimization methods that are efficient, in the sense that they require a limited number of forward calculations while still having a high probability of locating the global optimum, also for many unknowns, it becomes possible to search for all parameters of relevance by including them in the steering vector formulation. In addition, also parameters, such as those of the propagating medium, can be included as unknowns. Moreover, the energy function can be adapted to the situation at hand. It can account for multiple sound sources, reflections or refractions of the sound, thus representing the actual measurement environment to a large extent.

References

[1] A. M. N. Malgoezar, M. Snellen, R. Merino-Martinez, D. G. Simons, and P. Sijtsma, *On the use of global optimization methods for acoustic source mapping*, The Journal of the Acoustical Society of America **141**, 453 (2017), https://doi.org/10.1121/1.4973915 .

[2] B. D. Van Veen and K. M. Buckley, *Beamforming: A versatile approach to spatial filtering*, IEEE assp magazine **5**, 4 (1988).

[3] J. J. Grefenstette, *Optimization of control parameters for genetic algorithms*, and Cybernetics IEEE Transactions on Systems, Man **16**, 122 (1986).

[4] P. Gerstoft, *Inversion of seismoacoustic data using genetic algorithms and a posteriori probability distributions*, **95**, 770 (1994).

[5] M. Snellen and D. G. Simons, *An Assessment of the Performance of Global Optimization Methods for GEO-Acoustic Inversion*, Journal of Computational Acoustics **16**, 199 (2008).

[6] S. Kirkpatrick, C. D. Gelatt, and M. P. Vecchi, *Optimization by simulated annealing*, Science **220**, 671 (1983).

[7] C. E. Lindsay and N. R. Chapman, *Matched field inversion for geoacoustic model parameters using adaptive simulated annealing*, IEEE Journal of Oceanic Engineering **18**, 224 (1993).

[8] M. Dorigo, V. Maniezzo, and A. Colorni, *Ant system: optimization by a colony of cooperating agents*, Part B (Cybernetics) IEEE Transactions on Systems, Man, and Cybernetics **26**, 29 (1996).

[9] M. Dorigo, G. D. Caro, and L. M. Gambardella, *Ant algorithms for discrete optimization*, Artificial Life **5**, 137 (1999).

[10] R. Storn, *On the usage of differential evolution for function optimization*, in *Fuzzy Information Processing Society, 1996. NAFIPS., Biennial Conference of the North American* (IEEE, 1996) pp. 519–523.

[11] R. Storn and K. Price, *Differential evolution–a simple and efficient heuristic for global optimization over continuous spaces*, Journal of global optimization **11**, 341 (1997).

[12] T. F. Brooks and W. M. Humphreys, *A deconvolution approach for the mapping of acoustic sources (DAMAS) determined from phased microphone arrays*, Journal of Sound and Vibration **294**, 856 (2006).

[13] T. F. Brooks and W. M. Humphreys, *Extension of DAMAS phased array processing for spatial coherence determination (DAMAS-C)*, AIAA paper **2654** (2006).

[14] T. Yardibi, J. Li, P. Stoica, and L. N. Cattafesta, *Sparsity constrained deconvolution approaches for acoustic source mapping*. The Journal of the Acoustical Society of America **123**, 2631 (2008).

[15] T. Yardibi, J. Li, P. Stoica, N. S. Zawodny, and L. N. Cattafesta, *A covariance fitting approach for correlated acoustic source mapping*. The Journal of the Acoustical Society of America **127**, 2920 (2010).

[16] G. F. Edelmann and C. F. Gaumond, *Beamforming using compressive sensing*. The Journal of the Acoustical Society of America **130**, EL232 (2011).

[17] A. Xenaki, P. Gerstoft, and K. Mosegaard, *Compressive beamforming*. The Journal of the Acoustical Society of America **136**, 260 (2014).

[18] A. Xenaki and P. Gerstoft, *Grid-free compressive beamforming*. The Journal of the Acoustical Society of America **137**, 1923 (2015).

[19] *Benchmarking array analysis methods 2015*, (2015).

[20] D. F. Gingras and P. Gerstoft, *Inversion for geometric and geoacoustic parameters in shallow water: Experimental results*, **97**, 3589 (1995).

[21] D. Blacodon and G. Elias, *Level estimation of extended acoustic sources using a parametric method*, Journal of Aircraft **41**, 1360 (2004).

5

Investigation of pylon-propeller noise interaction

Using the tools from the previous chapters an experimental investigation was performed at the Large Low-speed Facility of the German-Dutch wind tunnels (DNW-LLF) to study the pylon interactions associated with pusher propellers. A pylon or any object in front of a propulsion system can change the inflow to be less uniform. A wake will be formed behind the object which can impinge on the blades of a fan or propeller. This effect can increase the noise levels. By using an active system in a pylon, such as blowing air, in order to eliminate the wake deficit could in turn negate the noise penalty of an installed pylon. In this research, the noise effects of pylon trailing edge blowing was evaluated using a microphone array. Of special interest in this work is the question whether high resolution methods can in practice distinguish sources in close proximity or reveal sources otherwise not seen present. In this problem the origin of the sources are expected to be mainly from both the propeller and any source caused by the installation of the pylon. Beamforming using a logarithmic spiral microphone configuration will be used to assess the noise sources. Effects of convection and shear layer refraction of sound have to be taken into account. In order to incorporate this, two different calibration sources are used to assess the resulting shift of sources. The found shift is then used for three different experiments: the isolated propeller; the installed pylon propeller; and the pylon propeller with air blowing from the trailing edge. The three setups will then be compared using both the spectra and three beamforming methods.

5.1. The APIAN-INF experiment

During the APIAN-INF measurements several experiments were performed on pylon propeller configurations to study pylon interactions associated with pusher propellers[1–3]. The experiments were performed as part of the ESWIRP project (European Strategic Wind tunnels Improved Research Potential)[4].

In this campaign the aerodynamic and aeroacoustic effects of pylon trailing edge blowing were investigated. This work focuses only on the noise emissions of the configurations. Experiments were done with an isolated propeller and a pylon installed upstream the propeller. For the installed pylon the blowing effects were also investigated. It is expected that blowing at a specific mass rate can negate the effect of the wake of the pylon. The effect of wake recovery is especially interesting for noise emissions. The measurement campaign was done in the Large Low-Speed Facility of the German-Dutch Wind Tunnels (DNW-LLF)[5].

5.1.1. DNW wind tunnel and used models

The DNW-LLF tunnel is an open jet configuration. The wind tunnel has an outlet of 8 m x 6 m and allows for a wind speed range of 0 – 80 m/s. The flow in the wind tunnel has a turbulence level of less than 0.02%. Views of the wind tunnel can be seen in Figure 5.1[1]. The DNW-LLF tunnel was designed to be anechoic.

(a) (b)

Figure 5.1: The DNW-LLF wind tunnel (a) view from the nozzle at the collector and (b) angled view to the nozzle.

After the needed equipment is placed in the wind tunnel, the floor is covered with acoustic wedges as seen in Fig. 5.1b to prevent ground reflections. The walls, by default, are covered by acoustic absorbent material. The DNW-LLF facility has many measurement systems[6] such as Particle Image Velocimetry (PIV) system as well as microphone arrays.

For the experiment a six bladed propeller was used. This was specifically designed for the European APIAN (Advanced Propulsion Integration Aerodynamics and Noise) project[7]. The propeller had a diameter of 0.508 m and the blade pitch angle of 40.4° at 75% of the radius. The propeller can be seen in Figure 5.2.

[1] All photos in this chapter are courtesy of Dr. ir. T. Sinnige

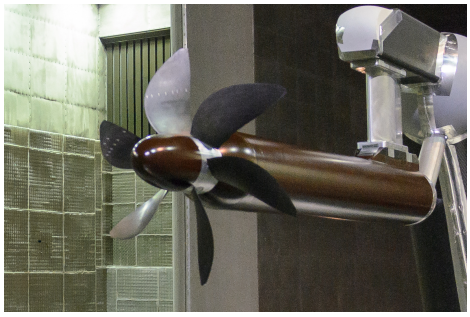

Figure 5.2: The six bladed propeller.

The pusher propeller configuration was achieved by positioning the propeller downstream of a pylon equipped with a trailing edge blowing system. The pylon model was constructed as a straight wing with a NACA0010 profile. The span was 0.9 m and the chord 0.489 m. In order to include an installation for a blowing system, the trailing edge thickness was set to 0.8% of the chord length. The installed pylon model together with the propeller can be seen in Figure 5.3. Tests

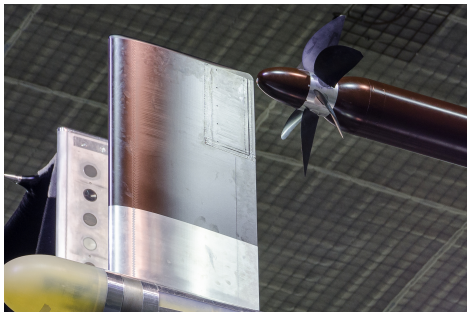

Figure 5.3: The installed pylon on the left and the six bladed propeller on the right.

were performed with and without the presence of the pylon. In order to perform beamforming, scan points are selected within a user desired scan plane. To assess where sound sources are originating from, it is important to have several reference points together with a defined coordinate system. This is shown in Fig. 5.4 for the setup of the pylon configured in front of the propeller.

The coordinate system is defined as such that x is pointing from the nozzle to the collector, y is pointed towards the wall away and z pointed to the ceiling of the wind tunnel. As a reference three coordinates are indicated in the figure at the left by the stars. Two are at the corners of the trailing edge of the pylon and one is positioned at the center of the propeller plane. All three points lie, together with the chord plane of the pylon, in the plane of $y = -1.0\,\mathrm{m}$. With these points it is easier to identify where sound is coming from relative to the pylon or propeller.

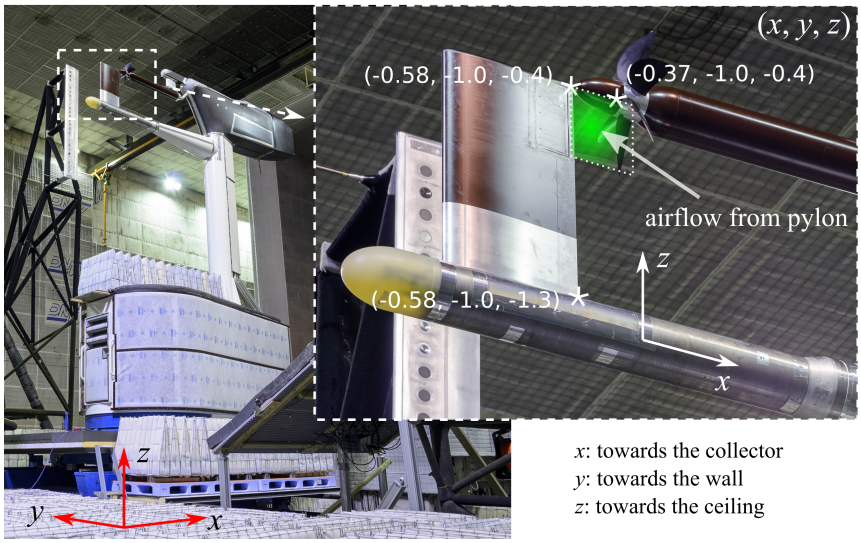

Figure 5.4: The installed pylon propeller configuration, with on the right a zoom-in. The coordinate system used can be seen together with three reference points.

5.1.2. The microphone array

For this experiment use was made of a custom made microphone array by the TU Delft. The array consisted of 63 microphone arranged in a 3 by 4 m plane as a logarithmic spiral[8]. The configuration can be seen in Fig. 5.5. The array has an

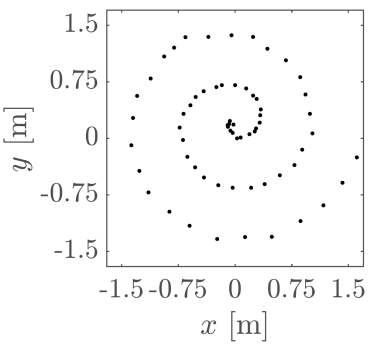

Figure 5.5: The array configuration used in the DNW wind tunnel. The logarithmic spiral consists of 63 microphones with an aperture of 3 m

effective diameter of 3 m. The microphone plane was angled around 30° relative to the ground. Each microphone was embedded in 10 cm of foam, primarily to adjust it in place and secondarily to prevent any reflections. The array was positioned outside the flow. The array inside the wind tunnel can be seen in Figure 5.6. The coordinates displayed in Fig. 5.4 are local coordinates. To obtain the tunnel

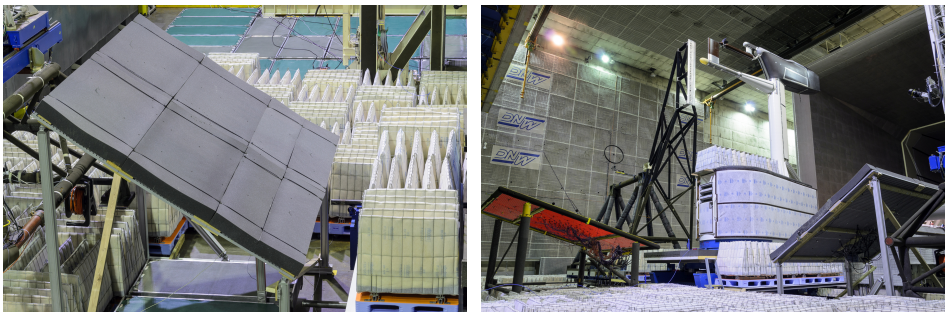

(a) (b)

Figure 5.6: The TU Delft 63 microphone array embedded in gray foam with (a) the view of only the array and (b) the view together with the pusher propeller configuration.

coordinates, in line with Fig. 5.4, only the corners of the microphone array were determined using a theodolite. Performing the measurement for all microphones was infeasible due to the large amount of positions and the embedding of the microphones in the foam. With the four corner position a rotation matrix is applied to each microphone position to obtain the positions in tunnel coordinates. With this coordinate system, an easy selection of scan planes can be made in beamforming corresponding to, or close to, positions of the setup.

The performance of beamforming is subjected to Rayleigh criterion given by Eq. (2.59). For these tests the aperture is $D = 3$ m, the distance of beamforming will be around $z_{\text{bf}} = 8.4$ m and the speed of sound $c = 344.5$ m/s. The long distance of 8.4 m will in general result in poor resolution. Propeller noise is also known to be relatively low frequent, usually lower than 5 kHz. Considering the close proximity of the propeller blades with the pylon's trailing edge, it is expected that source localization to discern the two will be difficult. To give an idea of the obtained resolution in the relevant frequency range, Table 5.1 is given.

Table 5.1: Examples of obtained resolution for various frequency within the range of interest.

f [Hz]	$\Delta\ell$ [m]
500	2.34
1000	1.17
2500	0.47
5000	0.23

From the table it can be seen that even for a frequency of 5000 Hz the distance for which two sources can be seperated is 23 cm which is still larger than 15 cm, the distance between the pylon's trailing edge and the propeller plane. The low resolution can be problematic as small errors of the array (microphone positions[9]

and de-coherency between microphones introduced by the shear layer[10–12]) can result in shifted source locations.

As explained in previous chapters, high resolution methods of beamforming have been developed which can surpass the Rayleigh criterion. Tests with simulated data proves to be successful. The experiments in this chapter will be used as a benchmark test to assess the performance of high resolution methods in practice.

For the data acquisition part, a CompactRIO by National Instruments was used. The signal is first recorded using an electret microphone. The electric signal from the microphone is then sent to a high pass filter to block the DC voltage using a cut-off frequency of 1.5 Hz. Using an operational amplifier the signal is amplified and sent to a low pass filter with a cut-off of 11.2 kHz to prevent aliasing. The digital signal processing is then performed by the CompactRIO to obtain and store the digital data. Recording of the signals of every microphone was performed at a sampling rate of 50 kHz. The measurement time was set to 32 s.

5.2. Wind corrections

Due to the presence of flow and the array being positioned out-of-flow two effects of the sound propagation need to be taken into account. There is convection of the sound by the wind and refraction when it leaves the flow[13]. It is therefore expected that the detected sound sources will be shifted. Due to the geometry of the wind tunnel and the position of the microphone array it is difficult to take the two effects into account during beamforming. The microphone array is not positioned such that every point on the array plane has a constant distance to the shear layer. In order to incorporate proper corrections for the shift, calibration sound sources are used where the position is determined beforehand. Using beamforming the shift can then determined as the deviation from the expected position. The sources used in these experiments are the Airbus loudspeaker and an Onera sparker source. The source is expected to lie at $(x, y, z) = (0, -1, 0)$ for the loudspeaker and $(x, y, z) = (-0.06, -1, 0)$ for the sparker. The sound sources can be seen in Figure 5.7. The use of both sources is to get a good estimate of the shift. Large discrepancies can indicate measurement errors.

For a given wind speed the shift in the source position is determined. The obtained shift is then applied to actual measurement data, i.e. the propeller data. The procedure can be summarized as follows

- Determine the position of the source with no wind using beamforming
- Determine the position of the source *with* wind using beamforming
- Determine the shift of the source due to the wind
- Apply the shift for the pylon-propeller data with the *same* wind condition

First the spectrum is determined for the loudspeaker for all microphones to characterize the source's spectral behaviour.

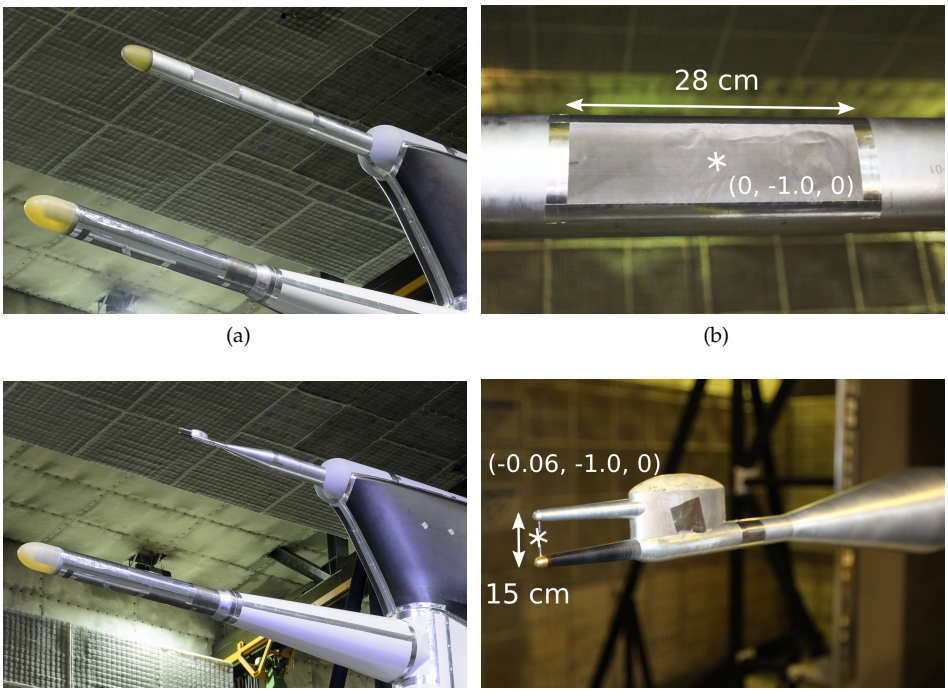

(a) (b)

(c) (d)

Figure 5.7: The Airbus loudspeaker in (a) and the (b) zoomed in and covered speakers. The Onera spark source is seen in both (c) and (d).

5.2.1. Loudspeaker source analysis

For the analysis of determining the shift of the sound source conventional beamforming is used. To understand the behaviour in the frequency domain, the spectrum level is calculated first. From this the corresponding frequency bands are determined using beamforming.

The spectrum level allows to check if the sound source emits within the given frequency band and how it might be affected if flow is applied. The flow speed used throughout the experiment is $U = 60$ m/s in the x direction, and therefore the same speed will be used for the calibration source as well. For one case the speaker is set to emit sound in octave bands at 1 and 2 kHz and the other case at 4 and 8 kHz. To obtain the spectrum level the procedure explained in Section 2.2 is used with Eq. (2.27). The PSD is obtained as an average over the 63 microphones to give the averaged behaviour for the array. For determining the levels, 50 Hz bands are used and the levels are relative to 20 µPa. The result can be seen in Fig. 5.8.

The octave band boundaries are given by the dashed vertical lines. It can be seen that for either case the emitted sound from the loudspeaker is around the given octave band. With the flow on, a general increase in broadband noise can be observed for all the frequencies. Especially at low frequencies, 500 Hz and lower,

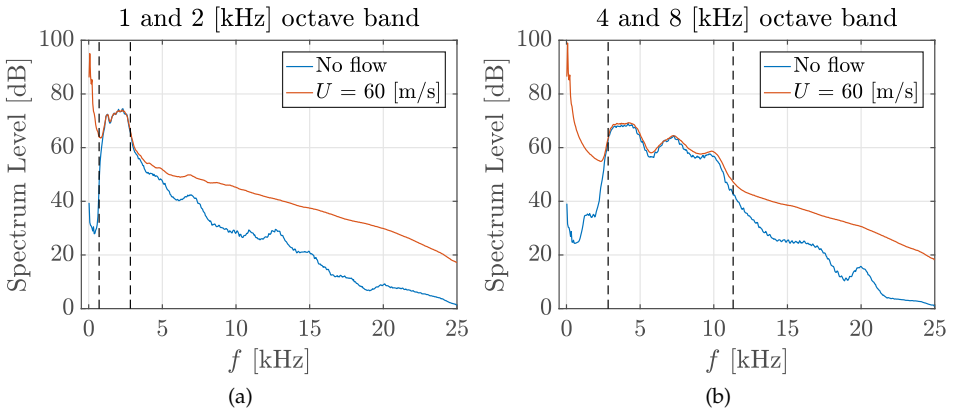

Figure 5.8: The spectrum levels of the Airbus Loudspeaker source for, (a) 1-, 2-kHz octave band and (b) 4-, 8-kHz octave band. The blue line indicates no flow and red line flow with a speed of 60 m/s

there is a significant increase of noise. Within the octave bands, where sound is supposed to be emitted, the sound is still clearly distinguishable. This is observed by the overlap of the red and blue line within the octave bands.

Confirming that indeed within the given frequency band the received signals stem from the acoustic sources, beamforming for this band can be applied to obtain the source position. Two scan planes are selected to observe the source position without flow and the shift with flow. The scan planes selected are the xz and the xy plane at $y = -1.0$ m and $z = 0$ respectively. According to wind tunnel operators, the source is expected to lie in these planes. The selected planes can be seen in Fig. 5.9.

The resulting beamforming plots are shown in Fig. 5.10 for the lower octave bands. The frequency range is between 707 and 2828 Hz. The higher octave bands are shown in Fig. 5.11 with the frequency range of 2828 Hz to 11.3 kHz. The figures both show the xz (left) and xy (right) planes and the result with the flow on (bottom row). The black cross indicates the position of the source according to the operators. The maximum found by beamforming is emphasized by the intersection of a dashed horizontal and vertical line.

From Fig. 5.10 (a) it can be seen that in the xz plane there is a clear shift in the z direction between the expected position and the maximum found by beamforming. This is still without flow, which means that any offset is unexpected. The position found is 41 cm lower than expected. The x coordinate is around zero and in accordance. In Fig. 5.10 (b), for the xy plane, a shift can also be seen in the y direction. The offset in y is 25 cm towards the wall, i.e. $-1 \rightarrow -0.74$ m. This can explain the offset in z seen in Fig. 5.10 (a). If the slice of xz is a mismatch in y, and in this case taken closer to the array at $y = -1$ m, the source will appear lower than expected due to the angle the array has.

With the flow on a clear shift can be seen in the flow direction in Fig. 5.10 (c) and (d). The offsets noted previously are approximately the same, indicating a constant

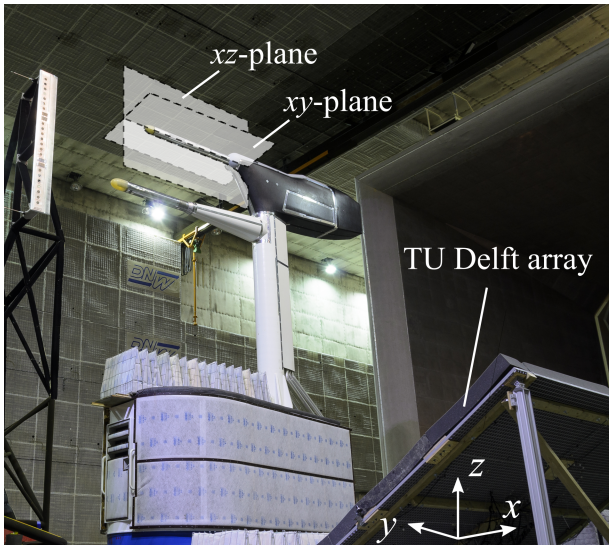

Figure 5.9: The planes selected for beamforming together with microphone array which is seen to be tilted.

behaviour in that respect and an incorrect measurement of the y coordinate only. The shift due to the wind is seen to be 0.64 m in (c) and 0.66 m in (d) in the positive x direction.

For the higher frequency octave bands similar beamforming analyses are made. Again, it will be checked what the corresponding offsets are. Figure 5.11 (a) and (b) show similar behaviour as Figure 5.10 (a) and (b) confirming that the position given for the loudspeaker is incorrect. The shift is slightly lower at 37 cm below the expected position in z and an offset of 23 cm towards the wall. These can be considered approximately the same as the lower octave bands.

The shift in x due to the flow can be seen in Figure 5.11 (c) and (d). The source seems to be spread out more over the given scan plane due to the wind. This can be caused by the spectral broadening of the sound by the wind tunnel shear layer[14] and becomes more prominent for higher frequencies.

The shift in x is seen to be 0.60 m in (c) and 0.63 m in (d) close to the values of the lower frequency bands. Together with the shift of the lower frequency octave band this leads to an average of $x_{\text{shift}} = 0.63$ m. The sparker source will be used to see if the shift is roughly the same. It will also provide an additional check to see if the unexpected shift in y still occurs and if it influences the shift in x due the flow.

5.2.2. Sparker source analysis

Next the sparker source is investigated. The source generates a spark every tenth of a second. The window for determining PSD is therefore set to 0.1 s. As the spark emits a pulse-like signal, it is expected that the source's frequency content will be very broad and relatively flat. Similar steps as for the loudspeaker are used to

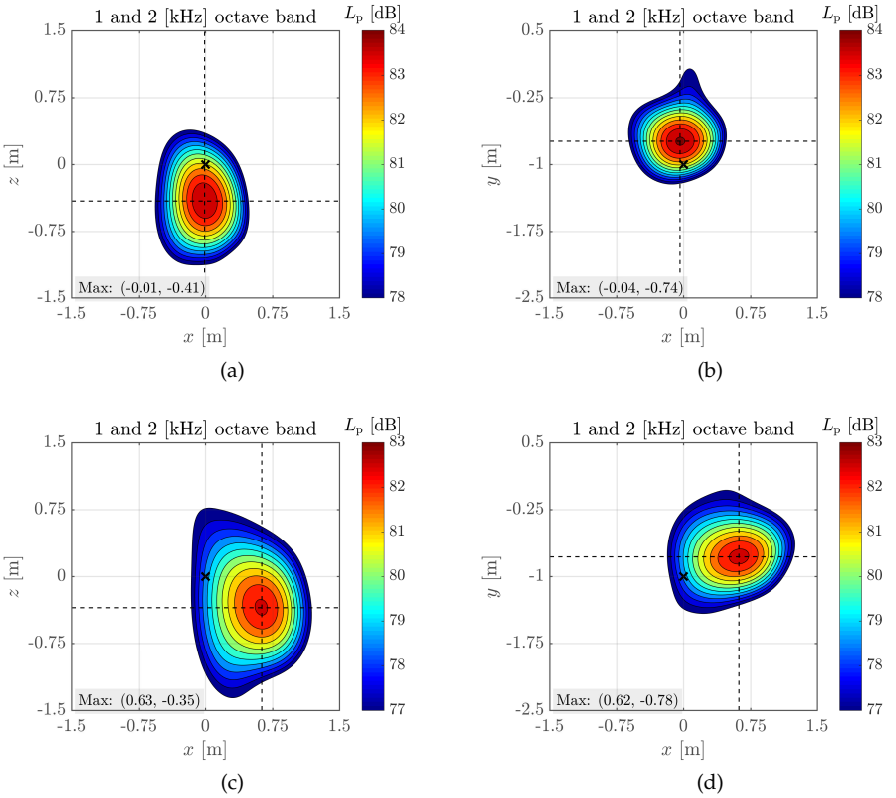

Figure 5.10: Beamforming for the loudspeaker over 1 and 2 kHz octave band, (a) xz-plane at $y = -1.0$ m no flow, (b) xy-plane at $z = 0$ m no flow, (c) and (d) have the addition of flow with $U = 60$ m/s.

calculate the spectrum level at the array. The spectrum level of the sparker source can be seen in Fig. 5.12.

In this figure three lines can be seen. The blue line presents the sparker source with no flow. In comparison with the loudspeaker, the sparker source does emit sound over a large frequency range up to 25 kHz and is relatively flat. For the red line, with the flow on, the lower frequencies increases significantly and the higher frequencies follow the blue line closely. To determine the frequency for which the sparker is distinguishable, the spectrum of the wind only in green is given as well. The green line overlaps the red line until the frequency of 1.5 kHz indicated by the dashed vertical line. Therefore, this frequency will be the lower frequency to beamform for. The upper frequency limit will be set to 10 kHz as this is the boundary of the frequency of interest for later experiments and still below the the cut-off frequency of the hardware. The results for beamforming are seen in Fig. 5.13.

From Fig. 5.13 (a) and (b), without the flow, an offset can be seen of 17 cm in

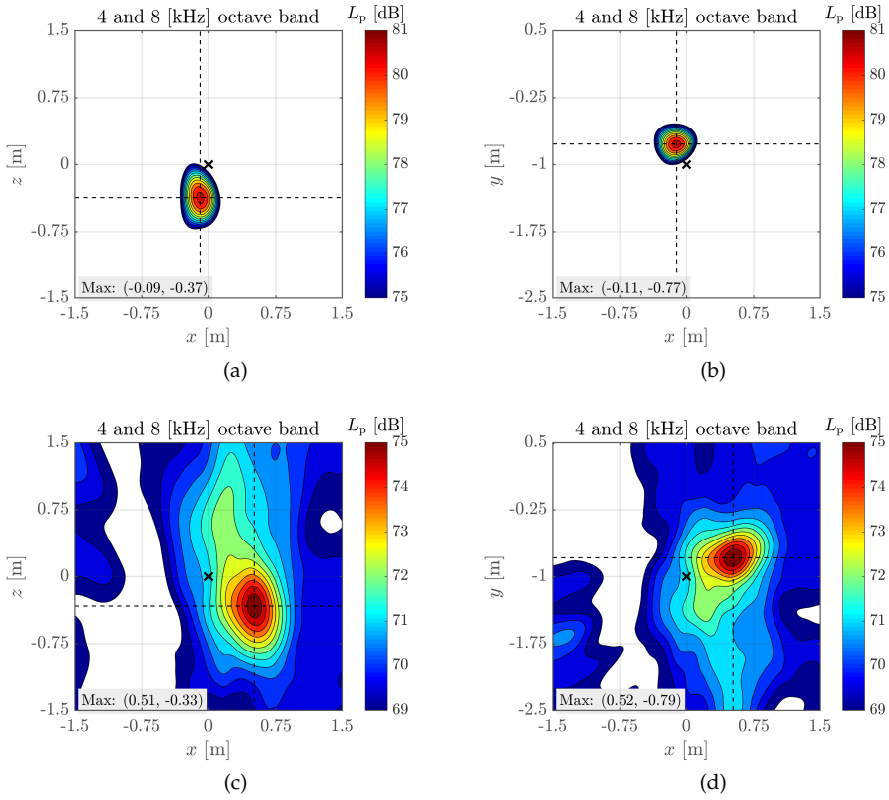

Figure 5.11: Beamforming for the loudspeaker over 4 and 8 kHz octave band, (a) xz-plane at $y = -1.0$ m no flow, (b) xy-plane at $z = 0$ m no flow, (c) and (d) have the addition of flow with $U = 60$ m/s.

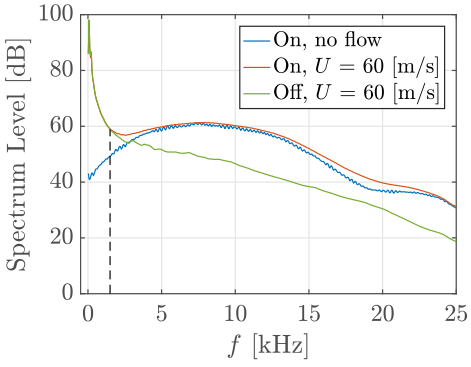

Figure 5.12: The spectrum levels of the Onera sparker source. The blue line indicates the source with no flow, red line with flow and green line flow but the sparker off. The speed of the wind is 60 m/s

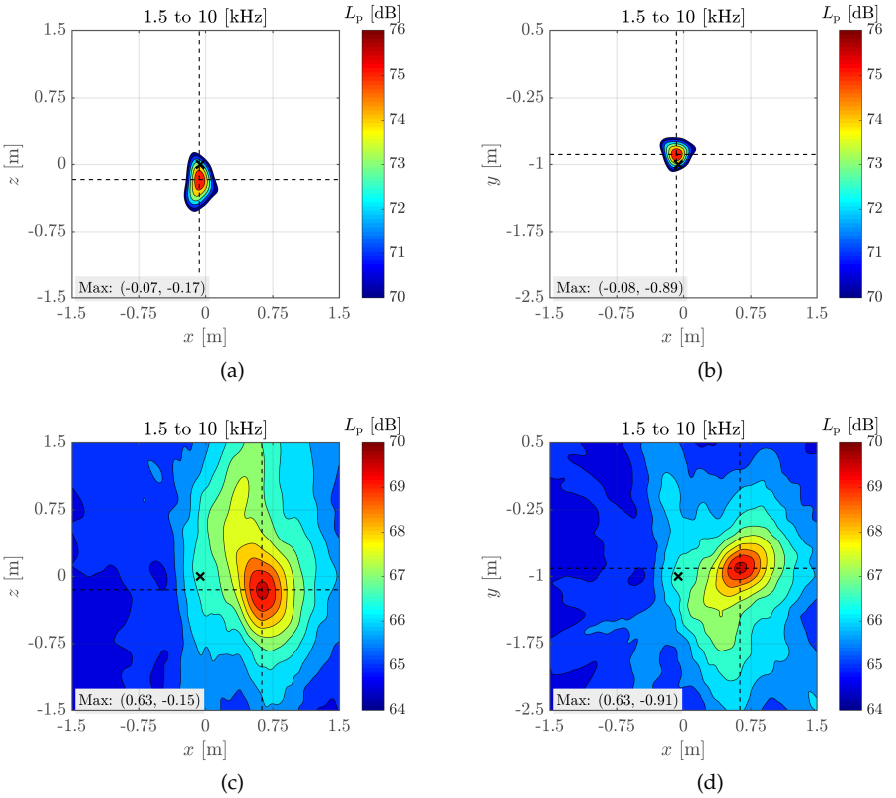

Figure 5.13: Beamforming for the Onera sparker source from 1.5 to 10 kHz, (a) xz-plane at $y = -1.0$ m no flow, (b) xy-plane at $z = 0$ m no flow, (c) and (d) have the addition of flow with $U = 60$ m/s.

z and 11 cm in y. Both offsets are similar to the loudspeaker source in the sense that the maximum of the beamform map is positioned lower in z and higher in y. However, the source is localized now much closer to the expected position, indicating no error in the position of the source. The offset in z could be attributed to the sound primarily coming from one end of the output terminal only, see Fig. 5.7 (d). Additionally, during discharge the path the electric takes is not necessarily straight and can cause additional small shifts.

From Fig. 5.13 (c) and (d) shows the shift in the x direction of the source with the flow on. The shift is seen to be 0.70 m in (c) and 0.71 m in (d). This shift is larger than the one found with the loudspeaker by 7 cm.

The shift used for the later experiments will be $x_{\text{shift}} = 0.705$ m for $U = 60$ m/s. The sparker source looks to be positioned more closely in the plane of $y = -1$ m which is of most interest for later experiments.

5.3. Pylon propeller experiment

The main topic for APIAN-INF analysis is to examine the effect of pylon blowing on the noise of the propeller. The focus in this section is on the localization of the noise sources. Furthermore, it will be investigated if the high resolution method, adaptive HR-CLEAN-SC, can improve beamform maps and recover noise sources not seen otherwise using conventional beamforming. As an intermediate step, results obtained from CLEAN-SC will be presented as well.

Three experiments are considered with incoming flow at 60 m/s:

- Isolated propeller at $J = 1.40$,
- Installed pylon with propeller at $J = 1.40$,
- Installed pylon with $\dot{m} = 60$ g/s and propeller at $J = 1.40$,

where J is the advance ratio of the propeller and $\dot{m}$ the mass flow rate when the pylon's trailing edge is blowing.

5.3.1. Spectrum levels

First the spectrum levels are calculated for the three experiments. The PSD is again obtained as the average over the microphones. The bands chosen this time are 5 Hz to put emphasis on the levels of the expected propeller tones. The result for all three experiments can be seen in Fig. 5.14. The frequency range was selected to be 10 kHz, as most interesting noise components are well within this range. This is confirmed in Fig. 5.14 as well.

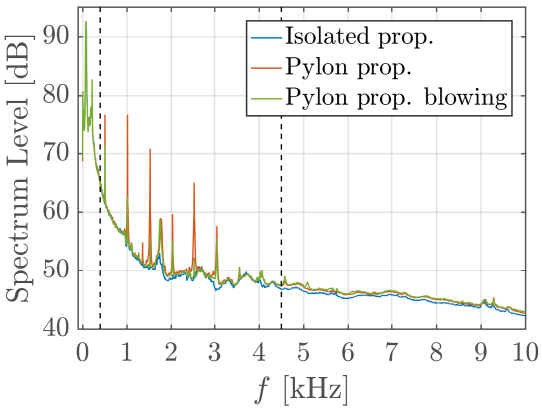

Figure 5.14: The spectrum levels in 5 Hz bands of the propeller in blue, together with the installed pylon in red and blowing enabled in green. The speed of the wind is 60 m/s

The blade passage frequency (BPF) is at 508 Hz and several harmonics can be seen as well depending on the configuration. A broad peak can be observed, which is not a multiple of the BPF, between 1.5 and 2 kHz. The configurations are seen to

overlap, making the difference hard to see. The vertical black dashed lines presents the region which has the most interesting behaviour and excludes the significant low frequency wind tunnel noise and the higher frequencies where only small differences can be seen. Therefore, to see the differences more clearly and quantify how much levels change between configurations, the spectrum level for each configuration separately is given in Fig. 5.15 between 500 Hz and 4.5 kHz.

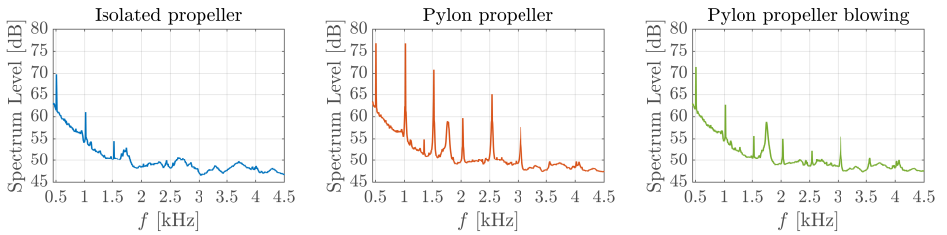

(a) (b) (c)

Figure 5.15: The spectrum levels of each configuration separately from Fig. 5.14 within the range of 500 Hz to 4.5 kHz in 5 Hz bands.

For the isolated propeller in Fig. 5.15 (a) the BPF is seen at 508 Hz and the 2nd and 3rd harmonic at 1018 Hz and 1528 Hz respectively. A broad noise peak, not related to the BPF, can also be seen between 1630 Hz and 1850 Hz. With the pylon installed in front of the propeller, as shown in Fig. 5.4, a clear increase can be seen in Fig. 5.15 (b) of the BPF as well as the 2nd and 3rd harmonic. Additionally, the generation of the 4th, 5th and 6th harmonic can be seen. The peculiar broadband noise observed in Fig. 5.15 (a) is present in (b) as well and amplified.

When blowing is applied through the pylon's trailing edge the result in Fig. 5.15 (c) is obtained, where most noise components introduced due to the installation of the pylon in Fig. 5.15 (b) are reduced. Some tones, such as the BPF, are close to the levels for the isolated propeller. The exception is the broadband noise peak observed between 1630 Hz and 1850 Hz with a peak around 1750 Hz. The noise in this range is of similar strength with blowing applied.

The values of the levels of the peaks in the 500 Hz to 4.5 kHz frequency range are listed in Table 5.2. The levels are given for 5 Hz frequency bands relative to 20 µPa.

From the table a large increase can be seen when the pylon is installed with values up to 16 dB. With blowing applied using a mass rate of $\dot{m} = 60$ g/s these values get significantly reduced. A small increase can still be seen compared to the isolated propeller up to 1.7 dB and the higher harmonics do not completely get masked by the wind tunnel noise like in the case for the isolated propeller. This can be verified in Fig. 5.15 (c) as the presence of small peaks starting at 2 kHz. It appears that for the broadband noise around 1750 Hz there is no effect of blowing. The peak is still around 6 dB higher compared to the isolated propeller. Using beamforming the origin of the noise sources for specific frequencies will be investigated later.

Table 5.2: The peak levels seen in Fig. 5.15 for the different configurations. With the exception of 1750 Hz the frequencies all consists of either the BPF or a multiple thereof. For the broadband noise around 1750 Hz only the peak value is taken. Within brackets is the increase relative to the isolated propeller.

f [Hz]	Isolated prop. [dB]	Pylon prop. [dB]	Pylon prop. blowing [dB]
508	69.8	76.8 (+7.0)	71.5 (+1.7)
1018	61.0	76.8 (+15.8)	62.7 (+1.7)
1528	54.5	70.8 (+16.3)	55.6 (+1.1)
1750*	53.0	59.0 (+6.0)	58.8 (+5.8)
2033	-	59.7	55.0
2543	-	65.1	52.3
3053	-	57.7	55.5

5.3.2. Conventional beamforming

To get the general behaviour of the location of the noise sources, beamforming was first applied to a broad frequency range of 900 Hz to 8 kHz. The BPF, at 508 Hz, was excluded from the first analysis by intention due to the expected low resolution. Further on narrowband beamforming analysis will be presented including the BPF clarifying this decision.

The scan plane was selected at $y = -1$ m according to Fig. 5.4 and the resolution for the grid spacing was set to 1 cm. The scan plane limits were $(x_{\min}, x_{\max}) = (-1.5, 1.5)$ and $(z_{\min}, z_{\max}) = (-2, 0.5)$ to encompass both the experimental setup and supporting structure. The duration of the recording for the microphone signals was 32 s. Time blocks of 25 ms were used with 50% overlap to obtain the cross spectral matrix (CSM) from 2559 estimates. This resulted in a frequency resolution of 40 Hz. The CSM is used for the beamforming process. After obtaining the map, the sources are shifted by 0.705 m in the x direction *towards* the flow to account for both convection and refraction of the sound. The shift was found in the previous section using the sparker source.

The result of conventional beamforming for the isolated propeller, pylon propeller and pylon propeller including blowing can be seen in Fig. 5.16. The values are given as absolute sound pressure levels with a dynamic range of 6 dB. An overlay was included in the beamform maps to indicate the position of the propeller, support and pylon. The two crosses indicate the propeller plane.

For the isolated propeller in Fig. 5.16 (a) two main source distributions can be seen around the propeller and on part of the support to the right. Both source distributions are around 69 dB in strength measured *at* the array. The source distribution at the propeller is expected, while the source around the support is preferably absent or relatively low compared to propeller. It can therefore be concluded that for the isolated propeller the noise coming off the support is of the same order as the propeller and can influence the measurements in the given frequency range of 900 Hz to 8 kHz. This region of the support consisted of a pipe for the air retour line and two horizontal stings holding and allowing for a sideslip angle. A simpler support of only one horizontal sting might avoid this issue.

With the pylon installed, the result of Fig. 5.16 (b) is obtained. As expected

from Fig. 5.15, a clear increase of noise can be seen (from 69 dB to 78 dB). Within the dynamic range of 6 dB all the sources are located in between the propeller and the pylon's trailing edge. Sources only at the lower half of the propeller diameter are found. This is expected as the lower part of the propeller rotates towards the microphone array.

In Fig. 5.16 (c) beamforming can be seen with pylon blowing from the upper part of the trailing edge. Also the same behaviour can be seen from Fig. 5.15, where the levels are close to the isolated propeller case at 70 dB in the region between the propeller and the trailing edge. Similar to Fig. 5.16 (a) a source distribution appears at the same position of the support. For this case there is a difference in strength between the two source distribution. The level around the support is seen to be 1 dB lower and the same level as Fig. 5.16 (a) but less distributed.

As noticed from Fig. 5.16 the resolution of the beamform images is relatively low as expected from Table 5.1. The next subsection will use the deconvolution technique CLEAN-SC and the high resolution version HR-CLEAN-SC to see if improvements can be made and (additional) sources can be distinguished.

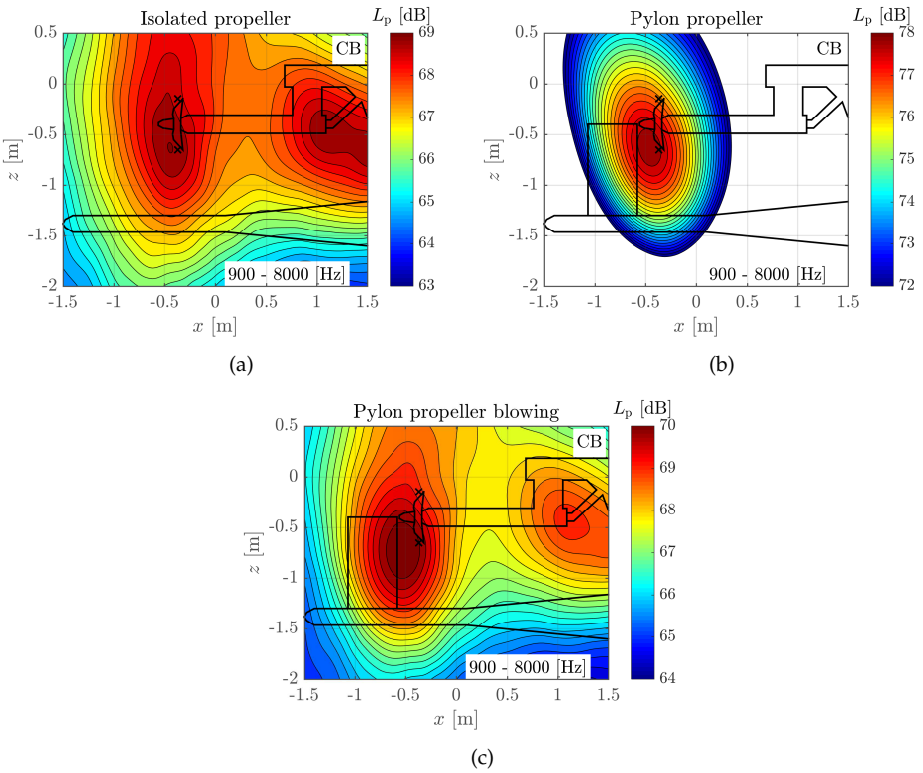

Figure 5.16: Conventional beamforming (CB) for the three configurations (a) isolated propeller, (b) pylon propeller and (c) pylon propeller with blowing. The configuration and support can be seen to be outlined. The crosses indicate the two ends of the propeller plane.

5.3.3. High resolution methods: CLEAN-SC and HR-CLEAN-SC

The beamforming analysis of the previous subsection is continued for the same frequency range using CLEAN-SC and HR-CLEAN-SC. The dynamic range is increased to 12 dB as sources are expected to be less spread by the deconvolution process and, as a consequence, allow for the detection of more sources. The result of beamforming is seen in Fig. 5.17. With the left column presenting CLEAN-SC and right HR-CLEAN-SC.

For the isolated propeller in Fig. 5.17 (a) it can be seen that for CLEAN-SC the result has become clearer where, as expected from Fig. 5.16 (a), sources are distributed in front of the propeller. For the noise sources originating from the support two main contributions can be seen. One is from the section at $x = 1.0$ m where the tube connects to the horizontal sting holding the propeller. The second disturbance can be seen around $x = 1.5$ m and is partially outside the scan plane boundaries, corresponding to the lamp post holding both stings for the propeller and pylon. The sources are also seen to be of lower strength indicated by the colour bar (which always has a range of 6 dB relative to the maximum found in beamforming). This can be explained by the deconvolution process in CLEAN-SC exposing sources, which are seemingly singular in Fig. 5.16 (a) to consist of multiple sources. Note that in general two sources of the same strength result in an increase of 3 dB for incoherent and 6 dB for coherent sources.

In Fig. 5.17 (b) the result for adaptive HR-CLEAN-SC can be seen for the isolated propeller. The map differs from Fig. 5.17 (a) where the sources originating from the support are more tightly localized. For the propeller, the source distribution is shifted mostly upwards away from the propeller plane, whereas with CLEAN-SC it was distributed in the lower half of the propeller. Apparently, the sources are shifted too much during the minimization procedure of the HR-CLEAN-SC algorithm. In the next section it will checked if the same behaviour can be seen for the peaks of the spectrum. For both methods it can again be concluded that for the isolated propeller the support downstream has a significant contribution to the noise levels.

For the installed pylon seen in Fig. 5.17 (c) and (d) it can be seen that the noise sources are localized closely to the propeller and no disturbance from other positions can be seen within the 12 dB range. For CLEAN-SC two sources of unequal strength can be seen in the lower half of the propeller plane. For the HR-CLEAN-SC procedure this would be an ideal test case as similar tests has been done by Sijtsma *et al.* [15] and proven to be successful. In Fig. 5.17 (d) the result can be seen where multiple sources have been found. Two sources can be seen around the propeller tip and two stronger sources at the spinner. This indicates sources from Fig. 5.17 (c) being split up and translated to the hub where interference from other sources is lowest. While noise can originate from the rotor, it is expected that most noise will come off the propeller blades. For Fig. 5.17 (d) the maximum strength is decreased from Fig. 5.17 (c). The same reasoning can be applied as going from conventional beamforming to CLEAN-SC. As explained in Section 2.4.5, HR-CLEAN-SC assumes the sources found in CLEAN-SC to possibly interfere with each other and by moving the sources around the interference can be minimized. This is ef-

fective when sources are closely spaced together increasing the resolution beyond the Rayleigh criterion, which also separate sources and decrease their strengths.

Figure 5.17 (e) and (f) shows the pylon blowing to eliminate the interaction noise of the wake with the propeller. Similar to the conventional beamforming result, the noise is reduced and sources can again be seen at the support. For Fig. 5.17 (e) several sources can again be seen in front of the lower half of the propeller similar to Fig. 5.17 (a). An additional noise disturbance is revealed at the lower-right region of the pylon. This can be attributed to the blowing mechanism, as air is pushed through a small corridor matching this source position. For adaptive HR-CLEAN-SC in Fig. 5.17 (f) similar behaviour is seen as Fig. 5.17 (b), where the sources are distributed too far off, up from the propeller plane. The sources around the support also move by a small amount while the source on the pylon stays at the same position.

The next subsections will perform narrowband beamforming to select the most interesting frequencies (peaks) found in Fig. 5.15 and see how it contributes to total map.

5.3.4. Narrowband analysis: isolated propeller

This section will go in more detail using narrowband data to beamform. Only the BPF and the multiples will be considered according to Table 5.2 with the exception of the broadband peak which will be treated in a later subsection. Bands of 50 Hz are used centered around the given peak. To increase resolution in frequency, time blocks of 100 ms are used to construct the CSM. The duration of the recording was again 32 s resulting in fewer blocks of 639 when using an overlap of 50%.

The result of conventional beamforming is seen in Fig. 5.18, including beamforming at the BPF for 508 Hz in Fig. 5.18 (a). The latter corresponds to the highest peak found in Fig. 5.15 (a) and would contribute the most if included for broadband beamforming in the previous subsection. From Fig. 5.18 (a) it can be seen that the source is localized far off from the propeller, but along the propeller plane. Explanation why this may happen were given in Section 5.1.2 and because the resolution is very low, small errors can results in big shifts. Additionally, the propeller radiates the BPF sound best around the Mach radius[16] which lies along propeller plane. This position is also where beamforming would place the sources and is confirmed as well in Fig. 5.18 (a).

For Fig. 5.18 (b) and (c) it can be seen that the peaks around the given frequency would contribute the most for having noise originating from the support. The higher peaks in Fig. 5.18 (d), (e) and (f) show the source primarily coming from the propeller, but still considerable source strengths are seen on the support with 1 to 3 dB below the maximum found on the propeller. It can therefore be concluded that for the isolated propeller, the tones highly interact with the support resulting in a beamform map seen in Fig. 5.16 (a).

The deconvolved maps in Fig. 5.19 confirm the findings of Fig. 5.18, where the sources are found at positions expected from Fig. 5.18. For the noise coming off the support several sources can be seen confirming that for the narrowband the source is distributed in the region around the tube connecting to the sting. When

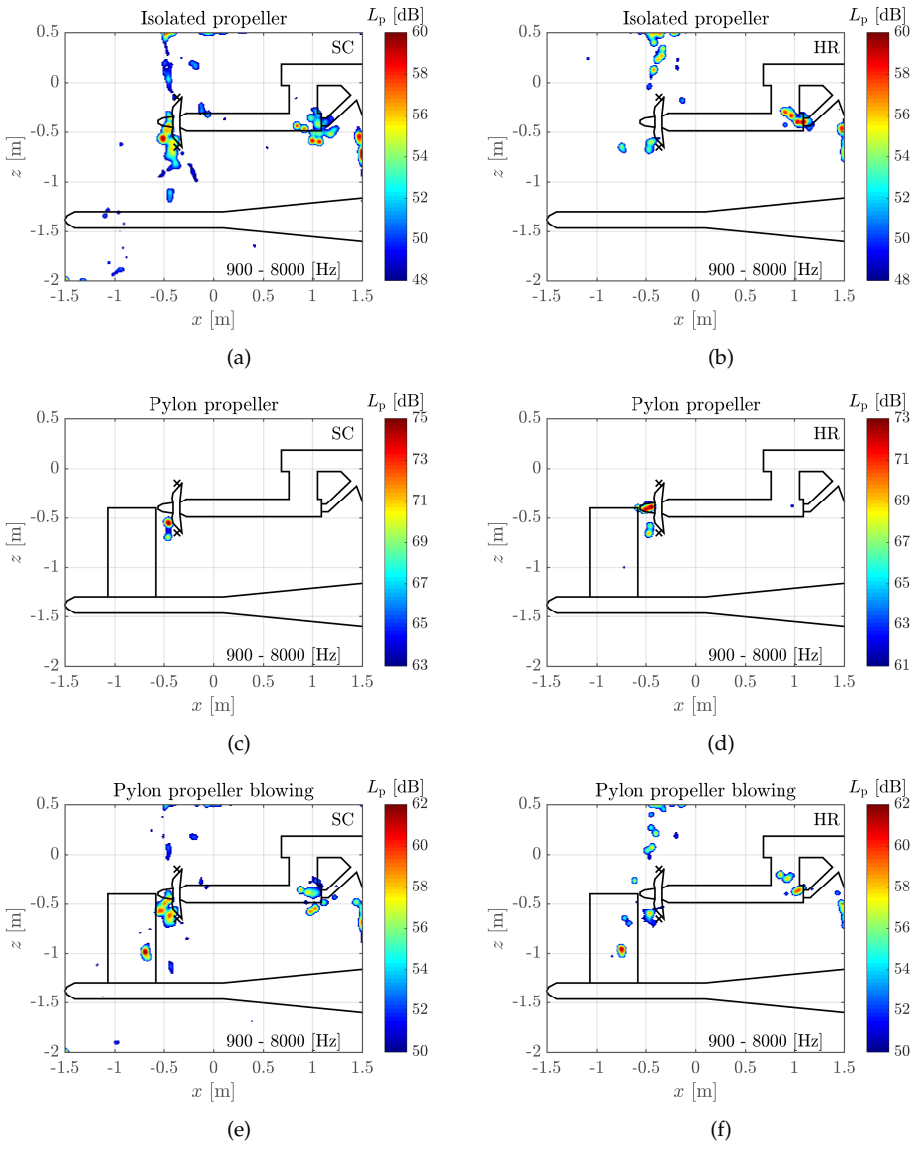

Figure 5.17: CLEAN-SC beamforming (SC) for (a), (c) and (e). Adaptive HR-CLEAN-SC (HR) for (b), (d) and (f). The three configurations isolated propeller, pylon propeller and pylon propeller with blowing can be seen arranged in the rows.

the source is originating from the propeller, the location is also seen to be focused on the lower propeller tip. With CLEAN-SC the difference in levels in Fig. 5.19 (c)-(f) between the sources coming off the support and the propeller is seen to be larger than in Fig. 5.18 (c)-(f). This is caused by the interaction noise on the support indirectly caused by the propeller and is coherent with sources originating

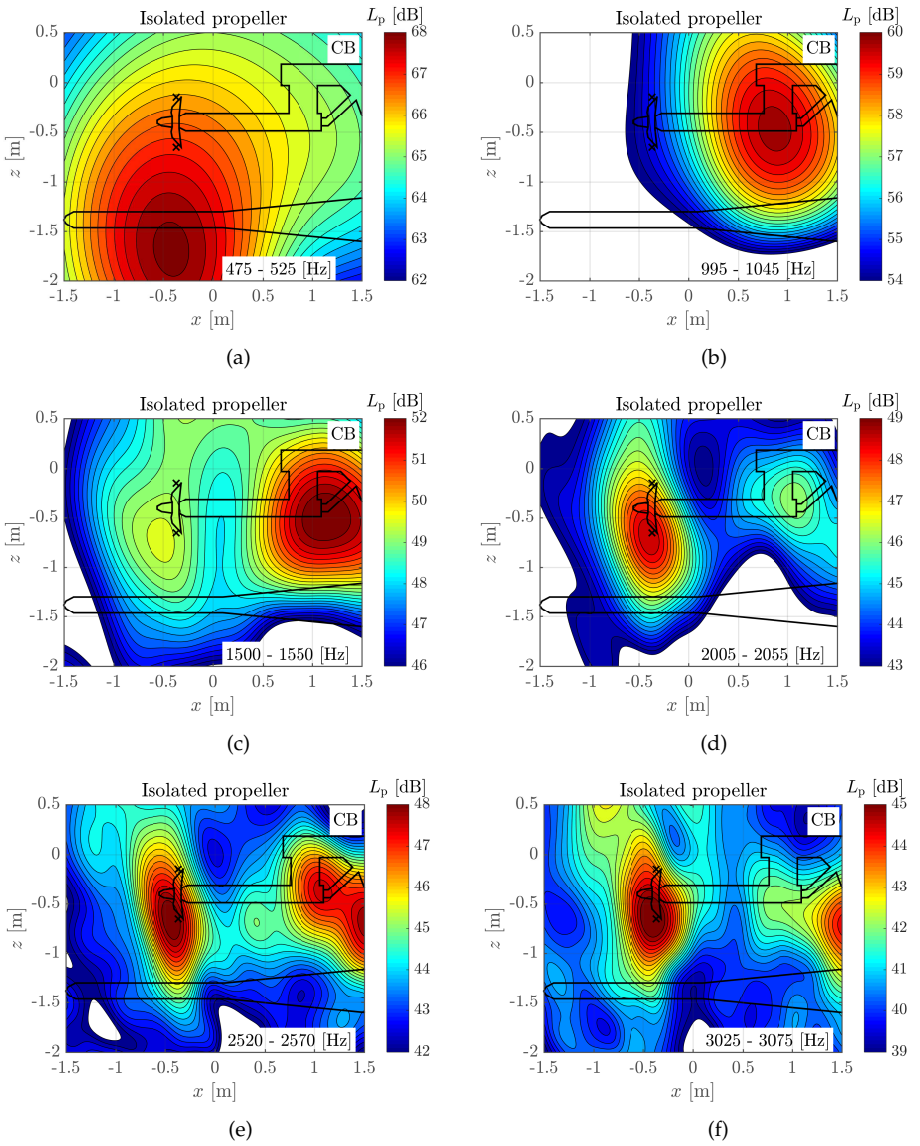

Figure 5.18: Narrowband conventional beamforming (CB) for the isolated propeller with frequencies listed in the subfigures.

directly from the propeller. CLEAN-SC is an iterative procedure, where for each peak found, coherent sources with the found are reduced or removed. If the highest peak is first found on the support then any secondary peak being coherent will be reduced, in this case the one directly from the propeller.

Using adaptive HR-CLEAN-SC in Fig. 5.20 results in slightly shifted source compared to Fig. 5.19. The source from the BPF is closer to the propeller and corre-

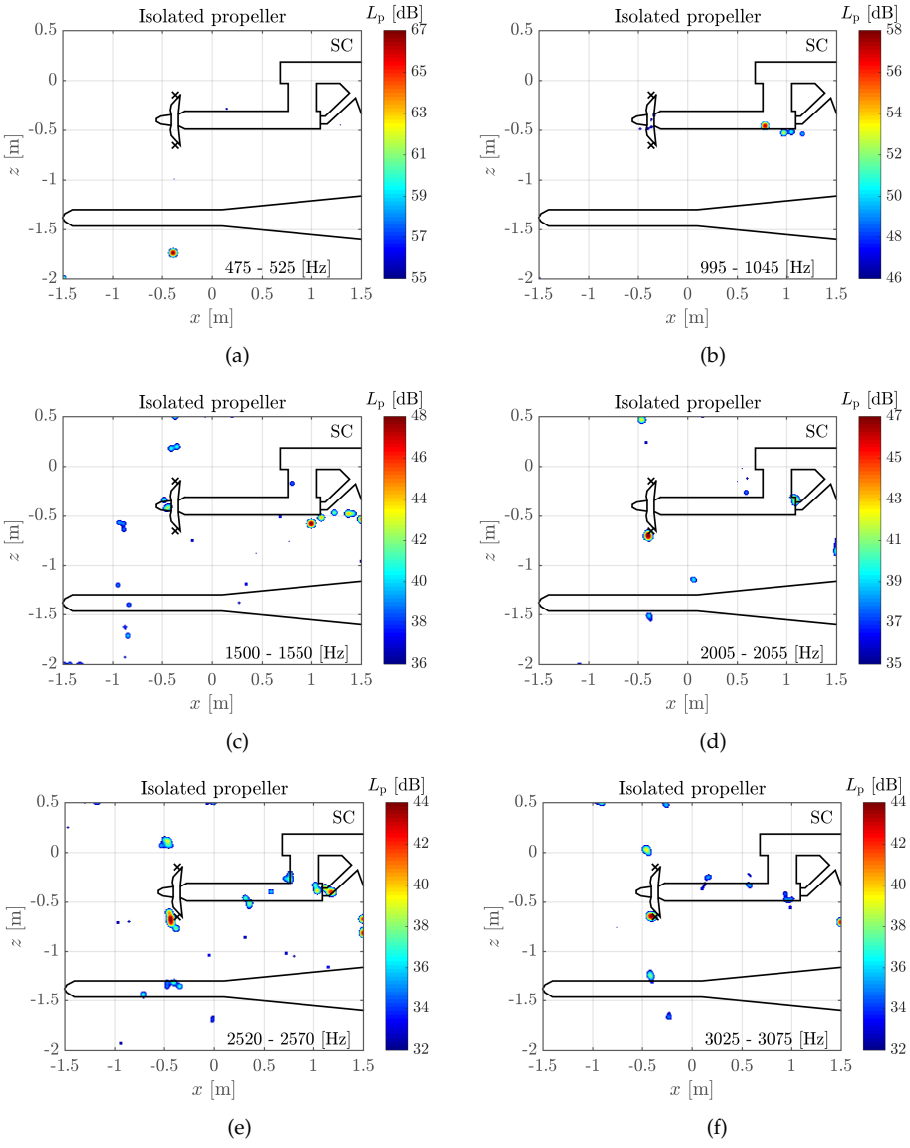

Figure 5.19: Narrowband CLEAN-SC beamforming (SC) for the isolated propeller with frequencies listed in the subfigures.

sponding Mach radius. In Fig. 5.20 (c) the source on the propeller is not visible in the 12 dB range, where according to Fig. 5.18 (c) a source is to be expected. More investigation is needed to explain this behaviour as to why the algorithm moves the source so far away. A possibility is that the method does not handle the movement of sources well if the source in consideration is the 4th or higher number of source found in regards to strength. For the other maps, the source is at the propeller tip

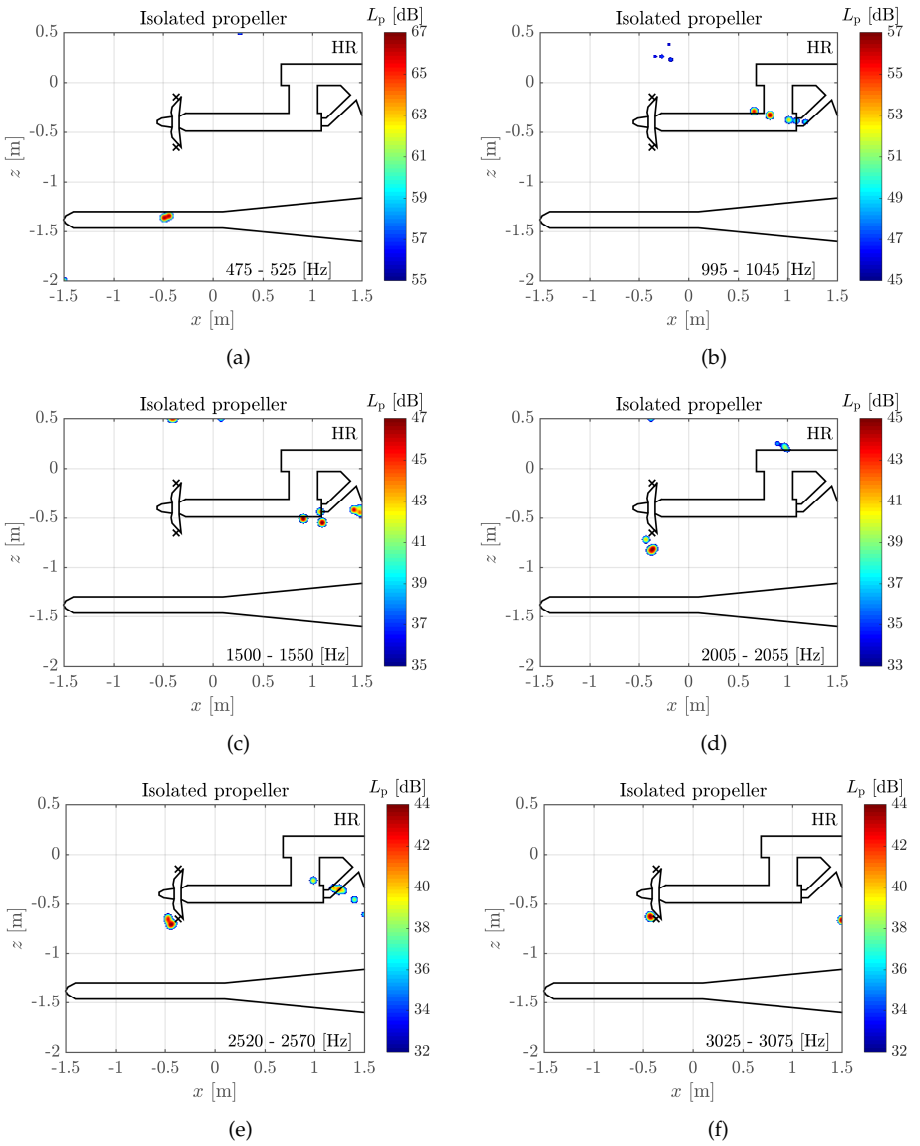

Figure 5.20: Narrowband adaptive HR-CLEAN-SC beamforming (HR) for the isolated propeller with frequencies listed in the subfigures.

as expected.

5.3.5. Narrowband analysis: pylon propeller

For the installed pylon without blowing, conventional beamforming places the source for all frequencies in the lower front of the propeller and behind the pylon trailing edge. The exception is Fig. 5.21 for the BPF where the source is positioned

downstream behind the propeller. It is not clear why the BPF source would be moved downstream when a pylon is installed.

For the harmonics of the BPF there is a strong amplification observed from Fig. 5.15 caused by installing the pylon. This results in Fig. 5.21 having the source location well defined in front of the propeller without any other disturbances within 12 dB from the maximum. With CLEAN-SC in Fig. 5.22 similar results can be seen, where for Fig. 5.22 (d)-(f) it reveals the sources to be slightly distributed in the x direction between the pylon trailing edge and the propeller tip.

For adaptive HR-CLEAN-SC in Fig. 5.23 the source for the BPF is moved in positive z direction. Sources from the propeller are expected to be in the region of the propeller rotating towards the microphone array, which means that HR-CLEAN-SC possibly incorrectly moved the source. Because it is not exactly known how the pylon interacts with the propeller this cannot be said with certainty. From Fig. 5.23 (b) the harmonic frequency responsibly for the spinner source in Fig. 5.17 (d) can be seen. This contributes the greatest to the total map as the BPF is excluded. For the other frequencies the sources are either at the propeller tip or distributed over several sources in the region between the pylon trailing edge and the lower half of the propeller plane.

5.3.6. Narrowband analysis: pylon propeller and blowing

From Fig. 5.15 it was observed that with blowing enabled with a mass rate of 60 g/s, sound levels were back close to the levels of the isolated propeller. For the higher harmonics in Fig. 5.24 (d)-(f) the sources are located at the lower tip of the propeller. These contribute less than the lower frequencies for the overall noise and thus, with blowing, most noise is again seen to come from the support at the right side of the map. This is seen in Fig. 5.24 (b) and (c) where the noise coming directly from the propeller is of lower strength. Similar to the pylon without blowing, the BPF source is positioned downstream on the sting. This is shown more clearly in Fig. 5.25 (a). Regarding source localization no significant differences are seen for the other frequencies using CLEAN-SC compared to Fig. 5.24. Figure 5.24 (b) and (c) show sources scattered around the lower propeller tip with its strength around 8 dB lower than found on the support. This could mean that the sources on the propeller are again reduced too much due to being coherent. Using adaptive HR-CLEAN-SC only small movements of sources are seen in Fig. 5.26 (c)-(f). For Fig. 5.26 (b) the propeller is void of any source within 12 dB, while for Fig. 5.26 (a) the source is again moved up in the z direction.

5.3.7. Broadband noise investigation: the 1610 - 1900 Hz peak

This section investigates the broad peak seen between 1610 to 1900 Hz. The peak is broad and likely not directly originates from the propeller as it was not a multiple of the BPF. The broad peak had its absolute peak around 1750 Hz. Sinnige *et al.* [3] found the peak to be caused by the vortex shedding at the trailing edge due to the installation of the pylon. To investigate if the source can be located likewise, a broadband range 1610 to 1900 Hz is used to perform beamforming. The results are limited to only conventional beamforming and adaptive HR-CLEAN-SC. All

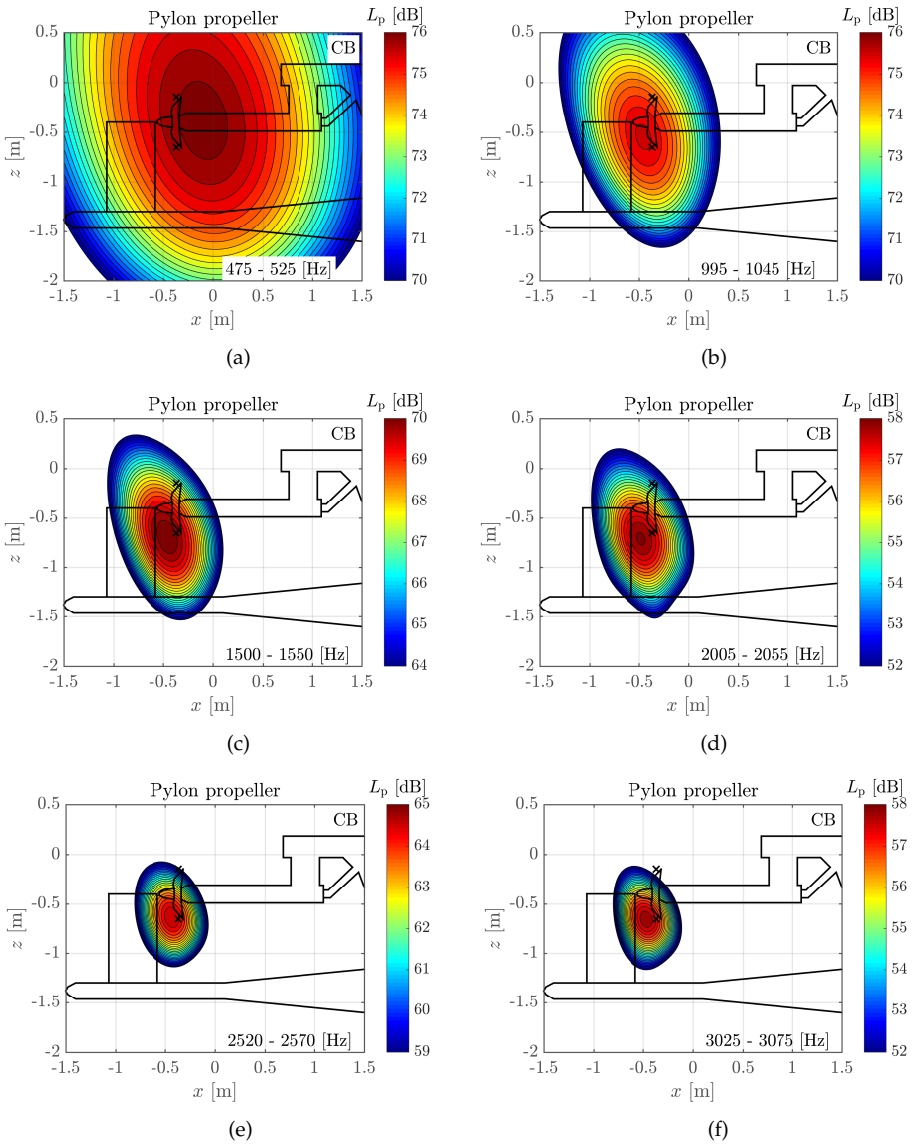

Figure 5.21: Narrowband conventional beamforming (CB) for the installed pylon and propeller with frequencies listed in the subfigures. No pylon blowing is applied.

three configurations are considered. For the isolated propeller the pylon was not installed, but broadband noise was seen for the same frequencies of lower strength in Fig. 5.15 (a). The results are shown in Fig. 5.27.

For the isolated propeller in Fig. 5.27 (a) and (b), the source is mostly located on the support in (a). A faint source in front of the lower propeller tip can be seen in (a) which is absent in (b). From Fig. 5.27 (a) and (b) it can be concluded that for the

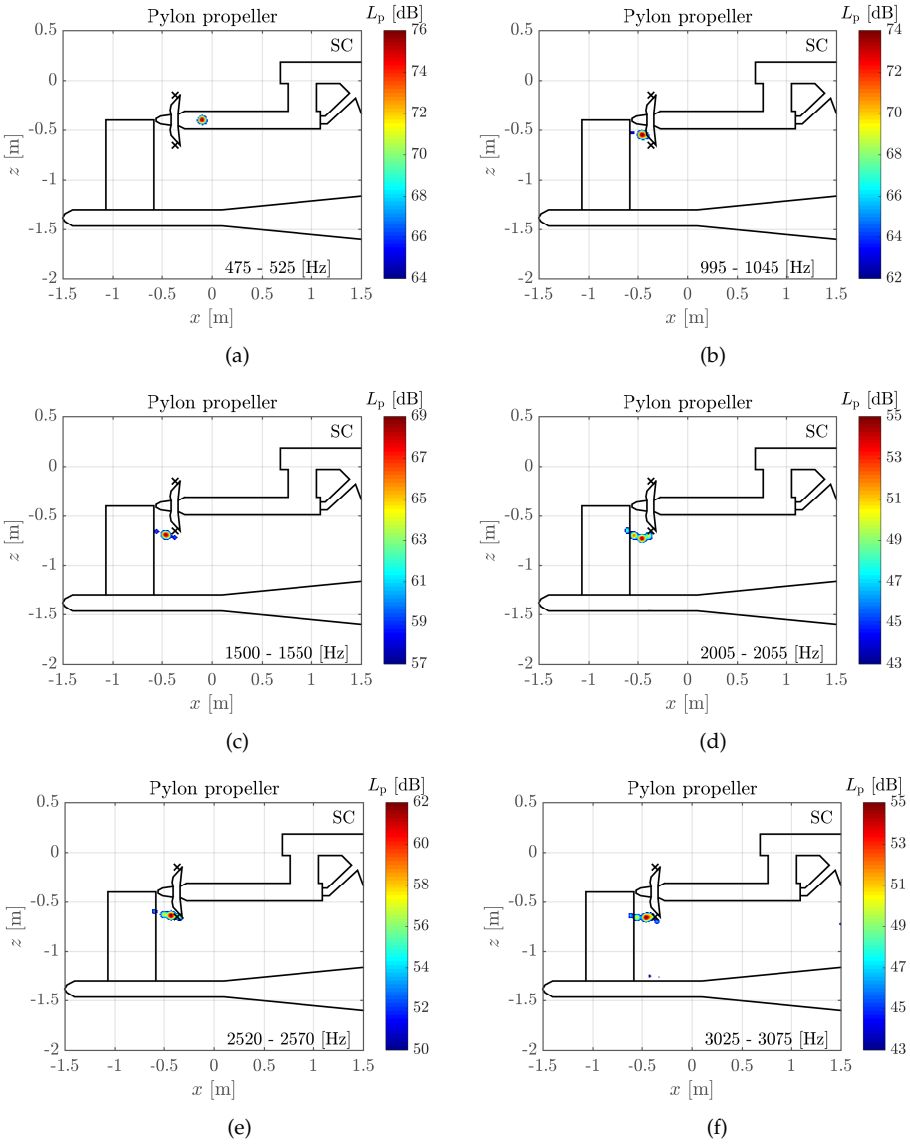

Figure 5.22: Narrowband CLEAN-SC (SC) for the installed pylon and propeller with frequencies listed in the subfigures. No pylon blowing is applied.

isolated propeller the small bump in the spectrum around 1750 Hz is broadband noise coming strongly from the support.

This source origin is still present in Fig. 5.27 (c)-(f), but now noise is originating more strongly from the lower half of the pylon. The adaptive HR-CLEAN-SC result in Fig. 5.27 (d) and (f) are indicating this source to be on the pylon and not at the trailing edge. It was already seen, and now confirmed by beamforming,

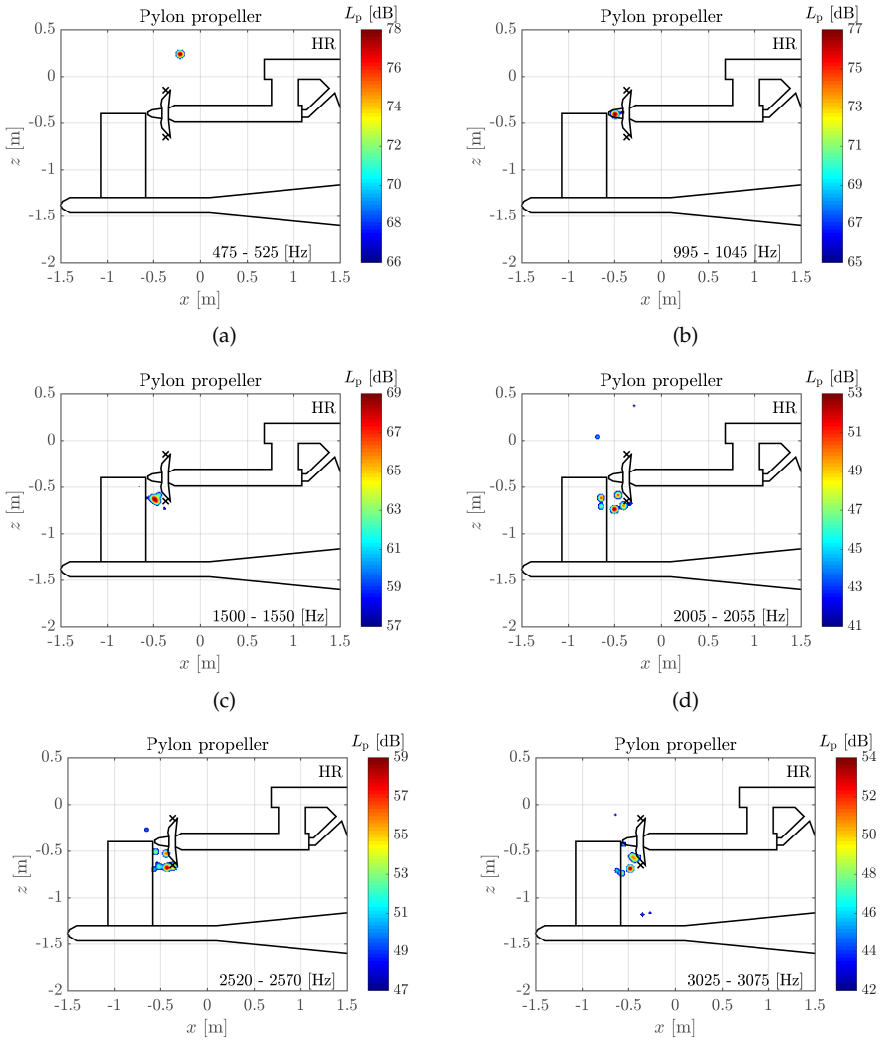

Figure 5.23: Narrowband adaptive HR-CLEAN-SC (HR) for the installed pylon and propeller with frequencies listed in the subfigures. No pylon blowing is applied.

that enabling blowing does not significantly alter the strength of the sources (only 1 dB). The source position using either conventional beamforming or adaptive HR-CLEAN-SC does not alter the position either. The position seems to indicate the channel inside the pylon where the airflow is routed. Though it must be noted that applying blowing has no effect on this source and its origin must only be due to the installation of the NACA0010 pylon.

No other sources were found besides the source on the support. Therefore, beamforming was unable to locate the source due to vortex shedding at the trail-

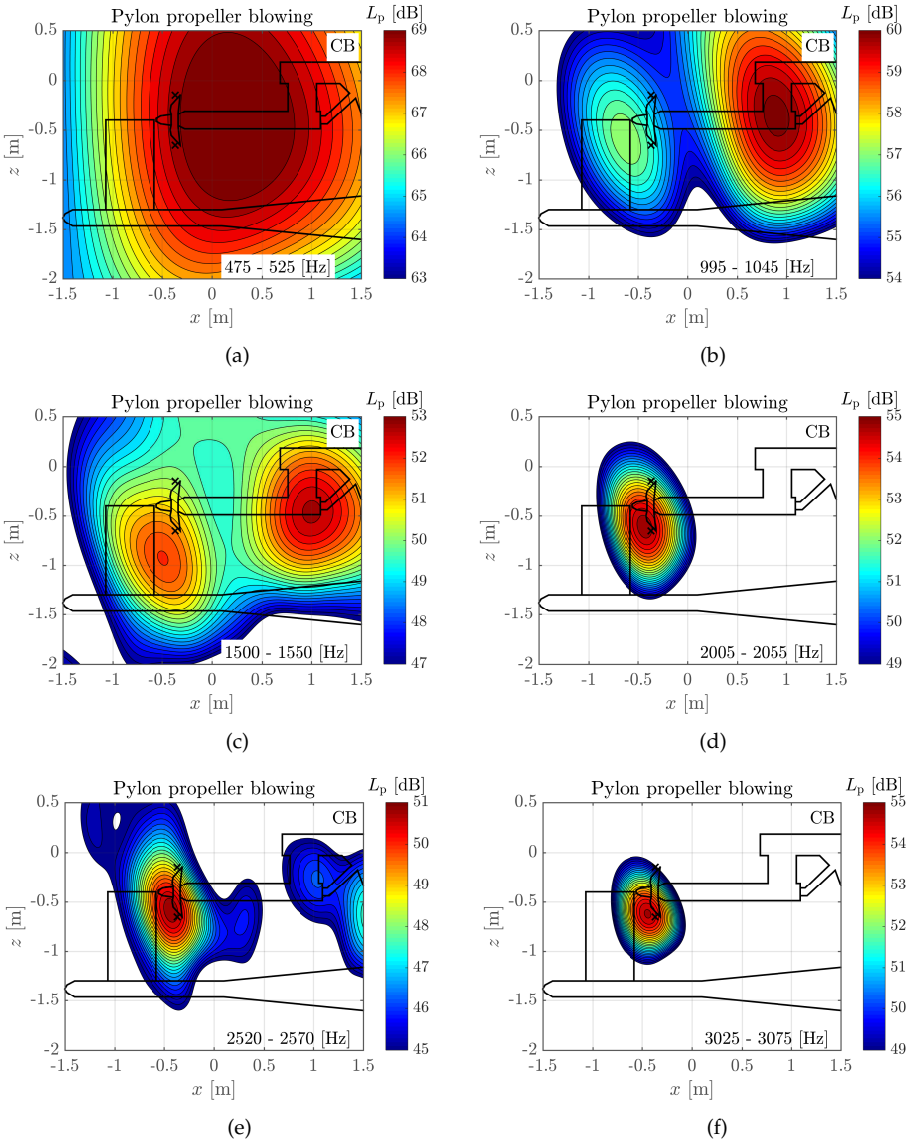

Figure 5.24: Narrowband conventional beamforming (CB) for the installed pylon and propeller with frequencies listed in the subfigures. Blowing is applied with a mass rate of 60 g/s.

ing edge. The explanation why the source for this frequency region was positioned on the pylon can also not be made with certainty. An additional shift of 10 to 14 cm down stream would put the source at the trailing edge. This would cause an additional shift *on top* of the shift found by both calibration sources. The resultant shift would then need to be applied for the propeller tones as well, which would put those sources all off-position.

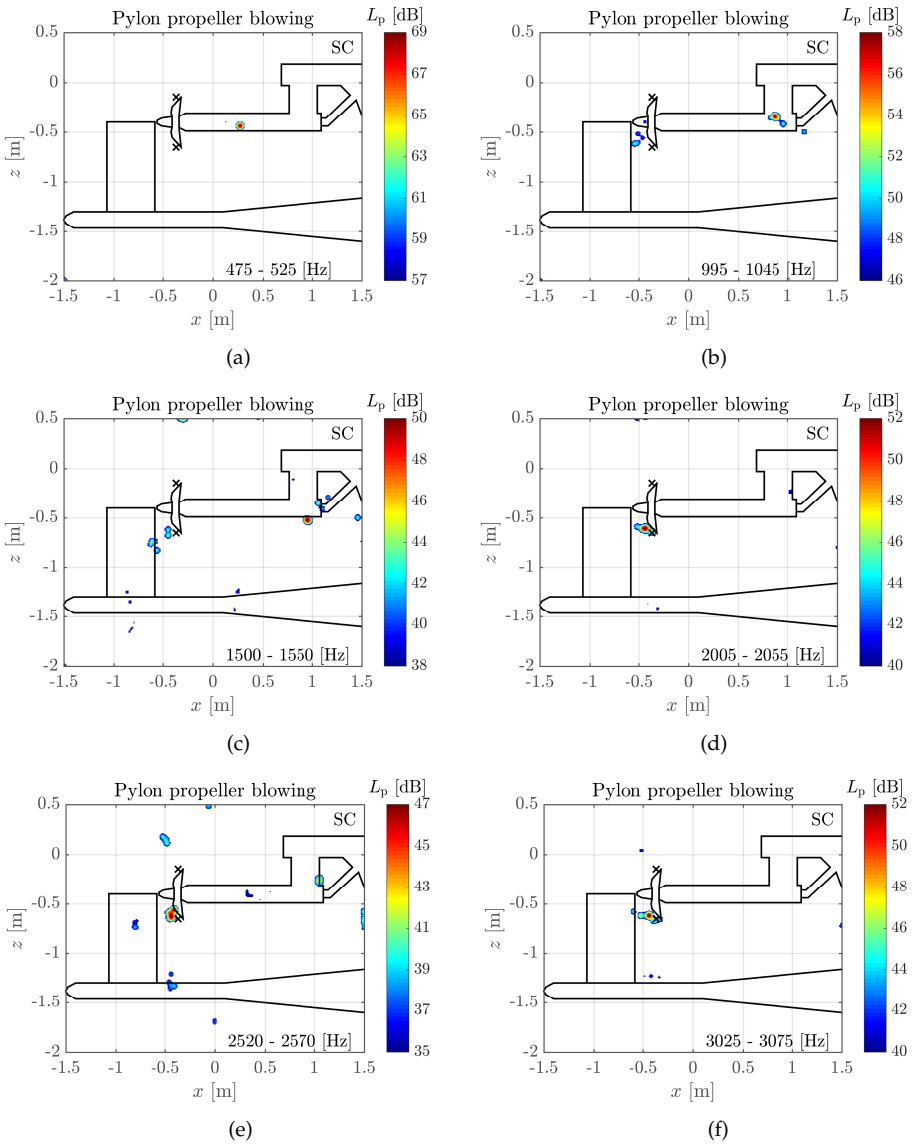

Figure 5.25: Narrowband adaptive CLEAN-SC (SC) for the installed pylon and propeller with frequencies listed in the subfigures. Blowing is applied with a mass rate of 60 g/s.

It can be argued that there were inconsistencies between the calibration sources regarding the shift. Still, only the sparker source shift (due to uncertainty of the measured loudspeaker source) was used, which was the largest of the two. The shift from the loudspeaker would result in position *further* away from the trailing edge (upstream).

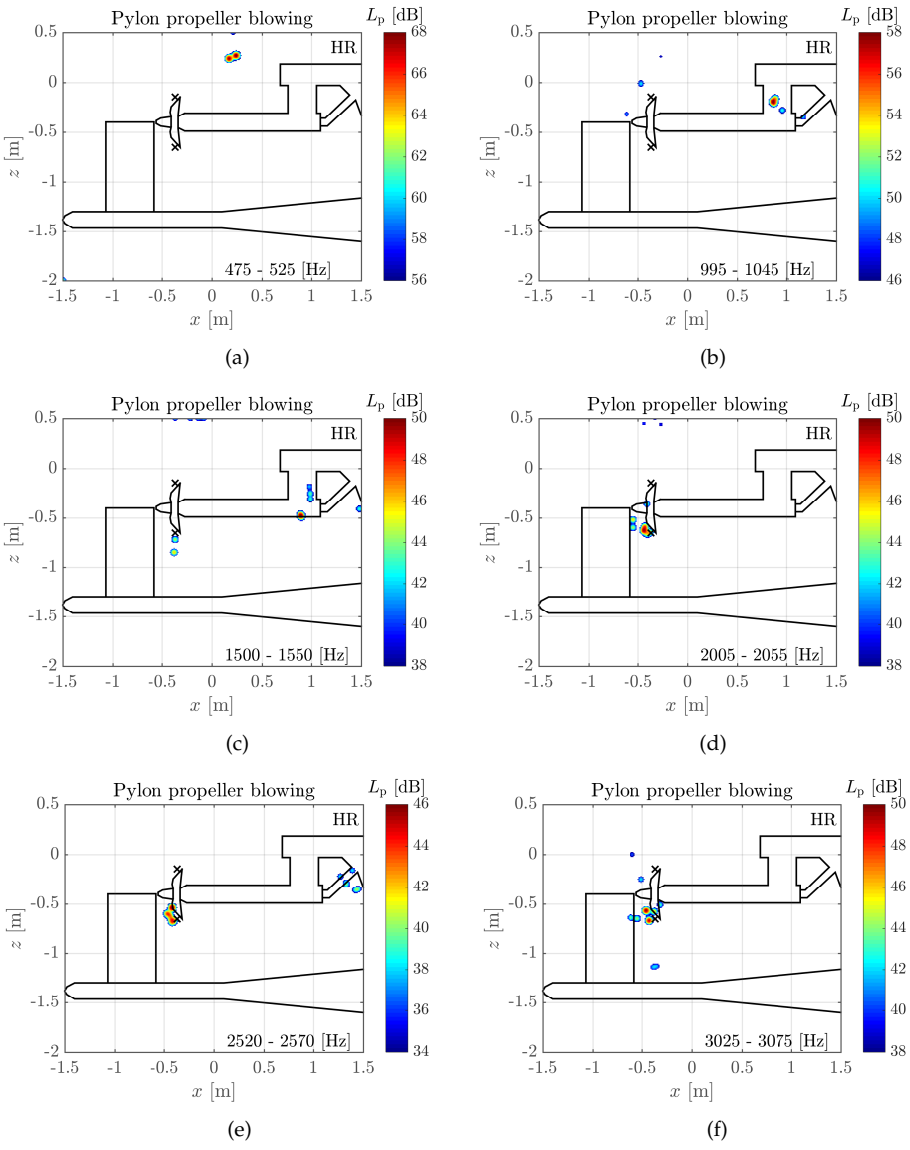

Figure 5.26: Narrowband adaptive HR-CLEAN-SC (HR) for the installed pylon and propeller with frequencies listed in the subfigures. Blowing is applied with a mass rate of 60 g/s.

5.4. Conclusions

In this chapter an in-depth analysis has been made for noise source localization and quantification of pylon interaction effects with pusher propellers. Blowing was used to assess the noise effect of negating the wake caused by the pylon. The incoming flow was set to 60 m/s for all experiments. For comparison three con-

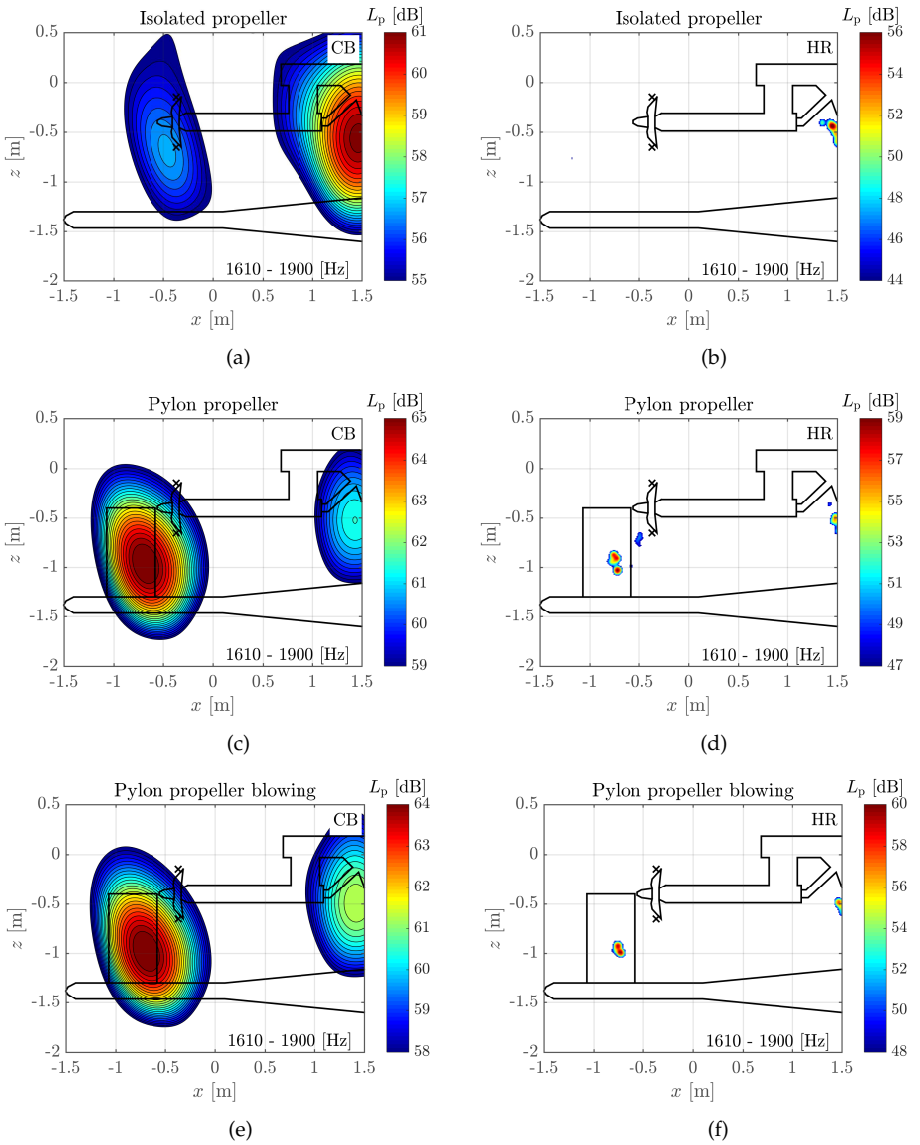

Figure 5.27: Conventional beamforming (CB) for 1610 to 1900 Hz for the isolated propeller (a), pylon propeller(c) and pylon propeller with blowing enabled (e). The same configurations using adaptive HR-CLEAN-SC can be seen in (b), (d) and (f) respectively.

figurations were considered: isolated propeller; installed pylon and propeller; and installed pylon blowing with propeller.

Due to the nature of the wind tunnel and the microphone array positioned outside the flow, convection and refraction of sound had to be taken into account during beamforming. Two calibration sources were used for this purpose. The com-

bined shift of convection and refraction was determined for the calibration sources with and without flow using beamforming. Afterwards this shift was used to correct the beamform maps for the three configurations.

Due to the aperture of the microphone array and typical low frequency noise originating from a propeller, it was expected that conventional beamforming would result in low resolution source localization. Therefore, deconvolution methods CLEAN-SC as well as high resolution method adaptive HR-CLEAN-SC were applied.

Averaged spectrum levels were obtained for the three configurations. These showed that installing the pylon results in a severe noise penalty at the blade passage frequency as well as its harmonics. Harmonics, otherwise not seen with the isolated propeller, appeared with the pylon installed. Using blowing, most of the tonal noise penalties found were reduced to the isolated propeller case. With the pylon installed the addition of broadband noise was observed with a peak at 1750 Hz. This broad peak was seen to be independent of blowing, indicating an installed pylon effect only. Previous work indicated the cause to the vortex shedding at the trailing edge.

Conventional beamforming for the band of 900 to 8000 Hz showed sources at the propeller and the support for the isolated propeller. With the installed pylon without blowing, sources were coming mainly from the propeller. This was likely due to the significant increase of the tonal components. With blowing enabled, sources appeared on the support as in the isolated propeller case and around the same position. The use of CLEAN-SC resulted in a clearer picture how sources are split around the propeller and support. For the noise disturbance around the support two separate parts were seen to be responsible. With the pylon blowing, a source was seen around the blowing channel contributing to the overall noise. Adaptive HR-CLEAN-SC which is able to reveal the positions of nearby sources, gave additional insights. Out of a group of sources seen on the propeller, some sources were found far away from the propeller plane while others stayed. However, noise sources on the support and pylon were identified at the same position independent of using adaptive HR-CLEAN-SC or CLEAN-SC. With narrowband beamforming it was possible to identify which tonal frequency components came from the support and which from the propeller. Some tonal components showed sources of even strength around the propeller and support indicating coherency. This proved to be slightly troublesome using both CLEAN-SC and adaptive HR-CLEAN-SC, where one source would either disappear or be reduced significantly, while the other retained its value. Most other frequencies did not show this behaviour and positioned sources at the propeller tip. In addition, adaptive HR-CLEAN-SC was able to localize the sources more specifically, where one source seen in CLEAN-SC would be split in multiple sources around the same position.

Beamforming for the vortex shedding frequencies resulted in sources originated on the pylon within 12 cm from the expected position at the trailing edge. Higher resolution methods did not alter the source position, but only split up the sources at the same distance from the trailing edge.

Using high resolution methods it was seen that CLEAN-SC, as a first step,

shows good improvement of the beamform maps. Coherency of sources remains, however, a problem and source strengths for these cases might deviate from the actual source strengths. CLEAN-SC does not provide resolution beyond the Rayleigh criterion while adaptive HR-CLEAN-SC does. The latter showed mixed results, where instances were seen where source localization seemed to be improved. Especially in small areas like the region around the propeller tip, it was seen that adaptive HR-CLEAN-SC was able to identify multiple sources otherwise not seen. Still, for some frequencies the sources seem to be shifted significantly off their expected positions. The adaptation of the μ-parameter during the procedure might be off for some frequencies, resulting in sources moving far off their expected positions. Also, simulations with multiple coherent *and* incoherent sources need to be assessed, preferably in two or more groups including convection and refraction of the sound to see how the method behaves.

References

[1] T. Sinnige, A. M. N. Malgoezar, D. Ragni, M. Snellen, G. Eitelberg, and L. L. M. Veldhuis, *Apian-inf: a low-speed aerodynamic and aeroacoustic investigation of pylon–pusher propeller interaction effects*, in *CEAS 2015: 5th CEAS Air and Space Conference" Challenges in European Aerospace", Delft, The Netherlands, 7-11 September 2015* (2015).

[2] T. Sinnige, D. Ragni, G. Eitelberg, and L. L. M. Veldhuis, *Mitigation of pusher-propeller installation effects by pylon trailing-edge blowing*, Journal of Aircraft, Vol. 54, No. 1 (2017), pp. 292-300. **54**, 292 (2017).

[3] T. Sinnige, D. Ragni, A. M. N. Malgoezar, G. Eitelberg, and L. L. M. Veldhuis, *Apian-inf: an aerodynamic and aeroacoustic investigation of pylon-interaction effects for pusher propellers*, CEAS Aeronautical Journal **9**, 291 (2018).

[4] G. Boyet, *Eswirp: European strategic wind tunnels improved research potential program overview*, CEAS Aeronautical Journal **9**, 249 (2018).

[5] H. Holthusen, A. Bergmann, and P. Sijtsma, *Investigations and measures to improve the acoustics characteristics of the german-dutch wind tunnel dnw-llf*, in *18th AIAA/CEAS Aeroacoustics Conference, Colorado Springs, US, AIAA Paper 2012-2176* (2012).

[6] G. Eitelberg and D. Eckert, *Some developments in experimental techniques of the german-dutch wind tunnels (dnw)*, in *21st Aerodynamic Measurement Technology and Ground Testing Conference* (2000).

[7] I. Philipsen, H. Hoeijmakers, and S. Hegen, *An overview of advanced propeller simulation tests in the german dutch wind tunnels (dnw)*, in *22nd AIAA Aerodynamic Measurement Technology and Ground Testing Conference, St. Louis, MO, USA* (2002).

[8] R. P. Dougherty, *Spiral-shaped array for broadband imaging*, (1998), US Patent 5,838,284.

[9] L. Koop, K. Ehrenfried, and S. Kroeber, *Investigation of the systematic phase mismatch in microphone-array analysis*, AIAA Paper 2005-2962 (2005), 10.2514/6.2005-2962.

[10] S. Oerlemans, L. Broersma, and P. Sijtsma, *Quantification of airframe noise using microphone arrays in open and closed wind tunnels*, International Journal of Aeroacoustics **6**, 309 (2007).

[11] P. Sijtsma, *Acoustic array corrections for coherence loss due to the wind tunnel shear layer,* in *Berlin Beamforming Conference 2008* (2008).

[12] R. Dougherty, *Turbulent decorrelation of aeroacoustic phased arrays: Lessons from atmospheric science and astronomy*, AIAA Paper 2003-3200 (2003), 10.2514/6.2003-3200.

[13] R. Ross, K. Young, R. Allen, and J. Van Ditshuizen, *Acoustic wave propagation through the shear layer of the dnw large open jet wind tunnel*, in *8th Aeroacoustics Conference, Atlanta, GA, U.S.A.* (1983).

[14] P. Sijtsma, S. Oerlemans, T. G. Tibbe, T. Berkefeld, and C. Spehr, *Spectral broadening by shear layers of open jet wind tunnels*, Tech. Rep. (National Aerospace Laboratory NLR, 2014).

[15] P. Sijtsma, R. Merino-Martinez, A. M. N. Malgoezar, and M. Snellen, *High-resolution clean-sc: Theory and experimental validation*, International Journal of Aeroacoustics **16**, 274 (2017).

[16] C. Horváth, E. Envia, and G. G. Podboy, *Limitations of phased array beamforming in open rotor noise source imaging*, **52**, 1810 (2014).

6

Ducted propeller noise shielding investigation

Ducted propellers are an interesting design choice for UAV concepts due to a potential increase of the propeller efficiency. In such designs, it is commonly assumed that introducing the duct also results in an overall noise reduction. The objective of this work is to experimentally analyze and quantify noise of a ducted propeller suitable to be installed on a medium size UAV (wingspan 5 – 10 m). A microphone array is used for recording the noise levels at each microphone position and used collectively to localize noise sources with beamforming. Different types of noise sources are considered (an omni-directional source and a propeller). In addition the effect of the presence of an incoming airflow is assessed. With no incoming airflow it is found that the duct significantly modifies the noise radiation both in the frequency and the spatial domain. With an incoming airflow, the effect of the duct on the frequency content of the signal is almost eliminated. The fact that for this case the harmonics become lower results in a reduction of the received noise levels. Also the directivity changes. These insights are of importance in efforts towards modeling the effects of ducts for complex noise sources such as propellers.

6.1. Introduction

The flexibility and wide range of possible applications make Unmanned Aerial Vehicles (UAVs) an object of continuous research. An important focus of such work is the propulsion system and ways of improving its efficiency. UAVs operate at low Reynolds numbers, meaning that the viscous effects are predominant, which decreases the efficiency of the propellers [1, 2]. A ducted propeller is a common solution to increase the efficiency of the propulsion system [3, 4], which is especially beneficial for UAVs driven by electric motors due to their limited battery capacity [5]. The duct increases the mass flow rate by reducing the slipstream contraction, increasing the overall thrust and suppressing vortex shedding. This supression leads to a reduction in tip induced drag [6, 7]. Additionally, ducts provide protection by containing the blades in the event of blade failure.

A ducted propeller is thus commonly referred to as a way of improving the propulsive efficiency of the UAV but also as a way of reducing noise emissions [8, 9], although recent work indicates a slight increment of noise when a hard wall duct, without lining, is introduced [10].

Sound propagation in a duct poses a complex problem. The total sound pressure field is expected to consist of a superposition of different propagating modes in the axial and the radial direction of the duct (azimuthal and radial modes) [11]. Higher frequency content of sound sources generates more modes, and per mode, the sound is expected to cut off at a certain frequency and decay exponentially in the lengthwise direction of the duct. This theoretical behavior is well understood for an infinite duct with and without axial flow. Work has been done to obtain approximations for semi-infinite ducts [12]. Still, prediction of sound propagation in finite ducts poses to be a difficult task and is usually estimated computationally. This becomes even more cumbersome in case a complex source such as a propeller is considered.

For propellers, the noise consists both of tonal and broadband noise [9, 13]. The different mechanisms that originate broadband noise are for example, the blade tip clearance, and the interaction of the wake generated by the fan blades with the duct boundary layer.

This work aims to experimentally assess the effect of a hard wall duct on the noise radiation of a propeller. Dimensions of the duct and the propeller used in the experiments are typical of a medium size UAV with a wingspan of $5-10\,\mathrm{m}$ [14]. The noise measurements are performed in an open-jet anechoic wind tunnel facility, with and without incoming airflow.

The design of the duct is out of scope of this work and the main objective is the characterization of the noise radiation of a simple duct, which serves as a baseline for later modifications.

An acoustic array is used to determine the noise levels at different microphone positions, providing a wide range of observer positions relative to the source. The microphones are used individually to record the levels of sound and collectively to perform beamforming. Beamforming identifies the most important sound sources in the experiments, and as such is an indispensable tool to understand the noise radiation.

As a first step, the noise behavior of an onmidirectional source in the duct without incoming flow is considered. In this way the resultant noise radiation is only due to the mode propagation and reflections inside the duct, and diffraction by the edges. The omnidirectional source is then replaced by the propeller and the two cases are compared. The propeller has a strong noise directivity and the wake generated by the blades interacts with the duct, which affects noise radiation. As a next step experiments are conducted with the ducted propeller under a uniform incoming airflow and the results are compared with the measured levels in case no flow is present.

When the duct is introduced, the propeller thrust changes, which affects the noise characteristics of the propeller. Therefore, changes in noise radiation verified between the ducted and unducted propeller can erroneously be attributed to the duct alone when in fact they are also due to changes of propeller noise. A final experiment investigates this effect by adjusting the rotational speed in order to obtain the same thrust for the isolated and ducted propeller. This clarifies how much the duct alone influences noise radiation.

This work contributes to a clearer assessment of noise attenuation by a duct and as such contributes to future designs of ducts and measures such as lining for reducing the acoustic footprint of an UAV.

From Chapter 2 the methods are used for assessing individual microphone pressure levels and beamforming. Section 6.2 discusses the experimental setup, describing the duct and propeller geometry as well as the acoustic room and the microphone array. Section 6.3 presents the findings of the different experiments. The final section presents the conclusions of this work.

6.2. Experiment

6.2.1. Duct geometry and noise sources

The duct used in the experiment is custom built at the TU Delft and is based on a Clark-Y profile. Although this is not a very efficient profile, it was selected so the propeller has constant tip clearance from x/c =0.3 m, which is useful for other experiments. This duct is not a final design, but simply a baseline for future modifications.

A cut section of the aluminum duct can be seen in Fig 6.1. The inner diameter of the duct is 30 cm, the chord length is 15 cm and the thickness is 11.7 % of the chord length.

Two different noise sources were used in the experiments: an omni-directional source and a propeller. Both sources are centered in the duct in the radial and axial direction as seen in Figure 6.1 and Figure 6.2. The distance of the source relative to the array is fixed at 1.46 m.

The omnidirectional source is a customized Miniature Sound Source type QindW developed by Qsources^{TM}. It has an oblong shape with a length of 11 cm and a diameter of 2.0 cm. The sound source has a flat frequency response from approximately 0.50 to 6.3 kHz when driven by white noise.

The small 3-blade propeller is a Master Airscrew E-MA1260T and is connected

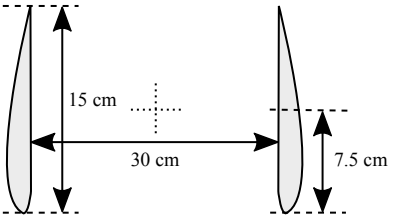

Figure 6.1: Cut section of the duct. The airfoil is a Clark-Y profile with chord of 15 cm. The inner diameter of the duct is 30 cm. The dotted cross at the center of the duct indicates the position of the omni-directional noise source and propeller.

(a) (b)

Figure 6.2: The omni-directial source (a) and the propeller (b) positioned in the center of the duct.

to a Kontronik PYRO 700-45 Brushless motor. The motor is controlled with an electronic speed control (ESC) using a Kontronik Jive PRO 80+ HV. The diameter of the propeller was initially 30 cm but it was trimmed in order to have a tip clearance of 2 mm inside the duct. The propeller was 3-D scanned (Figure 6.3) to obtain an approximate geometry and airfoil for the simulations (see Appendix D).

In the experiments with the propeller the power applied to the motor terminals was varied between 35 % to 90 % of the maximum power (210 W). In the results presented the propeller was set at 85 %, corresponding to a rotational speed of 7500 RPM. Other values of rotational speed were also analyzed but led to the same conclusions.

6.2.2. Anechoic room and microphone array configuration

The noise is measured using a microphone array consisting of 64 G.R.A.S. 40PH CCP free-field array microphones [15]. The microphones were calibrated individually using a G.R.A.S. 42AA pistonphone [16]. The data acquisition system (DAS) is composed of 5 National Instruments PXIe-4499 sound and vibration data acquisition modules controlled by a NI PXIe-8370 remote control module and a NI RMC-

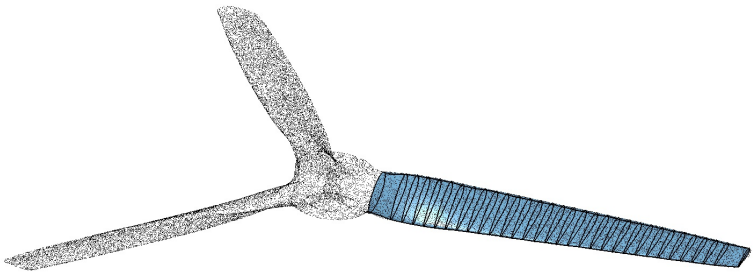

Figure 6.3: 3D scan of the propeller (black dots) and blade reconstruction in CATIA^{TM}.

8354 controller. The uncertainty associated to the measurements of the acoustic array was experimentally determined as 0.5 dB.

The structure of the array was designed to reduce acoustic reflections while allowing different microphone array configurations [17]. The free-field behavior of the anechoic room was assessed following the guidelines of the ISO3745 [18]. All frequency bands above 315 Hz fulfill the standards [19]. The average reverberation time is 0.25 s, which corresponds to the anechoic category of ISO3382 [20].The background noise was assessed and it is such that it is not expected to interfere with the noise measurements [19].

The test section is placed in the center of the anechoic room (5.4 m by 5.4 m) and has a circular shape with a 60 cm diameter. This means that the ducted propeller is contained in the jet. The experimental setup is illustrated in Figure 6.4.

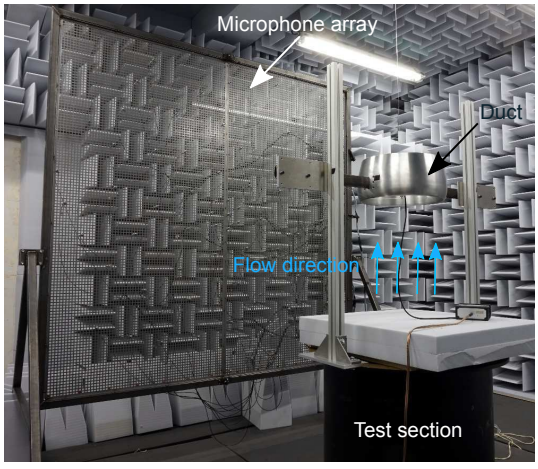

Figure 6.4: The experimental setup in the Anechoic Vertical Low Turbulence Wind Tunnel at the TU Delft. The duct is positioned in front of the TU Delft optimized array consisting of 64 microphones with an aperture of 1.9 m.

The microphone configuration used is the TU Delft Optimized Array distri-

bution [21, 22], which provides the best trade-off between the Main Lobe Width (MLW) and Maximum Side lobe Level (MSL) in beamforming. The recording time for every microphone is set to 60 s.

6.3. Results

6.3.1. Comparison of noise from ducted and unducted sources

Omni-directional source

The first case analyzed is the omni-directional source with no incoming airflow. There is no disturbance of the medium and the noise is affected only by the mode propagations of the duct, reflections and subsequent diffraction by the leading and trailing edge.

The Power Spectral Density (PSD) is obtained as an average over the microphones, and is shown in Fig. 6.5. The red line corresponds to the source only and is, as expected, approximately flat over frequencies of 400 – 6000 Hz. With the duct present, the spectrum changes, showing a periodic behavior, as expected for sound propagation in ducts. In general, there will be resonance and anti-resonance frequencies inside the duct [23, 24]. Furthermore, it is expected that different propagation modes will be generated each having its own cut-off frequency [25, 26]. As the duct used in this experiment is an open duct of small length, the exact behavior in the far field is hard to predict. Still, typical duct behavior can be seen in Fig. 6.5. As the omni-directional sound source is relatively flat in the given frequency range, Fig. 6.5 can also be seen as an approximated frequency response of the duct observed at the position of the array. To investigate whether also a change in directivity occurs due to the duct, Fig. 6.6 shows the noise changes in terms of Overall Sound Pressure Level (OSPL) at the microphone locations.

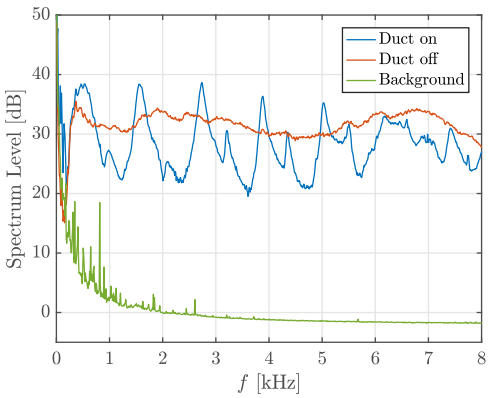

Figure 6.5: Averaged Spectrum Level over the microphones in the array for the omni-directional source in red and the modified spectrum with the duct on in blue. The green line indicates the background spectrum with the source off

Negative values indicate noise reduction when the duct is introduced (val-

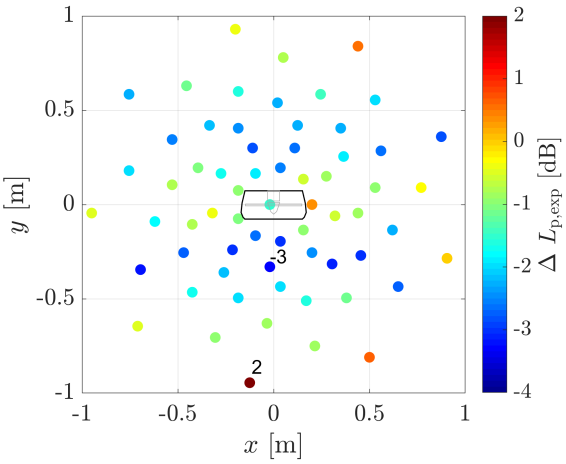

Figure 6.6: Difference in OSPL of the omnidirectional source over the acoustic array (bandpass filtered between 400 Hz to 6000 Hz) when the duct is introduced. The outline of the duct on the array is shown in the center. The red dashed lines at $y = \pm 0.35$ m indicate the region with maximum values of noise reduction.

ues calculated using Equation (2.26)) and positive values indicate amplification of noise. Two bands can be distinguished from the figure for which there is a reduction of roughly 2 to 3 dB at $y = \pm 0.35$ m (red dashed lines). At $y = 0$ m, which is at the center of the duct, there appears to be a slight reduction of the noise level of around 1 dB, a value that is close to the uncertainty associated to the measurement (0.5 dB). This region is in the shadow zone, which implies that the resulting sound is mostly due to diffraction by the duct's edges. There is some constructive interference for locations at the top and bottom of the microphone array with reinforcement of noise around 2 dB.

It can be concluded that placing the duct significantly affects the measured PSD but effects with regards to directionality are limited (3 dB).

Propeller without incoming airflow

The PSD of the propeller set at 85 % of the maximum power, with no incoming airflow, is shown in Fig. 6.7, both without duct (in red) and with duct (in blue). The spectrum of the ducted omni-directional source (in gray) is shown for comparison purposes. It is clear that there is an increase of noise for most frequencies when the duct is introduced, except for the first harmonic. Compared to the isolated propeller, the harmonics are no longer visible for frequencies above 2 kHz. Whereas the ducted propeller shows a PSD with a smooth oscillating behavior that is similar to that of the ducted omni-directional source, the frequencies of resonance and anti-resonance have changed completely.

A clear change in directivity is visible from Figure 6.8, showing the difference in OSPL with and without the duct. No regions with reduced levels of noise are

present and an increase of noise up to 12 dB is found at the top and bottom of the array. The spatial behavior is very different from that observed for the omni-directional source. The lower increase in noise level is at the center of the array, in contrast to what was observed in Figure 6.6.

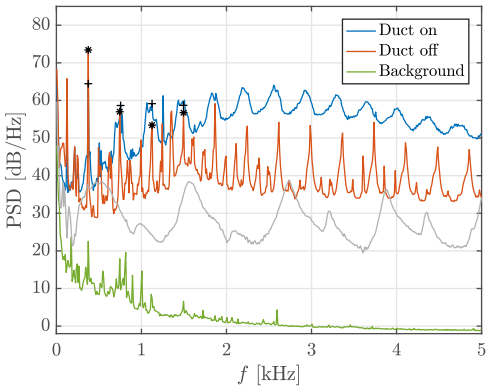

Figure 6.7: Averaged spectrum level over the microphones for the propeller at 85 % of the maximum power corresponding to a propeller speed of 7500 RPM. The stars and crosses indicate the BPF and its first three multiples for the isolated and ducted propeller, respectively. As a comparison the ducted omnidirectional sound source is shown in gray.

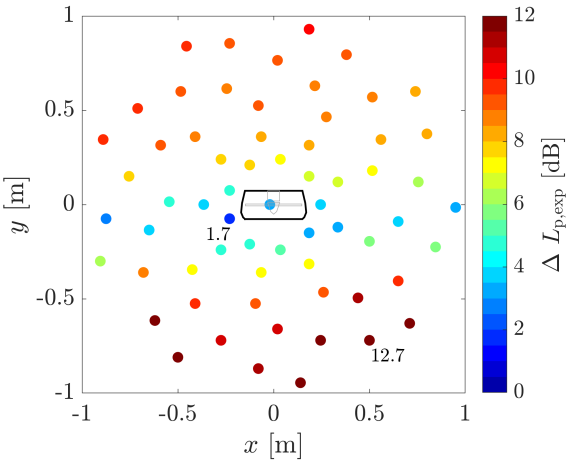

Figure 6.8: Difference in OSPL for the propeller at 7500 RPM, with no incoming airflow, in the acoustic array when the duct is introduced (filtered between 50 to 8000 Hz). The outline of the duct on the array is shown in the center.

It can be concluded that again, the PSD is completely modified due to the placement of the duct. In contrast to the omni-directional source, now only increases

in noise levels are found. This is hypothesized to be due to the creation of additional broadband noise sources as the propeller disturbs the quiescent medium and creates for example, trailing edge noise due to the propeller slipstream interaction with the duct. In addition, the directivity significantly changes due to the placement of the duct (see Figure 6.8). This means that when considering noise of a ducted propeller its radiation properties, both in the frequency and spacial domain, cannot be directly derived from the isolated propeller properties.

Propeller with incoming airflow

Figure 6.9 and Figure 6.10 show the effect of placing the duct around the propeller in case of airflow (10 m/s), on the PSD and the spatial distribution of the noise levels. The placement of the duct results in a slight increase of broadband noise, but a decrease in the levels of the harmonics. The latter is reflected in Figure 6.10, showing significant reduction in noise levels for all microphones. Compared with the situation without airflow, still the lower levels of noise are located at the center of the array.

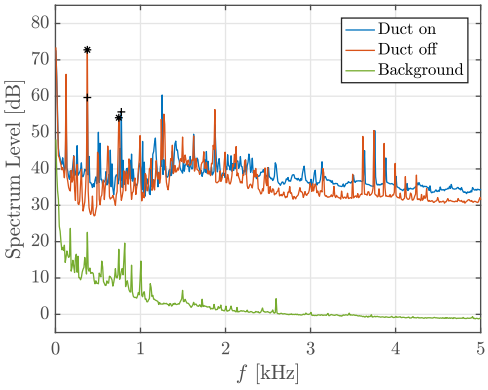

Figure 6.9: Averaged Spectrum Level over the microphones in the array for the propeller set at 85 % of the maximum power (with airflow at 10 m/s), and the modified signal with the duct on. The stars and crosses indicate the BPF and its first multiple for the isolated and ducted propeller respectively.

The effect of the duct now is very different compared to the case without airflow. Apparently the duct placed around a propeller with no incoming airflow creates an additional noise source, represented by the blue line of Figure 6.7. We hypothesize that this noise originates from the tip vortices interaction with the duct walls. These sources remain up their location as there is no airflow upstream. An observation supporting this hypothesis can be the relatively close agreement between the blue and gray line of Figure 6.7, representing a typical duct propagation. The absence of this source (blue line in Figure 6.8) in the case with airflow no longer dominates (and thus reveals) the PSD of the isolated propeller. These assumptions will be further investigated in the next section where beamforming is applied to localize noise sources.

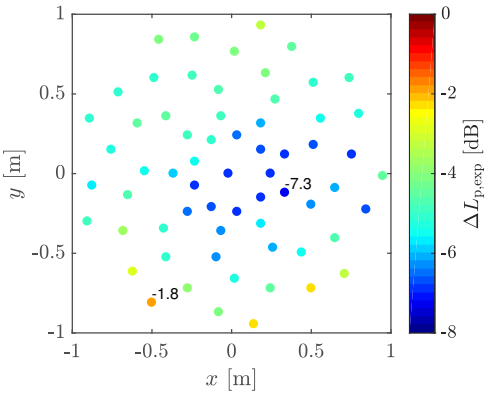

Figure 6.10: Difference in OSPL of the propeller at 7500 RPM, with incoming airflow, in the acoustic array when the duct is introduced (filtered between 50 to 8000 Hz). The outline of the duct on the array is shown in the center.

6.3.2. Beamforming

As a first step the ducted omni-directional source is considered, as this reflects a typical duct propagation configuration. Peaks and valleys of Fig. 6.5 were chosen for beamforming between 2 and 6 kHz, i.e. multiple frequency bands were chosen for either the valleys or peaks in this range. The frequency of 2 kHz was chosen as it is higher than the Rayleigh criterion so that sources at both sides of the duct can be discerned. The upper frequency of 6 kHz was chosen as it is close to the upper frequency limit for which the source could reliably emit sound omni-directional. In the case of noise reduction (Fig. 6.11a), the main source is located on the leading edge. However, for the case which corresponds to amplification of noise (Fig. 6.11b), there are sources of equal magnitude on the leading and trailing edges of the duct, reflecting variations in duct propagation with frequency.

In the case of the propeller, noise decrease is observed mostly at the first harmonic (according to the spectra of Figure 6.8) but beamforming of such a low frequency does not provide enough resolution to clearly identify noise sources. Therefore, beamforming was performed between 2 and 5 kHz.

It appears that the propeller noise sources without the duct do not lie exactly on the propeller plane as seen in Fig. 6.11c. The main source for both figures is located at the right which is the direction of the propeller rotation towards the array. Similar behavior was seen in previous work [27], where beamforming would not exactly position the sources at the propeller plane for certain tones due to the source being non-compact and coherent. Under no airflow the beamforming plots of the isolated and ducted propeller (Figure 6.11c and Figure 6.11d) are very different. Not only the strength of the noise sources increases as the duct is introduced, but also a new noise source is identified at the leading edge. This confirms the hypothesis stated before that the combined effect of the resonance (as also observed for the omni-directional source) and the interaction of the turbulent flow with the

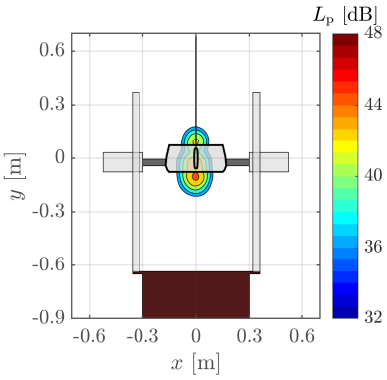

(a) Omni-directional source for valleys.

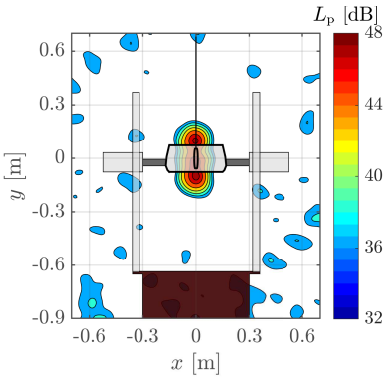

(b) Omni-directional source for peaks.

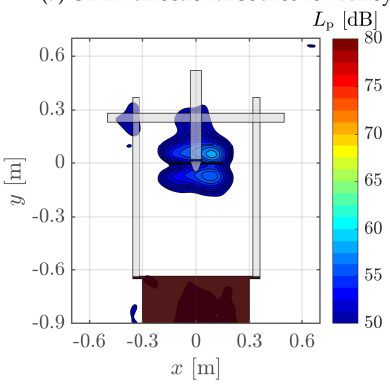

(c) Isolated propeller, with no incoming airflow.

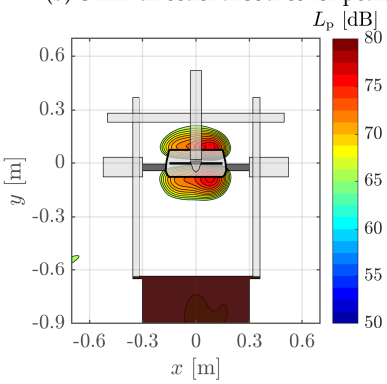

(d) Ducted propeller, with no incoming airflow.

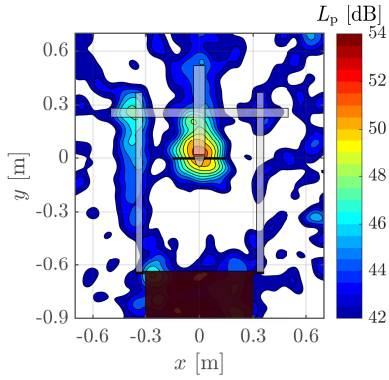

(e) Isolated propeller, with a constant incoming airflow.

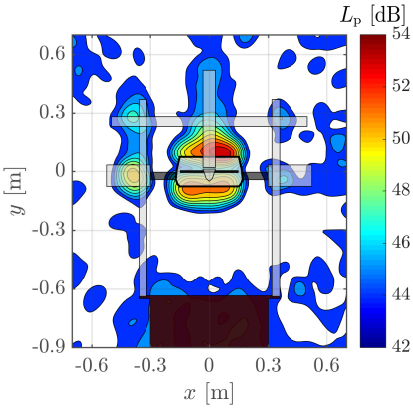

(f) Ducted propeller, with a constant incoming airflow.

Figure 6.11: Beamforming of (a) and (b) are from the spectrum in Fig. 6.5 between 2 to 6 kHz. Beamforming of (c), (d), (e) and (f) are between 2 to 5 kHz.

duct are the reasons behind an increase of noise levels.

The beamforming plots with incoming airflow of Figure 6.11e and Figure 6.11f

reinforce such assumptions since in this case there is no evidence of new noise sources when the duct is introduced. The slight increase of broadband noise between 2000 −5000 Hz is the responsible for the 2 dB increase between Figure 6.11e and Figure 6.11f. The constant airflow moves the turbulent noise sources upstream resulting in diffraction effects on the edges but not so much in duct propagation. No localized noise sources are seen on either of the duct edges.

6.3.3. Noise of a ducted propeller with thrust corrections

In the previous section, the *same power* was used for the isolated propeller and ducted propeller, and the maximum value of noise reduction found was around 7 dB (Figure 6.10). However, the duct affects the performance of the propeller, which results in a different value of thrust [10] for the same power of the motor. In this section it is evaluated if correcting the power, in order to obtain the same value of thrust for the isolated and ducted propeller, affects significantly the noise levels.

In this subsection, it is experimentally determined for which rotational speed of the propeller the value of thrust is the same with and without the duct. Subsequently the effect of the duct on noise radiation is reevaluated. The method used to determined the thrust experimentally is briefly explained below.

The thrust coefficient is approximated from

$$C_T = \frac{2\pi}{16\rho n_{\text{rev}}^2 R^4} \int_0^R \Delta p_s dr_p. \tag{6.1}$$

Here ρ is the air density, R is the radius of the propeller, n_{rev} is the number of rotations per second, r_p the distance to the root of the propeller and Δp_s is the difference in static pressure before and after the propeller disk plane.

In this work the static pressure p_s is approximated using the value of the total pressure p_t, since only small differences are expected between the total and static pressure in this experiment, conducted under low speed conditions.

The advance ratio of the propeller, J, was varied between 0.26 to 0.42 , and the incoming flow was set constant at 10 m/s. The advance ratio is calculated using

$$J = \frac{U}{2n_{\text{rev}}R}, \tag{6.2}$$

with U the undisturbed flow speed.

The thrust is determined for each value of J, both for the isolated and ducted propeller. Therefore, once all the values of J and C_{T} are determined, it is possible to determine which values of J correspond to the same C_{T} for the ducted and isolated propeller. This is done by the means of linear interpolation.

The value of Δp_t ($\approx \Delta p_s$) is determined by measuring the total pressure upstream of the propeller and in the free stream, using two Pitot tubes. The Pitot tube in the free stream is fixed and the Pitot tube upstream of the propreller disk is moved from the root to the tip of the blade in increments of 1 cm. This experimental setup is shown in Figure 6.12 and the thrust coefficients obtained for the

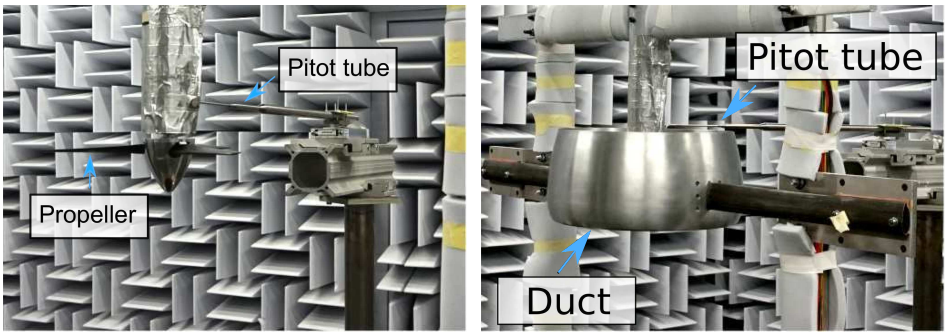

(a) Isolated propeller. (b) Ducted propeller.

Figure 6.12: Setup used in the experiment to measure the thrust of the propeller.

Advance ratio, J	0.42	0.38	0.35	0.33	0.31	0.29	0.27	0.26
Propeller C_T	2.3	3.7	4.3	5.1	5.3	5.8	5.9	6.2
Ducted propeller C_T	2.9	3.7	4.3	4.7	5.1	5.2	5.4	5.5

Table 6.1: Values of thrust coefficients C_T ($\times 10^2$) with and without the duct and with a constant incoming flow for advance ratios J.

isolated and ducted propeller are displayed in the first and second row of Table D.1, respectively.

In Appendix B, a model is used for predicting C_T to confirm that indeed the measured C_T values are of the order of magnitude as theoretically expected.

The experimental results of Table D.1 are used to find the advance ratio J for which the propeller and the ducted propeller have the same value of C_T. Table 6.2 shows the results for two selected values of C_T. For the lower values of J the thrust coefficient is higher for the isolated propeller than for the ducted propeller, indicating that the geometry of the duct is not the best design choice from a performance perspective.

The values of C_T were selected based on typical operational conditions during flight (corresponding to 75 % and 85 % of the total power). The corresponding propeller settings (J) do not differ much when corrected for the same thrust (less than 5 % of relative difference) but still can affect noise levels. Therefore the ducted propeller was set at the new values of J of Table 6.2 and the noise levels were measured again at the microphone array.

Figure 6.13 shows the histogram of the measured noise reduction by placing the duct when the rotational speed of the propeller is kept constant (red line) and when it is adjusted for the same thrust (black line). For the first case interpolated in Table 6.2, represented in Figure 6.13a, the majority of the microphones show noise reductions of -2 dB for both the adjusted and non-adjusted rotational speed. So, no significant error is obtained in this case by not considering the same thrust

Configuration	Advance ratio, J	$C_T \times 10^{-2}$
Isolated Propeller	0.310	5.3
Ducted propeller	0.302	
Isolated Propeller	0.270	5.9
Ducted propeller	0.263	

Table 6.2: Interpolated values of advance ratio (J) for equal values of the thrust coefficient.

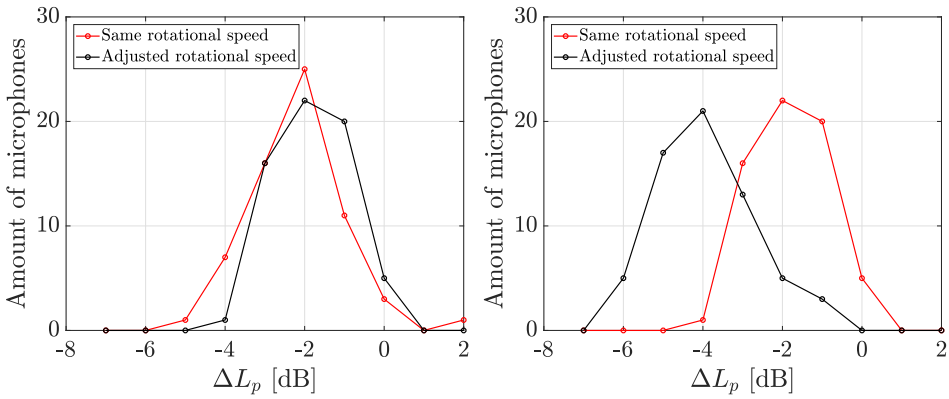

(a) $C_T = 5.3 \times 10^{-2}$. (b) $C_T = 5.9 \times 10^{-2}$.

Figure 6.13: Histogram of ΔL_p: a) Propeller and ducted propeller generating thrust equal to $C_T = 5.3 \times 10^{-2}$ and $C_T = 5.9 \times 10^{-2}$.

for the isolated and ducted propeller. However, for the second value of C_T, the histograms of Figure 6.13b are different. Before considering the same thrust for the isolated and ducted propeller the majority of the microphones correspond to noise reduction values of around -6 dB, and after the correction, this value is around -2 dB.

Therefore, the values of noise reduction due to placing a duct as presented in the previous section with airflow (seen in Fig. 6.10) were overestimated. This leads to the conclusion that the noise reduction for the same propeller rotational speed is also a consequence of the reduction of thrust caused by placing the propeller inside the duct and not only of the duct acting as a barrier between the noise source and observers.

6.4. Conclusions

The rapid increase of the UAV applications has initiated the need for capabilities to model the noise radiated by these systems. Typical UAV propulsion systems consist of a ducted propeller and as such a model for the noise radiation of these ducted propellers is needed. In this contribution, as a step towards the develop-

ment of these models, experiments have been conducted to investigate the characteristics of noise radiation from ducted propellers.

From experiments with an omni-directial noise source and a propeller, without incoming airflow, it is found that using measurements for the unducted case will not provide relevant information for the case with a duct placed around the noise source. The noise radiation behavior, once the duct is placed, changes drastically. Either complex modeling or dedicated measurements are needed to predict the noise radiation for the ducted case.

In case airflow is present the situation changes completely, and now the noise radiation from the unducted and ducted case are highly similar. It is hypothesized that in this case the turbulent structures created by the propeller are convected with the airflow and that as such these moving sources do not result in a source configuration that induces duct propagation.

The effects of the duct on the PSD are limited to:

- Increasing broadband noise,
- Decrease of the first harmonics.

For the case considered an overall decrease in noise level was found. But as stated above, the PSD of the unducted case is representative for the ducted case.

As such, this work has shown that using source characteristics measured without a duct can be used for modeling purposes in case a duct is introduced, since always airflow will be present in real applications. This especially holds for the PSD but can also be an initial assumption for the directivity.

For assessing the effect of the duct on the overall sound level, it is important to ensure that the aerodynamic performance of the propeller does not change due to the presence of the duct. An experimental investigation concluded that significant deviations can be present if this effect is not taken into account.

References

[1] R. MacNeill and D. Verstraete, *Blade element momentum theory extended to model low Reynolds number propeller performance*, The Aeronautical Journal **121** (2017), 10.1017/aer.2017.32.

[2] L. Oliveira, H. Muñoz, and F. Catalano, *Aerodynamic Analysis of High Rotation and Low Reynolds Number Propeller*, in *48th AIAA/ASME/SAE/ASEE Joint Propulsion Conference & Exhibit* (American Institute of Aeronautics and Astronautics, Atlanta, Georgia, 2012).

[3] S. Yilmaz, D. Erdem, and M. S. Kavsaoglu, *Performance of a ducted propeller designed for UAV applications at zero angle of attack flight: An experimental study*, Aerospace Science and Technology **45**, 376 (2015).

[4] P. Martin and C. Tung, *Performance and flowfield measurements on a 10-inch ducted rotor VTOL UAVs*, Tech. Rep. (Army Research Development and Engineering Command Moffett Field CA Aviation Aeroflight Dynamics Directorate, 2004).

[5] O. Gur and A. Rosen, *Optimizing electric propulsion systems for unmanned aerial vehicles,* Journal of aircraft **46**, 1340 (2009).

[6] A. Akturk and C. Camci, *Influence of tip clearance and inlet flow distortion on ducted fan performance in vtol uavs,* in *6 AHS Forum*, Vol. 338 (2010).

[7] S. Yilmaz, D. Erdem, and M. Kavsaoglu, *Effects of duct shape on a ducted propeller performance,* in *51st AIAA Aerospace Sciences Meeting including the New Horizons Forum and Aerospace Exposition, Grapevine (Dallas/Ft. Worth Region), Texas, AIAA Paper 2013-0803* (2013).

[8] M. D. Moore, *NASA personal air transportation technologies*, Tech. Rep. (SAE Technical Paper, 2006).

[9] R. Oleson and H. Patrick, *Small aircraft propeller noise with ducted propeller,* in *4th AIAA/CEAS Aeroacoustics Conference* (1998) p. 2284.

[10] J. L. Pereira, *Hover and wind-tunnel testing of shrouded rotors for improved micro air vehicle design* (University of Maryland, College Park, 2008).

[11] W. Devenport and S. Glegg, *Aeroacoustics of Low Mach Number Flows: Fundamentals, Analysis, and Measurement* (Academic Press, 2017).

[12] G. Gabard and R. Astley, *Theoretical model for sound radiation from annular jet pipes: far-and near-field solutions,* Journal of Fluid Mechanics **549**, 315 (2006).

[13] J. E. Marte and D. W. Kurtz, *A review of aerodynamic noise from propellers, rotors, and lift fans* (Jet Propulsion Laboratory, California Institute of Technology, 1970).

[14] P. Fahlstrom and T. Gleason, *Introduction to UAV systems* (John Wiley & Sons, 2012).

[15] *G.R.A.S. Sound & Vibration - 40 PH CCP Free-field array microphone,* `https://www.gras.dk/products/special-microphone/array-microphones/product/178-40ph` (), accessed: 2010-01-14.

[16] *G.R.A.S. Sound & Vibration - 42AA Pistonphone class 1,* `https://www.gras.dk/products/calibration-equipment/reference-calibrator/product/255-42aa` (), accessed: 2010-01-14.

[17] C. Vlemmix, *Acoustic Array Design: The design of a reconfigurable phased microphone array for aeroacoustic wind tunnel measurements,* (2017).

[18] *ISO norm 3745 - Acoustics - Determination of sound power levels and sound energy levels of noise sources using sound pressure - Precision methods for anechoic rooms and hemi-anechoic rooms,* Tech. Rep. 3 (International Organization for Standardization, 2012) ().

[19] R. Merino-Martinez, *Microphone arrays for imaging of aerospace noise sources,* (2018).

[20] *ISO norm 33382 - Acoustics - Measurements of room acoustics parameters,* Tech. Rep. 1 (International Organization for Standardization, 2012) ().

[21] A. M. N. Malgoezar, M. Snellen, P. Sijtsma, and D. G. Simons, *Improving beamforming by optimization of acoustic array microphone positions,* in *6th Berlin beamforming conference, BeBeC-2016-S5* (2016).

[22] S. Luesutthiviboon, A. M. N. Malgoezar, M. Snellen, and D. G. Simons, *Maximizing source discrimination performance by using an optimized array and adaptive high-resolution clean-sc beamforming,* in *Berlin Beamforming Conference 2018* (2018).

[23] U. Ingard and V. K. Singhal, *Effect of flow on the acoustic resonances of an open-ended duct,* The Journal of the Acoustical Society of America **58**, 788 (1975).

[24] A. Curtis, P. Nelson, S. Elliott, and A. Bullmore, *Active suppression of acoustic resonance,* The Journal of the Acoustical Society of America **81**, 624 (1987).

[25] L. E. Kinsler, A. R. Frey, A. B. Coppens, and J. V. Sanders, *Fundamentals of acoustics,* Fundamentals of Acoustics, 4th Edition, by Lawrence E. Kinsler, Austin R. Frey, Alan B. Coppens, James V. Sanders, pp. 560. ISBN 0-471-84789-5. Wiley-VCH, December 1999. **1** (1999).

[26] S. W. Rienstra, *Fundamentals of duct acoustics,* Von Karman Institute Lecture Notes (2015).

[27] C. Horváth, E. Envia, and G. G. Podboy, *Limitations of phased array beamforming in open rotor noise source imaging,* **52**, 1810 (2014).

7

Conclusions

The use of microphone arrays proves to be an indispensable tool for aeroacoustic experiments. Knowledge of the underlying principles of beamforming as well as acoustic propagation is very important and can result in obtaining good (or bad) results. Using this knowledge, advanced methods can be developed to restrict the uncertainty in results. The performance was seen to depend on several factors.

Optimization techniques were employed to minimize interpretation errors in comprehending the source map. This provided good results for the attainable spatial resolution for the main lobe surpassing Rayleigh's criterion, as well as providing a region around the main lobe which is seen to be clear of sidelobes. Still, in practice some limitations cannot be circumvented.

When dealing with low frequency noise the limitation of the microphone array's aperture has to be taken into account. The dominant propeller noise is usually at low frequencies (typically up to 500 Hz for the blade passage), and can therefore limit localization. In general, better spatial resolution can be achieved by either having a larger aperture array or positioning the array closer to the source. Due to experimental restrictions, limitations of positioning the array are not uncommon. Therefore determining the frequency content of interest for the measurement can help to determine if beamforming results are acceptable. The use of an optimized array or high resolution methods somewhat circumvent these restrictions, but source identification can still prove to be limited for these low frequencies.

The appearance of sidelobes was seen to be reduced in an area of interest using the optimization procedure. For further reduction, increasing the amount of microphones is helpful, and generally the sidelobe level goes down with increasing number of microphones. Especially for the higher frequencies the improvement will be seen to be evident. Further increasing the amount of microphones for a fixed frequency can appear stagnant in regards to beamforming, but improvement is still likely to be seen for a higher frequency. For the experiments performed in this thesis sidelobes were not seen to be of big concern, indicating that increasing the number of microphones (for a fixed aperture) is not required.

For wind tunnel experiments with flow, convection and refraction of sound has to be accounted for with great care, since this will, regardless of the method, result

in incorrect source positions. It was seen that a simple refraction correction can provide very good results. To make the correction easy to perform, it is preferable to have the wind tunnel nozzle geometry resulting in a shear layer parallel to the microphone array plane. Otherwise, a calibration sound source has to be used to determine the offset in position. The offset can depend on where the source is positioned in the flow, so it is still preferable to use (at least a simple) refraction correction which can be based on a calibration source as well.

In general, coherent sources are not specifically taken into account during the beamform process. For aeroacoustic experiments sources are more often than not coherent. In this regard conventional beamforming (even though it is not a specific coherence method) can still provide additional information which other advanced methods cannot. This can be of importance for airfoil noise or interaction noise of a propeller. For airfoil noise the distributed sources can be coherent while a harmonic of a propeller can highly interact with the (supporting) structure.

Therefore, wind tunnel experiments conventional beamforming should always be applied and any additional (advanced) method should be seen as a convenient addition. It is also very helpful to perform beamforming for scan planes perpendicular to the array plane. Using only a single plane parallel to the microphone array requires to know the beamforming distance in advance. This is not necessarily known for every experiment and several noise sources can arise at different beamforming distances. Using the optimization method of Chapter 4 for source positioning in 3-D, or an additional scan plane perpendicular to the parallel scan plane, can help to confirm (or find) the proper beamform distance. More planes can also further help in finding disturbances (such as reflections) in the wind tunnel environment which can possibly affect results. For using perpendicular planes, attention has to be put on the spatial resolution in the direction perpendicular to the array. For a planar array the resolution is very low.

It would be recommended to use 3-D conventional beamforming to obtain all noise sources in a wind tunnel environment as a first step using a very coarse grid (and possibly part of troubleshooting). Having seen the general noise source behaviour, and confirming the absence of external disturbances, scan planes can subsequently be selected with a fine grid for an area of interest. To overcome the low resolution in the third dimension, a microphone array configuration could be developed encompassing the whole test section. As no parametric model exist for effectively configuring a 3-D microphone array, an optimization procedure would provide to be the ideal method. To determine the positions for these microphones, a set of desired constraints can be formulated and imposed on the objective function. The objective function can be a generalized form of the ones presented in Chapter 3. To restrict the computational times, high resolution optimization methods would only be recommended after deciding the planes of interest from the 3-D beamforming result.

A

Objective function for array optimization I

The integrand of Eq. (3.16) can be written as

$$\begin{aligned}\left|\sum_{n=1}^{N} \mathrm{e}^{-i(k_x x_n + k_y y_n)}\right|^2 &= \sum_{m=1}^{N}\sum_{n=1}^{N} \mathrm{e}^{-i(k_x x_m + k_y y_m)} \mathrm{e}^{i(k_x x_n + k_y y_n)} \\ &= \sum_{m=1}^{N}\sum_{n=1}^{N} \mathrm{e}^{-i[k_x(x_m - x_n) + k_y(y_m - y_n)]}.\end{aligned} \tag{A.1}$$

It is convenient to transform the integration to spherical coordinates using

$$\begin{aligned}k_x &= k\cos(\theta)\sin(\phi) \\ k_y &= k\sin(\theta)\sin(\phi)\end{aligned}, \tag{A.2}$$

where the relation can be seen in Figure 3.2. The change in coordinates (k_x, k_y) to (θ, ϕ) requires the change of 'surface' element $\mathrm{d}k_x \mathrm{d}k_x$ to $\mathrm{d}\theta\mathrm{d}\phi$. We can get this from the Jacobian using

$$\mathbf{J} = \begin{bmatrix} \frac{\partial k_x}{\partial \theta} & \frac{\partial k_x}{\partial \phi} \\ \frac{\partial k_y}{\partial \theta} & \frac{\partial k_y}{\partial \phi} \end{bmatrix} = \begin{bmatrix} k\sin(\theta)\sin(\phi) & -k\cos(\theta)\cos(\phi) \\ -k\cos(\theta)\sin(\phi) & -k\sin(\theta)\cos(\phi) \end{bmatrix}, \tag{A.3}$$

and the change in surface element for the integral according to

$$\mathrm{d}k_x \mathrm{d}k_y = |\det(\mathbf{J})|\,\mathrm{d}\theta\mathrm{d}\phi = k^2\cos(\phi)\sin(\phi)\mathrm{d}\theta\mathrm{d}\phi \tag{A.4}$$

Using Eq. (A.1) and the coordinate transformation given by Eqs. (A.2), Eq. (3.16) becomes

$$J(\vec{x_1}, \cdots, \vec{x_N}) = \frac{1}{N^2}\sum_{m=1}^{N}\sum_{n=1}^{N}\int_{\phi_{min}}^{\phi_{max}}\int_{0}^{2\pi} k^2\cos(\phi)\sin(\phi)\mathrm{e}^{-ik\sin(\phi)[(x_m - x_n)\cos(\theta) + (y_m - y_n)\sin(\theta)]}\mathrm{d}\theta\mathrm{d}\phi. \tag{A.5}$$

Integration takes place over all angles, $0 \leq \theta \leq 2\pi$, this means that the addition of *any* constant angle β will not change the result of the integration, i.e.

$$\int_0^{2\pi} f(\theta)\,\mathrm{d}\theta = \int_0^{2\pi} f\left(\theta+\beta\right)\mathrm{d}\theta. \tag{A.6}$$

Applying this to Eq. (A.5) results in

$$J(\vec{x_1},\cdots,\vec{x_N}) = \frac{1}{N^2}\sum_{m=1}^{N}\sum_{n=1}^{N}\int_{\phi_{min}}^{\phi_{max}}\int_0^{2\pi} k^2\cos(\phi)\sin(\phi)\mathrm{e}^{-ik\sin(\phi)[(x_m-x_n)\cos(\theta+\beta)+(y_m-y_n)\sin(\theta+\beta)]}\mathrm{d}\theta\mathrm{d}\phi. \tag{A.7}$$

To obtain a solution we will use for the constant angle β

$$\tan(\beta) = \frac{y_m - y_n}{x_m - x_n}. \tag{A.8}$$

In Figure A.1 we can see the relation between the angle β and the distance d_{mn}

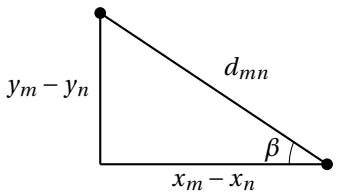

Figure A.1: Relation between the angle φ and the sides of the triangle.

between two microphones n and m. From this figure we get

$$\begin{aligned} x_m - x_n &= d_{mn}\cos(\beta) \\ y_m - y_n &= d_{mn}\sin(\beta), \end{aligned} \tag{A.9}$$

with

$$d_{mn} = \sqrt{(x_m - x_n)^2 + \left(y_m - y_n\right)^2}. \tag{A.10}$$

The exponent of the integrand in Eq. (A.7) can be rewritten as

$$\begin{aligned} &(x_m - x_n)\cos(\theta+\beta) + (y_m - y_n)\sin(\theta+\beta) \\ &\quad = d_{mn}\left[\cos(\beta)\cos(\theta+\beta) + \sin(\beta)\sin(\theta+\beta)\right] \\ &\quad = d_{mn}\cos(\theta), \end{aligned} \tag{A.11}$$

which simplifies Eq. (A.7) to

$$J(\vec{x_1},\cdots,\vec{x_N}) = \frac{1}{N^2}\sum_{m=1}^{N}\sum_{n=1}^{N}\int_{\phi_{min}}^{\phi_{max}} k^2\cos(\phi)\sin(\phi)\int_0^{2\pi}\mathrm{e}^{-ik\sin(\phi)d_{mn}\cos(\theta)}\mathrm{d}\theta\mathrm{d}\phi. \tag{A.12}$$

The inner integral over θ can be written as

$$\int_0^{2\pi} \mathrm{e}^{-ik\sin(\phi)d_{mn}\cos(\theta)}\,\mathrm{d}\theta = \int_0^{2\pi} \cos\left[-k\sin(\phi)d_{mn}\cos(\theta)\right]\mathrm{d}\theta + i\int_0^{2\pi} \sin\left[k\sin(\phi)d_{mn}\cos(\theta)\right]\mathrm{d}\theta, \tag{A.13}$$

where the integrand of the imaginary part is an odd function with period 2π which results in the integral being zero. For the integral containing the cosine, it can be graphically seen as the integrand to be a periodic function with frequency 2θ. This results in

$$\int_0^{2\pi} \mathrm{e}^{-ik\sin(\phi)d_{mn}\cos(\theta)}\,\mathrm{d}\theta = 2\int_0^{\pi} \cos\left[k\sin(\phi)d_{mn}\cos(\theta)\right]\mathrm{d}\theta \tag{A.14}$$

The integral on the right-hand side of Eq. (A.14) is known as the Bessel function of the first kind with zero order, i.e. $\int_0^{\pi} \cos\left(k\sin(\phi)d_{mn}\cos(\theta)\right)\mathrm{d}\theta = \pi J_0(k\sin(\phi)d_{mn})$. Using the Bessel function we can write the objective function as

$$J(\vec{x_1},\cdots,\vec{x_N}) = \frac{2\pi}{N^2}\sum_{m=1}^{N}\sum_{n=1}^{N}\int_{\phi_{min}}^{\phi_{max}} k^2\cos(\phi)\sin(\phi)J_0\left(k\sin(\phi)d_{mn}\right)\mathrm{d}\phi. \tag{A.15}$$

For the case $m = n$, $d_{mn} = 0$ so $J_0(0) = 1$. Using this given information we can split up the summation as

$$J(\vec{x_1},\cdots,\vec{x_N}) = \frac{\pi}{N^2}\left[\sum_{n=1}^{N}\int_{\phi_{min}}^{\phi_{max}} 2k^2\cos(\phi)\sin(\phi)\mathrm{d}\phi + 2\sum_{m=1}^{N}\sum_{\substack{n=1\\ n\neq m}}^{N}\int_{\phi_{min}}^{\phi_{max}} k^2\cos(\phi)\sin(\phi)J_0\left(k\sin(\phi)d_{mn}\right)\mathrm{d}\phi\right]. \tag{A.16}$$

Using $\mathrm{d}(\sin^2\phi) = 2\cos(\phi)\sin(\phi)\mathrm{d}\phi$ the first part on the right-hand side is

$$\sum_{n=1}^{N}\int_{\phi_{min}}^{\phi_{max}} k^2\mathrm{d}(\sin^2\phi) = \sum_{n=1}^{N}\left[k^2\sin^2\phi\right]_{\phi_{min}}^{\phi_{max}} = Nk^2\left[\sin^2(\phi_{max}) - \sin^2(\phi_{min})\right]. \tag{A.17}$$

The second part can be solved using the substitution $u = k\sin(\phi)d_{mn}$, $\mathrm{d}u = k\cos(\phi)d_{mn}\mathrm{d}\phi$ to get

$$\int_{\phi_{min}}^{\phi_{max}} k^2\cos(\phi)\sin(\phi)J_0\left(k\sin(\phi)d_{mn}\right)\mathrm{d}\phi = \frac{1}{d_{mn}^2}\int_{k\sin(\phi_{min})d_{mn}}^{k\sin(\phi_{max})d_{mn}} uJ_0(u)\,\mathrm{d}u, \tag{A.18}$$

which can be related to the derivative of $J_1(u)$ as

$$\begin{aligned}\int_{k\sin(\phi_{min})d_{mn}}^{k\sin(\phi_{max})d_{mn}} uJ_0(u)\,\mathrm{d}u &= \int_{k\sin(\phi_{min})d_{mn}}^{k\sin(\phi_{max})d_{mn}} \frac{\mathrm{d}}{\mathrm{d}u}\left[uJ_1(u)\right]\mathrm{d}u \\ &= k\sin(\phi_{max})d_{mn}J_1[k\sin(\phi_{max})d_{mn}] - k\sin(\phi_{min})d_{mn}J_1[k\sin(\phi_{min})d_{mn}]\end{aligned}. \tag{A.19}$$

A

Using Eq. (A.17), Eq. (A.18) and Eq. (A.19) in Eq. (A.16) and the fact $d_{mn} = d_{nm}$ we get for the objective function

$$J(\vec{x}_1, \cdots, \vec{x}_N) = \frac{\pi k}{N^2} \Big(Nk \left[\sin^2(\phi_{max}) - \sin^2(\phi_{min}) \right] + 4 \sum_{m=1}^{N-1} \sum_{n=m+1}^{N} \frac{\sin(\phi_{max}) J_1[k \sin(\phi_{max}) d_{mn}] - \sin(\phi_{min}) J_1[k \sin(\phi_{min}) d_{mn}]}{d_{mn}} \Big), \tag{A.20}$$

where we notice the summation boundary changed reducing the amount of calculations for J by half.

B

Microphone array limits

Additional simulations for various microphone configurations are performed to see the difference and effect on beamforming. The resuls can be seen in Fig. B.1 and Appendix B for a source at the origin with SPL of 100 dB and frequency of 2000 Hz.

Figure B.1 depicts a 106 and 2016 microphone configuration. For an increasing amount of microphones beamforming of a source set at the origin shows a pattern resembling more the Airy pattern.

In Appendix B the intersection at $y = 0$ m is given. Here it can clearly be seen that by increasing the amount of microphones by a large amount, the maximum sidelobe level reaches slowly the theoretical value for an infinite amount of microphones at $100 - 17.57 = 82.43$ dB. The sidelobes depends strongly on the amount of microphones.

In Fig. B.3 it can be seen that the spatial resolution, i.e. the main lobe width, depends on the array aperture. Here only the intersection at $y = 0$ m is depicted.

As a last example the microphone configuration in Fig. B.1 (b) is taken and the result of beamforming at $y = 0$ m is seen in Fig. B.4 for the four different steering vector formulation presented in Section 2.4.2. For the given microphone array configuration it is first seen that both Formulation I and IV do not provide the correct level at 100 dB. For the sidelobe, differences are noticeable between all four formulations. Formulation II gives the highest levels of sidelobes followed by Formulation III, I and IV.

B

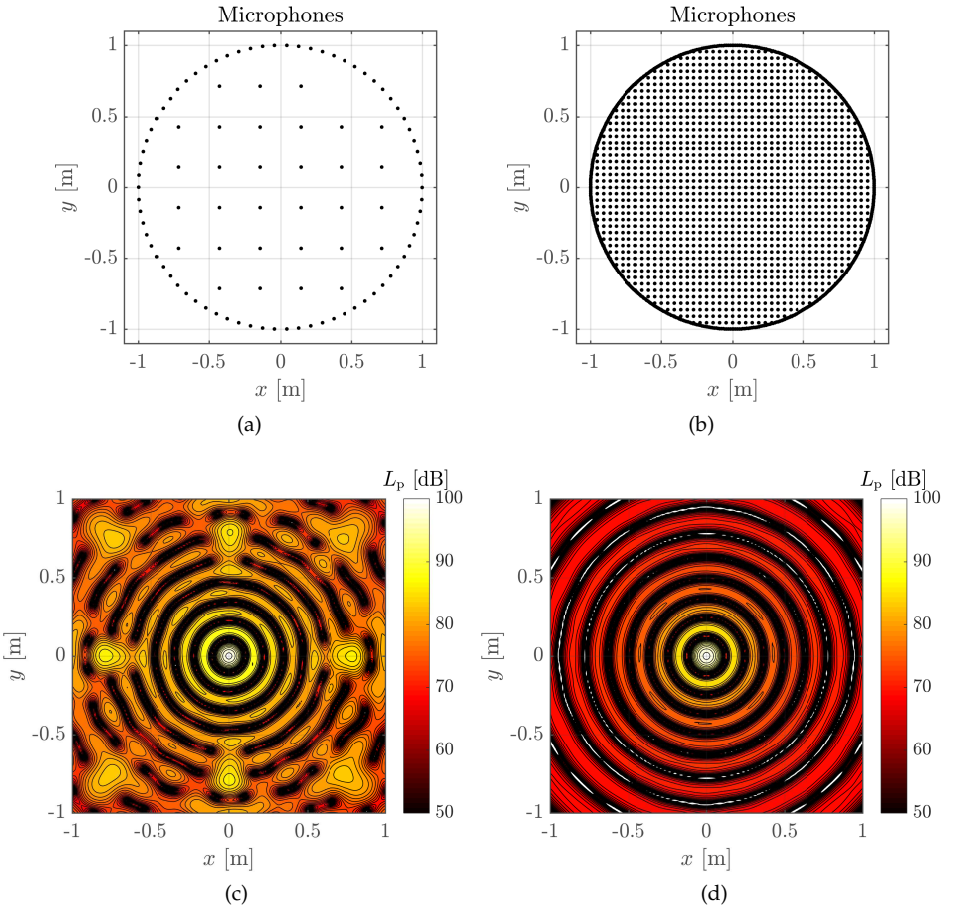

Figure B.1: The effect on beamforming for increasing microphone numbers. In (a) a 106 and (b) 2016 microphone configuration.

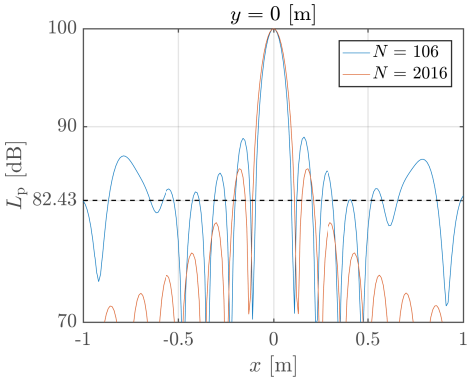

Figure B.2: Intersection of the two microphone configurations given in Fig. B.1. The lowest attainable MSL is given by the dashed line.

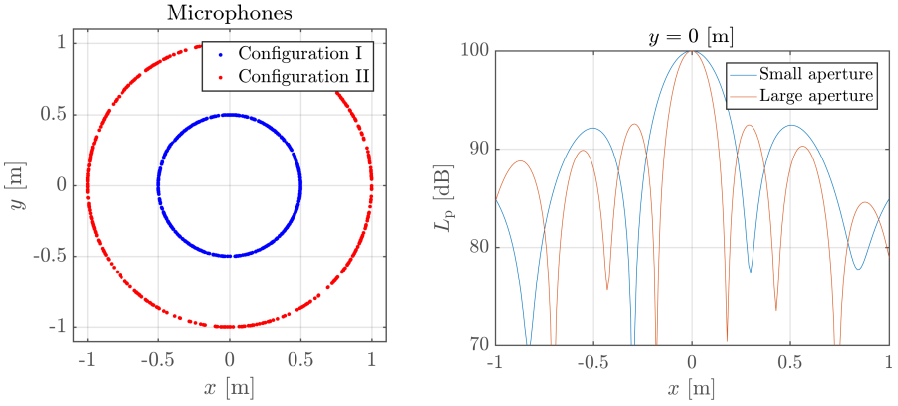

Figure B.3: Two circular configurations where microphone are solely placed at aperture distance (a) and (b) the beamforming result at $y = 0$ m.

B

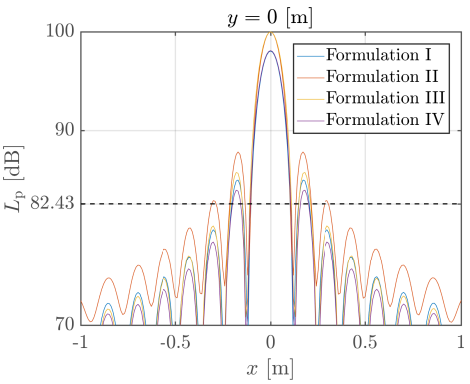

Figure B.4: Intersection of the microphone configurations given in Fig. B.1 (b) and the beamforming result $y = 0$ m for four different steering vector formulations. The lowest attainable MSL is given by the dashed line.

C

Pylon-propeller noise interaction: additional beamforming

C.1. Higher frequency beamforming

In Chapter 5 for the propeller pylon configuration additional small peaks were seen in the spectrum level. This was apparent for the case of the pylon installed and blowing disabled. Here, beamforming for the two other peaks are presented as well. As a comparison the other configurations are included for the same frequency range. The maps can be seen in Figs. C.1 to C.3

C.2. Broadband peak, 1610 - 1900 [Hz]: CLEAN-SC and xy-plane

In Section 5.3.7 only results were shown for conventional beamforming and adaptive HR-CLEAN-SC. This subsection adds the comparison between CLEAN-SC and adaptive HR-CLEAN-SC shown in Fig. C.4.

For beamforming in the xy plane Fig. C.5 is given. Only conventional beamforming is presented here. Beamforming in xy plane results in a top-view of the experiment indicated by the outline. Beamforming was performed at the $z = -0.97$ m, which is around the maxima found in Fig. 5.27 (c) - (f). For the isolated propeller the source is seen on the support. For both pylon propeller configurations, the source is found close to the trailing edge of the pylon, off by 10 to 12 cm.

C.3. Settings for CLEAN-SC and adaptive HR-CLEAN-SC

The settings for using the beamforming methods are presented here as well for reproduction purposes. For CLEAN-SC $\lambda = 480$ was used for the width of the clean

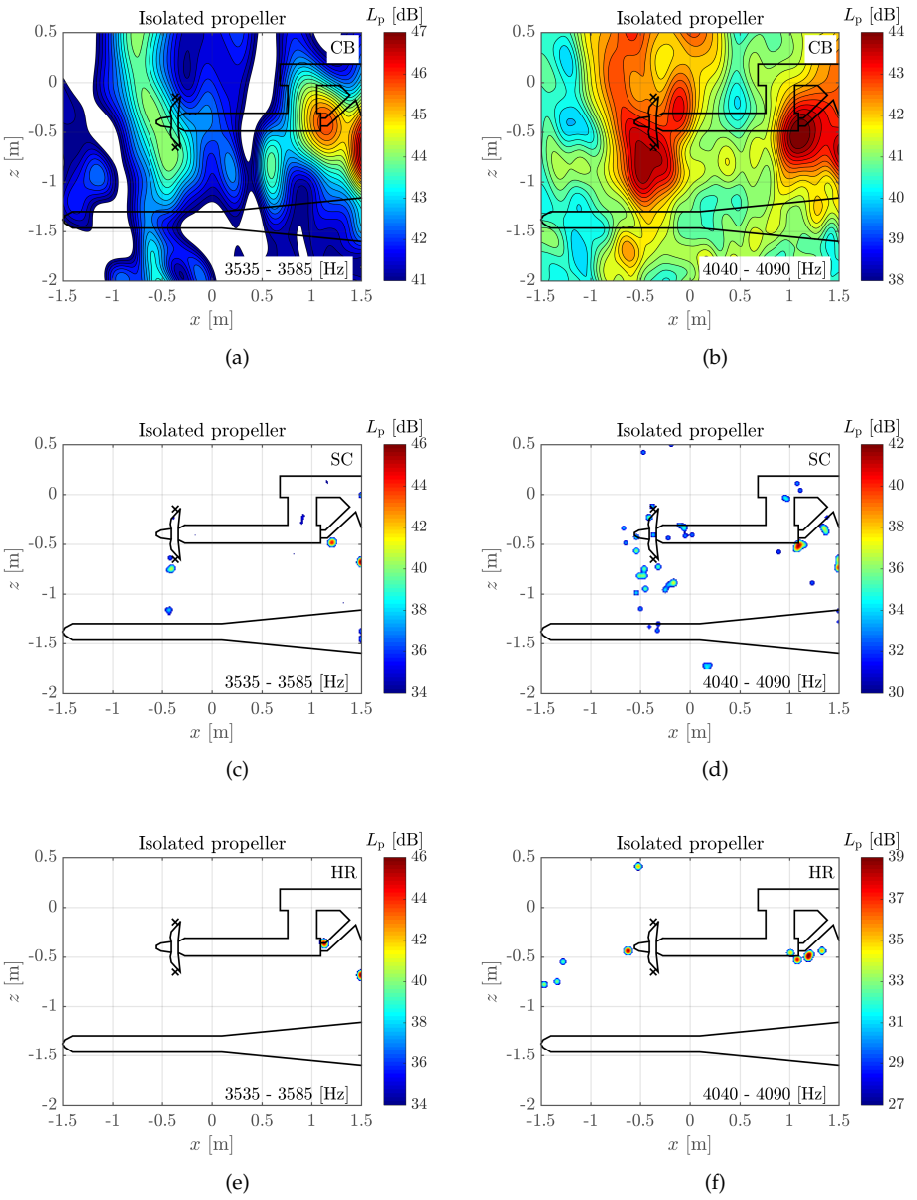

Figure C.1: Narrowband beamforming for the isolated propeller with frequencies listed in the subfigures. Conventional beamforming (CB) in (a) and (b); CLEAN-SC in (c) and (d); and adaptive HR-CLEAN-SC in (e) and (f).

beams. The loop gain was set to $\phi = 0.99$ For the iteration procedure the stop condition is used that the dirty map does not include more info the the previous

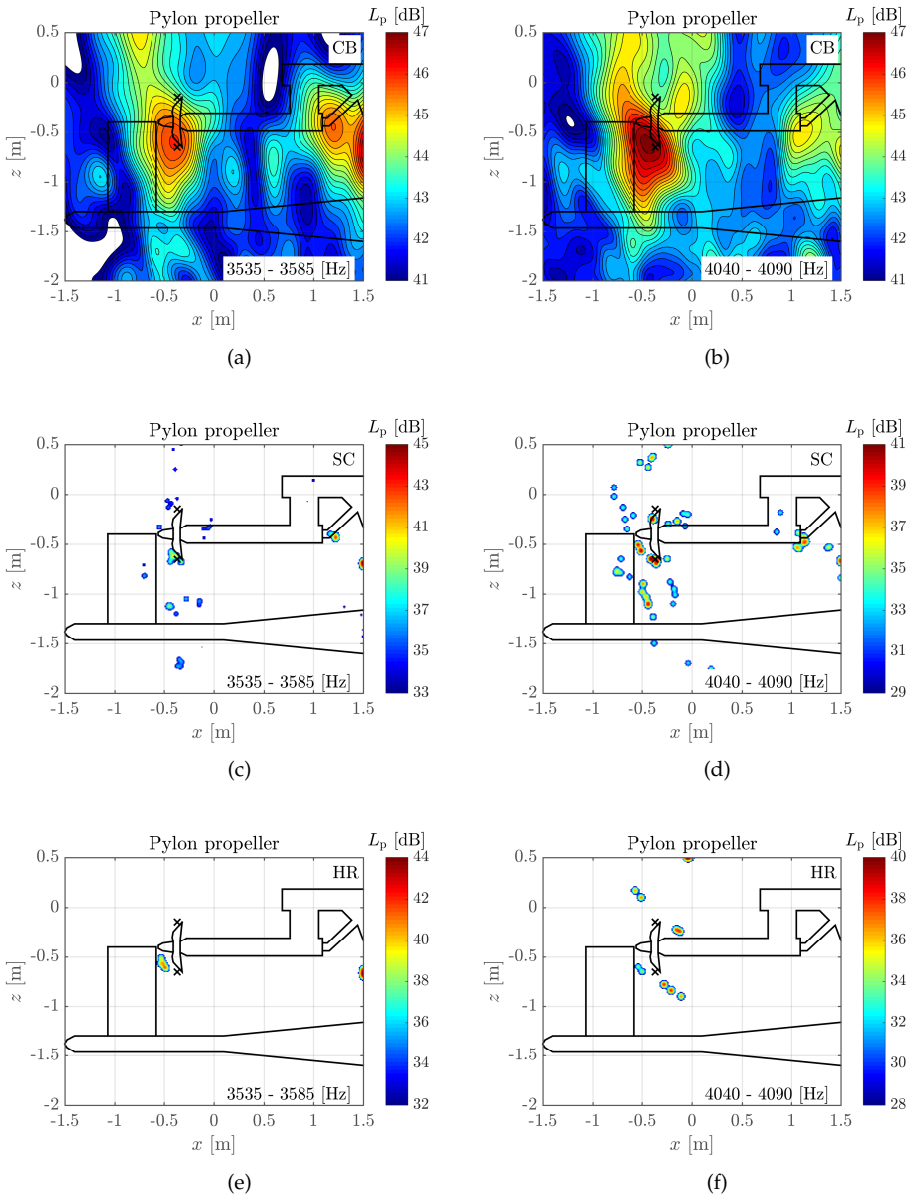

Figure C.2: Narrowband beamforming for the installed pylon and propeller with frequencies listed in the subfigures. Conventional beamforming (CB) in (a) and (b); CLEAN-SC in (c) and (d); and adaptive HR-CLEAN-SC in (e) and (f).

'cleaner' map or that the iteration does not exceed more than 10 for a single frequency in consideration. Negative pressures during the iteration are removed and

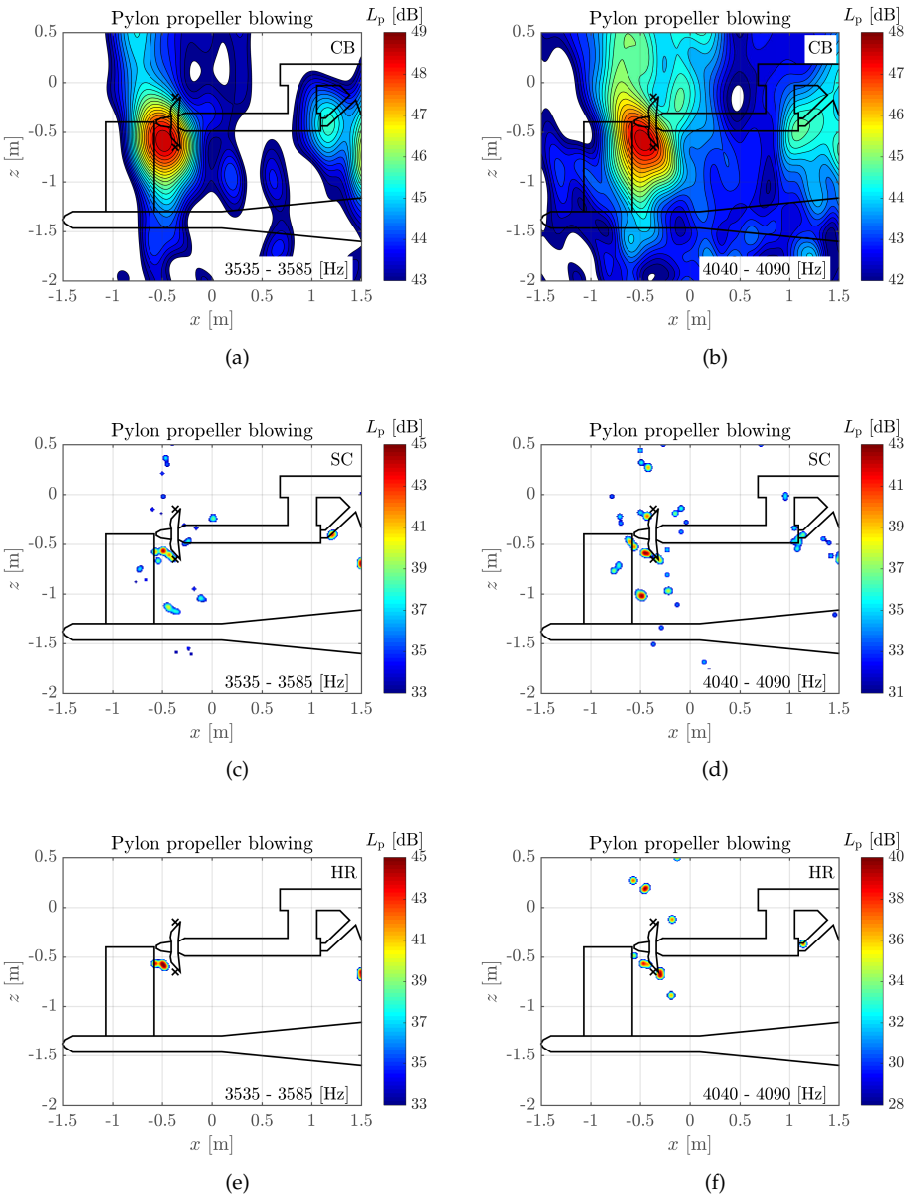

Figure C.3: Narrowband beamforming for the installed pylon and propeller with frequencies listed in the subfigures. Blowing is applied with a mass rate of 60 g/s. Conventional beamforming (CB) in (a) and (b); CLEAN-SC in (c) and (d); and adaptive HR-CLEAN-SC in (e) and (f).

the result of the clean beam maps are summed. No use is made of diagonal removal of the CSM.

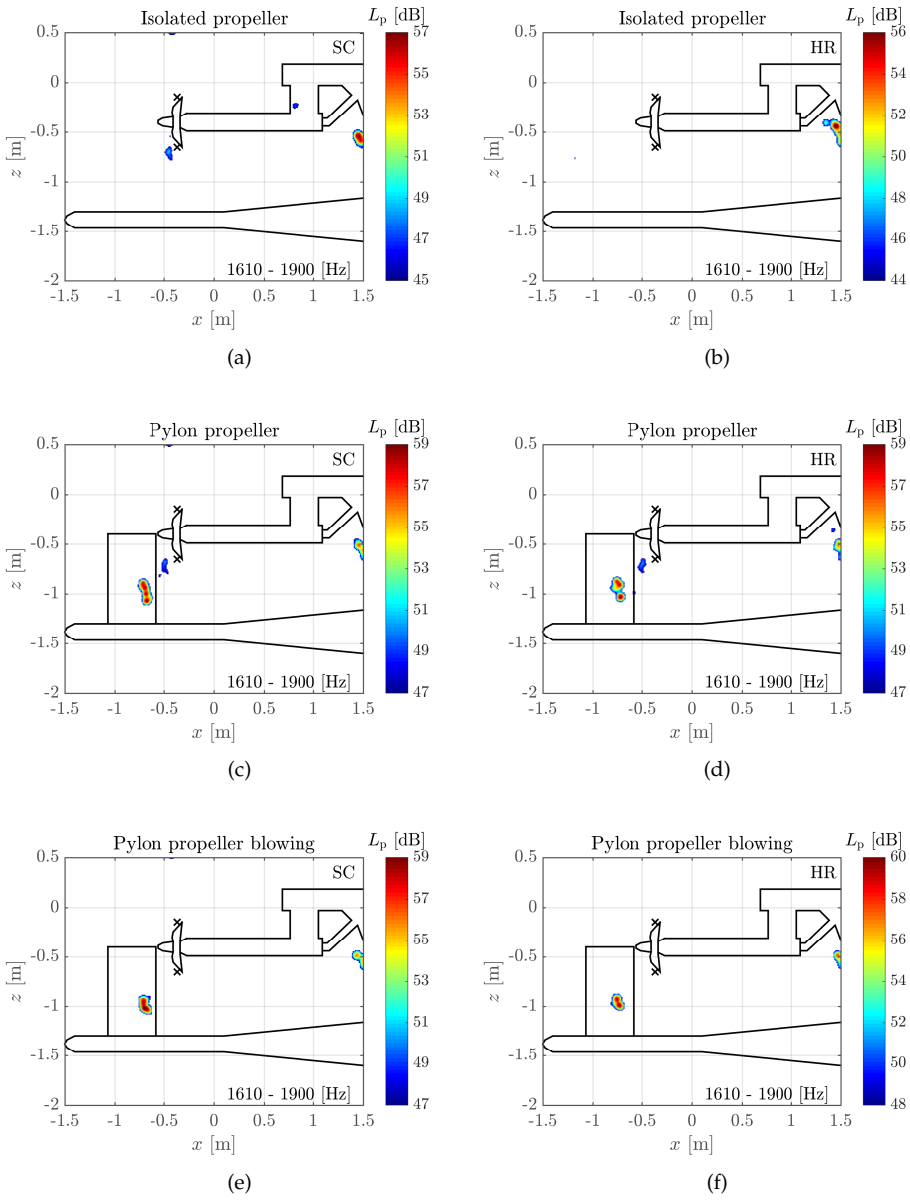

Figure C.4: CLEAN-SC (SC) and adaptive HR-CLEAN-SC (HR) for 1610 to 1900 Hz for the three configurations.

For the adaptive HR-CLEAN-SC, an additional parameter setting was required. This was the number of sources for which a peak found using CLEAN-SC is ob-

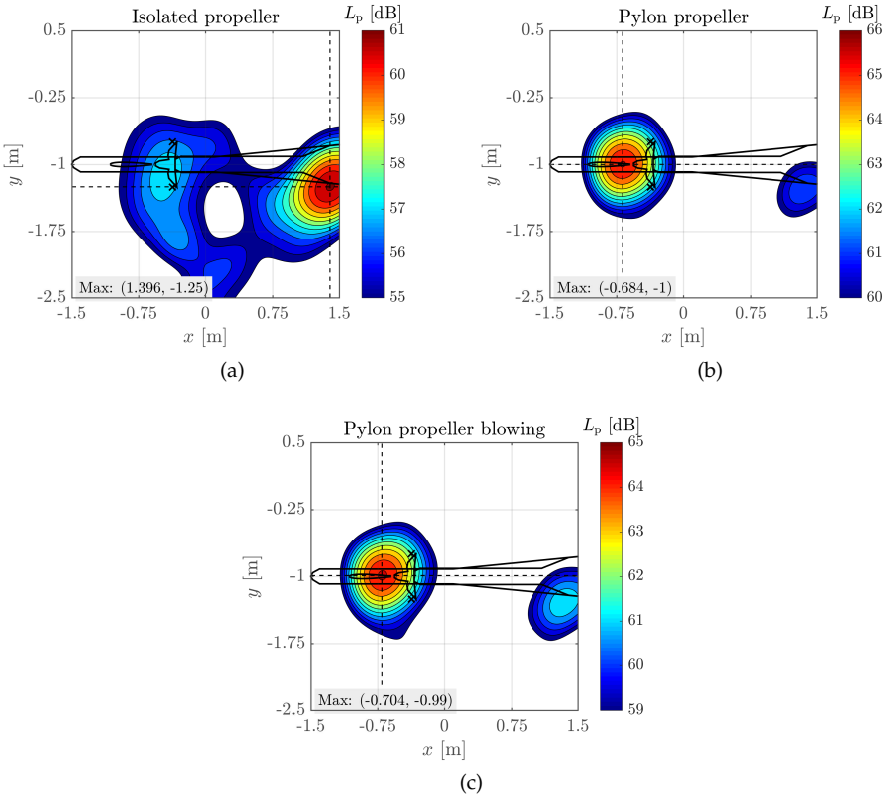

Figure C.5: Conventional beamforming (CB) in the xy plane at $z = -0.97$ m for the three configurations (a) isolated propeller, (b) pylon propeller and (c) pylon propeller with blowing. The configuration and support can be seen to be outlined. The crosses indicate the two ends of the propeller plane.

fuscated by, this not necessarily limits the amount of sources found per frequency. The setting throughout the chapter was set to 2. No clear difference was found by increasing the number to 3 or 4, with the exception of the increase in computational time.

C.4. Towards a better shear layer correction

It was observed that a shear layer correction[1] can be applied as well obtaining good (and similar as in Chapter 5) results by finding an approximate distance to the shear layer using the calibration sources. This can be achieved using an estimate from the equation

$$U_{\text{corrected}} = U_{\text{flow}} \frac{z_{\text{bf}} - z_{\text{sl}}}{z_{\text{bf}}}, \tag{C.1}$$

for z_{sl}. This assumes a microphone distribution varying in x and y only, or Eq. (C.1) has to be applied for every microphone differently. Another assumption is that the

distance of each scan point to the shear layer z_{sl} is constant.

For determining the distnace, the measured position of the calibration source, $\mathbf{x}_{calib}$, is important. This value can then be compared to the maximum value found using conventional beamforming, $\mathbf{x}_{bf,max}$. By varying z_{sl}, it is possible to find

$$z_{sl} \quad \text{subject to} \quad \|\mathbf{x}_{calib} - \mathbf{x}_{bf,max}\| = 0 \tag{C.2}$$

Having obtained the z_{sl} from the calibration sources, this value can be used in turn for the experiment using any beamforming algorithm with convection (and without the need of any other shear layer correction). The more calibration data used the better the estimate,

$$\hat{z}_{sl} = \frac{1}{n} \sum_{n} z_{sl,n}. \tag{C.3}$$

It provides a single value for z_{sl} for the combined wind tunnel array configuration which can have a complicated shear layer geometry. For z_{bf} an average value gave good results for the experiment in Chapter 5, as the used scan planes had some variation in z.

References

[1] P. Sijtsma, *Acoustic beamforming for the ranking of aircraft noise*, Tech. Rep. (National Aerospace Laboratory NLR, 2012).

[2] S. F. Ramdin, *Prandtl tip loss factor assessed*, Master's thesis, Aerodynamics, Wind Energy & Propulsion, Delft University of Technology (2017).

D

Predicting C_T

For determining the values of C_T in Section 6.3.3, the value of Δp_s was approximated as Δp_t. No significant differences are expected between the static and total pressure due to the low value of the airflow used in the experiments (10 m/s). In this Appendix, the values of C_T determined experimentally are compared with predictions using a BEM model, in order to verify if the C_T values are of the same order of magnitude.

The BEM model used for the predictions was developed in TU Delft with the purpose of propeller design. Several steps are required to obtain realistic input for the BEM model. The propeller was first scanned using a 3D scanner and reconstructed in CATIA™. The geometrical characteristics of the blade were extracted from the CAD model and introduced in XFOIL in order to obtain the lift and drag polars, a required input for the BEM model.

The predictions and experimental results are first compared in terms of Δp_t, to verify if the BEM model was correctly applied, since this value was determined directly in the experiment without any approximations. Figure D.1 shows the Δp_t curves determined experimentally (solid lines) for the isolated propeller at different values of J. The dotted lines are obtained with the BEM model, and only three are presented for clarity of the plot. As expected, the Δp_t increases for lower values of J, and the prediction and experimental curves are very similar, except at the tip. This difference is caused by the Prandtl tip loss factor implemented in the BEM mode, which significantly underpredicts the tip loss [2].

Still, the agreement indicates that there are no major flaws in the implementation of the BEM model.

Table D.1 displays the values of C_T for the isolated propeller, determined experimentally and with the BEM model. The values are of the same order of magnitude and get closer for lower values of J, i.e. higher values of rotational speed, which are of more interest for the UAV operational conditions. The agreement between modelled and measured C_T values gives confidence in the experimental setup and subsequent analyses.

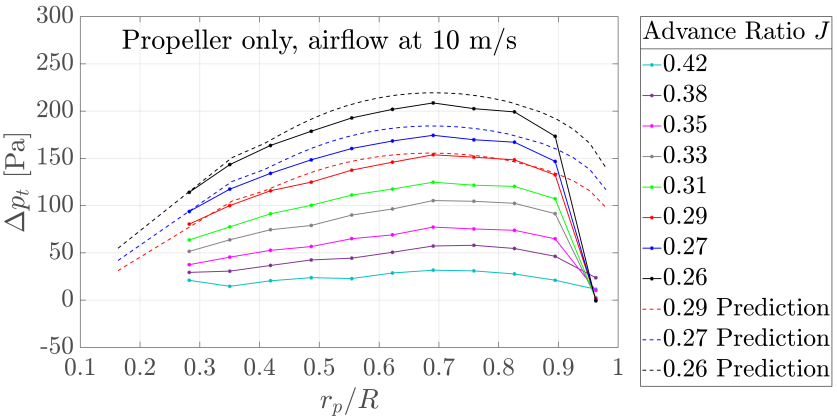

Figure D.1: Difference over the blade span between the total pressure above the propeller disk and the free stream total pressure, Δp_t. Solid lines are determined from experiment and dotted lines from the BEM model.

Advance ratio, J	0.42	0.38	0.35	0.33	0.31	0.29	0.27	0.26
Propeller C_T	2.3	3.7	4.3	5.1	5.3	5.8	5.9	6.2
Propeller prediction C_T	1.5	2.6	3.4	4.1	4.6	5.1	5.5	5.8

Table D.1: Experimental and predictions values of the thrust coefficient C_T ($\times 10^2$), obtained for the propeller under an incoming flow, for advance ratios J.

E

3-D beamforming

This section shows some results from various measurements using 3-D beamforming. The results show that this approach can provide additional information of the test setup. Having some reference objects, such as an array or nozzle, can help for better understanding where disturbances originate from. Figure E.1 shows beamforming the propeller noise in a band of 1 to 8 kHz. In Fig. E.1 (b) the result is seen when the wing is positioned between the array and the propeller. Similar conclusions can be drawn as in Section 6.3.1 where it is clearly seen that sources are moved to the leading and trailing edges. 3-D beamforming clearly shows that the strongest source is coming from the support of the propeller-motor when the wing is placed. The clear advantage is seen of using 3-D beamforming for troubleshooting. In this case the propeller noise shielding study can provide erroneous values, as a high disturbance is confirmed not originating from the propeller and mostly free of shielding.

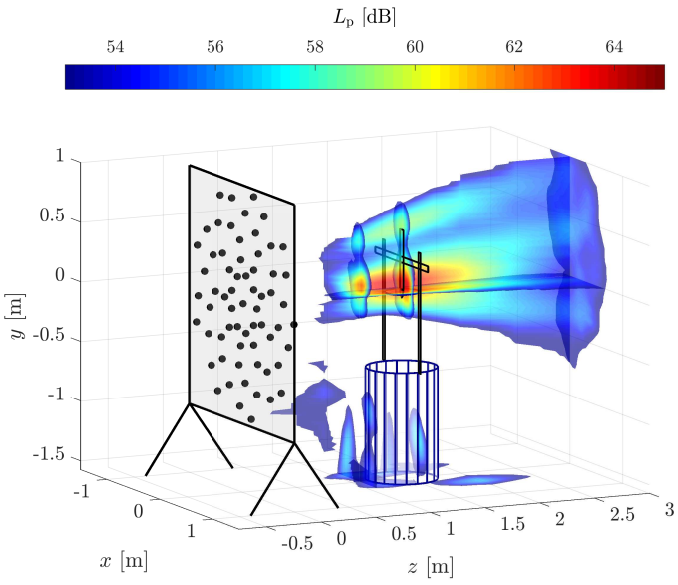

(a)

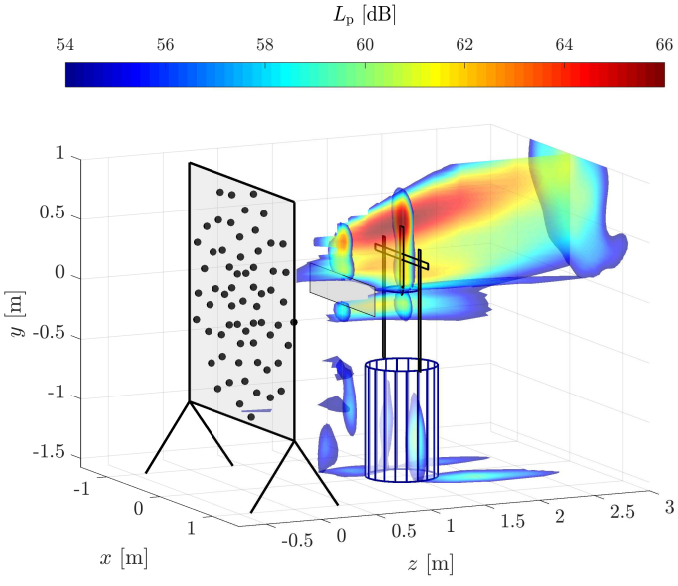

(b)

Figure E.1: 3-D conventional beamforming between 1 to 8 kHz without the wing (a) and with the wing acting as the shielding object (b). The microphone array, nozzle, wing, propeller and support can be seen as well.